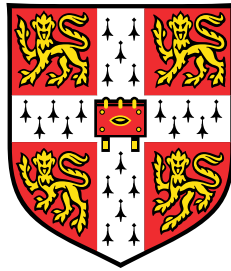


Flow and mixing in complex porous media



Japinder S. Nijjer

Supervisor: Dr. D.R.Hewitt
Dr. J.A.Neufeld

Department of Applied Mathematics and Theoretical Physics
University of Cambridge

This dissertation is submitted for the degree of
Doctor of Philosophy

Churchill College

June 2019

To Nani (1921-2018)

Declaration

This thesis is the result of my own work and includes nothing which is the outcome of work done in collaboration except as declared in the Preface and specified in the text. It is not substantially the same as any that I have submitted, or, is being concurrently submitted for a degree or diploma or other qualification at the University of Cambridge or any other University or similar institution except as declared in the Preface and specified in the text. I further state that no substantial part of my thesis has already been submitted, or, is being concurrently submitted for any such degree, diploma or other qualification at the University of Cambridge or any other University or similar institution except as declared in the Preface and specified in the text. It does not exceed the prescribed word limit for the relevant Degree Committee.

Japinder S. Nijjer
June 2019

Acknowledgements

First and foremost, I would like to thank my two supervisors Dr. Duncan Hewitt and Dr. Jerome Neufeld for their mentorship, guidance, and overall support over the last few years. Their unending enthusiasm was incredibly contagious, and always motivated me to keep going. They were always willing to chat, and I will always be grateful that I had the opportunity to work with, and learn from both of them.

I would also like to thank everyone in the broader DAMTP and Cambridge community. In particular, I am especially grateful for the stimulating conversations had during the many CCS, DAMTP, and ITG coffees and lunches. Special thanks also go out to everyone in the lab who helped build and set up my experimental apparatus, namely David, Colin, Paul, Andy, John and Mark.

I have been lucky to have been surrounded by so many amazing people who have made my time at Cambridge unforgettable. Special thanks go out to DAMTP members old and new: the Canadians, Alexis and Jason; my fellow basketball enthusiast, Zhong; the GBBO crew, Emily and Amalia; and the croquet/table tennis/football/Churchill lunch club Kanwar, David, Niall and Jamie as well as so many others.

Thank you Priya for being there every step of the way and for making every day easier and more enjoyable than the last. Thank you for listening to my sometimes incoherent ramblings and being a rock of emotional and nutritional support.

Finally, I'd like to thank my entire family. Thank you mom, dad and Aman for instilling in me the importance of hard work and for your love and support. Special shout-out to my big brother Bobby for always looking out for me, and for being someone I have always looked up to.

Financial support for this work was provided by the Gates Cambridge Scholarship, as well as, Churchill College Cambridge and the Department of Applied Mathematics and Theoretical Physics.

Abstract

The flow and mixing of fluids in complex porous media is important in a large range of environmental settings, from groundwater flows to the geological storage of carbon dioxide (CO₂). This thesis investigates two distinct and fundamental features of such flows; the mixing of miscible fluids of differing viscosity and density in both homogeneous and heterogeneous porous media, and the flow-induced deformation of soft, poroelastic media. In all cases the approach is to combine detailed numerical or experimental observations with simplified mathematical models of the key physical phenomena. Throughout this thesis the results are considered in the context of field-scale CO₂ sequestration case studies.

In chapter 2, the dynamics of the miscible viscous-fingering instability are investigated. It is found that the dynamics can be divided into three regimes: at early times, the flow is well described by linear stability theory; at intermediate times, the flow is dominated by non-linear finger interactions; and at late times, the flow is composed of an exponentially slowing single-finger exchange-flow. In the course of this study, a critical Péclet number for the instability in the first regime is identified, an improved averaged model for the flow in the second regime is derived and a detailed explanation of the asymptotic fate of the fingering instability in the third regime is provided.

In chapters 3 and 4, miscible displacements in layered heterogeneous porous media are studied. Specifically, the combined effects of viscosity and permeability variations are examined. It is found that when the permeability variations are large compared to the viscosity variations or when the injected fluid is more-viscous than the ambient, the interface is hydrodynamically stable and the flow tends to follow the permeability structure imposed. When the injected fluid is less-viscous than the ambient fluid and the viscosity variations are much larger than the permeability variations, the interface is unstable and there is a competition between the evolving wavelength of the viscous fingering and the imposed wavelength of the permeability structure. At intermediate times, depending on the relative magnitude of the viscosity and permeability variations, this competition leads to different dynamics including channelling and fingering. At

late times, the dynamics are instead dominated by shear-enhanced (Taylor) dispersion, which asymptotically becomes independent of the viscosity ratio.

In chapter 5, miscible displacements are considered in which the injected and ambient fluids have different densities as well as viscosities. A range of different behaviour is observed depending, on the relative importance of viscosity and density variations, including fingering, gravitational slumping and shear-enhanced dispersion. The different dynamical regimes are identified along with their dependence on the governing parameters, and simple reduced-order models for the evolution of the concentration field are derived.

The final portion of this thesis (chapter 6) examines the fluid-driven compaction of a deformable porous medium. Experimental studies of water injection into a water-saturated packing of soft hydrogel spheres are presented. Solutions to a one-dimensional axisymmetric model are discussed and comparisons to the experimental results are made. In doing so, particular focus is given to the role of confinement on both the steady-state and transient dynamics of the system.

Table of contents

List of figures	xv
1 Introduction	1
1.1 Carbon capture and storage (CCS)	1
1.2 Constraints on the safe storage of CO ₂	3
1.3 Instabilities and mixing in porous media	4
1.4 Flow through deformable porous media	6
1.5 Thesis structure	7
2 Miscible viscous fingering in homogeneous porous media	11
2.1 Introduction	11
2.2 Problem formulation	13
2.2.1 Governing equations	13
2.2.2 Boundary conditions	15
2.2.3 Diagnostic quantities	16
2.2.4 Numerical Method	17
2.3 Fingering pattern and regimes	18
2.3.1 Scalings	21
2.4 Early- and intermediate-time regimes	23
2.4.1 Early times: linearly unstable regime	23
2.4.2 Intermediate times: non-linear coalescence regime	27
2.5 Late times: single-finger exchange-flow regime	32
2.5.1 Numerical observations	32
2.5.2 Asymptotic model	34
2.5.3 Total convective mixing	36
2.6 Discussion and Conclusions	37
2.6.1 Summary	37
2.6.2 Implications for carbon sequestration	39

3	Stable displacements in layered porous media	41
3.1	Introduction	41
3.2	Problem Formulation	43
3.3	Uniform viscosity displacements $R = 0$	45
3.3.1	Early-time behaviour: initial diffusion	47
3.3.2	Intermediate-time behaviour: advection	47
3.3.3	Late-time behaviour: shear-enhanced dispersion	48
3.4	Small viscosity variations $ R < \sigma$	51
3.4.1	Vertical flow equilibrium	51
3.4.2	Intermediate-time behaviour: viscously coupled advection	52
3.4.3	Late-time behaviour: viscosity-dependent shear-enhanced dispersion	54
3.5	Large stabilizing viscosity variations $ R > \sigma, R < 0$	58
3.5.1	Concentration model	59
3.5.2	Comparison to numerical simulations	61
3.6	Non-sinusoidally varying permeability	61
3.7	Discussion and Conclusions	64
	Appendix 3.A Comparison of mixing length metrics	66
	Appendix 3.B Asymptotic solutions for uniform viscosity displacements	66
4	Unstable displacements in layered porous media	69
4.1	Introduction	69
4.2	Problem formulation	71
4.3	Displacement pattern and regimes	71
4.4	Regime I: fingering within layers	74
4.4.1	Concentration model	75
4.5	Regime II: stable channelling	77
4.5.1	Concentration model	78
4.6	Regimes III and IV: viscous fingering across layers	80
4.7	Non-sinusoidally varying permeability	82
4.8	Discussion and Conclusions	84
5	Miscible displacements with gravity override	87
5.1	Problem formulation	89
5.2	Limiting cases	91
5.2.1	Uniform viscosity, $R = 0$	91
5.2.2	Uniform density, $G = 0$	93

5.2.3	Comparison of the two limiting cases	94
5.3	Overall dynamics	95
5.4	Slumping regime	97
5.5	Intermediate-time fingering and gravity current regime	98
5.5.1	Gravity stabilization of viscous fingering	98
5.5.2	Concentration model	100
5.5.3	The effect of mixing on current propagation	105
5.6	Late-time shutdown and viscously-enhanced Taylor slumping regime	107
5.6.1	Concentration model	107
5.7	Discussion and conclusions	111
5.7.1	Summary	111
5.7.2	Implications for carbon sequestration	113
6	Flow and deformation in a confined poroelastic medium	117
6.1	Introduction	117
6.2	Experiments on flow through a deformable matrix	118
6.2.1	Experimental setup	119
6.2.2	Calibration	121
6.2.3	Validation	122
6.2.4	Experimental results	122
6.3	Mathematical modelling	124
6.3.1	Governing equations	124
6.3.2	Initial and boundary conditions	125
6.3.3	Constitutive equations	126
6.3.4	Nondimensionalization	127
6.3.5	Model results	129
6.4	Steady-state experimental results	132
6.5	Transient experimental results	136
6.5.1	Transient behaviour for $\Phi \approx \phi_0$	136
6.5.2	Transient dynamics for $\Phi > \phi_0$	137
6.6	Conclusions	138
6.6.1	Asymmetric flows	139
	Appendix 6.A List of experiments	140
	Appendix 6.B Large pressure drop limit of the model	140

7	Conclusions and Future Work	143
7.1	Conclusions	143
7.2	Future work	146
	References	149
	Appendix A Numerical method	161
A.1	Introduction	161
A.2	Gridding	163
A.3	Streamfunction equation	164
A.4	Advection-diffusion equation	164
A.5	Validation	165

List of figures

2.1	Schematic of the model geometry.	13
2.2	Evolution of the concentration field from a typical simulation.	18
2.3	Plots of the mixing length, number of fingers and Nusselt number for different R and Pe	20
2.4	Rescaled plots of the mixing length, number of fingers and Nusselt number for early and late times.	21
2.5	Transition from stable to unstable displacements.	24
2.6	Evolution of the transversely averaged concentration and transverse variance at intermediate times.	27
2.7	Concentration profiles along and across fingers at intermediate times.	30
2.8	Comparison of the effective viscosity ratio extracted from the numerical simulations and the predictions of the simple Koval model, the empirically fit effective viscosity, and the analytically derived model with parabolic transverse profiles.	32
2.9	Colourmaps of the concentration field, concentration deviations, stream-wise velocity and vertical velocity in the late-time regime.	33
2.10	Evolution of the concentration field in the late-time regime.	33
2.11	Plot of the re-scaled late-time transversely averaged concentration.	34
2.12	Plots of the decay rate of the concentration deviations and the steady slope of the transversely averaged concentration.	36
2.13	Total convective flux due to miscible viscous fingering.	37
3.1	Schematic of the layered model geometry.	43
3.2	Evolution of the concentration field for uniform viscosity displacements ($R = 0$).	46
3.3	Evolution of the mixing length and transversely averaged concentration for $R = 0$ in the intermediate-time regime.	48

3.4	Evolution of the mixing length and transversely averaged concentration for $R = 0$ in the late-time regime.	49
3.5	Colourmaps of the concentration field with overlain streamlines for $ R < \sigma$	50
3.6	Evolution of the mixing length and transversely averaged concentration for $ R < \sigma$ in the intermediate-time regime.	53
3.7	Plot of the convective flux, \mathcal{S} vs. $ \beta $ for $R < 0$ and $R > 0$	55
3.8	Evolution of the mixing length and transversely averaged concentration for $ R < \sigma$ in the late-time regime.	57
3.9	Evolution of the concentration field for stable displacements $ R > \sigma$, $R < 0$	58
3.10	Plot of normalized \mathcal{S} in the small- and large- $ \beta $ limit.	59
3.11	Evolution of the mixing length and transversely averaged concentration for $ R > \sigma$, $R < 0$	61
3.12	Salt Creek permeability data.	62
3.13	Evolution of the concentration field for a constant viscosity displacement in a complex permeability structure.	62
3.14	Evolution of the concentration field with overlain streamlines for $ R > \sigma$, $R < 0$ and a complex permeability structure.	63
3.15	Long-time evolution of $\bar{c}(x, t)$ for stable and unstable displacements.	64
3.16	Plot of two different measures of the mixing length, h	65
4.1	Evolution of the concentration field for $ R > \sigma$ and $R > 0$	72
4.2	Evolution of the concentration field for $R > \sigma$ in regime I.	74
4.3	Measure of the mixing zone variance as a function of the log-permeability variations.	75
4.4	Evolution of the concentration field for $ R > \sigma$ and $R > 0$ in the channelling regime.	77
4.5	Plot of the model and theoretical solutions of the transversely averaged concentration for $ R > \sigma$ and $R > 0$ in the channelling regime.	78
4.6	Evolution of the concentration field for $ R > \sigma$ and $R > 0$ in the viscous fingering across layers regime.	81
4.7	Salt Creek permeability data.	82
4.8	Evolution of the mixing length and number of fingers for unstable displacements in an idealized two-mode permeability field and an analogue reservoir.	83

4.9	Evolution of the concentration field for unstable displacements in the fingering regime in porous media with idealized and realistic permeability structures.	84
4.10	Regime diagram for viscously-dominated stable displacements, permeability-dominated displacements, and viscously-dominated unstable displacements.	85
5.1	Schematic of the model geometry.	89
5.2	Evolution of the concentration field for the uniform viscosity case.	92
5.3	Evolution of the concentration field for the uniform density case.	93
5.4	Evolution of the concentration field for both $R \neq 0$ and $G \neq 0$	95
5.5	Colourmaps of the concentration field in the slumping regime.	97
5.6	Evolution of the mixing length in the slumping regime.	98
5.7	Gravity stabilization of viscous fingering.	99
5.8	Phase diagram delineating stable vs. unstable displacements.	100
5.9	Reduced-order model for the hydrodynamically stable evolution of the concentration field at intermediate times.	101
5.10	Comparison of the two dimensional numerical simulations with the diffuse-interface and sharp-interface models.	103
5.11	Evolution of the mixing length in the stable and unstable limits.	105
5.12	Colourmaps of the concentration field, concentration deviations and streamwise velocity in the late-time regime.	106
5.13	Evolution of the concentration field in the shutdown regime.	107
5.14	Evolution of the transversely averaged concentration field in the viscously-enhanced Taylor-slumping regime.	110
5.15	Regime diagrams delineating all of the possible dynamics.	112
5.16	Evolution of the displacement front in the three carbon sequestration case studies.	115
6.1	A Schematic of the experimental setup.	119
6.2	Calibration data for the dye-attenuation technique and histogram of sphere sizes.	120
6.3	Validation of the dye attenuation technique through uniaxial compression of the packing of spheres.	121
6.5	Transient results of the theoretical model.	128
6.6	Steady-state results of the theoretical model.	130
6.7	Experimental measurements of steady-state azimuthally-averaged depth-averaged porosity for different Φ and Q/d	132

6.8	Steady-state comparison of experimental and model results.	134
6.9	Transient evolution of the azimuthally-averaged porosity field and cavity size for moderately confined media.	136
6.10	Transient evolution of the azimuthally-averaged porosity field and cavity size for weakly confined media.	137
6.11	Experiments with asymmetric behaviour.	139
7.1	Preliminary numerical simulations of less-viscous more-dense fluid injected into a layered porous medium saturated with a more-viscous, less-dense fluid.	146
A.1	Domain spatial discretization.	163
A.2	Validation of the numerical scheme.	166

Chapter 1

Introduction

1.1 Carbon capture and storage (CCS)

In 2015, the Paris climate agreement saw the first globally concerted effort to combat one of the greatest problems facing our generation - global climate change. The purpose of the agreement was to curb anthropogenic greenhouse-gas emissions in order to limit the increase in global temperatures to less than 2°C above pre-industrial levels. In the UK, there are numerous ongoing efforts to reduce atmospheric carbon dioxide (CO₂) emissions, such as increasing the usage of renewable energy (i.e. biomass and offshore wind), phasing out coal, improving the energy efficiency of buildings, and decarbonizing transport (Gummer et al., 2018). However, given current trends in energy consumption, and the current reliance on fossil fuels, in order to reach targets set out in the Paris agreement, it is becoming abundantly clear that there needs to be a transition from net-positive to net-negative CO₂ emissions (European Academies Science Advisory Council, 2018).

One proposed solution to help mitigate the global increase in anthropogenic greenhouse gases is carbon capture and storage (CCS), where CO₂ is captured and geologically sequestered. CCS technologies can be used as part of carbon neutral strategies, for example, by using CO₂ in enhanced oil recovery or sequestering CO₂ released from burning fossil fuels; or, as part of a carbon-negative strategies, by sequestering CO₂ that is captured directly from the air (DACCS - direct air capture with CCS) or from the combustion of biomass (BECCS - bio-energy with CCS). Moreover, CCS technologies can also be used to de-carbonise key industrial processes that are highly dependent on fossil fuels as key inputs, such as the production of steel, cement and certain chemicals. Therefore, given its wide use, CCS technologies will likely play a critical role in the global reduction of greenhouse gas emissions.

Briefly, the process of carbon capture and storage involves first capturing CO₂ from a large localized source (i.e. a steel or cement factory, or a fossil fuel or biomass power plant). The CO₂ is then compressed and transported to a storage site, such as a deep saline aquifer or a depleted oil reservoir, where it is injected, at depth, as a supercritical liquid. Since the CO₂ is less dense than the surrounding fluid, it tends to rise and spread as a buoyant plume. However, as the plume rises, it becomes trapped in the pore-space via a hierarchy of trapping mechanisms. Initially, in most storage sites, a relatively impermeable caprock prevents the unbounded upward migration of the CO₂ plume and can trap the CO₂ due to anticlines or non-transmissive faults in the geology. As it spreads the CO₂ becomes residually trapped in the pore space due to surface tension, leaving behind a trail of CO₂ (Hesse et al., 2008). CO₂ may be residually trapped in upwards of 10-35% percent of the pore-space, which ultimately helps limit the extent of the plume. Concurrently, the CO₂ is also soluble in saline brine and can be trapped as a dissolved phase. On its own molecular diffusion is quite slow, but the rate of dissolution is significantly enhanced through a number of different mechanisms (Huppert and Neufeld, 2014). One such mechanism that has been widely studied is convective dissolution, which is a hydrodynamic instability that occurs because CO₂-saturated brine is more dense than brine alone (Ennis-King and Paterson, 2005). The convective instability results in greatly enhanced dissolution rates (Hewitt et al., 2013; Neufeld et al., 2010) and ultimately can also limit the extent of the migrating CO₂ plume (MacMinn and Juanes, 2013).

The dissolution of CO₂ is inherently limited by the free CO₂-brine surface area over which dissolution occurs. Macroscopic flow structures due to viscous fingering or flow through heterogeneous reservoirs can greatly increase this surface area but to date their impact on dissolution remains poorly constrained. Viscous fingering occurs because CO₂ is less viscous than the ambient displaced fluid and leads to fingering of the free CO₂-brine interface (Saffman and Taylor, 1958). Furthermore, the permeability of geological formations varies on a range of scales from the pore-scale to the reservoir-scale. These variations introduce flow heterogeneity, which also tends to deform or distort the free CO₂-brine interface. Both viscous fingering and permeability heterogeneities increase the area over which dissolution occurs and can significantly increase solubility trapping. However, the extent to which they do enhance dissolution remains unknown. A primary goal of this thesis is to further elucidate this.

Ultimately as the CO₂ is dissolved it can react with ambient minerals and lead to mineral trapping. This is the most permanent form of trapping, as CO₂ is trapped in

an immobile solid phase. Although this can occur relatively quickly in some geological formations (Matter et al., 2016), in general this process occurs very slowly.

To date, a few large industrial-scale CCS projects have been completed, or are currently in operation. In this thesis three different case studies will be considered: (1). The Sleipner gas field in the North Sea, where, for over 20 years, CO₂ has been separated from natural gas production and has been sequestered in a deep saline aquifer (Bickle et al., 2007; Boait et al., 2012); (2). The In Salah oil field in Algeria, where from 2004 and 2011, CO₂ was separated from gas produced and sequestered in a depleted gas reservoir (Vasco et al., 2010); (3). Salt Creek, where for over 25 years, CO₂ has been injected as part of an enhanced oil recovery strategy at Salt Creek (Bickle et al., 2017). These three case studies represent a cross-section of previous CCS experiments, which will be discussed throughout this thesis.

1.2 Constraints on the safe storage of CO₂

Although a promising strategy, outstanding questions remain regarding the safe, long-term storage of CO₂ following injection underground. For a given aquifer, there are two main constraints when considering the safe storage of CO₂: first, the total amount of CO₂ that can be safely trapped within the aquifer, and second, the rate at which CO₂ can be safely injected before pressure build-up induces seismicity (Szulczewski et al., 2012). In this thesis, the aim is to better understand these two constraints by examining simplified versions of each of these problems using computational, experimental and theoretical approaches.

First, when supercritical CO₂ is injected underground, it is less viscous and less dense than the ambient brine which leads to a predicted channelization of the flow and only minimal pore occupancy at the plume scale (Celia et al., 2015). Therefore, the true storage capacity of a given reservoir is only a fraction of its total volume. However, once CO₂ dissolves it may convect, which makes more of the pore-space accessible to the CO₂. As alluded to earlier, a number of mechanisms can enhance this dissolution, and this thesis focuses specifically on viscous fingering and permeability-heterogeneity enhanced mixing. Although CO₂ and brine are only partially miscible, the limiting simplified problem involving two fully miscible fluids is addressed. Note that, the other limiting problem involving two fully immiscible fluids is typically modelled using a Buckley-Leverett-type formulation for the evolution of the saturation, which is analogous to the fully miscible system. In chapters 2-5 displacement-driven mixing of miscible fluids in porous media is examined using high resolution numerical simulations,

and in doing so, the aim is to understand the overall life cycle of the displacement process.

Second, when CO_2 is injected in deep saline aquifers, if the injection occurs too quickly, pressure build-up can create fractures or trigger faults. This occurs since the fluids are only moderately compressible and any injection requires the displacement of ambient fluid which requires a transient pressure field. In chapter 6, idealized experiments of flow through a packing of soft spheres are used to understand how pressure propagates in a deformable porous medium and to understand the deformation that can result.

1.3 Instabilities and mixing in porous media

Throughout this thesis, the spreading and mixing of two fully miscible fluids will be discussed. We will consider the parameters from a series of CO_2 sequestration case studies as illustrative examples of the relevant parameters in geophysically relevant flows. However, the fluids in these cases are only partially miscible and the mixing and dissolution rates are therefore overestimated. In other contexts, discussed in more detail below, the two fluids are much more miscible, and the analysis can be applied directly.

The mixing of miscible fluids in porous media is notoriously difficult due to the absence of inertia, and lies at the heart of many real-world problems. Ultimately mixing occurs as molecular diffusion acts to reduce local concentration gradients. Mixing is, therefore, most effective when both concentration gradients, and the surface areas across which they act, are large. While fluids at high Reynolds numbers can be vigorously stirred by turbulence, other mechanisms are required to stir fluids in porous media.

There are a number of ways that fluid mixing is enhanced in porous media. At the pore-scale, natural variations in the pore geometry introduce significant heterogeneities in the flow field, which tend to mix the fluids (Le Borgne et al., 2013; Villiermaux, 2012). Throughout this thesis the length scale of the flow is assumed to be much larger than the pore-scale where the effects of pore-scale mixing can be homogenized. Note that this pore-scale mixing is often modelled as dispersive, having a velocity-dependent effective dispersivity, which can be orders of magnitude larger than diffusion alone (Woods, 2015).

On the much larger continuum scale, fluids can also be effectively mixed through interfacial instabilities, which increase the area over which dispersion acts. These instabilities can be driven by a number of different mechanisms including chemical

reactions (Almarcha et al., 2010) and unstable buoyancy gradients (Lyu and Woods, 2016). This thesis will focus primarily on unstable viscosity gradients, that is, the displacement of a more-viscous fluid by a less-viscous fluid. This configuration is hydrodynamically unstable and leads to fingering behaviour known as viscous fingering or Saffman-Taylor fingering (Homsy, 1987). In addition to interfacial instabilities, spatial variations in the permeability field can also increase the area over which dispersion acts and therefore enhances mixing (Dentz et al., 2011). In this thesis, the effect of viscous fingering, permeability heterogeneities, and buoyancy gradients, on the overall lifecycle of mixing will be studied. In chapters 2-5 the previous work done on these topics is discussed in more detail.

In the context of carbon capture and storage, the goal is to maximize dissolution by maximizing free CO₂-brine surface area through flow heterogeneity. In other circumstances, such as in enhanced oil recovery, the goal may be to minimize instabilities, as instabilities tend to lead to poor recovery. Thus a fundamental understanding of the different displacement patterns and their dependence on the various control parameters is critical in optimizing and controlling the displacement front and the amount of mixing that occurs.

Although the motivation for studying this problem is the geological storage of carbon dioxide, there are a number of other contexts where mixing in porous media is relevant. Some of these areas are described below.

Enhanced oil recovery: Enhanced oil recovery involves the extraction of residually-trapped oil in a reservoir by injecting miscible gasses (for example CO₂), polymers or steam. In certain cases mixing is desirable, for instance to mobilize the trapped oil by reducing its viscosity. However, in other cases it is undesirable, such as during polymer floods where the aim is to prevent instabilities to increase the volume of the reservoir contacted by the injected fluid (Lake, 1989).

Coastal aquifer dynamics: Fresh-water aquifers along the coast are hydraulically linked to the surrounding sea. Understanding how the two water masses mix is necessary to understand the viability of the aquifer as a water resource (Fleury et al., 2007).

Geothermal power generation: Geothermal power generation involves the injection of a cool liquid into a superheated reservoir. The cool liquid displaces the ambient hot fluid, which is extracted downstream. This hot fluid is then used to generate power. The efficiency of the geothermal energy conversion process is therefore intimately linked to the flow and transport of heat in the subsurface (Murphy et al., 1981; Woods, 1999).

Subsurface contaminant transport: Agricultural or industrial contaminants can be carried to the subsurface through seepage or rain and pollute groundwater aquifers.

Also, contaminants intentionally buried in the subsurface, such as nuclear waste, can also be transported to groundwater aquifers by natural subsurface flows. Understanding how these contaminants mix and disperse is important for understanding water quality (Abriola, 1987; Miller et al., 2000).

Chromatography: In chromatography, a mixture is pumped through a porous medium to separate out its constituents. As the mixture displaces the ambient fluid, the flow can be unstable and lead to poor separation performance (Catchpoole et al., 2006; Mayfield et al., 2005).

Magmatic flow: Melt in the upper mantle flows through a deformable porous network, which is critical to the thermal and compositional transport in the earth (Rees-Jones and Katz, 2018). Recent work has also suggested the planform morphology of the Icelandic plume as it spreads laterally is due to a miscible viscous fingering instability (Schoonman et al., 2017).

Mixing in microfluidic systems: Mixing in microfluidic settings, which is analogous to mixing in porous media, is crucial in many engineering applications. The ability to control mixing and reactions is a key design criteria in microfluidics. (Stone et al., 2004).

PEM Fuel cells: The rate of reaction in proton-exchange membrane fuel cells is, in part, dictated by the ionic transport and mixing of the fuel gases. Maximizing oxygen and hydrogen transport and water removal is therefore critical to highly efficient fuel cells (Litster and McLean, 2004; Mukherjee et al., 2011).

1.4 Flow through deformable porous media

In porous media, fluid flowing through the pore-space can couple to the solid matrix mechanically. This occurs both when the solid matrix is compressed or stretched or when fluid is injected into a porous medium. Fluid-solid coupling in porous media arises in a variety of contexts, including something as simple as fluid wicking into a sponge, and plays an important role in our understanding of a number of physical processes ranging from magma dynamics (McKenzie, 1984) to intracellular flow mechanics (Mogilner and Manhart, 2017).

When fluid flows through a porous medium, if the medium is sufficiently soft, the fluid pressures and viscous shear stresses can substantially deform the medium. There are two main prototypical problems used to study this fluid-solid coupling: the consolidation problem, where only the solid phase of a fluid-saturated porous medium is compacted resulting in the expulsion of fluid, and the fluid-driven compaction problem,

where fluid is forced to flow through the porous medium leading to compaction. Although the former problem has received significant attention, there are relatively few simple experiments of flow-induced compaction of a deformable porous medium. Two earlier examples are the works of Parker et al. (1987) and Lanir et al. (1990) who studied flow through foams. In this thesis, following the works of Hewitt et al. (2016); Lee et al. (2018); MacMinn et al. (2015), flow-induced deformation of a packing of deformable spheres is examined experimentally. Specifically, the effect of pre-stressing the porous matrix on its deformation and flow properties is considered.

In the context of carbon capture and storage, fast CO₂ injection can lead to fracturing of the storage formation, which can be detrimental to the safe storage of CO₂. Below, a few other applications where fluid flow couples to solid deformation in porous media are highlighted.

Hydraulic fracturing: In hydraulic fracturing, fluid is injected into a reservoir at very high pressures in order to fracture the rock and stimulate oil production (Detournay, 2016).

Drying colloids: As a suspension dries, the colloids in the suspension compact into a porous structure. As the solvent continues to evaporate, it is drawn out of a compacting porous medium and can cause it to crack (Boulogne et al., 2016).

Magmatic systems: Flow of melt in the upper mantle leads to deformation of the surrounding rock and can lead to channeling, which is important in understanding melt transport (Katz et al., 2006).

Erosion dynamics: Flow through an erodible porous media, such as soil, can lead to channelization of flow and erosion of the medium (Kudrolli and Clotet, 2016; Mahadevan et al., 2012). This type of erosion, known as seepage erosion, plays a key role in shaping many geological features such as rivers, valleys and canyons (Berhanu et al., 2012).

Membrane filtration: Membrane filtration is used to separate mixtures based on particle size. However, as particles are separated from the mixture, a cake builds up which increases the resistivity of the filter, which can be modelled as a deformable porous medium (Krupp, 2017).

Bone: Fluid flow in the bone is, in part, driven by deformation of the bone itself. This deformation plays a critical role in the bone's mechanosensory system. (Cowin, 1999; Fritton and Weinbaum, 2009)

Pulp and paper: Dewatering of suspensions, done by squeezing fluid out of a fluid-solid mixtures, plays a key role in the pulp and paper production processes (Hewitt et al., 2016).

1.5 Thesis structure

This thesis investigates two distinct and fundamental features of flow in porous media: the mixing of miscible fluids of different viscosity and density in both homogeneous and heterogeneous porous media, and the flow-induced compaction of deformable porous media.

In chapters 2-5, fluid injection into a semi-infinite planar porous medium saturated with another fully miscible fluid is considered. This problem is studied using two complementary approaches: direct numerical simulations of the fully nonlinear, two-dimensional problem, and simplified reduced-order modelling. The detailed description of the problem formulation as well as the underlying assumptions are given in §2.2 and the numerical method used to solve the problem is given in appendix A. Throughout these chapters the results are applied to the field-scale CO₂ sequestration case studies discussed above, though the results are applicable more broadly.

In chapter 2, the case where the injected fluid is less viscous than the ambient leading to viscous fingering is considered. Viscous fingering results in the generation of finger-like structures that evolve nonlinearly and coarsen in time. First the different flow regimes through which the instability evolves and the dominant physical balances and scalings in each of these regimes are identified. At early times the flow is well-described by linear stability theory, at intermediate times nonlinear fingers elongate and coarsen leading to, on average, advective growth of the mixing region, and at late times a single pair of counter-propagating fingers remain and slow exponentially. It is found that the instability eventually shuts down and the total amount of convective mixing the instability can generate is finite, which is parameterized in terms of the Peclet number and the logarithm of the viscosity ratio. In the course of this study, a critical Peclet number for the instability is identified, an improved averaged model for the flow in the intermediate-time regime is derived and a detailed explanation of the asymptotic fate of the instability is provided.

In chapters 3 and 4, flow in layered heterogeneous porous media is considered, which is motivated by the fact that many geological reservoirs consist of alternating regions of high and low permeability. Specifically, the idealized case where the log-permeability is sinusoidally varying with a single frequency is examined. In chapter 3, the case where the two fluids have the same viscosity is first reviewed to identify the dominant physical balances at early, intermediate, and late times. Then the case where the injected fluids differ in viscosity, but when the viscosity difference is smaller than the large-scale permeability difference is considered. For each of the regimes identified in the uniform viscosity case, the effect of changing the viscosity contrast on the evolution

of the displacement front is considered. Next, the case where the injected fluid is more viscous than the ambient fluid and the viscosity variations are larger than the permeability variations is examined. Finally, a non-idealized permeability field derived from a real reservoir is considered and the results of the reduced-order models are compared to the direct numerical simulations.

In chapter 4, the work in chapter 3 is extended to consider the case where the injected fluid is less viscous than the ambient fluid and the viscosity variations are larger than the permeability variations. As in chapter 2, this configuration is hydrodynamically unstable and results in a competition between the evolving wavelength of the viscous fingering instability and the imposed wavelength of the permeability structure. At intermediate times this competition leads to four different regimes: fingering within layers, channelling along layers, fingering across layers, and single-finger exchange flow. At early and late times, the dynamics are the same as what is described in chapter 3.

In chapter 5, unstable displacements in homogeneous porous media again examined, but now where the injected and ambient fluids have different densities as well as different viscosities. First the case where the injected and ambient fluids have the same viscosity but different densities is reviewed and the dominant physical balances and scalings are determined. Then the overall dynamics, when both the density and viscosity vary, are considered. At early times, a slumping regime is identified where vertical flow is important. At intermediate times, vertical flow and diffusion can be neglected and in this limit there are three different limiting solutions: the fingering limit, the pressure-driven gravity current limit, and the density-driven gravity current limit. Finally at late times, transverse diffusion becomes important and there is a transition from the shutdown regime (analogous to the shutdown regime in chapter 2) to the viscously-enhanced Taylor-slumping regime. In each of the regimes, the dominant scalings are identified and reduced order models for the evolution of the concentration field are developed.

The final portion of this thesis (chapter 6) examines the fluid-driven compaction of a deformable porous medium. Experimental studies of water injection into a water-saturated packing of soft hydrogel spheres are presented. Solutions to a one-dimensional axisymmetric model are discussed and comparisons to the experimental results are made. In doing so, particular focus is given to the role of confinement on both the steady-state and transient dynamics of the system.

Finally, in chapter 7 the work in the thesis is summarized and potential avenues of further work are discussed.

Chapter 2

Miscible viscous fingering in homogeneous porous media

The material in this chapter forms the basis of the publication (Nijjer et al., 2018): Nijjer, J. S. & Hewitt, D. R. & Neufeld, J. A. (2018). The dynamics of miscible viscous fingering from onset to shutdown. *Journal of Fluid Mechanics* **837**. 520–545.

2.1 Introduction

Viscous fingering is an interfacial instability that occurs when a less-viscous fluid displaces a more-viscous one in a porous medium or Hele-Shaw cell. This phenomenon was first described by Hill (1952) and later by Saffman and Taylor (1958). The instability results in a series of fine fingers whose length scale can depend on a variety of factors including surface tension and diffusion. Saffman and Taylor showed that in the case of immiscible flows (when the fluids do not mix) in a channel of finite width these fingers tend to coalesce to a single steadily-propagating finger. Since the work of Saffman and Taylor, there have been a variety of studies on both the initial instability and the stability of the single-finger state (see McCloud and Maher 1995).

If the interfacial tension is zero, Saffman and Taylor's theory predicts maximal growth of infinitesimally small fingers. However, experiments with miscible fluids in Hele-Shaw cells indicate that either the plate spacing (Lajeunesse et al., 1999; Paterson, 1985) or diffusion (Chui et al., 2015) between the fluids leads to finite wavelength fingers. Tan and Homsy (1986) used linear stability theory, and a slowly diffusing background flow, to predict the most unstable mode and its growth. In subsequent work, they compared their theory to numerical simulations of the full 2D problem (Tan and Homsy, 1988). Since then much work has been done to understand the onset and

early-time behaviour while considering the effects of anisotropic and velocity dependent dispersion (Norouzi and Shoghi, 2014; Zimmerman and Homsy, 1991, 1992b), geometry (Chen and Meiburg, 1998a,b; Riaz and Meiburg, 2003; Tan and Homsy, 1987), chemical reactions (De Wit and Homsy, 1999; Sharma et al., 2019), finite blobs of fluid (Mishra et al., 2008; Pramanik et al., 2015), and double diffusive effects (Mishra et al., 2010).

Some recent attempts have been made to model the impact of viscous fingering on mixing beyond the onset. Jha et al. (2011a,b) examined the long-time mixing of a viscously unstable system containing high or low viscosity blobs in a doubly periodic domain. Informed by numerical experiments, they developed a model for the evolution of the mixing rate. In this chapter, the evolution of a single viscously unstable planar interface is investigated from onset to shutdown.

Although previous work has looked at the onset problem and early-time behaviour of miscible viscous fingering, the late-time behaviour remains poorly understood. In previous work, Tan and Homsy (1988) determined a critical Peclet number beyond which tip-splitting occurs, and they hypothesized that this value might have implications for the asymptotic fate of the fingers. Zimmerman and Homsy (1992b) similarly suggested that the asymptotic behaviour may include multiple steadily propagating fingers under the assumption that tip splitting may balance the upwards cascade in the scale of the fingers, but were unable to extend their numerical simulations to a final state. In experiments in a radial geometry, Chui et al. (2015) showed a transition in finger growth from a scaling with t to one with $t^{\frac{1}{2}}$ corresponding to the shutdown of the instability. However, the ultimate fate and final form of the fingers remains unclear.

This chapter has two main aims. The first aim is to identify and provide a detailed explanation of the asymptotic fate of the fingering instability. Then, given an understanding of the late-time behaviour, the second aim is to examine the full life cycle of miscible viscous fingering from “onset” to “shutdown” which draws together previously disjoint or contradictory observations and claims. It is found that the dynamics can be divided into three regimes: (i) at early times, the flow is well-described by linear stability theory; (ii) at intermediate times, the flow is dominated by non-linear finger interactions; and (iii) at late times, the flow is composed of exponentially slowing single-finger exchange-flow. Ultimately, once the fingers have slowed enough, diffusion in the direction of the flow dominates the dynamics. In the course of this study, a critical Peclet number for the instability in the first regime is identified and an improved averaged model for the flow in the second regime is derived.

This chapter is laid out as follows. In §2.2 the problem is formulated and the numerical method used to solve it is briefly discussed. In §2.3 numerical results

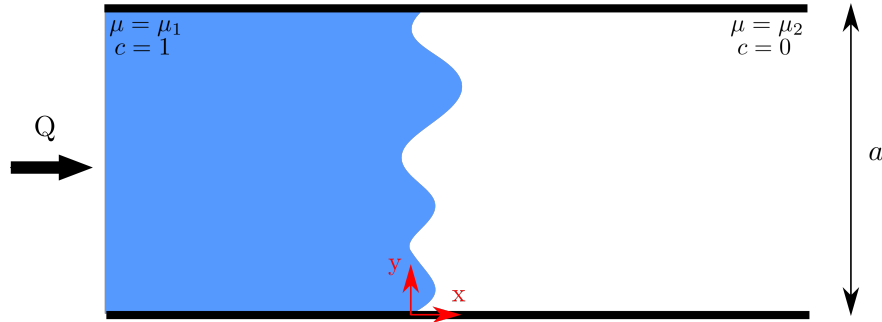


Fig. 2.1 An illustration of the model setup. The porous medium is taken to be an infinite strip of width a initially filled with a fluid with viscosity μ_2 . A fluid with viscosity μ_1 is injected at a constant flow rate Q into the medium. We measure the concentration of the injected fluid, which is one upstream and zero downstream.

across a range of parameter settings are presented and the dominant scalings in each regime are identified. The early-time linearly unstable and intermediate-time non-linear coalescence regimes are discussed in more detail in §2.4. Finally, in §2.5, the late-time behaviour is discussed, for which an analytic solution for the new single-finger state is derived and compared to the results of the numerical simulations.

2.2 Problem formulation

Note that for brevity the detailed problem formulation is outlined once in this thesis here as the model setup is similar in chapters 3,4, and 5.

We consider a two-dimensional, isotropic porous strip of infinite streamwise extent and finite transverse width a (figure 2.1). The medium has uniform porosity ϕ and permeability k , and is initially saturated with an ambient fluid which has viscosity μ_2 . Another fluid, which is fully miscible with the ambient fluid and has viscosity μ_1 , is injected at a flow rate Q . The diffusivity between the fluids is D and in this chapter gravity is neglected. Note that, in general, the diffusivity and permeability may be described by second-rank tensors, and can depend on a variety of factors including the concentration of either fluid, fluid velocity, time, and space. For simplicity, the diffusion-dispersion tensor is assumed to be isotropic and constant throughout this thesis. The permeability is assumed to be isotropic and constant in this chapter, and we explore the effect of spatial variations in the permeability in chapters 3 and 4.

2.2.1 Governing equations

The two fluids are incompressible and fully miscible. The flow obeys Darcy's law and the concentration of the injected fluid is described by an advection-diffusion equation,

$$\nabla \cdot \mathbf{u} = 0, \quad (2.1)$$

$$\mathbf{u} = -\frac{k}{\mu(c)} \nabla p, \quad (2.2)$$

$$\phi \frac{\partial c}{\partial t} + \mathbf{u} \cdot \nabla c = \phi D \nabla^2 c. \quad (2.3)$$

Here $\mathbf{u} = (u, v)$ is the Darcy velocity or fluid flux, p the pressure, and c the concentration, which varies between 0 (in the ambient fluid) and 1 (in the injected fluid). The viscosity $\mu(c)$ varies with the concentration, and we follow the convention of previous authors (e.g. Pramanik and Mishra, 2015; Tan and Homsy, 1986; Zimmerman and Homsy, 1991) by assuming an Arrhenius-like exponential dependence,

$$\mu(c) = \mu_2 e^{-Rc}, \quad (2.4)$$

where $R = -\ln(\mu_1/\mu_2)$.

We non-dimensionalize the equations by the height of the domain a , velocity U , time $\phi a^2/Q$, permeability k , viscosity of the ambient fluid μ_2 , and pressure $\mu_2 Q/k$, leading to

$$\frac{\partial u^*}{\partial x^*} + \frac{\partial v^*}{\partial y^*} = 0, \quad (2.5)$$

$$-u^* \mu^* = \frac{\partial p^*}{\partial x^*}, \quad -v^* \mu^* = \frac{\partial p^*}{\partial y^*}, \quad (2.6)$$

$$\frac{\partial c}{\partial t^*} + u^* \frac{\partial c}{\partial x^*} + v^* \frac{\partial c}{\partial y^*} = \frac{1}{\text{Pe}} \left(\frac{\partial^2 c}{\partial x^{*2}} + \frac{\partial^2 c}{\partial y^{*2}} \right), \quad (2.7)$$

$$\mu^*(c) = e^{-Rc}, \quad (2.8)$$

where $(\cdot)^*$ denotes a dimensionless quantity. For notational simplicity, we drop the asterisks from all subsequent quantities. The key dimensionless parameters are the log-viscosity ratio and the Peclet number, defined as

$$R = -\ln \left(\frac{\mu_1}{\mu_2} \right), \quad \text{Pe} = \frac{Q}{\phi D}. \quad (2.9)$$

When the injected fluid is more viscous than the ambient ($R < 0$), the interface is stable and the concentration evolves by diffusion alone (in the moving frame), with a classical error-function profile. However, when the injected fluid is less viscous than the ambient ($R > 0$), the interface can be unstable, leading to complex fingering patterns. We focus on the latter problem here. The Peclet number provides a ratio of the characteristic timescales for diffusion and advection: when $Pe \ll 1$, diffusion dominates the dynamics, and when $Pe \gg 1$, advection dominates. In the diffusive limit, the instability can be suppressed (as will be shown later) so we will, therefore, focus predominantly on the limit $Pe \gg 1$.

We note that the Peclet number here is a macroscopic quantity defined with respect to the width a of the porous medium. It is distinct from the pore Peclet number, $Pe_p = Qb/aD = (b/a)Pe$, which is defined with respect to the intrinsic length-scale b of the medium, i.e. the pore size, or, in a Hele-Shaw cell, the gap width. The assumption of Darcy flow relies on the pore Peclet number being small, $Pe_p < O(1)$ (Yang and Yortsos, 1997), or, equivalently, $a/b > O(Pe)$. In this limit, diffusion acts quickly to homogenize flow structures at the pore scale. This limit is assumed throughout this chapter as well as the subsequent chapters. If, instead, Pe_p were not small, the flow structures across the pore or gap width would affect the global dynamics, leading to qualitatively different macroscopic behaviour (Lajeunesse et al., 1999; Paterson, 1985).

We work in a reference frame moving with the average velocity of the injected fluid, and introduce transformed variables

$$\tilde{u} = u - 1, \quad \tilde{x} = x - t. \quad (2.10)$$

In this frame, equations (2.5-2.7) become

$$\frac{\partial \tilde{u}}{\partial \tilde{x}} + \frac{\partial v}{\partial y} = 0, \quad (2.11)$$

$$-(\tilde{u} + 1)\mu = \frac{\partial p}{\partial \tilde{x}}, \quad -v\mu = \frac{\partial p}{\partial y}, \quad (2.12)$$

$$\frac{\partial c}{\partial t} + \tilde{u} \frac{\partial c}{\partial \tilde{x}} + v \frac{\partial c}{\partial y} = \frac{1}{Pe} \left(\frac{\partial^2 c}{\partial \tilde{x}^2} + \frac{\partial^2 c}{\partial y^2} \right). \quad (2.13)$$

Again, for notational convenience, we drop the tildes from all subsequent quantities.

2.2.2 Boundary conditions

Similar to previous work (Tan and Homsy, 1988), we impose periodicity at the top and bottom boundaries. The upstream and downstream concentration are fixed at $c = 1$ and $c = 0$ respectively, the horizontal velocity is fixed at $u = 0$ (in the moving frame) and there is no mean cross-flow. The boundary conditions are thus

$$c(x, 0, t) = c(x, 1, t), \quad u(x, 0, t) = u(x, 1, t), \quad v(x, 0, t) = v(x, 1, t), \quad (2.14)$$

$$c(-\infty, y, t) = 1, \quad c(\infty, y, t) = 0, \quad (2.15)$$

$$u(-\infty, y, t) = u(\infty, y, t) = 0, \quad \int_{-\infty}^{\infty} v dx = 0. \quad (2.16)$$

2.2.3 Diagnostic quantities

As the instability develops and an array of fine fingers form, the local fingering dynamics become chaotic and are controlled by non-linear interactions between fingers. Instead of examining the behaviour of each individual finger, we aim to examine how the fingering dynamics evolve globally. To do so, we compute the average concentration over the transverse direction,

$$\bar{c}(x, t) = \int_0^1 c(x, y, t) dy. \quad (2.17)$$

Using this definition, and defining the deviations $c'(x, y) = c(x, y) - \bar{c}(x)$, (2.13) can be written as two coupled equations for the mean and perturbed concentrations,

$$\frac{\partial \bar{c}}{\partial t} + \frac{\partial \overline{uc'}}{\partial x} = \frac{1}{\text{Pe}} \frac{\partial^2 \bar{c}}{\partial x^2}, \quad (2.18)$$

$$\frac{\partial c'}{\partial t} + \frac{\partial uc'}{\partial x} + \frac{\partial u\bar{c}}{\partial x} - \frac{\partial \overline{uc'}}{\partial x} + \frac{\partial vc'}{\partial y} = \frac{1}{\text{Pe}} \left(\frac{\partial^2 c'}{\partial x^2} + \frac{\partial^2 c'}{\partial y^2} \right). \quad (2.19)$$

We will use this decomposition throughout this thesis.

In this chapter, we also examine three global quantities over time: the mixing length h , which quantifies the streamwise extent of interpenetration of the two fluids; the average number of fingers n , which gives an inverse measure of the transverse length scale; and the Nusselt number, Nu , which quantifies the total convective mixing

rate. These quantities are defined as,

$$h = x|_{\bar{c}=0.01} - x|_{\bar{c}=0.99}, \quad (2.20)$$

$$n = \frac{1}{h} \int_{x|_{\bar{c}=0.99}}^{x|_{\bar{c}=0.01}} \eta(x) dx, \quad (2.21)$$

$$\text{Nu} = \int_{-\infty}^{\infty} \int_0^1 u \left(c - \frac{1}{2} \right) dy dx, \quad (2.22)$$

where the number of fingers $\eta(x)$ is calculated by counting the number of local maxima in a vertical slice. Note that, the Nusselt number is often defined as $\text{Nu}^* = 1 + \text{Pe Nu}$, which is the ratio between total transport and diffusive transport (Zhou, 2013). Here we instead use the Nusselt number simply to quantify the total convective transport. Although other quantities can give more direct measurements of the total amount of mixing (e.g. the scalar dissipation rate; Jha et al., 2011a), we choose to measure these quantities as they provide clear and physically useful measures of the region over which the two fluids have spread and are mixing as well as the rate at which they are mixing.

Throughout we will make reference to the interface between the two fluids. Since the two fluids are fully miscible, there is no precise boundary. Instead, where we refer to the interface, we loosely mean the region around the $c = 1/2$ contour over which the concentration varies significantly.

2.2.4 Numerical Method

We briefly summarize the numerical method here; for more details see appendix A. Given that the fluids are incompressible, we write the velocity in terms of a streamfunction $(u, v) = (\partial\Psi/\partial y, -\partial\Psi/\partial x)$. Combining (2.12) and (2.8) results in a non-linear elliptic equation for the streamfunction,

$$\frac{\partial^2 \Psi}{\partial x^2} + \frac{\partial^2 \Psi}{\partial y^2} - R \frac{\partial c}{\partial x} \frac{\partial \Psi}{\partial x} - R \frac{\partial c}{\partial y} \frac{\partial \Psi}{\partial y} = R \frac{\partial c}{\partial y}, \quad (2.23)$$

with boundary conditions

$$\Psi(x, 0, t) = \Psi(x, 1, t), \quad (2.24)$$

$$\Psi(-\infty, y, t) = \Psi(\infty, y, t) = 0, \quad (2.25)$$

from (2.14) and (2.16).

In order to simulate an infinite strip, we impose boundary conditions (2.15) and (2.25) at $x = \pm\Gamma/2$, where Γ grows in time and is chosen to be sufficiently large

such that the boundaries are always far from the fingered region. Each simulation is initialized with an almost sharp interface and an added small random perturbation centred at $x = 0$,

$$c_0 = \frac{1}{2} + \frac{1}{2} \operatorname{erf} \left(-\frac{x}{\sqrt{t_0}} \right) + r(x, y) e^{-x^2/t_0}, \quad (2.26)$$

where the function $r(x, y)$ returns a uniformly distributed random number on the interval $[0, 10^{-5}]$.

At each time step, we solve (2.23) using an iterative multi-grid solver (Adams, 1999) with the solution at the previous time step used as an initial guess. We use sixth-order compact finite differences (Lele, 1992) to discretise the spatial derivatives in (2.23) and (2.13), and advance (2.13) in time using a third-order Runge-Kutta scheme.

2.3 Fingering pattern and regimes

Figure 2.2 shows a sequence of snapshots from a typical simulation for log-viscosity ratio $R = 2$ and Peclet number $Pe = 2000$. At early times, the initially very sharp interface begins to smooth out and a series of fine fingers develop (figure 2.2(a)). At intermediate times, once the fingers reach a certain amplitude, they begin to interact, which drives coarsening in the vertical direction and growth in the horizontal direction (figures 2.2(b-d)). Overall, these non-linear interactions lead to coalescence until a single broad finger remains (figures 2.2(e,f)).

All of our numerical simulations, which have Pe ranging from 100 to 16000 and R ranging from 1 to 5, show this qualitative behaviour. In general, we find that at early times the interface diffuses and a set of fingers develop. The number of fingers that develop increases with both the Peclet number and the log-viscosity ratio. The fingers then interact non-linearly via a variety of different mechanisms. These include shielding, when a longer finger widens at the tip and shields the growth of smaller neighbouring fingers; fading, when a finger stops growing and diffuses into the ambient; and coalescence, when two or more fingers merge together. When the Peclet number and log-viscosity ratio are large, the fingers also exhibit more complex behaviour including tip-splitting, when a finger splits into two at the tip; and branching, when a finger sheds fingers from its side (Islam and Azaiez, 2005; Tan and Homsy, 1988; Zimmerman and Homsy, 1991).

Regardless of the Peclet number and log-viscosity ratio, these interactions, on aggregate, lead to coalescence until a single broad finger remains. This finding is contrary to previous suggestions that the final state may include multiple fingers (Tan

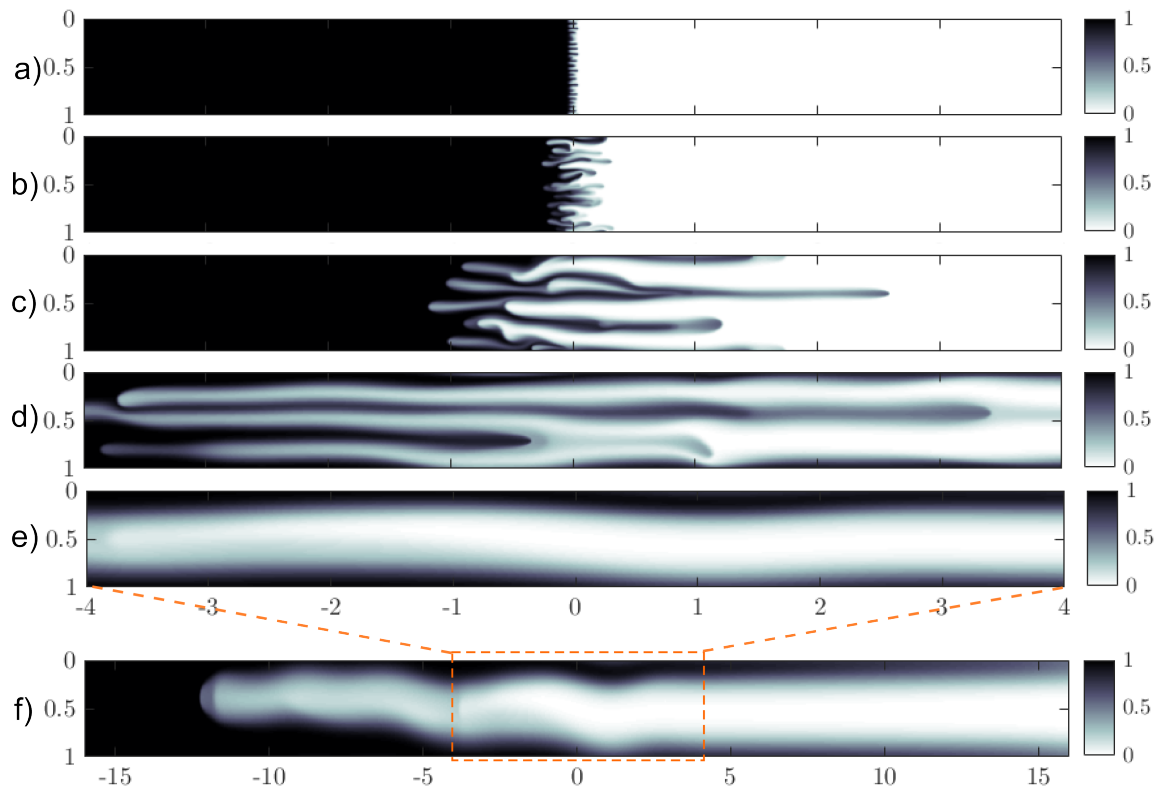


Fig. 2.2 Colourmaps of the concentration field (in a frame moving with the interface) over the course of a simulation. Here, $R = 2$ and $Pe = 2000$. Snapshots, from top to bottom, are taken at (a) $t = 0.5$, (b) $t = 1$, (c) $t = 3$, (d) $t = 10$, (e,f) $t = 31$. Note that the numerical domain is significantly larger than shown in the lower 3 panels. Panel (f) is zoomed out to include the full finger, and note that the figure is horizontally compressed by a factor of 4.

and Homsy, 1988; Zimmerman and Homsy, 1992b). The single finger that remains diffuses while propagating at an exponentially slowing speed, ultimately leaving a linear background concentration gradient that is gradually smoothed out by diffusion. We find that the final mixing zone length increases with both R and Pe .

Figure 2.3 shows the mixing length h , number of fingers n , and Nusselt number Nu as functions of time for different Peclet numbers (left) and log-viscosity ratios (right). Figures 2.3(a,b) show that the mixing length initially grows, then steepens, before finally slowing towards a constant. The early-time mixing length is larger for small Peclet numbers and is independent of the log-viscosity ratio whereas the final mixing length increases with both the Peclet number and log-viscosity ratio. Figures 2.3(c,d) show that the average number of fingers is fairly constant at early times, decays to one at intermediate times, and stays constant at one at late times. Although the initial number of fingers increases with the Peclet number and log-viscosity ratio, the flow always tends to a single finger eventually, irrespective of the parameters. Finally, figures 2.3(e,f) show that the Nusselt number first grows exponentially, then grows more slowly and finally decays exponentially.

Based on these sets of observations we partition the flow into three distinct regimes: (i) an early-time, linearly unstable regime: the mixing zone grows diffusively and fingers grow exponentially; (ii) an intermediate-time non-linear regime: fingers coalesce and the mixing length and Nusselt number exhibit power-law growth; and, (iii) a late-time, single-finger, exchange-flow regime: a single pair of counter-propagating fingers slow exponentially.

Each regime shows different dynamics and exhibits different scalings. We explore these scalings in the following subsection, before examining each regime in more detail in sections 2.4 and 2.5.

2.3.1 Scalings

At the start of all simulations, the interface is relatively sharp and the concentration and velocity perturbations are small. Diffusion across the interface dominates the growth of the mixing zone, and a diffusive balance $\frac{c}{t} \sim \frac{c}{Pe h^2}$ gives the scaling for the mixing length $h \sim \left(\frac{t}{Pe}\right)^{\frac{1}{2}}$, as can be seen in figure 2.4(a). In this linearly unstable regime, the aspect ratio of the fingers is $O(1)$; hence, from incompressibility, $\frac{u}{x} \sim \frac{v}{y} \Rightarrow u \sim v$. The linearized elliptic equation (2.23) further suggests a balance $\frac{u}{y} \sim \frac{v}{x} \sim \frac{Rc}{y}$, or $u \sim v \sim R$. The linear scaling of the velocity with the log-viscosity ratio, together with an advection-diffusion balance in (2.13), indicates that $\frac{c}{t} \sim \frac{uc}{x} \sim \frac{c}{Pe x^2}$, or $t \sim \frac{1}{R^2 Pe}$

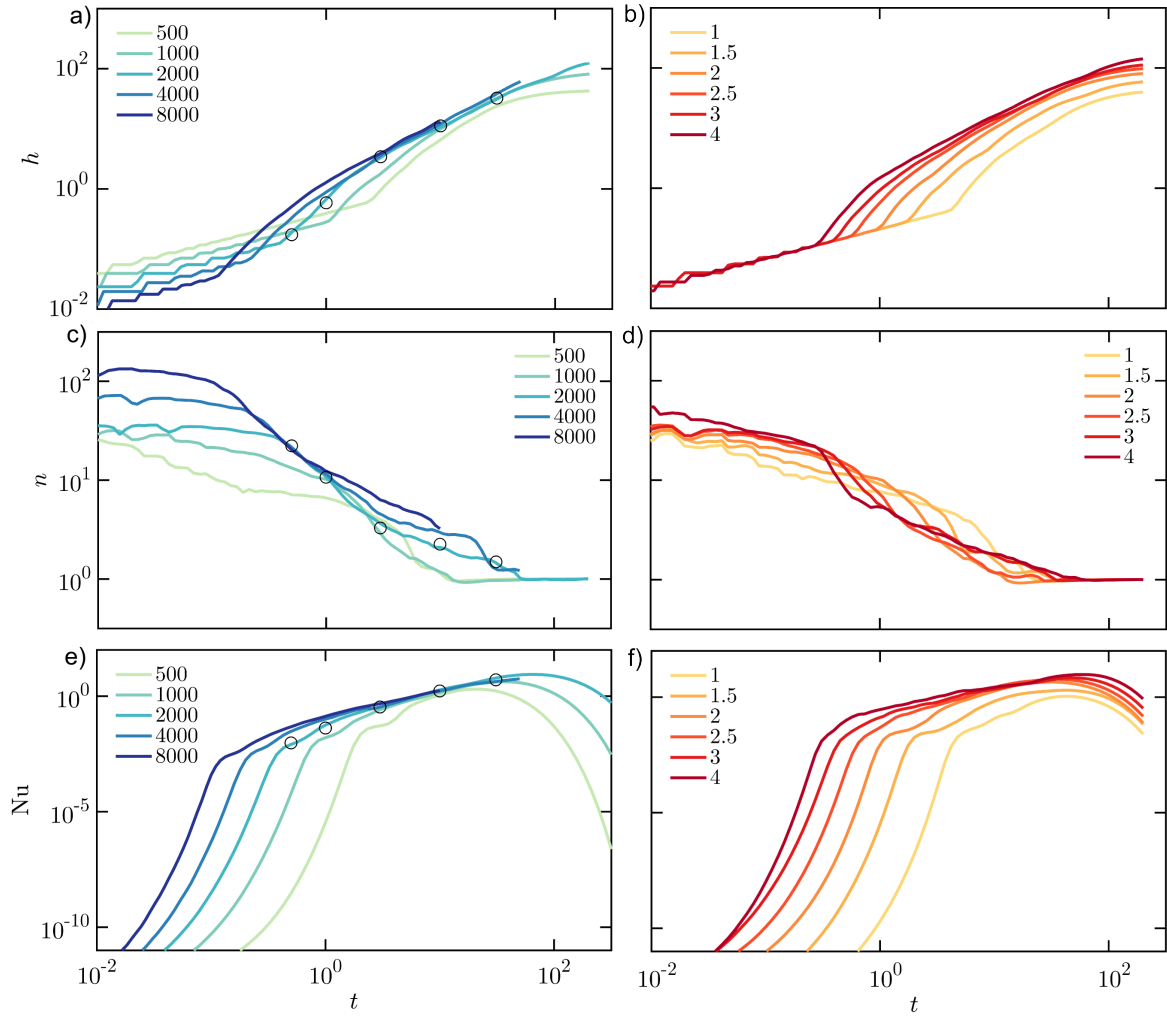


Fig. 2.3 Plots of (a,b) the mixing length h , (c,d) the number of fingers n , and (e,f) the Nusselt number Nu as functions of time plotted on logarithmic axes. To reduce the noise in the data, two different simulations are averaged for each plotted trajectory. (a,c,e) Data for log-viscosity ratio $R = 2$ and different Peclet numbers Pe as marked. The black circles correspond to the snapshots in figure 2.2. (b,d,f) Data for $Pe = 1000$ and different values of R as marked.

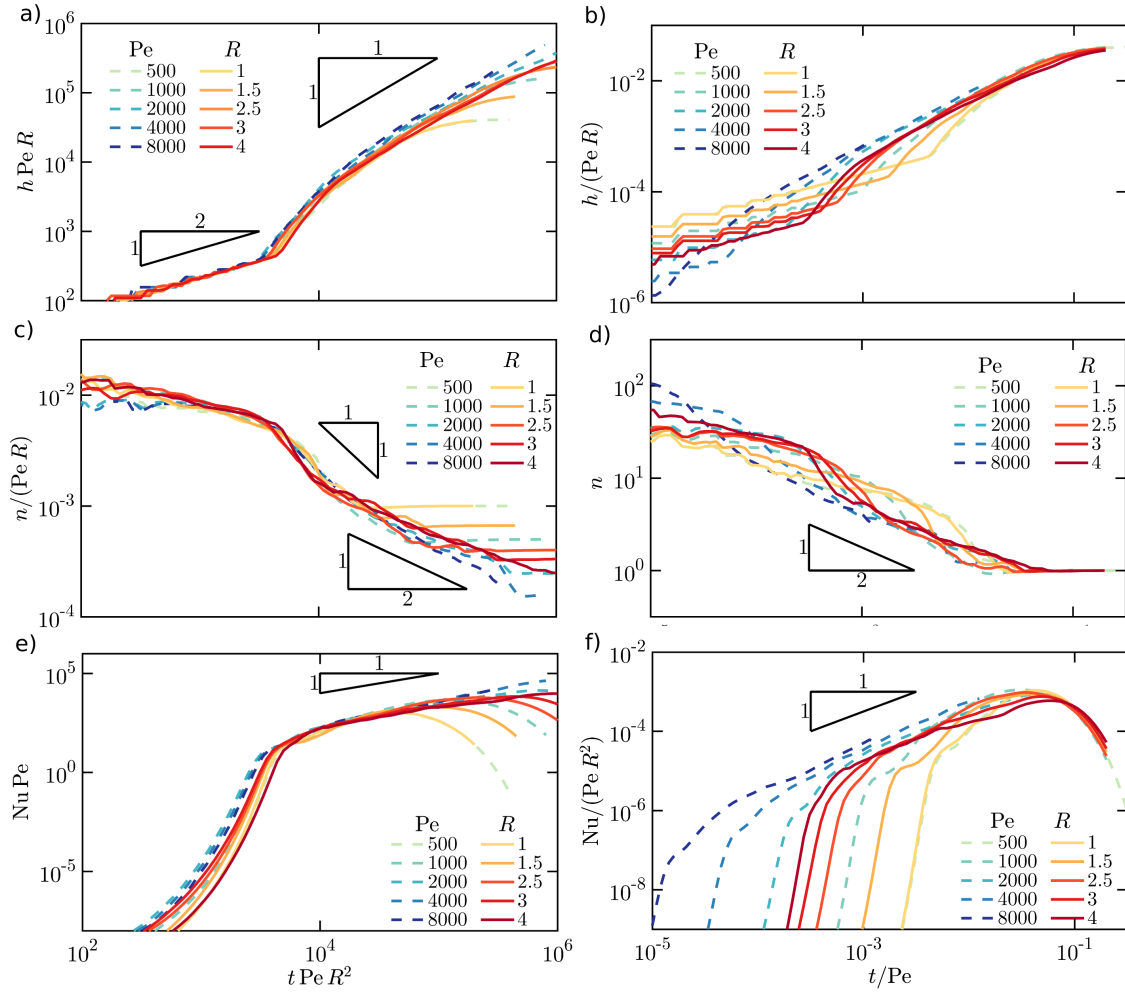


Fig. 2.4 Rescaled plots of (a,b) h , (c,d) n , and (e,f) Nu for early times (left) and late times (right). The dashed lines are for constant $R = 2$ and different Pe as marked, while the solid lines are for constant $Pe = 1000$ and different R as marked. To reduce the noise in the data, two different simulations are averaged.

and $x \sim \frac{1}{R\text{Pe}}$. That is, at early times, the number of fingers scales linearly with both R and Pe . Figure 2.4(c) shows a rescaled plot of the number of fingers which collapses well with this scaling. Finally, the Nusselt number is defined as the product of the exponentially growing velocity $u \sim R e^{\sigma t}$ and concentration perturbations $c' \sim e^{\sigma t}$ integrated over the size of the perturbations $x \sim \frac{1}{R\text{Pe}}$ (where σ is the growth rate of the instability). Given the time scale identified above, $t \sim \frac{1}{R^2\text{Pe}}$, we collapse the data for the Nusselt number with the scaling $\text{Nu} \sim e^{tR^2\text{Pe}}/\text{Pe}$ (figure 2.4(e)).

At intermediate times the fingers interact non-linearly causing them to elongate and coarsen. The horizontal velocity remains relatively constant and is solely a function of the log-viscosity ratio, $u = U(R)$. An advective balance in (2.13) gives the scaling $\frac{Uc}{h} \sim \frac{c}{t}$, or $h \sim U(R)t$, and this linear growth of the mixing zone in time can be seen in figures 2.4(a,b). In fact, we return to the functional form of the velocity $U(R)$ in §2.4.2, and find that it can be approximated by $U \sim R$ for $R \sim O(1)$. The number of fingers, n , in the intermediate-regime, follows two distinct coalescence regimes. Initially the coalescence is advectively dominated, and in this limit (2.13) gives the scaling $\frac{vc}{1/n} \sim \frac{c}{t}$. Assuming that the transverse velocity is $O(R)$ and constant, then $n \sim \frac{1}{Rt}$. Subsequently, the flow becomes diffusively dominated and (2.13) gives the scaling $\frac{c}{t} \sim \frac{c}{\text{Pe}/n^2} \Rightarrow n \sim (t/\text{Pe})^{-\frac{1}{2}}$. These two scaling laws can be seen in figures 2.4(c,d). In the intermediate-time regime, the Nusselt number scales with the width of the mixing region ($h \sim Rt$) and the average convective flux, which scales with the velocity $U \sim R$. Together, this gives the scaling $\text{Nu} \sim R^2t$ (see figures 2.4(e,f)). These observations suggest that the Nusselt number and growth of the mixing zone are independent of the Peclet number and, after a small amount of time spent advectively coalescing, the finger coalescence becomes independent of the viscosity ratio.

Finally, at late times, a single pair of long, thin fingers counter-propagate and decay through a background concentration gradient. As seen in figure 2.4(d), all simulations tend to this single-pair (single-maxima) state. Assuming that the concentration deviations from the background are small and applying a long, thin approximation to equation (2.23), results in the scaling $u \sim R$ (as discussed in more detail in §2.5). Balancing longitudinal advection and transverse diffusion over a single finger yields the scaling $\frac{Rc}{h} \sim \frac{1}{\text{Pe}} \Rightarrow h \sim R\text{Pe}$. A diffusive balance, $\frac{c}{t} \sim \frac{1}{\text{Pe}}$, suggests that the time should be scaled by the Peclet number in this late-time regime. Applying the same argument as before, the Nusselt number decays exponentially like $\text{Nu} \sim \text{Pe}R^2 e^{-t/\text{Pe}}$.

The transitions between these different regimes are controlled by the relevant time scalings in each regime. The transition from the early-time to intermediate-time regime occurs once the concentration perturbations saturate and the flow becomes nonlinear.

Early times	Intermediate times	Late times
$h \sim \left(\frac{t}{\text{Pe}}\right)^{\frac{1}{2}}$	$h \sim Rt$	$h \sim R\text{Pe}$
$n \sim R\text{Pe}$	$n \sim \frac{1}{Rt} \quad n \sim \left(\frac{t}{\text{Pe}}\right)^{-\frac{1}{2}}$	$n = 1$
$\text{Nu} \sim e^{tR^2\text{Pe}}/\text{Pe}$	$\text{Nu} \sim R^2t$	$\text{Nu} \sim R^2\text{Pe}e^{-t/\text{Pe}}$

Table 2.1 Scalings for h , n , and Nu for early, intermediate, and late times. The transition from the early-time to intermediate-time regime occurs at $t \sim O\left(\frac{1}{R^2\text{Pe}}\right)$ and the transition from the intermediate-time to late-time regime occurs at $t \sim O(\text{Pe})$.

Since the perturbations grow exponentially, and the time-scale of their growth is $t \sim \frac{1}{R^2\text{Pe}}$, the perturbations will reach a certain amplitude at a time, $t \sim O\left(\frac{1}{R^2\text{Pe}}\right)$. The transition to the late-time regime occurs once the flow coarsens to a single-finger. Since this coarsening process is diffusively dominated, the fingers will coarsen to one finger once the flow has diffused over the entire transverse length. This means the transition between the intermediate-time and late-time regime occurs at $t \sim O(\text{Pe})$.

The scalings are summarized in table 2.1. In the following sections, we discuss each of these regimes in more detail with an emphasis placed on understanding the evolution of the transversely averaged concentration.

2.4 Early- and intermediate-time regimes

2.4.1 Early times: linearly unstable regime

The concentration gradient between the two fluids, which are not moving relative to each other, is initially very high and spreads by diffusion. Neglecting the very small initial perturbations in (2.26), the resultant concentration profile is one-dimensional and given by

$$c(x, t) = \frac{1}{2} + \frac{1}{2} \operatorname{erf} \left(-\frac{x}{\sqrt{4t/\text{Pe}}} \right). \quad (2.27)$$

Therefore, before the instability manifests itself, the concentration front widens like $(t/\text{Pe})^{\frac{1}{2}}$, which corresponds to the early-time scaling of h (see figure 2.4(a)).

When $R > 0$, the flow rapidly develops a viscous-fingering instability in which perturbations grow exponentially. Many authors have explored the onset of viscous fingering in a variety of contexts using linear stability theory. Tan and Homsy (1987) found that the instability can be suppressed for all times, in a radial geometry, if the

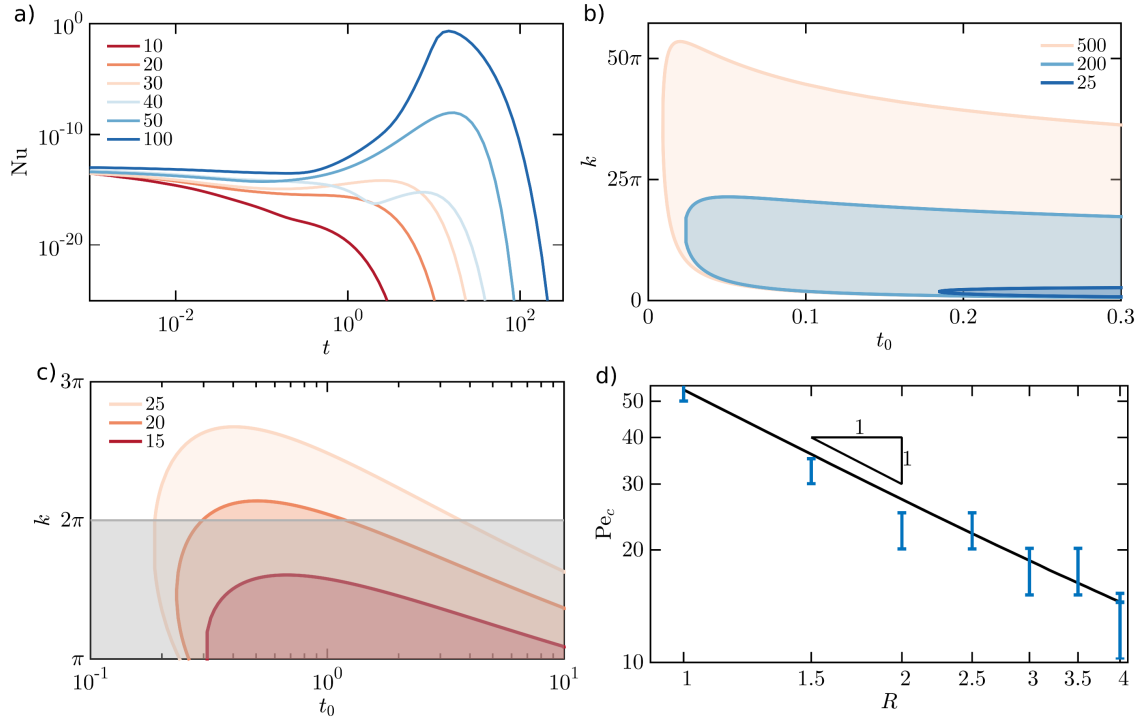


Fig. 2.5 (a) $Nu(t)$, attained from direct numerical simulations, plotted on logarithmic axes for $R = 2$ and different Pe as marked. The Nusselt number is strictly decreasing for $Pe = 20$, but has a period of growth for $Pe = 30$, suggesting a point of marginal stability between $Pe = 20$ and 30 . (b,c) Marginal stability curves ($\sigma = 0$; outlines) and regions of instability ($\sigma > 0$; shaded areas), for $R = 3$ and (b) $Pe = 25, 200, 500$ and (c) $Pe = 15, 20, 25$. Wavenumbers less than $k = 2\pi$ cannot be contained within the domain, and so the flow is stable for $k < 2\pi$, as indicated by the grey region in (c). (d) Plot of the critical Peclet number versus log-viscosity ratio based on the linear stability analysis (black line) and numerical simulations (blue ranges). The lower and upper estimated values of Pe_c from our simulations in (d) are given, respectively, by the largest Pe for which $Nu(t)$ monotonically decreases, and by the smallest Pe for which $Nu(t)$ increases at any time.

Peclet number is below some critical value. In a planar geometry, however, Pramanik and Mishra (2015) found a time-dependent critical Peclet number which decreases in time, and suggested that there may be no Peclet number for which the flow is always stable.

In this section, by noting the fact that the domain is transversely finite and that there is a restriction on the largest permissible mode inside the domain, we show that there is, in fact, a critical Peclet number below which the flow is always stable. To motivate the existence of this critical Peclet number, figure 2.5(a) shows $\text{Nu}(t)$ for $R = 2$ and small Peclet numbers. For the range of Peclet numbers plotted, the Nusselt number never transitions to power-law growth, suggesting that there are choices of parameters where the flow never enters the non-linear regime. In fact, we notice that for Peclet numbers less than or equal to 20, the Nusselt number is strictly decreasing, implying the configuration is stable for all times, while for Peclet numbers greater than or equal to 30, the Nusselt number goes through a period of growth. In this section, we perform a linear stability analysis to show the existence of a critical Peclet number for the instability.

We start with a diffusive base-state solution of the unperturbed system $c_0(x, t)$ given by equation (2.27). To accommodate the rapidly varying base-state at early times we use a similarity transformation $\xi = x/\sqrt{t}$, in terms of which (2.27) is steady,

$$c_0(\xi) = \frac{1}{2} \left[1 + \operatorname{erf} \left(\frac{-\xi\sqrt{\text{Pe}}}{2} \right) \right]. \quad (2.28)$$

We then linearize equations (2.13) and (2.23) about this base-state and look for perturbations of the form $u'(\xi, y, t) = \phi(\xi)\tau(t)e^{iky}$ and $c'(\xi, y, t) = \beta(\xi)\tau(t)e^{iky}$, which satisfy,

$$\left(\sigma(t_0) - \frac{\xi}{2t_0} \frac{d}{d\xi} - \frac{1}{\text{Pe} t_0} \frac{d^2}{d\xi^2} + \frac{k^2}{\text{Pe}} \right) \beta = -\frac{1}{\sqrt{t_0}} \frac{dc_0}{d\xi} \phi, \quad (2.29)$$

$$\left(\frac{1}{t_0} \frac{d^2}{d\xi^2} - \frac{R}{t_0} \frac{dc_0}{d\xi} \frac{d}{d\xi} - k^2 \right) \phi = -Rk^2 \beta, \quad (2.30)$$

where $\sigma(t_0) \equiv \frac{1}{\tau} \frac{d\tau}{dt} |_{t=t_0}$ is the instantaneous growth rate at $t = t_0$, such that $\tau = e^{\int_0^t \sigma dt_0}$ (see also Pramanik and Mishra, 2015). We note that this formulation does not require any assumption of a slowly-varying or quasi-steady background. We solve (2.29) and (2.30) by discretizing the domain using standard second-order finite-difference approximations for the differential operators, which yields the matrix eigenvalue problem

$$\mathbf{M}\beta = \sigma\beta. \quad (2.31)$$

The growth rate of the most unstable mode is given by the maximum eigenvalue of the matrix \mathbf{M} . This growth rate depends on Pe and R , as well as, time t_0 and the wavenumber of the perturbation k .

Figure 2.5(b) shows the marginal stability curve $\sigma(k, t_0) = 0$, where σ is the growth rate of the most unstable mode, for $R = 3$ and a variety of Peclet numbers. The system is always initially stable and goes unstable at a critical time $t_0^* > 0$. Zooming into the region around wavenumber $k = 2\pi$ (figure 2.5(c)), which is the largest mode that is permissible inside the domain, we notice that for $\text{Pe} = 20$, the marginal stability curve lies above $k = 2\pi$ for only a finite amount of time: once the marginal stability curve falls below this value, the flow is again stable. In fact, this transition back to stability at large t_0 is a general feature for all R and Pe and this intermittent stability suggests that if the interface is diffuse enough, the instability can be suppressed, in agreement with experimental evidence (Loggia et al., 1999). Finally, we notice that for Peclet numbers smaller than some critical value $\text{Pe}_c(R)$, the growth rate is only positive for wavenumbers smaller than 2π . These modes do not fit in the domain and the interface is therefore always stable. For example, in figure 2.5(c) the critical Peclet number lies between 15 and 20.

The transitions out of, and back into, stability, occur as diffusion tends to arrest the instability. The system is initially stable because, for small t , the growth of the interface ($O(t^{-\frac{1}{2}})$) outpaces the exponential growth of the perturbations. Matching the diffusive length-scale ($\frac{t^{1/2}}{\text{Pe}^{1/2}}$) to the length-scale of the most unstable perturbation ($\frac{1}{R\text{Pe}}$) gives a transition time $t \sim \frac{1}{R^2\text{Pe}}$. At sufficiently large times, the base flow is again stable, because the background concentration gradient has weakened to such an extent that transverse diffusion ($\frac{1}{\text{Pe}y^2}$) can smear out the advective growth of perturbations ($u \frac{\partial \bar{c}}{\partial x} \sim R \frac{\text{Pe}^{1/2}}{t^{1/2}}$). Balancing these two terms for $y \sim O(1)$ gives a transition time to return to stability, $t \sim R^2\text{Pe}^3$. At some critical Peclet number, Pe_c , the time-scales of the initial instability and subsequent stabilization match, and the instability is completely suppressed. This balance gives $\text{Pe}_c \sim \frac{1}{R}$. The transition back to stability also indicates that fingering can be prevented by allowing the interface to diffuse before injection for a time $O(R^2\text{Pe}^3)$, or by initializing (for example by pre-mixing) a concentration gradient of width $O(R\text{Pe})$.

Figure 2.5(d) shows $\text{Pe}_c(R)$ calculated from the linear stability analysis, which agrees with this predicted scaling. The figure also shows estimates of Pe_c from direct numerical simulations, which give a reasonable agreement with the theory.

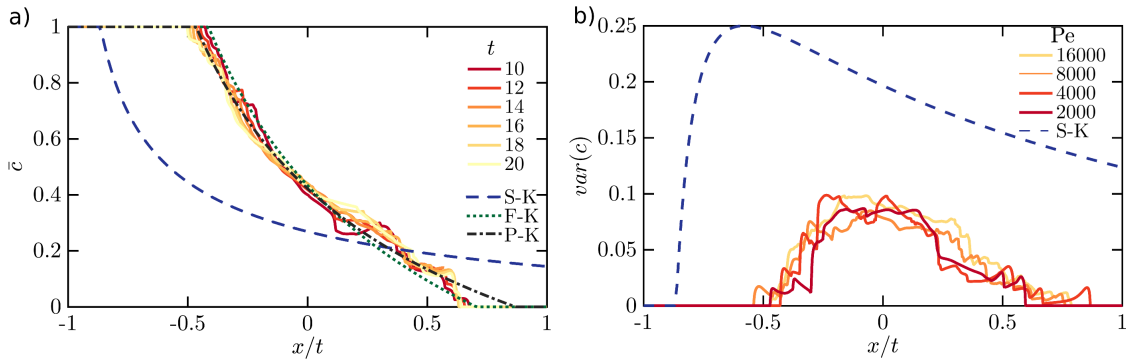


Fig. 2.6 (a) Plot of the transversely averaged concentration against the similarity variable x/t . Here $R = 2$, $Pe = 1000$ and the time, given by the colour, ranges from 10 to 20. Each curve plotted represents the average of five different simulations. The dashed lines represent the three different model solutions: simple Koval (blue, dashed), fitted Koval (green, dotted), and parabolic Koval (black, dot-dashed). (b) Plot of the transverse variance in concentration for $Pe = 2000, 4000, 8000$, and 16000 at $t = 8, 4, 2$ and 1 . By sampling at these different times, we normalize for the effect of the onset of the instability. The variance calculated from the simple Koval model is given by the blue dashed line.

2.4.2 Intermediate times: non-linear coalescence regime

The linear instability results in a number of fingers which grow exponentially and independently of their neighbours. After some time, the fingers begin to interact with each other. Although the non-linear finger interactions exhibit complex and chaotic patterns and vary significantly over time and from simulation to simulation, the number of fingers, mixing length, and Nusselt number are largely indifferent to the exact intermediary mechanisms (see rescaled data in figure 2.4). The transversely averaged concentration is asymmetric, non-linear, and evolves in a self-similar fashion (figure 2.6(a)). There have been many attempts to model the behaviour of the transversely averaged concentration, with one of the simplest and most widely used models being the empirically derived formula of Koval (1963). While this model has been revisited by multiple authors (Booth, 2010; Yortsos and Salin, 2006), a fully closed model is yet to be derived. In this section we start by re-deriving the simple model that was first proposed by Koval (hereafter, the ‘simple Koval model’), and comment on its strengths and shortcomings. In order to address one of these shortcomings, we then propose a simple improvement to the model, which gives a qualitative improvement when compared with the numerical simulations.

The simple Koval model can be derived in the limit where both the aspect ratio of the fingers and the Peclet number are large, ($hn \gg 1$ and $Pe \gg 1$ respectively). Under these conditions the flow is predominantly horizontal and longitudinal diffusion

is negligible. The velocity is calculated by taking the leading order expansion in hn in (2.23),

$$\frac{\partial u}{\partial y} - Ru \frac{\partial c}{\partial y} = R \frac{\partial c}{\partial y}, \quad (2.32)$$

which has solution

$$u = \frac{e^{Rc}}{\int_0^1 e^{Rc} dy} - 1. \quad (2.33)$$

Substituting this form for the velocity into (2.18) and neglecting longitudinal diffusion gives,

$$\frac{\partial \bar{c}}{\partial t} + \frac{\partial}{\partial x} \left(\frac{\int_0^1 c e^{Rc} dy}{\int_0^1 e^{Rc} dy} - \bar{c} \right) = 0. \quad (2.34)$$

The simple Koval model proceeds under the assumption that the fingered region consists of $\eta_b(x)$ leftward-propagating fingers of width $w_b(x)$ with uniform concentration $c = 0$ and $\eta_f(x)$ rightward-propagating fingers of width $w_f(x)$ with uniform concentration $c = 1$. Under these assumptions, (2.34) becomes

$$\frac{\partial \bar{c}}{\partial t} + \frac{\partial}{\partial x} \left(\frac{\eta_f \int_{-w_f}^{w_f} e^R dy}{\eta_f \int_{-w_f}^{w_f} e^R dy + \eta_b \int_{-w_b}^{w_b} 1 dy} - \bar{c} \right) = 0. \quad (2.35)$$

In addition, the total area of the fingers has to add up to one, $\eta_f w_f + \eta_b w_b = 1$, and the total concentration in the forward propagating fingers has to equal the transverse average, $\eta_f w_f = \bar{c}$. Combining these constraints and simplifying (2.35) results in a hyperbolic equation for \bar{c} ,

$$\frac{\partial \bar{c}}{\partial t} + \frac{\partial}{\partial x} \left(\frac{M \bar{c}}{M \bar{c} + 1 - \bar{c}} - \bar{c} \right) = 0, \quad (2.36)$$

where $M \equiv e^R = \mu_2/\mu_1$ is the viscosity ratio between the two unmixed fluids. The solution to (2.36) is

$$\bar{c}(x, t) = \begin{cases} 1 & x/t < \frac{1}{M} - 1 \\ \frac{1}{M-1} \left(\sqrt{\frac{M}{x/t+1}} - 1 \right) & \frac{1}{M} - 1 \leq x/t \leq M - 1 \\ 0 & x/t > M - 1. \end{cases} \quad (2.37)$$

Although coalescence occurs through a nonlinear diffusive process, the longitudinal spreading of the interface is advectively dominated. As a result, the flow is self-similar in the variable x/t and has finite forward velocity $M - 1$ and finite backward velocity $1/M - 1$. This asymmetry comes from the fact that in order to maintain a transversely uniform pressure, the leading, less viscous fingers must travel M times faster than

the more viscous surrounding fluid downstream, and the trailing more viscous fingers must travel $1/M$ times as fast as the less viscous surrounding fluid upstream, in the non-travelling frame. Figure 2.6(a) compares (2.37) to the numerical simulations. The simple Koval model accurately predicts two qualitative features of the non-linear spreading process: an asymmetric concentration profile, and self-similarity in the variable x/t . However, this model greatly over-predicts the spreading of the mixing zone (figure 2.6(a)). To account for the difference between the model and experiments, Koval, in their original work, empirically fit an effective viscosity M_e to the experiments of Blackwell et al. (1959), yielding,

$$M_e = \left[0.22e^{R/4} + (1 - 0.22) \right]^4. \quad (2.38)$$

The prediction of (2.37) with M replaced by M_e in (2.38), which we denote the ‘fitted Koval’ model, gives a remarkably good fit with our numerical results (figure 2.6(a)). Indeed, the agreement in figure 2.6(a) is all the more surprising given that (2.38) was fitted for fluids with a different relationship between viscosity and concentration than we are using here. Nonetheless, in spite of recent attempts, there is no rigorous derivation of this form of effective viscosity ratio. Furthermore, this fitted model tends to break down for large M (Malhotra et al., 2015).

One of the critical assumptions of the Koval model is that the concentration is either exactly one or exactly zero. We interrogate this assumption by plotting the concentration field from a simulation with a large Peclet number ($Pe = 16000$) in figure 2.7(a). We find that even at very large Pe , the concentration is not just one or zero but varies in both the streamwise and transverse direction. The concentration along the local maxima and minima of the fingers (figure 2.7(b)) decreases and increases towards the tips, respectively. In the transverse direction, the concentration takes on a single maximum or minimum in each finger, which, in its simplest form, can be approximated by a parabola (figure 2.7(c)). These two factors together result in a much smaller prediction for the transverse variance in concentration than the simple Koval model predicts (figure 2.6(b)). Interestingly, in this limit of large Pe , the variance is independent of the Peclet number, which suggests that the Peclet number has no effect on the effective viscosity in this regime in agreement with the fact that (2.37) and (2.38) have no dependence on Pe .

Motivated by these observations, we suggest a very simple improvement to the simple Koval model, which addresses one of its main assumptions. In the simple Koval model, the viscosity is uniformly given by e^R or 1 in each finger, which follows from the assumption of uniform concentration in each finger. However, we observe

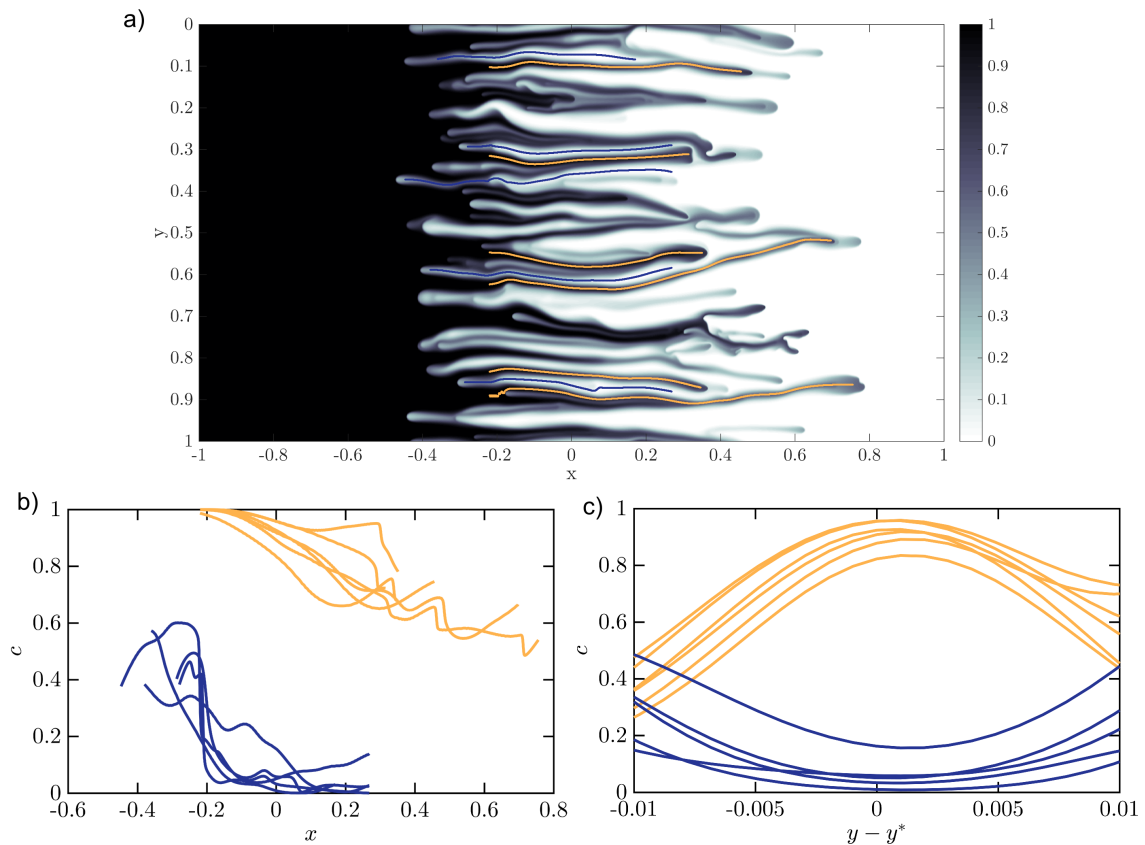


Fig. 2.7 (a) Snapshot of the concentration profile at $t = 1$ for a simulation with $Pe = 16000$ and $R = 2$. Superimposed are lines which follow the peaks (orange) and troughs (blue) in concentration. (b) Concentration profile along peaks (orange) and troughs (blue). (c) Concentration profile in the transverse direction at $x = 0$ centred around the peaks (orange) and troughs (blue).

that the concentration actually varies across the fingers, and we can approximate this variation as being parabolic. In fact, the significant improvement to the simple model by the empirical fit (2.38) suggests that the main consequence of ignoring this variation is an inaccurate calculation of the effective viscosity. We therefore propose a simple modification of the Koval model in which the viscosity varies with a quadratic concentration profile across each finger; that is, $\mu(y) = e^{R(1-y^2/w_f^2)}$ and $\mu(y) = e^{R(y^2/w_b^2)}$ in the forward and backward propagating fingers, respectively. Note that we find that the model results do not depend very strongly on the transverse profiles so long as it has a roughly parabolic shape and provided the mean viscosity in the fingers is the same. For instance, the effective viscosity found by assuming the fingers have Gaussian transverse profiles is similar to the parabolic case (not shown). In all other respects, we retain the same assumptions as in the simple Koval model: the fingers are still assumed to be horizontally uniform, and to obtain a simple analytical solution with the same functional form as the simple Koval model, the mean concentration in each finger is still assumed to be either zero or one.

Under these assumptions, (2.35) instead becomes

$$\frac{\partial \bar{c}}{\partial t} + \frac{\partial}{\partial x} \left(\frac{\eta_f \int_{-w_f}^{w_f} e^{R(1-y^2/w_f^2)} dy}{\eta_f \int_{-w_f}^{w_f} e^{R(1-y^2/w_f^2)} dy + \eta_b \int_{-w_b}^{w_b} e^{R(y^2/w_b^2)} dy} - \bar{c} \right) = 0. \quad (2.39)$$

Combining (2.39) with the same constraints as before, and solving, results in the same expression for \bar{c} as (2.37) but with an effective viscosity ratio

$$M_e = \frac{e^R \operatorname{erf}(\sqrt{R})}{\operatorname{erfi}(\sqrt{R})}, \quad (2.40)$$

where $\operatorname{erfi}(x)$ is the imaginary error function. We denote this model as the ‘parabolic Koval’ model. Note that, as with the simple Koval model, the improved model does not depend on the width or the number of fingers as observed in the numerical simulations. However, in common with the simple Koval model, this choice of viscosity leads to discontinuous transverse concentration profiles. Although discontinuous, this form for the concentration allows one to improve on the simple model by accounting for measured variations in the concentration across the fingers.

Figure 2.8 plots the effective viscosity ratio extracted from the numerical simulations (dots), together with the predictions of the simple Koval model (S-K), the empirically fit effective viscosity (F-K) (2.38), and the analytically derived model with parabolic transverse profiles (P-K) (2.40). The simple Koval model overpredicts the effective

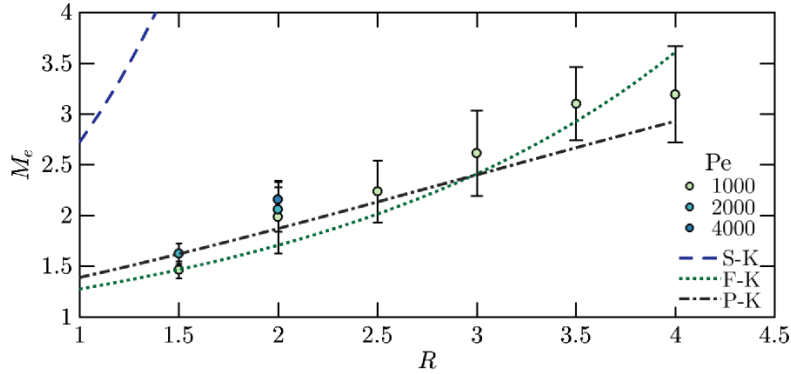


Fig. 2.8 Plot of the effective viscosity ratio measured for different values of R and Pe . Each point plotted is calculated by extracting the value of M from a least-squares fit of (2.37) to the transversely averaged concentration profiles $\bar{c}(x, t)$, at five different times $t = 10, 11, 12, 13, 14$ and five different simulations. These measurements are then averaged and the error bars represent one standard deviation in these measurements. The three different model predictions are: simple Koval (blue, dashed), fitted Koval (green, dotted), and parabolic Koval (black, dot-dashed)

viscosity of the fingered region, whereas the parabolic model agrees well with both the empirical fit and numerical experiments. In fact, the parabolic model predicts smaller effective viscosities than the empirical fit for $R > 3$ in qualitative agreement with experiments by Malhotra et al. (2015). Although the model agrees well with the data, it remains, of course, an approximation: it does not take into account the along-flow variations in concentration, and it still assumes the concentration (but not the viscosity) is either one or zero in each finger. Nevertheless, we have shown that an accurate effective viscosity in the Koval model can be derived simply by assuming the viscosity varies smoothly in the transverse direction.

2.5 Late times: single-finger exchange-flow regime

2.5.1 Numerical observations

At late times, we find a new flow regime which, to leading order, involves a single pair of fingers counter-propagating through a linear background concentration gradient as shown by the snapshots in figure 2.9. The concentration field is dominated by a nearly uniform background gradient in the horizontal direction with some small transverse deviations superimposed (figure 2.9(a)). The concentration deviations (figure 2.9(b)) are horizontally uniform and have a single maximum (i.e. they form a single finger).

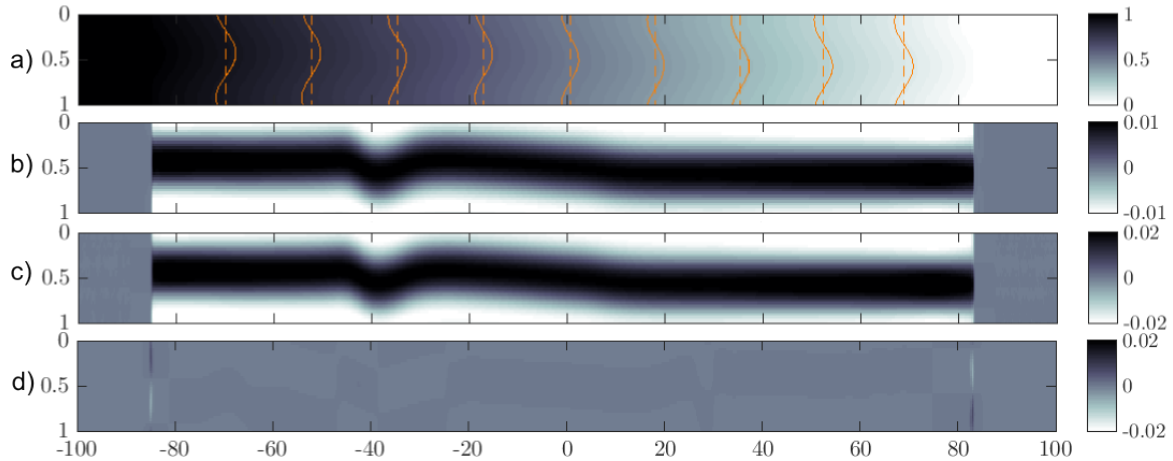


Fig. 2.9 Snapshots at $t = 500$ for $R = 2$, $Pe = 2000$. (a) Colourmap of the concentration with overlain contours of the raw (solid) and transversely averaged (dashed) concentration. (b) Colourmap of $c'(x, y) = c(x, y) - \bar{c}(x)$. (c) Colourmap of the horizontal velocity u . (d) Colourmap of the vertical velocity v . Note that the x-axis has been compressed by a factor of 10 in these plots.

The horizontal velocity u (figure 2.9(c)) tracks closely the concentration deviations while the vertical velocity v (figure 2.9(d)) is only appreciable at the tips.

Figure 2.10 shows how the concentration field evolves over time. We find that the transversely averaged concentration, $\bar{c}(x)$, is linear and steady in the interior. The fluid flow only widens the mixing region by filling in the linear profile (inset to figure 2.10(a)). In addition, we find that \bar{c} is no longer skewed and $\bar{c} = 1/2$ is in the middle of the domain. These features are in stark contrast to the previous regime in which $\bar{c}(x)$ was asymmetric and non-linear. Superimposed on this background concentration field are horizontally uniform deviations which are sinusoidal in the transverse direction (figure 2.10(b)). These deviations decay in time, which ultimately results in a one-dimensional linear concentration field that evolves purely by diffusion in the x direction.

We find that the single-finger state is stable, that is, no tip-splitting occurs. The manner by which these fingers are stabilized is distinct from the classical Saffman-Taylor finger where surface tension acts as the stabilizing force. In this case, weak longitudinal concentration gradients and transverse diffusion not only stabilize the fingers but also cause them to decay.

2.5.2 Asymptotic model

The late-time regime is characterized by a linear background gradient with a single pair of counter-propagating fingers superimposed. The fingers have a very large aspect

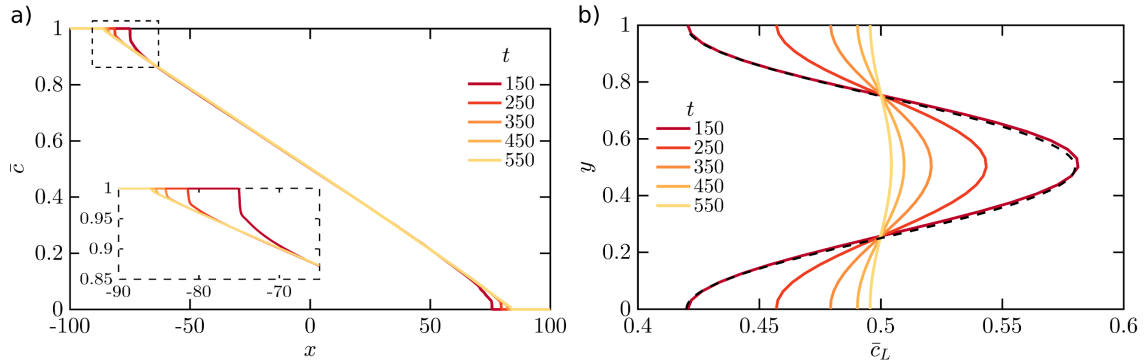


Fig. 2.10 (a) Plot of the transversely averaged concentration. (b) Plot of the longitudinally averaged concentration $\bar{c}_L(y) = \int_{-\Gamma/2}^{\Gamma/2} c(x, y) dx = \frac{1}{2} + \int_{-\Gamma/2}^{\Gamma/2} c'(x, y) dx$. A sinusoidal fit for $t = 150$ is given by the dashed black line. In both plots $R = 2$, $Pe = 2000$ and the time, given by the colour, ranges from 150 to 550.

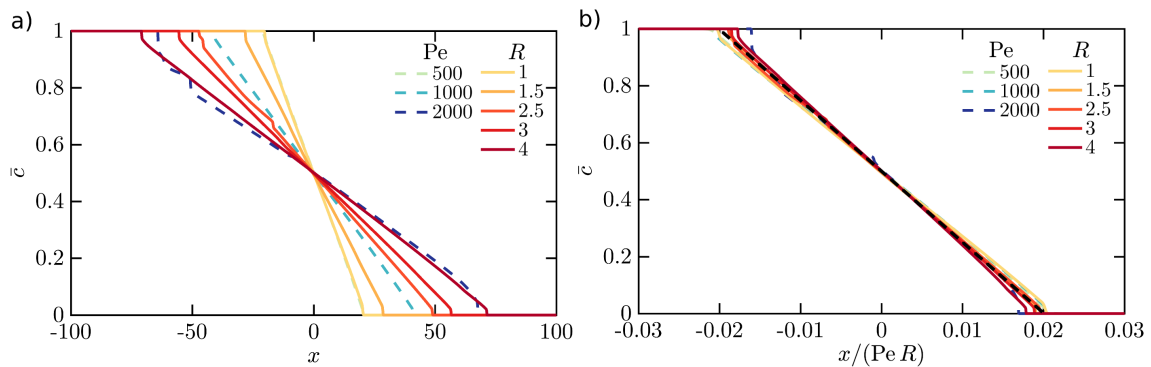


Fig. 2.11 (a) Plots of $\bar{c}(x)$ for $R = 2$, $Pe = 500, 1000, 2000$ (dashed) and $Pe = 1000$ and $R = 1, 1.5, 2.5, 3, 4$ (solid) at $t = 200$. (b) \bar{c} as a function of $x/(RPe)$, with the fitted line $\bar{c} = 1/2 - 24.9x/RPe$ (black, dashed)

ratio, and so the velocity is given by (2.33), which for small deviations c' , reduces to

$$u = Rc' + O(c'^2). \quad (2.41)$$

We look for a steady interior solution for \bar{c} , for which (2.18) becomes

$$\frac{1}{\text{Pe}} \frac{\partial^2 \bar{c}}{\partial x^2} = O(c'^2), \quad (2.42)$$

or

$$\bar{c} = -\alpha x + \frac{1}{2} + O(c'^2). \quad (2.43)$$

Given that the net change in concentration of the two fluids must be equal and opposite, the concentration at the mid-plane must be $1/2$, which determines the constant of integration in (2.43).

Substituting the steady transversely averaged concentration (2.43) and velocity (2.41) into equation (2.19) results in a partial differential equation for the evolution of the deviations,

$$\frac{\partial c'}{\partial t} - \alpha Rc' = \frac{1}{\text{Pe}} \frac{\partial^2 c'}{\partial y^2} + O\left(\frac{c'}{\text{Pe}h^2}\right) + O(c'^2). \quad (2.44)$$

The leading order behaviour of (2.44) is a balance between the growth/decay of the concentration deviations, advection of the background concentration gradient and transverse diffusion. Advection of the background tends to cause the deviations to grow since positive deviations tend to move high concentrations downstream (and negative deviations move low concentrations upstream), while diffusion causes them to attenuate. This competition results in the exponential decay of the fingers and eventual shutdown of the instability. Furthermore, this equation is independent of x ; therefore, the deviations must be horizontally uniform, as observed. The single-finger solution to the leading order truncation of (2.44) is,

$$c'(y, t) = \sin(2\pi y) e^{-\gamma(t-t^*)}, \quad (2.45)$$

where t^* is a virtual origin relating to the transition between regimes and

$$\gamma = \frac{4\pi^2}{\text{Pe}} - \alpha R. \quad (2.46)$$

Note that, while a solution of (2.44) with any integer number of fingers is permissible, solutions with more fingers decay more rapidly over time, and the solution with $k = 2\pi$ (2.45) is the slowest decaying mode.

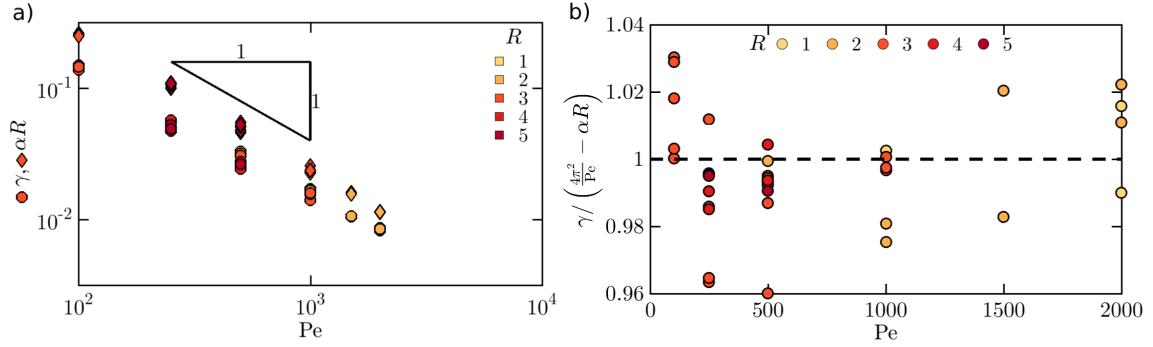


Fig. 2.12 (a) Plot of γ (circles) and αR (diamonds) as functions of Pe and R (colours). (b) Ratio of γ , measured from the simulations as the decay rate of the maximum of c' at $x = 0$, to $\gamma(\alpha R)$, calculated using equation (2.46) where α is the slope of \bar{c} measured at $t > 200$.

The slope α of the interior profile in (2.43) is set by the amount of mixing that occurs during the intermediate and late-time regimes. In both regimes $u \sim R$ and $t \sim Pe$. Therefore, once the system has shutdown, the width of the mixing zone will have become $h \approx 1/\alpha \sim RPe$, such that $\alpha R = \hat{A}/Pe$, for some constant \hat{A} . We fit $\hat{A} = 24.9$ to the collapsed transversely averaged concentration profiles (figure 2.11(b)).

We verify this model by measuring α and γ from the numerical simulations. We calculate α by measuring the slope of \bar{c} at $x = 0$ at some late time, and γ by measuring the decay rate of the maximum of c' at the mid-plane. Plots of the numerically measured γ and αR are given in figure 2.12(a) and both quantities exhibit the predicted $1/Pe$ scaling. Finally, the validity of equation (2.46) is tested by plotting the ratio of γ measured from the simulations and $\gamma(\alpha)$ calculated using equation (2.46). This quantity is plotted in figure 2.12(b) and deviates by a maximum of 4% over a range of Peclet numbers and log-viscosity ratios.

2.5.3 Total convective mixing

One of the major implications of this final single-finger exchange-flow regime is that the viscous-fingering instability can only generate a finite amount of convective mixing. In figure 2.13a we plot the time-integral of the convective flux through the midplane,

$$F = \int_0^\infty \int_0^1 uc'|_{x=0} dy dt, \quad (2.47)$$

as a function of the Peclet number and log-viscosity ratio. We find that the flux increases linearly with both Pe and R for $Pe \gg 1$, and can be fit by the functional form $F = \hat{a}R(Pe - \hat{b}/R)$, where the shift in the Peclet number, \hat{b}/R , corresponds to

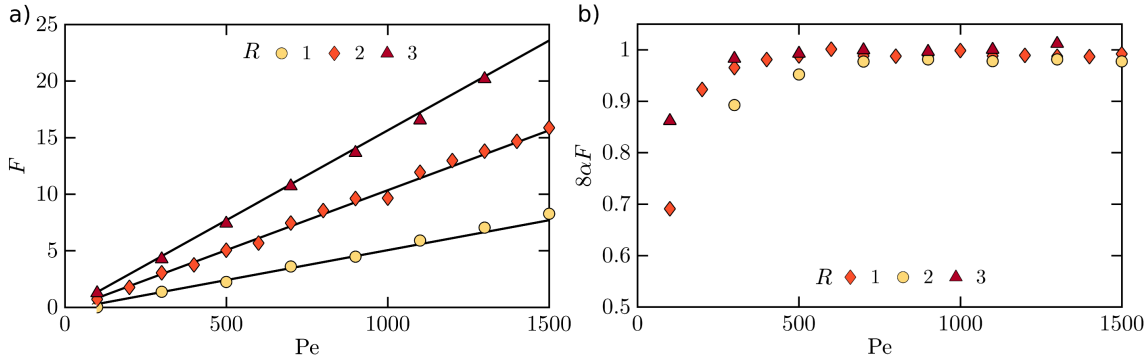


Fig. 2.13 (a) Time-integrated convective exchange flux F (2.47) between the two fluids as a function of Pe and R (colours), as calculated from the numerical simulations. In order to calculate the infinite time integral in (2.47), we integrate the numerical data out to $t = 200$, which is well into the late-time regime in all simulations, and fit a decaying exponential function $E(t)$ to the flux $\int_0^1 uc'|_{x=0} dy$ for subsequent times such that $F = \int_0^{200} \int_0^1 uc'|_{x=0} dy dt + \int_{200}^{\infty} E(t) dt$. The lines of best fit (black) correspond to the fit $F = 5.3 \times 10^{-3} R(Pe - 45/R)$. (b) Ratio of the time-integrated convective exchange flux and the final slope of the transversely averaged concentration.

the onset of the instability as described in section 2.4.1. We find that the numerical data is best fit with $\hat{a} = 5.3 \times 10^{-3}$ and $\hat{b} = 45$ (solid lines in figure 2.13(a)).

Of course, provided advection dominates the horizontal transport, the quantity F can also be directly related to the slope α of the late-time profiles, by mass conservation. Such a balance gives

$$F \approx \int_0^{\infty} \bar{c} dx \approx \frac{1}{8\alpha}. \quad (2.48)$$

For the three values of R plotted, we find that this prediction gives good agreement for $Pe > O(100)$ (figure 2.13(b)), which suggests that for the range of R plotted, horizontal diffusion plays a negligible role in mixing for $Pe > O(100)$.

2.6 Discussion and Conclusions

2.6.1 Summary

In this chapter, miscible viscous fingering in a semi-infinite planar geometry was investigated using high-resolution simulations. Three distinct regimes were identified: an early-time linearly unstable regime, an intermediate-time non-linear regime, and a late-time single-finger exchange-flow regime. In each of these regimes, the predominant balances and scalings for the mixing length h , the number of fingers n , and the total convective transport Nu were identified (table 2.1).

Early-times	Intermediate-times	Late-times
$X \sim D^{1/2}T^{1/2}$	$X \sim \frac{RU}{\phi}T$	$X \sim \frac{RUa^2}{\phi D}$
$Y \sim \frac{\phi D}{RU}$	$Y \sim \frac{RU}{\phi}T, \quad Y \sim D^{1/2}T^{1/2}$	$Y \sim a$

Table 2.2 Dimensional length scales X and Y as a function of dimensional time T . We define a mean injection velocity $U = Q/a$. The transition from the early-time to intermediate-time regime occurs at $T \sim O(\frac{\phi^2 D}{R^2 U^2})$ and the transition from the intermediate-time to late-time regime occurs at $T \sim O(\frac{a^2}{D})$. The vertical length-scale in the intermediate regime first grows advectively, then diffusively, as discussed in section 2.3.1.

The dimensional characteristic length scales of the flow structures are summarized in table 2.2. The early-time fingering dynamics are set by a local balance of advection and diffusion at the finger scale and hence are independent of the width of the porous medium a . The flow is more unstable - that is, the flow has finer structures and faster growth rates - when the viscosity contrast and velocity are large, or the diffusivity is small. The fingers then spread longitudinally while coarsening, also independent of the width of the porous medium. Finally, once the instability has had enough time to diffuse transversely across the entire width of the porous medium, which occurs at a time scale $T \sim a^2/D$, the flow enters the late-time regime. In this case, a single pair of counter-propagating fingers remain, which occupy half of the width of the domain respectively.

In section 2.4.1, it was shown that for sufficiently small Peclet numbers, the flow can skip the intermediate regime, and for even smaller Peclet numbers, the instability can be suppressed altogether. Linear stability analysis was used to identify this cut-off for the instability and compared to numerical experiments.

In section 2.4.2 an improvement on current models for the transversely averaged concentration in the non-linear regime was derived. First the simple Koval model was derived, disagreements with the numerical simulations were identified, and an improvement on one of its shortcomings was made by including a simple model of the nearly parabolic concentration profile across propagating fingers. This ansatz was used to derive the effective viscosity of the fingered region (2.39), in good agreement with both the numerical simulations and the empirical fit to the Koval model.

Finally, in section 2.5 a new single-finger exchange-flow regime in which the flow consists of a linear background gradient and counter-propagating fingers was identified. These fingers exponentially decay and convection stops leaving a linear background gradient. A model for the asymptotic behaviour was derived, which agreed with the

numerical simulations. One important consequence of this eventual shutdown is that there is a maximum amount of convective mixing that the instability can generate. Since diffusion coefficients for typical pairs of fluids tend to be very small, this shutdown is most relevant when the displacement process occurs at very small scales (small a) or very long times.

2.6.2 Implications for carbon sequestration

To illustrate the relevant length and time scales in the late-time regime, we use parameter values from the CO₂ sequestration project at Sleipner to estimate the ‘shutdown time’, T_{sd} , taken to reach the late-time regime and the ‘final’ mixing zone width H . For simplicity, we assume the two fluids are fully miscible, even though CO₂ and brine are only partially miscible, and take the parameter values of the carbon-dioxide/brine system to be as follows (Boait et al., 2012; Neufeld et al., 2010): background velocity, which is the buoyancy velocity, $U = 4 \times 10^{-6} \text{ ms}^{-1}$; log-viscosity ratio $R = 2.5$; porosity $\phi = 0.3$; aquifer thickness $a = 10 \text{ m}$; and diffusivity $D = 2 \times 10^{-9} \text{ m}^2\text{s}^{-1}$. In this case, the diffusivity is taken to be the molecular diffusivity of carbon dioxide and brine D_m . Note that this is only valid when the pore-scale Peclet number, defined as Ua_p/D_m (a_p is the size of the pores), is small; otherwise the effective diffusivity is given by an anisotropic velocity-dependent dispersion tensor that could be significantly larger than D_m (Lake, 1989).

Using these parameters, the Peclet number of the flow is $\text{Pe} = 7 \times 10^4$. The time until shutdown can be approximated from the numerical simulations as $T_{sd} \approx 10^{-1}a^2/D$ which gives a shutdown time of approximately 150 years. Furthermore, the mixing zone can be approximated as $H = 10^{-1.5}Ra^2U/\phi D$ which gives a 50 km long mixing zone upon shutdown. In contrast, if the interface were stable and the mixing at the interface only occurred through diffusion, the width of the mixing zone would grow like $\sqrt{4Dt}$, which, after 150 years, would be approximately 5 m.

In a real porous medium, some of the assumptions made during the analysis may no longer hold. In addition to the fluids only being partially miscible, we also neglect velocity-dependent dispersion. When one fluid displaces another in a porous medium, the natural tortuosity of the flow paths tend to aid in their dispersal and mixing. When flow rates are small, this mechanical dispersion is negligible and mixing is dominated by molecular diffusion, which is isotropic and constant (Woods, 2015). When flow rates are large, mixing becomes dominated by mechanical dispersion, which is Fickian and depends on the flow velocity. At early times, we expect this to enhance the diffusion rate, but not to qualitatively impact the dynamics. At intermediate times,

when diffusion is negligible, and the flow is advectively dominated, we expect this to have little quantitative effect on the dynamics. At late times, mechanical dispersion is important and can lead to faster transverse homogenization and earlier shutdown. In the Sleipner example above, the flow rate and pore-size are sufficiently small such that mechanical dispersion is negligible ($Ua_p/D_m \sim 10^{-2}$). In this chapter, we have also neglected any spatial variations in the permeability field and the fact that the fluids can have different densities. In the following chapters, the effect of these different factors on the evolution of the displacement front, from onset to shutdown, will be examined.

Chapter 3

Stable displacements in layered porous media

The material in this and the following chapter form the basis of the publication (Nijjer et al., 2019): Nijjer, J. S. & Hewitt, D. R. & Neufeld, J. A. (2019). Stable and unstable miscible displacements in layered porous media. *Journal of Fluid Mechanics* **869**. 468-499.

3.1 Introduction

Many physically relevant porous media are not homogeneous but vary on a wide range of length scales from the pore-scale to the reservoir-scale in both an ordered and disordered manner (Weber, 1986). In chapters 3 and 4, a similar approach as chapter 2 is taken to look at the role of permeability heterogeneities on the temporal evolution of the displacement front in the case of stable (chapter 3) and unstable (chapter 4) displacements.

Here, large-scale permeability variations that are perpendicular to the flow direction are specifically focused on. This structure is widespread in nature, being characteristic of geological formations consisting of different sedimentary sequences. When the injected and ambient fluids have the same viscosity, the presence of permeability heterogeneities tends to focus the flow through high-permeability regions leading to spreading and mixing of the two fluids. Previous work has found that in general three different flow regimes are found: an early-time diffusive regime, an intermediate-time advective (ballistic) regime, and a late-time shear enhanced dispersion regime (Camacho, 1993; Dentz and Carrera, 2007). The focus in this chapter and the next is

to consider the effect of viscosity differences between the injected and ambient fluids on the evolution of the displacement front in a layered porous medium.

A number of studies have considered the combined effects of *randomly varying* permeability fields and viscosity variations on miscible displacements using theoretical (Welty and Gelhar, 1991), numerical (Camhi et al., 2000; Chen and Meiburg, 1998c; Nicolaidis et al., 2015; Talon et al., 2004; Tan and Homsy, 1992; Tchelepi et al., 2004; Waggoner et al., 1992) and experimental (Jiao and Hotzl, 2004; Tchelepi et al., 2004) approaches. These studies have demonstrated that the flow can exhibit a range of dynamical behaviour, including dispersing, channelling and fingering and highlight the complexity of the flow patterns that arise. While these studies highlight some of the interesting qualitative behaviour that can be observed in miscible displacement flows when heterogeneity and viscosity variations interact, they do not provide a full overview of the different dynamical regimes that occur and the temporal evolution of the flow between them.

In contrast to randomly heterogeneous porous media, stable miscible displacements in layered porous media with viscosity variations have received less attention. Two notable exceptions are the works of Loggia et al. (1996) and Woods and Mingotti (2016). Loggia et al. (1996) found in experiments in layered bead packs that when the injected fluid is more viscous than the ambient, channelling is observed when the viscosity ratio is smaller than the ratio of permeabilities, and a shock-front is attained when the viscosity ratio is larger than the ratio of permeabilities. Similarly, Woods and Mingotti (2016) found in experiments in a Hele-Shaw cell, that injecting a more-viscous fluid reduced the focusing effect due to the permeability variations and also found that injecting a less-viscous fluid intensified the focusing effect. However, in both of these works a sharp-interface between the fluids was assumed and mixing was neglected.

The aim of this chapter is to identify the full life-cycle and evolution of stable miscible displacements in layered porous media. Having achieved this, reduced-order models for the spreading and dispersion of the fluids will be developed, which can be used to quantitatively predict and up-scale flow in heterogeneous porous media.

This chapter is laid out as follows. In §3.2, the problem setup is briefly outlined. In §3.3, uniform viscosity displacements where the two fluids have the same viscosity are considered. In §3.4 the effect of small viscosity variations, both stabilizing and destabilizing are examined and in §3.5 large stabilizing viscosity variations are considered. In each of §3.3-3.5 the time-evolution of the concentration field and the different regimes through which the flow evolves are discussed, and reduced-order models for the evolution of the concentration field are derived and compared to the direct numerical

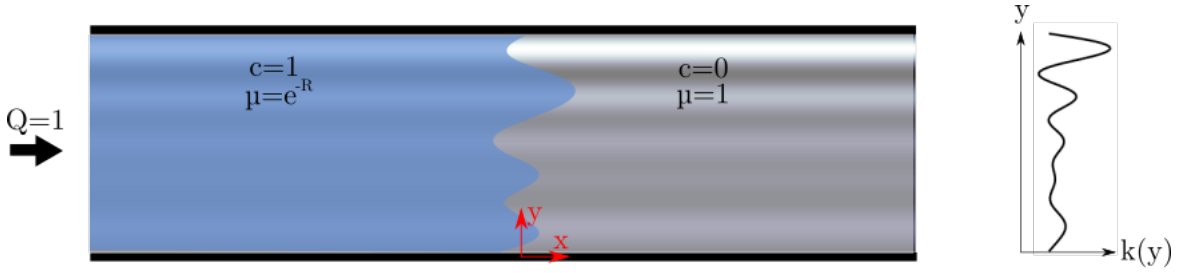


Fig. 3.1 A schematic of the model geometry. The porous medium is semi-infinite and has a permeability structure that is only a function of the transverse coordinate, y . The porous medium is initially saturated with a fluid of viscosity $\mu = 1$. Another fluid, with viscosity $\mu = e^{-R}$, which is fully miscible with the first, is injected at a constant unit flow rate.

simulations. In §3.6 stable displacements in geological contexts with a more realistic and complex permeability structure are considered.

3.2 Problem Formulation

A schematic of the problem geometry is shown in figure 3.1. As described in detail in chapter 2 for a homogeneous reservoir, we consider a semi-infinite, two-dimensional porous strip of finite width. We assume the fluid flow obeys Darcy's law and is incompressible. We also assume that the viscosity depends on the concentration of the injected fluid, which evolves through advection and diffusion. These equations are given in dimensionless form as

$$-(u+1)\mu = k \frac{\partial p}{\partial x}, \quad -v\mu = k \frac{\partial p}{\partial y}, \quad (3.1)$$

$$\frac{\partial u}{\partial x} + \frac{\partial v}{\partial y} = 0, \quad (3.2)$$

$$\mu(c) = e^{-Rc}, \quad (3.3)$$

$$\frac{\partial c}{\partial t} + u \frac{\partial c}{\partial x} + v \frac{\partial c}{\partial y} = \frac{1}{\text{Pe}} \left(\frac{\partial^2 c}{\partial x^2} + \frac{\partial^2 c}{\partial y^2} \right). \quad (3.4)$$

Note that as before, the velocity (u, v) is given relative to a moving frame that is travelling with the average speed of the injected fluid. Whereas in chapter 2 a constant permeability was assumed, here we consider a spatially varying permeability field.

We consider flows that are periodic in the transverse (\hat{y}) direction,

$$c(x, 0, t) = c(x, 1, t), \quad u(x, 0, t) = u(x, 1, t), \quad v(x, 0, t) = v(x, 1, t). \quad (3.5)$$

The upstream and downstream flux is zero (in the moving frame) and the transverse velocity vanishes in the far-field so that,

$$\int_0^1 u \, dy \rightarrow 0 \quad \text{for } x \rightarrow \pm\infty, \quad (3.6)$$

$$\frac{\partial c}{\partial x} \rightarrow 0 \quad \text{as } x \rightarrow \pm\infty, \quad (3.7)$$

$$v \rightarrow 0 \quad \text{for } x \rightarrow \pm\infty. \quad (3.8)$$

We initialize the concentration field to have a step jump,

$$c(x, t = 0) = c_0(x) = H(-x), \quad (3.9)$$

where $H(x)$ is the Heaviside function.

The system is described by two non-dimensional parameters, the Peclet number $Pe = Q/D$, and the log-viscosity ratio R , as well as the non-dimensional permeability. As before, we focus on the limit of large but finite Peclet number, which is typical in most geologic scenarios. In this chapter we also consider three different cases for the log-viscosity ratio: the uniform viscosity case $R = 0$, where the injected and ambient fluids have the same viscosity; the small viscosity limit, where the viscosity ratio between the injected and ambient fluids is small compared to the permeability variations; and the stable limit, where the injected fluid is more viscous than the ambient fluid and the viscosity ratio is large compared to the permeability variations. In chapter 4 we consider the unstable limit, where the injected fluid is less viscous than the ambient fluid and the viscosity ratio is large compared to the permeability variations.

In chapters 3 and 4, we consider only layered heterogeneous media for which $k = k(y)$. In fact, for most of the numerical results presented here, we further restrict our attention to log-permeabilities which vary sinusoidally (De Wit and Homay, 1997a,b; Sajjadi and Azaiez, 2013):

$$\ln(k) = -\sigma \cos(2\pi ny) - \ln(I_0(\sigma)), \quad (3.10)$$

where I_0 is the modified Bessel function of the first kind, which ensures a unit average dimensionless permeability. This simplification retains the dominant physics of permeability heterogeneities in the form of layering, and can be described by two parameters instead of the infinite space of possible permeability functions. These two parameters are the log-permeability variance σ and wavenumber n , which measure the strength and inverse of the length scale of the permeability variations, respectively. We solve (3.1)-(3.4) along with the form of the permeability, (3.10), numerically (for more details see appendix A). While some of our results are presented for general $k(y)$, most the numerical simulations use (3.10) as the form for the permeability structure. In §3.6 and §4.7 we briefly consider the dynamics in more complex permeability structures.

In the absence of hydrodynamic instabilities, as is the case in this chapter, there is no mechanism for dynamic interactions between layers, and so n can be scaled out of the system. This is done by introducing rescaled variables $\hat{y} = ny$, $\hat{x} = nx$, $\hat{t} = n^2t$, in which case the flow evolves exactly as it would with $n = 1$, but with an effective Peclet number $\hat{\text{Pe}} = \text{Pe}/n^2$. For clarity, we therefore limit our analysis in this chapter to the case where $n = 1$.

In order to investigate how the macroscopic features of the flow evolve, we again focus on the evolution of the transversely averaged concentration $\bar{c}(x, t) = \int_0^1 c dy$ and the mixing length $h(t)$. In chapters 3-5 we define the mixing length to be the variance in concentration about the initial condition $c_0(x)$ (3.9),

$$h(t) = \sqrt{\frac{\int_{-\infty}^{\infty} x^2 (\bar{c} - c_0)^2 dx}{\int_{-\infty}^{\infty} (\bar{c} - c_0)^2 dx}}. \quad (3.11)$$

Note that we use this measure instead of the more common definition, $h^* = x|_{\bar{c}=0.01} - x|_{0.99}$, which was used in the previous chapter, because it more accurately captures the spreading behaviour when the concentration field has long-tails (see appendix 3.A).

3.3 Uniform viscosity displacements $R = 0$

We first consider the case where the injected and ambient fluids have the same viscosity. While this case has been explored by a number of authors (e.g. Berentsen et al., 2005; Camacho, 1993; Dentz and Carrera, 2007), we outline it here both for completeness and to set the stage for the analysis in chapters 3 and 4. Results from a representative simulation are given in figure 3.2. As was noted earlier, if the flow is hydrodynamically stable, n can be scaled out of the problem and so we only consider the case where $n = 1$. In this case, the permeability is highest in the centre of the channel and lowest

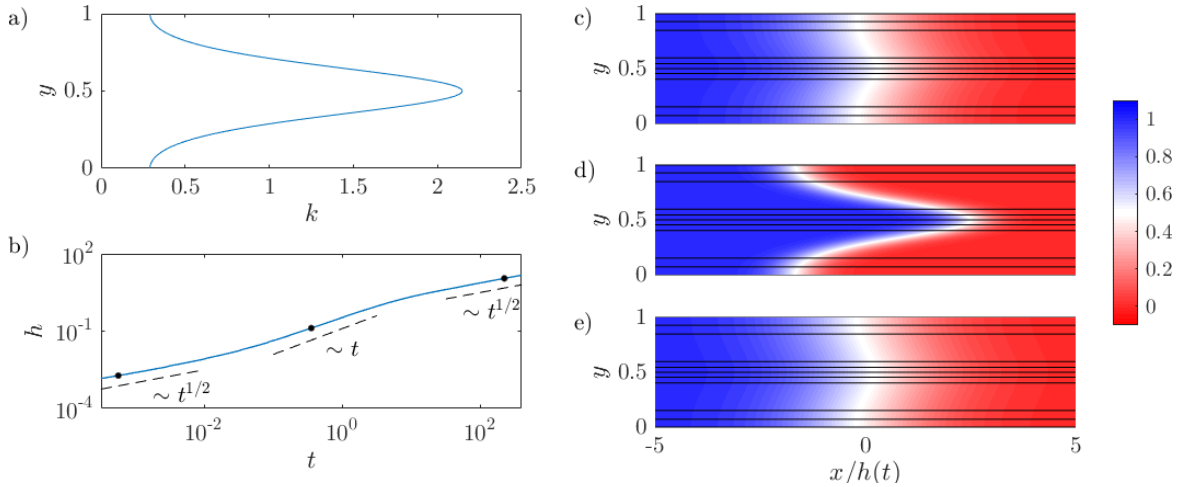


Fig. 3.2 Evolution of the concentration field for $R = 0$ and $(\sigma, \text{Pe}) = (1, 100)$. (a) The imposed permeability $k(y) = e^{-\cos(2\pi y)}/I_0(1)$. (b) Evolution of the mixing length, h , as a function of time, t . The dots correspond to the snapshots (c-e). (c-e) Plots of the concentration field with overlain streamlines vs. x/h and y at (c) $t = 5 \times 10^{-4}$, (d) $t = 0.32$ and (e) $t = 200$.

at the top and bottom boundaries (figure 3.2(a)) resulting in faster flow in the middle compared to the top and bottom boundaries. In the moving frame, this causes the fluid in the middle of the channel to move to the right and the fluid near the top and bottom boundaries to move to the left. This shear spreads and mixes the fluids. To quantify this spreading, we plot the evolution of the mixing length, $h(t)$, in figure 3.2(b). We find that the mixing evolves through three distinct regimes each with a different scaling behaviour. The concentration fields corresponding to each of these regimes are plotted in figures 3.2(c-e). In the first and third regimes, the concentration fields look nearly indistinguishable: the concentration is nearly transversely uniform and relatively diffuse in the streamwise direction. In the second regime, there is a relatively sharp interface aligned with the permeability variations. Based on these observations, we expect that in the first (early-time) and third (late-time) regimes, the streamwise transport is diffusively dominated, whereas in the second (intermediate-time) regime, the streamwise transport is advectively dominated.

Since $R = 0$, the concentration acts as a passive tracer. This means that the velocity is decoupled from the concentration field, and is given from (3.1) by

$$u(y) = k(y) - 1, \quad v = 0. \quad (3.12)$$

In the case of sinusoidally varying log-permeability (3.10), the velocity is,

$$u = \frac{e^{-\sigma \cos(2\pi y)}}{I_0(\sigma)} - 1, \quad v = 0. \quad (3.13)$$

Given this fixed, known velocity the concentration simply evolves via the advection-diffusion equation (3.4). In the following sections, we consider the dominant balances in (3.4) to determine how the concentration field evolves in time.

3.3.1 Early-time behaviour: initial diffusion

At early times, the streamwise concentration gradient between the fluids is large and the concentration is transversely homogeneous. In this case, diffusion across the interface dominates and the primary balance in the advection-diffusion equation is

$$\frac{\partial c}{\partial t} = \frac{\partial \bar{c}}{\partial t} = \frac{1}{Pe} \frac{\partial^2 c}{\partial x^2}. \quad (3.14)$$

Using the initial and boundary conditions (3.9) and (3.7) the concentration evolves self-similarly as

$$c = \bar{c} = \frac{1}{2} + \frac{1}{2} \operatorname{erf} \left(-\frac{x}{\sqrt{4t/Pe}} \right), \quad (3.15)$$

which holds at all times when the permeability is homogeneous ($k = 1$). The mixing length grows like $h \sim t^{1/2}$ and can be calculated explicitly by substituting (3.15) into (3.11) (figure 3.3(a)).

This behaviour always holds initially, irrespective of the parameter choices, since diffusive growth of the interface $O(t^{1/2}/Pe^{1/2})$ always outpaces advective spreading $O(\Delta u t)$ (where Δu is a characteristic spreading velocity, related to the permeability field through (3.12)). In fact, the transition to the intermediate regime occurs precisely when the growth rates become equal, giving a transition time $t = O(1/Pe\Delta u^2)$.

3.3.2 Intermediate-time behaviour: advection

After a time $O(1/Pe\Delta u^2)$, spreading induced by the difference in permeability overtakes longitudinal diffusion. The leading-order balance in (3.4) becomes

$$\frac{\partial c}{\partial t} + u \frac{\partial c}{\partial x} = 0, \quad (3.16)$$

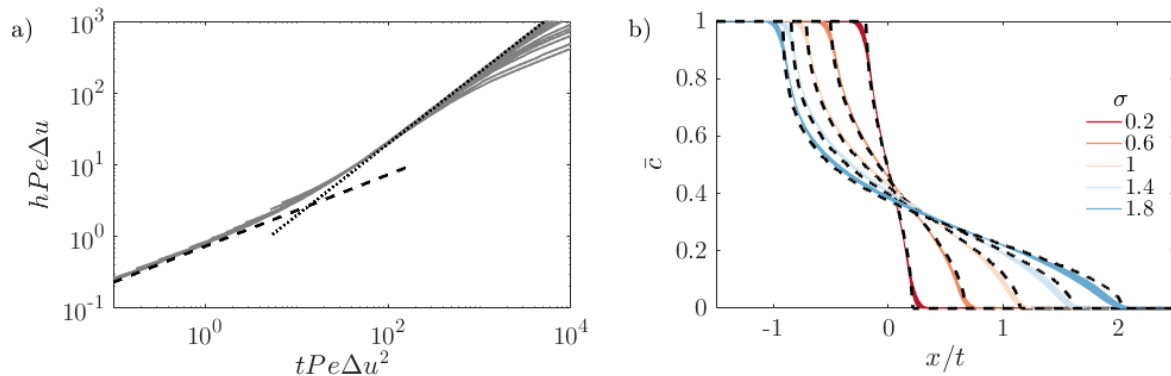


Fig. 3.3 Evolution of the mixing length and transversely averaged concentration for $R = 0$ in the intermediate-time regime. (a) Scaled plot of the mixing length $h(t)$ for Pe ranging from 100 to 2000 and σ ranging from 0.1 to 2. The black lines correspond to the predictions for the mixing length calculated from the analytical solutions (3.15) (dashed) and (3.18) (dotted). (b) Plot of the transversely averaged concentration, $\bar{c}(x, t)$ vs. x/t for $(R, Pe) = (0, 500)$, σ ranging from 0.2 to 1.8 and ten logarithmically spaced times between 1 and 3. The characteristic spreading velocity is taken to be the maximum velocity difference between the layers, $\Delta u \sim \sinh(\sigma)/I_0(\sigma)$.

and the flow simply stretches the diffused solution that arises from the early-time regime. In fact, since the rate of advective stretching is much faster than diffusion to good approximation, we can ignore the effects of the early-time regime completely and the solution to (3.16) is simply the travelling wave

$$c = c_0 [x - u(y)t] = H [u(y) - x/t], \quad (3.17)$$

given the initial condition, (3.9). The transversely averaged concentration, $\bar{c}(x, t)$ can be calculated by averaging (3.17),

$$\bar{c}(x, t) = \int_0^1 H [u(y) - x/t] dy. \quad (3.18)$$

The model gives good agreement with the numerical simulations (figure 3.3(b)) and is able to reproduce the asymmetric profiles, which arise due to the fact that the permeability is not symmetric about $k = 1$. Since the interface is stretched at a constant rate, the mixing length grows like $h \sim \Delta ut$ (figures 3.3(a), 3.4(b)).

3.3.3 Late-time behaviour: shear-enhanced dispersion

The transition to the late-time regime occurs once the concentration has diffused across the entire channel, homogenizing the concentration in the transverse direction; this

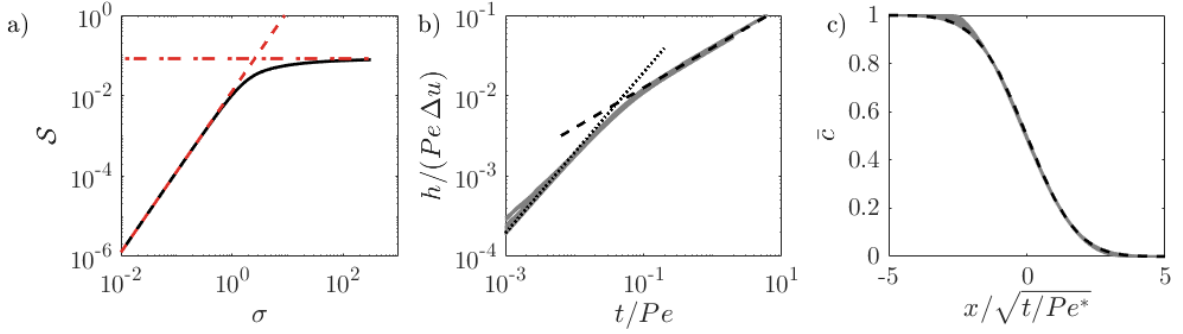


Fig. 3.4 Evolution of the mixing length and transversely averaged concentration for $R = 0$ in the late-time regime. (a) Shear enhanced dispersivity \mathcal{S} versus σ with asymptotic limits (3.46) (dashed) and (3.49) (dot-dashed). (b) Scaled plot of h vs. t for Pe ranging from 100 to 2000 and σ ranging from 0.1 to 2. The black lines correspond to the predictions for the mixing length calculated from the analytical solutions (3.18) (dotted) and (3.15) with (3.22) (dashed). (c) Plot of the transversely averaged concentration, $\bar{c}(x, t)$ vs. the late-time similarity variable $x/\sqrt{t/Pe^*}$ for the same parameters as (b) at $t = 200$. The theoretical solution (3.15) with (3.22) is given by the dashed line.

occurs at a time $O(Pe)$. In this case, the mixing zone is long and thin and transverse diffusion balances longitudinal advection (cf. Taylor dispersion e.g. Aris, 1956; Taylor, 1953). This is in contrast to the previous regime, when the flow evolved purely by longitudinal advection. In the limit of small deviations from the mean ($c' \ll \bar{c}$) and a long, thin mixing zone, the evolution equation for the concentration deviations (2.19) reduces to

$$(k - 1) \frac{\partial \bar{c}}{\partial x} = \frac{1}{Pe} \frac{\partial^2 c'}{\partial y^2}, \quad (3.19)$$

while the transversely averaged concentration still evolves according to (2.18). Given that \bar{c} is independent of y , we integrate this equation twice and impose periodicity and zero-mean deviations ($\int_0^1 c' = 0$), to give

$$c' = Pe \frac{\partial \bar{c}}{\partial x} \left[\int_0^y \int_0^\zeta (k(\eta) - 1) d\eta d\zeta - \int_0^1 \int_0^s \int_0^\zeta (k(\eta) - 1) d\eta d\zeta ds \right]. \quad (3.20)$$

Substituting and solving for the convective flux in (2.18), using the expression for the velocity (3.12), leads to

$$\frac{\partial \overline{uc'}}{\partial x} = -Pe \frac{\partial^2 \bar{c}}{\partial x^2} \left[\int_0^1 \left(\int_0^y (k(\eta) - 1) d\eta \right)^2 dy \right]. \quad (3.21)$$

This convective flux can be written in the form of an effective diffusivity such that (2.18) reduces to

$$\frac{\partial \bar{c}}{\partial t} = \frac{\partial}{\partial x} \left[\frac{1}{\text{Pe}^*} \frac{\partial \bar{c}}{\partial x} \right], \quad \frac{1}{\text{Pe}^*} = \frac{1}{\text{Pe}} (1 + \text{Pe}^2 \mathcal{S}) \quad (3.22)$$

where

$$\mathcal{S} = -\frac{1}{\text{Pe} \partial \bar{c} / \partial x} \int_0^1 u c' dy = \int_0^1 \left(\int_0^y (k(\eta) - 1) d\eta \right)^2 dy \quad (3.23)$$

is the shear-enhanced dispersivity, which only depends on the permeability structure (cf. Van den Broeck and Mazo, 1983).

For our choice of sinusoidally varying log-permeability, this integral cannot be solved analytically, but is instead integrated numerically for varying σ and plotted in figure 3.4(a). In appendix 3.B, we derive the asymptotic limits of the shear-enhanced dispersivity for large and small σ (given as dashed and dot-dashed lines respectively in figure 3.4(a)).

The solution to equation (3.22) is again the similarity solution (3.15), but now with a modified Peclet number Pe^* (figure 3.4(c)). When the total dispersivity is dominated by the shear-enhanced dispersivity, $\text{Pe}^2 \mathcal{S} \gg 1$, the effective dispersion scales like $\text{Pe}^* \sim 1/(\text{Pe} \Delta u^2)$. In figure 3.4(b) we use this scaling to collapse the mixing length as a function of time over a range of parameters.

In summary, in the presence of permeability layering but in the absence of viscosity variations, the flow evolves through three regimes: early-time diffusion, intermediate-time advection and late-time shear-enhanced dispersion.

3.4 Small viscosity variations $|R| < \sigma$

Next we consider the effect of viscosity variations that are weak compared to the permeability; that is, the log-viscosity ratio is smaller than the log-permeability variance, $|R| < \sigma$.

Recall as in chapter 2, in the absence of permeability variations and when $R < 0$, the flow is hydrodynamically stable and evolves as a simple diffusing front. When $R > 0$ and the Peclet number is sufficiently large, the flow is unstable and a set of complex nonlinearly evolving fingers develop. However, if permeability layering is introduced, the flow tends to be forced along the permeability pathways (De Wit and Homsy, 1997b; Shahnazari et al., 2018) and as the permeability variance is increased, the flow becomes more and more channelized. In this case flows that would otherwise

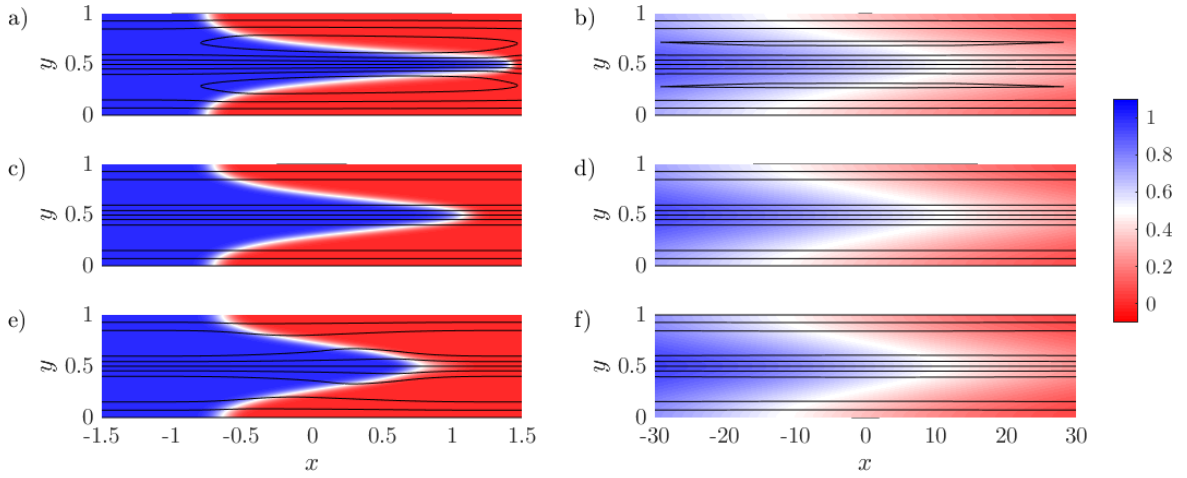


Fig. 3.5 Colourmaps of the concentration field with overlain streamlines for $|R| < \sigma$. (a,b) $R = 0.4$, (c,d) $R = 0$ and (e,f) $R = -0.4$ and $(\sigma, Pe, n) = (1, 500, 1)$. The snapshots are taken at (a,c,e) intermediate times ($t = 1$) and (b,d,f) late times ($t = 31$). Note that the aspect ratios of the late-time figures are distorted.

be fingering become stabilized. This is especially true when the permeability variability dominates over viscous variability, $\sigma > |R|$. Although instabilities are still possible (and are further discussed in chapter 4), in this section we focus on flows that remain hydrodynamically stable and follow the permeability pathways imposed.

Figure 3.5 shows the concentration field overlain with streamlines for $\sigma = 1$ and $R = 0.4, 0$ and -0.4 at intermediate times (left) and late times (right). For all three values of R , we find that the concentration field evolves in qualitatively the same manner: after an early-time diffusive regime, as in §3.3.1, at intermediate times the flow is dominated by advective stretching (figure 3.5(a,c,e)); and at late times the flow is dominated by shear enhanced dispersion (figure 3.5(b,d,f)). The main difference between flows where $R \neq 0$ and $R = 0$ is that at intermediate-times the interface is either stretched ($R > 0$) or compressed ($R < 0$) relative to the uniform viscosity case owing to the viscosity-enhanced or viscosity-tempered streamwise velocity. At late-times, the viscosity contrast seems to have little effect and the concentration field and streamlines look nearly indistinguishable. In the following subsections we examine the effects of small viscosity variations on the evolution of the three regimes identified in §3.3. We begin in §3.4.1 with a consideration of how viscosity contrasts affect the fluid velocity.

3.4.1 Vertical flow equilibrium

Unlike when the viscosities are equal, $R = 0$, we cannot simply integrate (3.1) to give a fixed expression for the velocity. Near the interface, when the injected fluid is more viscous than the ambient, $R < 0$, the streamwise velocity is reduced, whereas when the injected fluid is less viscous than the ambient, $R > 0$, the streamwise velocity is increased. Under the assumption that the flow is long and thin, the pressure is only a function of the longitudinal coordinate and is constant along any transverse slice. This limit, often referred to as ‘vertical flow equilibrium’ (Yortsos, 1995), implies that

$$\frac{\mu(u+1)}{k} = -\frac{dp}{dx}. \quad (3.24)$$

Combining (3.24) with the fact that the flux vanishes in any transverse slice in the moving frame, the velocity can be written as

$$u(x, y, t) = \frac{k(y)}{\mu(x, y, t)} \left[\int_0^1 \frac{k(s)}{\mu(x, s, t)} ds \right]^{-1} - 1. \quad (3.25)$$

If the viscosity is uniform, then the permeability sets the velocity, $u = k - 1$, as in (3.12). If, instead, the permeability is uniform, then the viscosity sets the velocity, $u(y) = \mu^{-1} / \int_0^1 \mu^{-1} dy - 1$ (this leads to the fast low-viscosity fingers and slow high-viscosity fingers characteristic of the viscous-fingering instability as described in §2.4.2). When both the permeability and viscosity vary, depending on the sign of R and c' , the permeability and viscosity can interact either constructively or destructively. The effect of varying viscosity is only important at the interface; far upstream and downstream, where the viscosity is uniform, the velocity variations are simply imposed by the structure of the permeability field.

Decomposing the concentration into the transverse average and deviations $c = \bar{c}(x) + c'(x, y)$, (3.25) becomes independent of the average concentration and only depends on the transverse variations,

$$u(x, y, t) = \frac{k(y)}{e^{-Rc'(x, y, t)}} \left[\int_0^1 \frac{k(s)}{e^{-Rc'(x, s, t)}} ds \right]^{-1} - 1. \quad (3.26)$$

In the case of sinusoidal log-permeability variations, (3.26) may be expressed as

$$u(x, y, t) = \frac{e^{-\sigma \cos(2\pi y) + Rc'(x, y, t)}}{\int_0^1 e^{-\sigma \cos(2\pi s) + Rc'(x, s, t)} ds} - 1. \quad (3.27)$$

3.4.2 Intermediate-time behaviour: viscously coupled advection

After the early-time diffusion regime the flow transitions to the intermediate-time regime dominated by advective spreading. The effect of a non-zero viscosity ratio on the evolution of the mixing length is shown in figure 3.6(a). Similar to the case when $R = 0$, the mixing zone grows linearly in time. However as R is increased, the growth rate of the mixing zone, $\dot{h} = dh/dt$, increases. The nearly uniform spacing between the curves suggests that the growth rate varies linearly in R . The transversely averaged concentration is again asymmetric and evolves self-similarly (figure 3.6(b)), although it differs appreciably from the uniform viscosity case at the downstream tips (cf. snapshots in figure 3.5(a,c,e)).

We first note that diffusion is negligible in this regime. This results in concentration deviations that are almost exactly either $c' = -\bar{c}$ or $c' = 1 - \bar{c}$ (figure 3.6(c)). To estimate the overall effect of the deviations on the velocity, we average the deviations across the length of the fingered region, which leads to a roughly sinusoidal variation across the domain aligned with the permeability structure and with magnitude $\simeq 1/2$ (dashed black line in figure 3.6(c)). Substituting these average deviations into (3.27), the mean streamwise velocity reduces to

$$u = \frac{e^{-(\sigma+R/2)\cos(2\pi y)}}{\int_0^1 e^{-(\sigma+R/2)\cos(2\pi s)} ds} - 1. \quad (3.28)$$

This approximate model results in intermediate-time dynamics that are equivalent to the uniform viscosity case, but with an effective log-permeability ratio $\sigma_{\text{eff}} = \sigma + R/2$. Given (3.28), we can calculate h as in §3.3.2, and extract \dot{h} by fitting a linear profile $h = \dot{h}t$. Modelling the effective permeability in this way gives reasonably good agreement with the numerical simulations (figure 3.6(d)), although it underestimates the spreading rate for large $|R|$. This is because, at the boundary of the forward and backward propagating tips, the velocity is faster, $u = e^{\sigma+R}/I_0(\sigma)$, and slower, $u = e^{-(\sigma+R)}/I_0(\sigma)$, respectively, than this model predicts.

3.4.3 Late-time behaviour: viscosity-dependent shear-enhanced dispersion

At late times, after advectively spreading, the concentration evolves diffusively again. This evolution is analogous to the late-time behaviour of the uniform viscosity case but the addition of viscosity variations modifies the effective diffusivity.

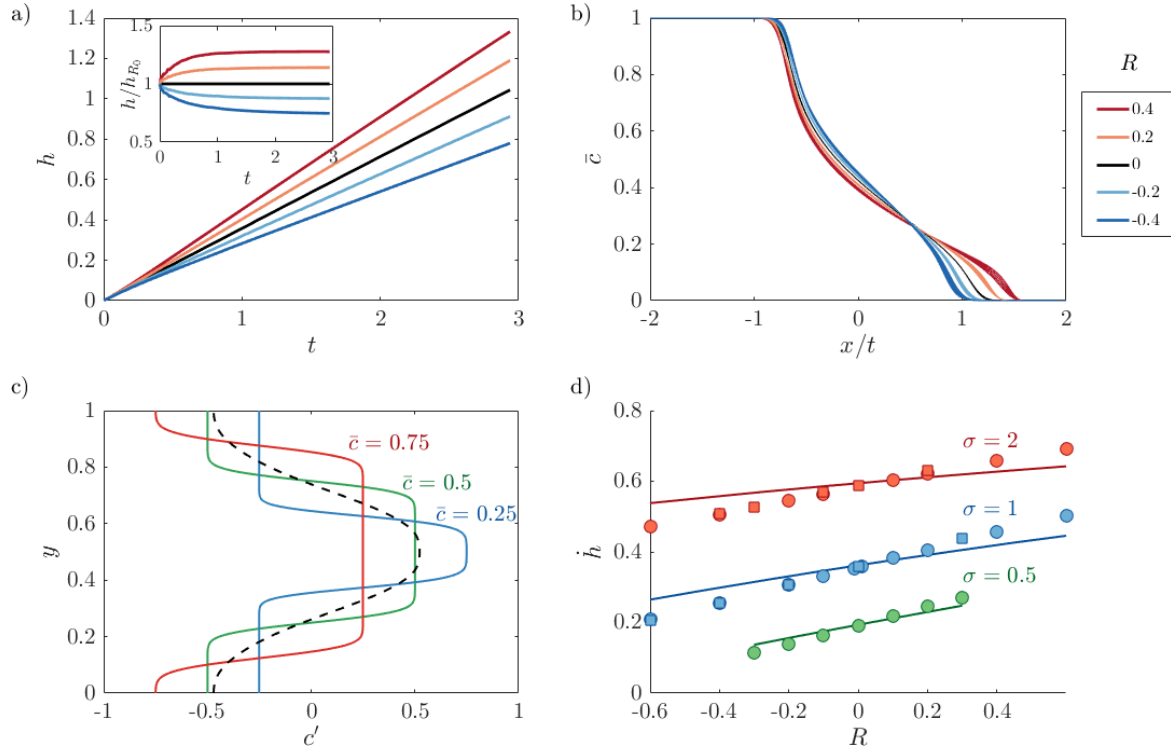


Fig. 3.6 Evolution of the mixing length and transversely averaged concentration for $|R| < \sigma$ in the intermediate-time regime. (a) Evolution of the mixing length for $(\sigma, Pe) = (1, 2000)$ and R ranging from -0.4 to 0.4 ; the inset shows the same data normalized by the uniform viscosity displacement mixing length. (b) Plot of \bar{c} vs. x/t for the same parameters as (a) for 10 logarithmically spaced times in the range $1 \leq t \leq 3$. (c) Plot of the concentration deviations c' as a function of y at three different points in x corresponding to $\bar{c} = 0.75$ (red), $\bar{c} = 0.5$ (green) and $\bar{c} = 0.25$ (blue) for $(R, \sigma, Pe) = (-0.4, 1, 2000)$. The longitudinally averaged concentration deviations (averaged over the mixing zone), $\int_h c' dx/h$, is given by the dashed black line. (d) Plot of the spreading rate \dot{h} calculated by least-squares fitting a function of the form $h = h_0 + \dot{h}t$ to the numerical results for t in the range $1 \leq t \leq 3$, for $Pe = 2000$ (circles) and $Pe = 4000$ (squares). The theoretical predictions for \dot{h} , calculated using (3.28) and (3.18), are given by the solid lines.

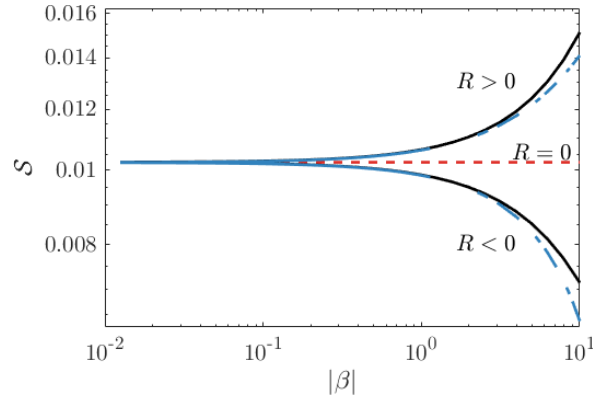


Fig. 3.7 Plot of \mathcal{S} vs. $|\beta|$ for $R < 0$ and $R > 0$. The solid black lines correspond to \mathcal{S} , (3.31), calculated by numerically integrating (3.30). The leading order small- $|\beta|$ asymptotic behaviour, which is equal to when $R = 0$, is given by the dashed red line and the next order corrections in β are given by the dot-dashed blue lines, (3.35).

As in §3.3.3, we assume that the flow is long and thin, transverse velocities are negligible so the fluid flow is predominantly in the streamwise direction and the concentration deviations are small and evolve on a much faster time-scale than their transverse average. Equation (2.18) remains unchanged, but (3.19) becomes

$$\left(\frac{ke^{Rc'(x,y,t)}}{\int_0^1 ke^{Rc'(x,s,t)} ds} - 1 \right) \frac{\partial \bar{c}}{\partial x} \text{Pe} = \frac{\partial^2 c'}{\partial y^2}(x, y, t) \quad (3.29)$$

because of the dependence of the velocity on the concentration through (3.26). Again we impose periodic boundary conditions and zero-mean deviations.

Before solving, we first rescale the deviations, $\tilde{c} = Rc'$, such that (3.29) becomes

$$\left(\frac{ke^{\tilde{c}}}{\int_0^1 ke^{\tilde{c}} ds} - 1 \right) \beta = \frac{\partial^2 \tilde{c}}{\partial y^2}, \quad (3.30)$$

where $\beta = R \text{Pe} \partial \bar{c} / \partial x = \text{Pe} \partial \ln \mu(\bar{c}) / \partial x$, incorporates all of the parameters in the problem, and can be thought of as a rescaled bulk concentration or viscosity gradient. Since β is independent of y , we can solve for \tilde{c} by integrating (3.30) twice. We perform this integration numerically, although the limits of small β , which is relevant here and is considered in §3.4.3, and large β , which we find to be useful and is considered later in §3.5.1, can be treated analytically. Having solved for \tilde{c} , we then calculate the shear-enhanced dispersivity,

$$\mathcal{S} = -\frac{1}{\beta} \int_0^1 u \tilde{c} dy, \quad (3.31)$$

(cf. 3.23). Solutions of \mathcal{S} for $\sigma = 1$ and $R > 0$ and $R < 0$ are given in figure 3.7. When $R = 0$, (3.30) reduces to (3.19) and \mathcal{S} is exactly as described by (3.23), a permeability-dependent constant. When the viscosity varies, the dispersivity is enhanced when the injected fluid is less viscous ($R > 0$) and diminished when the injected fluid is more viscous ($R < 0$), than the ambient fluid. Since $\beta \propto \partial\bar{c}/\partial x$, and diffusion always causes concentration gradients to diminish in time, β generally decreases over time. When $|\beta|$ is large (i.e. the viscosity gradient is large, as at early times), and $R > 0$, \mathcal{S} diverges, whereas when $R < 0$, \mathcal{S} tends to zero. The former limit is unphysical and corresponds to scenarios where the interface is unstable. The latter case is discussed in more detail in section 3.5, in the context of stable injections. When $|\beta|$ is small (i.e. the viscosity gradient is small, as at late times), \mathcal{S} becomes independent of β and tends to the value for $R = 0$. This suggests that at late enough times, the effective diffusivity will always become independent of the log-viscosity ratio, and the flow will always evolve like the uniform viscosity case.

When $|R| < \sigma$, we need to only consider the small- $|\beta|$ limit because by the time the flow reaches the late-time regime, β is inevitably small. We can justify this claim using a scaling argument: once the flow reaches the late-time regime, which occurs at a time $t = O(\text{Pe})$, the mixing length will have grown to a width $h = O(\text{Pe}\Delta u)$, or equivalently, the concentration gradient is $\partial\bar{c}/\partial x = O(1/\text{Pe}\Delta u)$. This means that when the flow transitions to the late-time regime, $|\beta| = O(R/\Delta u) < O(1)$.

Small viscosity gradient limit: $|\beta| \ll 1$

For $\beta \ll 1$, we start by expanding the concentration deviations as $\tilde{c} = \beta\tilde{c}_1 + \beta^2\tilde{c}_2 + O(\beta^3)$. Substituting into (3.29), expanding, and equating powers of β gives

$$\frac{\partial^2\tilde{c}_1}{\partial y^2} = k - 1, \quad \frac{\partial^2\tilde{c}_2}{\partial y^2} = \left(k\tilde{c}_1 - k\overline{k\tilde{c}_1}\right). \quad (3.32)$$

Given that the concentration deviations must satisfy periodicity and have vanishing mean, we find that

$$\tilde{c}_1 = \mathcal{I}(k - 1) - \overline{\mathcal{I}(k - 1)}, \quad (3.33)$$

$$\tilde{c}_2 = \mathcal{I}\left(k\tilde{c}_1 - \overline{k\tilde{c}_1}\right) - \overline{\mathcal{I}\left(k\tilde{c}_1 - \overline{k\tilde{c}_1}\right)}, \quad (3.34)$$

where $\mathcal{I}(f) = \int_0^y \int_0^\zeta f d\eta d\zeta$ for a given function $f(\eta)$ and, as before, the overbar refers to a transverse average. The shear-enhanced dispersivity, \mathcal{S} , is thus

$$\mathcal{S} = -\frac{1}{\beta} \int_0^1 u\tilde{c} dy = \overline{k\tilde{c}_1} + \beta \left(\overline{k\tilde{c}_1^2} - \overline{k\tilde{c}_1}^2 + \overline{k\tilde{c}_2}\right) + O(\beta^2). \quad (3.35)$$

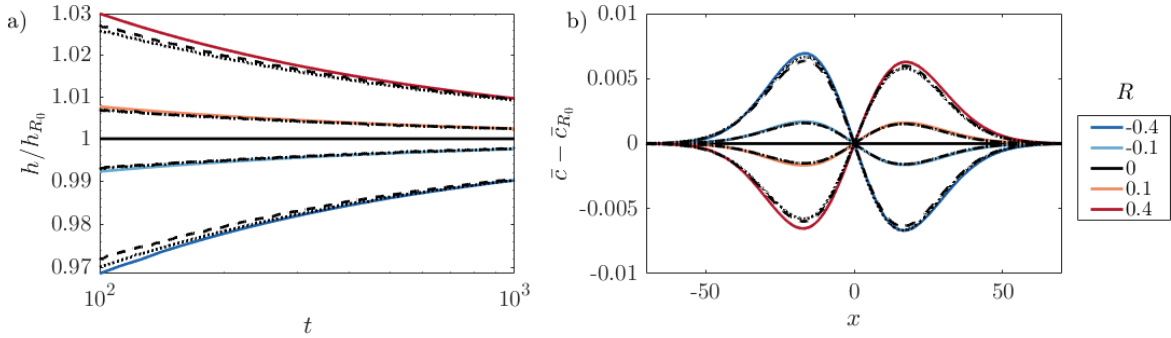


Fig. 3.8 Evolution of the mixing length and transversely averaged concentration for $|R| < \sigma$ in the late-time regime. (a) Evolution of the mixing length h , normalized by the uniform viscosity displacement mixing length $h_{R=0}$ for $(\sigma, \text{Pe}) = (1, 100)$ and R ranging from -0.4 and 0.4 . (b) Plot of the difference between \bar{c} for $R \neq 0$ and $R = 0$. The profiles are measured at $t = 100$ for the same parameters as (a). The theoretical predictions, found by solving (3.36) with either the exact solution of \mathcal{S} (by solving (3.30)), or (3.35), are given by the dashed and dotted black lines respectively.

The leading-order contribution to \mathcal{S} is identical to the $R = 0$ limit in §3.3.3 and is plotted in figure 3.7 as a dashed red line. The first-order corrections are given by dot-dashed blue lines.

Comparison to numerical simulations

We now use the calculated shear-enhanced dispersivity to determine how \bar{c} evolves in time. Allowing \mathcal{S} to vary in space, (2.18) yields a nonlinear diffusion equation for \bar{c} ,

$$\frac{\partial \bar{c}}{\partial t} = \frac{1}{\text{Pe}} \frac{\partial}{\partial x} \left\{ \left[1 + \text{Pe}^2 \mathcal{S}(\beta(x)) \right] \frac{\partial \bar{c}}{\partial x} \right\}, \quad (3.36)$$

where $\beta(x) = R \text{Pe} \partial \bar{c} / \partial x$ depends on the local mean concentration gradient. We solve (3.36) numerically with no flux boundary conditions in the far-field using a Crank-Nicolson predictor-corrector method. We use both the exact form for \mathcal{S} (by solving (3.30) and calculating (3.31)), and the small- $|\beta|$ approximation, (3.35). The model concentration fields are initialized with a diffuse error-function solution although the long-time results are indifferent to the exact initial conditions. The non-uniform dispersion results in profiles that deviate from the classical error-function solution owing to the enhanced or diminished dispersion in regions of large concentration gradients.

Figure 3.8(a) shows the evolution of the normalized mixing length, h/h_{R_0} , where $h_{R_0} = h(t, R = 0)$, for different R , from the full 2D numerical simulations (solid coloured lines) and model results (dashed and dotted black lines). As expected, increasing R

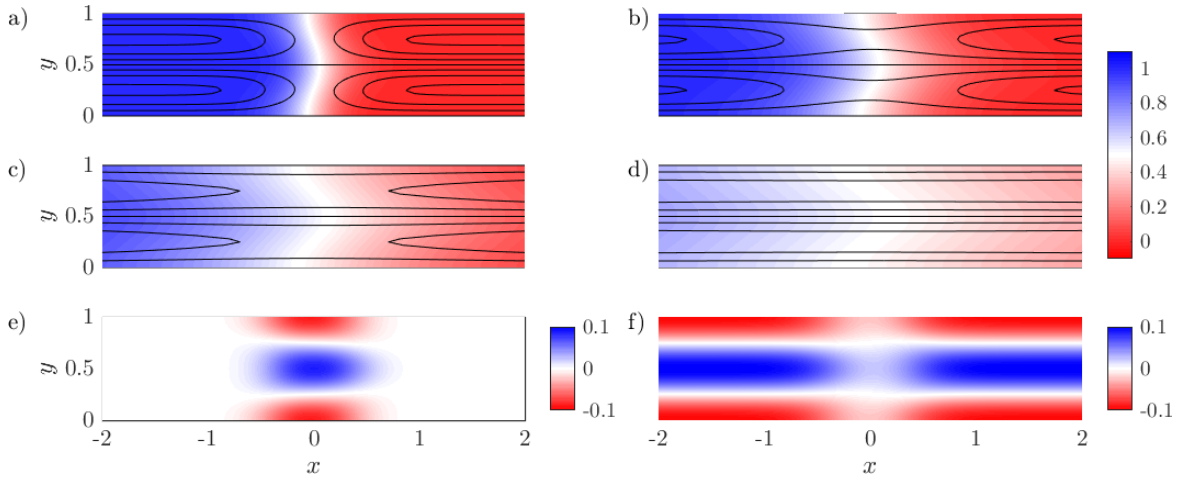


Fig. 3.9 Evolution of the concentration field for stable displacements $|R| > \sigma$, $R < 0$. $(R, \sigma, \text{Pe}) = (-1, 0.1, 100)$. (a-d) Colourmaps of the concentration field with overlain streamlines at (a) $t = 3.6$, (b) $t = 17.8$, (c) $t = 89.1$ and (d) $t = 447$. (e) Colourmap of the concentration deviations $c' = c - \bar{c}$ at $t = 3.6$. (f) Colourmap of the streamwise velocity u at $t = 3.6$.

results in increased spreading, while the effects of variations in the viscosity reduce as t is increased. The reduced-order model not only captures this behaviour but also accurately predicts the manner in which the flow evolves. This can be further seen in figure 3.8(b) which compares the reduced-order model predictions for \bar{c} with the full 2D numerical simulations. The very good agreement between both of the model solutions and the numerical results suggests that the late-time behaviour can be accurately modelled by (3.36) with (3.35).

3.5 Large stabilizing viscosity variations $|R| > \sigma$, $R < 0$

Whereas in the previous section the flow evolves in qualitatively the same manner as the uniform viscosity case ($R = 0$), when the viscosity ratio is larger than the permeability ratio, the concentration evolves in a qualitatively different manner. Here we consider the case where the injected fluid is more viscous than the ambient fluid ($R < 0$) and the magnitude of the log-viscosity ratio is larger than the log-permeability ratio.

Figures 3.9(a-d) show a sequence of snapshots of the concentration field in this limit. The interface is initially not stretched by the permeability variations owing to the large streamwise gradient in viscosity (figure 3.9(a)). This is because, for large

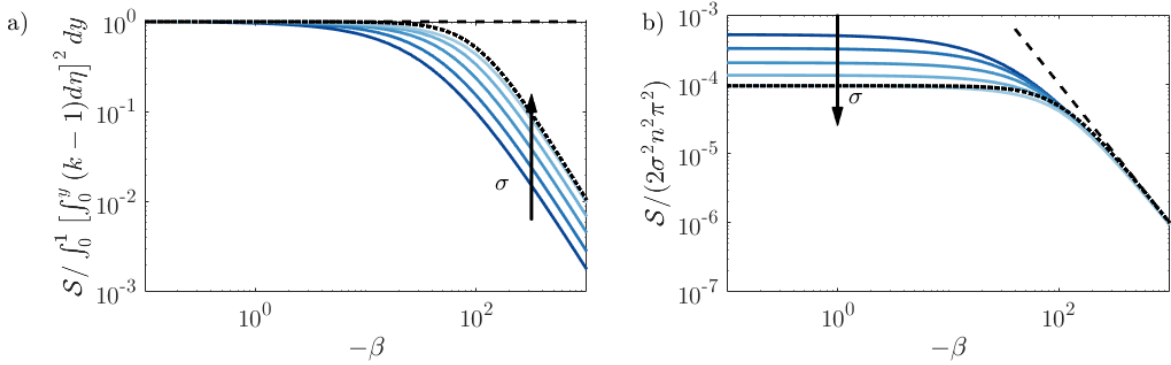


Fig. 3.10 (a) Plot of \mathcal{S} normalized by its small- $|\beta|$ limit vs. β and (b) plot of \mathcal{S} normalized by its large- $|\beta|$ limit vs. β for σ ranging from 1 to 5. The dashed black lines denote the asymptotic limits (3.35) and (3.40) in (a) and (b) respectively and the dotted lines correspond to the approximate solution (3.42) for $\sigma = 5$.

$|\partial c / \partial x|$, distorting the interface generates large transverse gradients in concentration. These correspond to large, stable transverse gradients in viscosity (and hence pressure) which tend to force the profile back to vertical. Ultimately, this results in a stationary interface (in the moving frame) where the streamwise velocity goes to zero (figure 3.9(f)). Far upstream and downstream, where the viscosity is transversely uniform, the velocity is imposed by the permeability. The abrupt change in velocity at the interface drives a circulation on either side of the interface carrying concentration away from it. As the fluids mix, the concentration, and hence viscosity gradients at the interface weaken. Over time, the stabilizing viscous forces become sufficiently weak that the streamwise velocity can grow and streamlines begin to penetrate through the interface (figures 3.9(b,c)). Eventually the interface becomes very diffuse and the velocity becomes predominantly longitudinal (figures 3.9(d)) as in the cases considered in previous sections. In contrast to those cases, however, where the concentration deviations, (c') , are $O(1)$ until the late-time regime, the concentration deviations here are always small because the concentration remains relatively transversely uniform with no large-scale channelling into layers.

3.5.1 Concentration model

As found in §3.4.3, the shear enhanced dispersivity \mathcal{S} is given by (3.31) where $\beta = RPe \partial \bar{c} / \partial x$ and \tilde{c} is given by (3.30) and u by (3.26). However, unlike in §3.4.3, for viscosity-stabilized flows, we now expect this model to apply for all time, rather than just at late times, given that the flow remains nearly transversely uniform ($c' \ll 1$). In

particular, $|\beta|$ is not just small but can take on any value. We thus first consider the large- β limit.

We start by expanding \tilde{c} in powers of $1/\beta$, $\tilde{c} = \tilde{c}_0 + \tilde{c}_1/\beta + O(1/\beta^2)$. Substituting into (3.30) expanding and equating different powers of β , we find

$$\frac{ke^{\tilde{c}_0}}{\int_0^1 ke^{\tilde{c}_0} dy} - 1 = 0, \quad (3.37)$$

and so,

$$\tilde{c}_0 = -\ln(k) + \overline{\ln(k)}, \quad \tilde{c}_1 = \frac{\partial^2 \tilde{c}_0}{\partial y^2}, \quad (3.38)$$

and

$$\tilde{c}_1 = -\left(\frac{kk'' - (k')^2}{k^2}\right), \quad (3.39)$$

where we have again used the fact that $\int_0^1 \tilde{c}_0 = \int_0^1 \tilde{c}_1 = 0$. To leading order, the concentration deviations align themselves such that the streamwise velocity is zero. The shear-enhanced dispersivity in this limit is

$$\mathcal{S} = \frac{1}{\beta} \int_0^1 u \tilde{c} dy = \frac{1}{\beta^2} \int_0^1 \ln(k) \left(\frac{kk'' - (k')^2}{k^2}\right) dy + O\left(\frac{1}{\beta^3}\right). \quad (3.40)$$

In the case of sinusoidally varying log-permeability, this limit corresponds to

$$\mathcal{S} = \frac{2\sigma^2\pi^2}{\beta^2} + O\left(\frac{1}{\beta^3}\right). \quad (3.41)$$

Equations (3.35) and (3.40) correspond to the small- and large-viscosity gradient asymptotic limits of the shear-enhanced dispersivity and are plotted on top of the full solutions in figures 3.10(a,b) respectively. We can also combine the two limits into a very simple approximate analytical composite solution; for example for the case of a sinusoidally varying log-permeability,

$$\mathcal{S}_{comp} = \left(\frac{1}{\mathcal{S}^*} + \frac{\beta^2}{2\sigma^2\pi^2}\right)^{-1}, \quad (3.42)$$

where $\mathcal{S}^* = \int_0^1 [f_0^y(k-1)d\eta]^2 dy$ is the leading-order behaviour in (3.35). This approximate solution reasonably captures the general behaviour of the shear-enhanced dispersivity without having to solve (3.30) exactly (see dotted lines in figure 3.10, which recover the $\beta \ll 1$ and $\beta \gg 1$ limits).

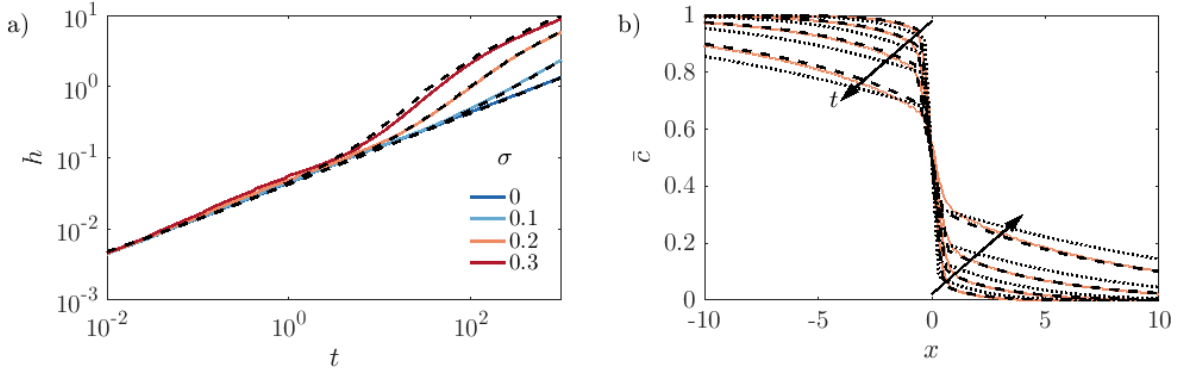


Fig. 3.11 Evolution of the mixing length and transversely averaged concentration for $|R| > \sigma$, $R < 0$. (a) Plot of h vs. t for $(R, \text{Pe}) = (-2, 300)$ and σ ranging from 0 to 0.3. (b) Plot of $\bar{c}(x, t)$ for $(R, \sigma, \text{Pe}) = (-2, 0.2, 300)$ and $t = 32, 100, 320, 1000$. The theoretical predictions, found by solving (3.36), with either the exact solution of \mathcal{S} (found by solving (3.30)), or (3.42), are given by the dashed and dot-dashed black lines respectively.

3.5.2 Comparison to numerical simulations

We solve the reduced-order model (3.36) both directly and using the approximate composite solution (3.42), in the same manner as §3.4.3 with a step initial condition (3.9). The comparisons to the transversely averaged concentration profiles from the full numerical simulations are given in figure 3.11(b). The exact solution of the reduced model is not only able to capture the sharp interface and the long tails, but it also accurately predicts the evolution of the concentration field. Using the composite approximation of \mathcal{S} in the reduced model also captures the qualitative evolution of the transversely averaged concentration although it slightly overestimates the amount of spreading that occurs. The mixing length is also shown as a function of time for different σ in figure 3.11(a). The very good agreement between the reduced-order model and the full simulations over a range of σ and t , suggests that the full 2D problem can be reduced to solving a 1D nonlinear diffusion equation for all times in this limit.

3.6 Non-sinusoidally varying permeability

The reduced-order models, thus far, have been derived for arbitrary permeability fields, but the numerical simulations have been restricted to log-permeabilities that vary sinusoidally in space at one frequency. In this section, we briefly consider stable miscible displacements in a more complex porous medium (figure 3.12). For more details about the permeability structure used, see the Salt-Creek derived permeability field in §4.7.

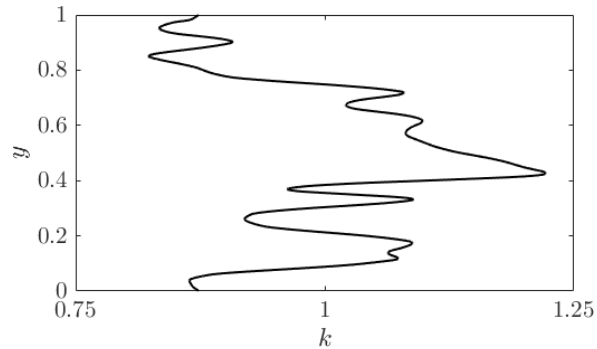


Fig. 3.12 (a) Permeability data used in the numerical simulations. The permeability structure is derived from the measurements at Salt Creek (Bickle et al., 2017). See §4.7 for more details.

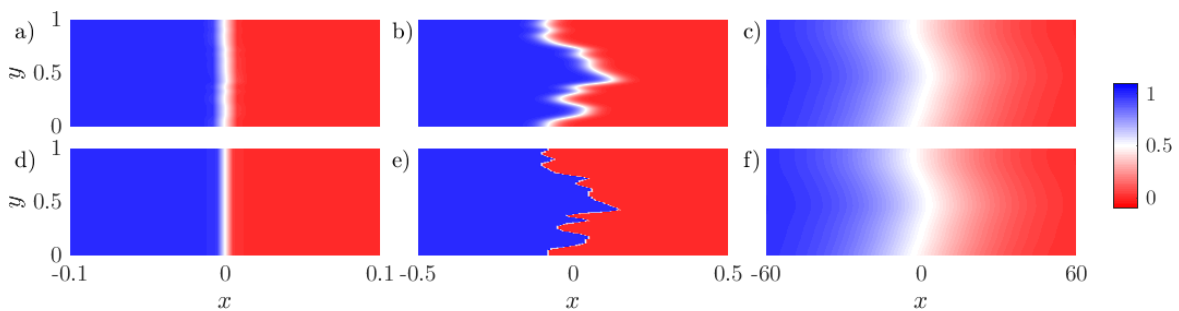


Fig. 3.13 Evolution of the concentration field for a constant viscosity displacement in a complex permeability structure and $(R, Pe) = (0, 500)$. (a,b,c) The results of the numerical simulations, and (d,e,f) the model solutions. The snapshots are taken at (a,b) early times ($t = 0.002$), (c,d) intermediate times ($t = 6$), and (e,f) late times ($t = 100$).

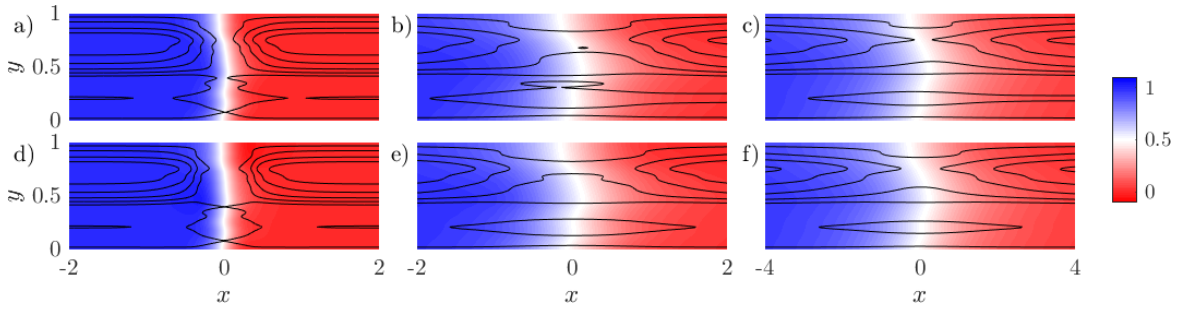


Fig. 3.14 Evolution of the concentration field with overlain streamlines for $|R| > \sigma$, $R < 0$ and a complex permeability structure. The results of the (a,b,c) numerical simulations, and (d,e,f) model solutions. The snapshots are taken at (a,b) $t = 1.5$, (c,d) $t = 25$, and $t = 100$.

Figure 3.13 shows the evolution of the concentration field for a uniform viscosity displacement in a porous medium composed of many Fourier modes. Since $R = 0$, the fluid flow is purely horizontal and given by (3.12). As was found in §3.3, the flow evolves through the three regimes. At early times, the interface grows diffusively (figures 3.13(a,d)). At intermediate times, the interface is stretched by the heterogeneous flow-field and diffusion is relatively unimportant (figures 3.13(b,e)). At late times, the concentration field is vertically well-mixed and the interface evolves through shear-enhanced dispersion (figures 3.13(a,d)). In general, we find that the reduced-order models derived in §§3.3.1-3.3.3 show good agreement with the full 2D simulations.

Figure 3.14 shows the evolution of the concentration field for a stabilizing viscosity contrast and with the same porous medium. When the injected fluid is more-viscous than the ambient fluid, the viscosity difference between the fluids tends to suppress channeling due to the permeability heterogeneities. We find that far upstream and downstream, where the viscosity is transversely uniform, the velocity is imposed by the permeability field, whereas, at the interface the concentration deviations align with the permeability field to ensure zero horizontal flow. This change in velocity results in a circulation on either side of the interface. Whereas in §3.5 this circulation was symmetric, here it is asymmetric, being more pronounced near the top of the domain where the permeability variation is large. In the non-travelling frame, the interface travels as a shock-like front that travels with the average injection velocity. Over time, due to the circulation and streamwise diffusion, the viscosity gradient at the interface weakens. Eventually, the viscosity gradient is insufficient to maintain the shock-like front and streamlines penetrate through the interface (figures 3.14(b,c,e,f)). In this case, the fluid flow becomes dominated by the imposed permeability and the interface evolves through shear-enhanced dispersion. The reduced-order model found

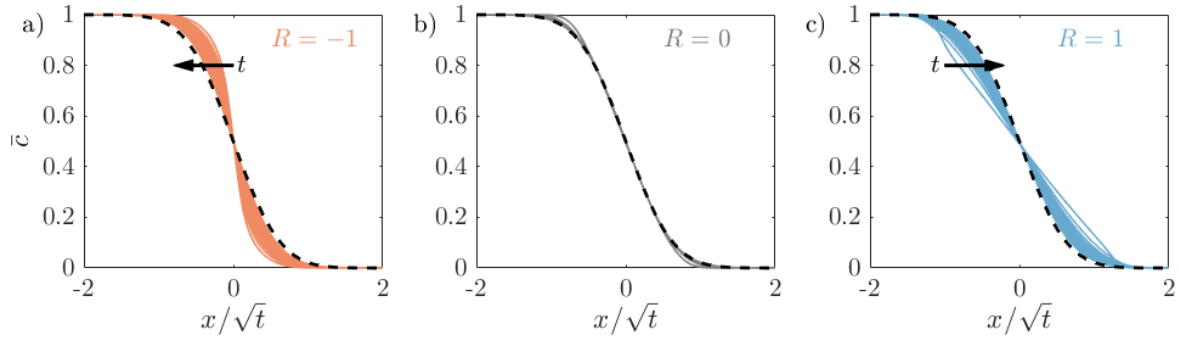


Fig. 3.15 Long-time evolution of $\bar{c}(x, t)$ for $\sigma = 0.3$, $(Pe) = (100)$ and t ranging from 10 – 1000. The viscosity ratio is (a) stabilizing $R = -1$, (b) uniform viscosity $R = 0$ and (c) de-stabilizing $R = 1$. The asymptotic, viscosity-independent solution, (3.15) with (3.22) is given by the dashed line.

by solving (3.36) with (3.30) is able both to capture these qualitative features and to quantitatively predict the evolution of the concentration field.

3.7 Discussion and Conclusions

In this chapter, stable miscible displacements in heterogeneous porous media were examined. The main goal throughout this chapter has been to better understand the structure and evolution of the concentration field during stable displacement processes through the use of high-resolution numerical simulations and reduced-order modelling. Motivated by the fact that many geological formations consist of layered sedimentary sequences, permeability structures that vary perpendicular to the flow direction were considered. Furthermore, in this chapter the following viscosity configurations were examined: injected fluids that were equally-viscous, nearly equally-viscous, and more-viscous than the ambient fluid. In general it was found that the flow evolves through three main flow regimes.

At early times, the concentration field evolves through diffusion across an initially sharp interface and is independent of both the log-viscosity ratio, R , and log-permeability ratio, σ (see §3.3.1). Once advection begins to outpace diffusion ($t \sim O(1/Pe)$) the flow transitions to the intermediate-time regime. At intermediate times, the interplay between viscosity and permeability variations leads to different behaviour depending on the relative size of R and σ . When permeability effects dominate ($\sigma > |R|$; §3.4); the viscosity modulates the effective permeability of the medium but otherwise evolves qualitatively in the same manner as when the two fluids have equal viscosity. When the injected fluid is more viscous than the ambient ($|R| > \sigma$ and $R < 0$;

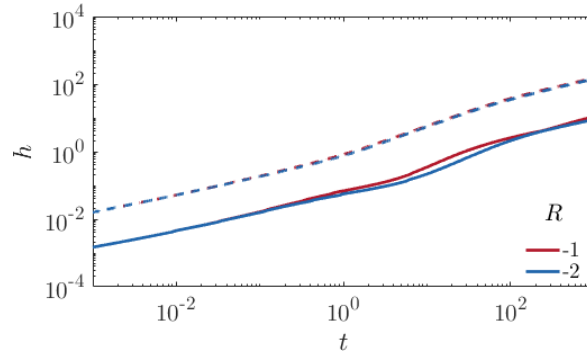


Fig. 3.16 Plot of two different measures of h vs. t for $(\sigma, \text{Pe}) = (0.3, 300)$ and $R = -1, -2$. The solid lines correspond to (3.11) and the dashed lines correspond to (3.43)

§3.5), the viscosity contrast tends to prevent channelling at the interface and reduces spreading of the two fluids relative to the equal viscosity, $R = 0$ case. Finally, once the interface has become long and thin and transversely homogenized ($t \sim O(\text{Pe})$) the flow transitions to the late-time regime. At late times, the flow becomes dominated by shear-enhanced dispersion which asymptotically becomes independent of the viscosity ratio and only depends on the permeability structure. Figure 3.15 demonstrates this behaviour: it shows the evolution of the concentration field for $R = 0$, $R < 0$, and $R > 0$. Although spreading is initially hindered ($R < 0$), or enhanced ($R > 0$), at late times they both tend to the same viscosity-independent self-similar solution. This means that for processes that occur over very small length scales or very long time scales, the viscosity difference becomes insignificant and the permeability structure dictates the rate of spreading and mixing of the two fluids. Note that these different possible regimes are summarized in the following chapter in figures 4.10(a,b).

In summary, the flow evolves through three distinct regimes: an early-time regime dominated by longitudinal diffusion, an intermediate-time regime dominated by longitudinal advection and a late-time regime dominated by shear-enhanced dispersion. Informed by high resolution numerical simulations, simple models that capture the dominant physics in each of the regimes were developed, which provide an easy way of quantitatively predicting the average behaviour of these systems.

Appendix 3.A Comparison of mixing length metrics

Figure 3.16 shows a comparison of the mixing length quantity used in chapters 3-5 (3.11) and the more typical measure

$$h = h^* = x|_{\bar{c}=0.01} - x|_{\bar{c}=0.01}. \quad (3.43)$$

It can be seen that h calculated using (3.43) shows no discernible difference between the two simulations, whereas h calculated using (3.11) is noticeably different at intermediate times. This is because the simulations shown in figure 3.16 correspond to large stabilizing viscosities whose concentration profiles are composed of a sharp gradient at the interface, which depends on the viscosity ratio, and long tails upstream and downstream, which are independent of the viscosity ratio. Since (3.43) only picks up the growth of the tail regions, it is independent of R , whereas (3.11) accounts for the evolution of the sharp concentration gradient and hence depends on R . We therefore use (3.11) to measure the mixing length due to this sensitivity to the structure of the concentration field.

Appendix 3.B Asymptotic solutions for uniform viscosity displacements

When the variations in the permeability are small ($\sigma \ll 1$), equation (3.13) becomes

$$u = k - 1 \simeq -\sigma \cos(2\pi y), \quad (3.44)$$

such that at intermediate times, the characteristic spreading velocity is

$$\Delta u = 2\sigma, \quad (3.45)$$

and at late times, the shear-enhanced dispersivity, (3.23), is

$$S = \int_0^1 \left[\int_0^y (k(\eta) - 1) d\eta \right]^2 dy \simeq \frac{\sigma^2}{8\pi^2}. \quad (3.46)$$

When the variations in the permeability are large ($\sigma \gg 1$), the fluid velocity diverges at $y = 1/2$ and tends to -1 everywhere else. The characteristic spreading

velocity is

$$\Delta u \simeq (2\pi\sigma)^{1/2}. \quad (3.47)$$

At late times, the shear-enhanced dispersivity, \mathcal{S} , is given by (3.23). Taylor-expanding $I_0(\sigma)$ as $\sigma \rightarrow \infty$, (3.23) becomes,

$$\mathcal{S} = \int_0^1 \left[\int_0^y \left(\frac{e^{-\sigma \cos(2\pi\eta)}}{e^\sigma [(2\pi\sigma)^{-1/2} + O(\sigma^{-3/2})]} - 1 \right) d\eta \right]^2 dy. \quad (3.48)$$

Solving using Laplace's method gives,

$$S = \int_0^1 [-y + H(y - 1/2)]^2 dy + O(\sigma^{-1}) = \frac{1}{12} + O(\sigma^{-1}). \quad (3.49)$$

Chapter 4

Unstable displacements in layered porous media

The material in this and the preceding chapter form the basis of the publication (Nijjer et al., 2019): Nijjer, J. S. & Hewitt, D. R. & Neufeld, J. A. (2019). Stable and unstable miscible displacements in layered porous media. *Journal of Fluid Mechanics* **869**. 468-499.

4.1 Introduction

In many geological contexts, including during carbon capture and storage, both permeability heterogeneities and viscous fingering can play important roles in controlling the evolution of the displacement front and the interpenetration of the fluids. Whereas in chapter 2 miscible viscous fingering in homogeneous porous media was examined, and in chapter 3 stable miscible displacements in heterogeneous porous media were examined, in this chapter the combined effects of permeability heterogeneities and viscous fingering on the mixing and spreading of the injected and ambient fluids are considered. The interplay between permeability variations and the viscous fingering instability can lead to a rich set of dynamics. For example, spatial gradients in permeability (Al-Housseiny et al., 2012; Rabbani et al., 2018), time-varying permeabilities (Zheng et al., 2015b), or reactive permeabilities (Pihler-Puzovic et al., 2012) can be used to suppress instabilities, while structured permeabilities can be used to template fluid patterns (Chen, 1987; Chen and Wilkinson, 1985).

As in chapter 3, specific attention is paid to layered porous media where permeability variations are perpendicular to the flow direction. Here, however, the focus is on unstable viscosity variations where a less-viscous fluid is injected into a porous medium

saturated with a more-viscous fluid. In chapter 3 it was found that when the fluid flow remained stable the characteristic length scale of the flow was imposed by the permeability. However, when the interface is unstable, a new evolving characteristic length-scale is introduced by the fingering instability and the interplay between these two length scales can lead to different dynamics. Although a number of studies have examined unstable displacements in randomly heterogeneous porous media (Afshari et al., 2018, 2019; Araktingi and Orr Jr., 1993; Chen and Meiburg, 1998c; Fayers et al., 1992; Jiao and Hotzl, 2004; Khataniar and Peters, 1992; Nicolaidis et al., 2015; Tchelepi et al., 2004), there has been relatively little work on unstable displacements in layered porous media.

One simple but widely used method to parameterize the combined effects of viscous fingering and permeability heterogeneities on the spreading of the injected and ambient fluids is the Koval K-factor model (Koval, 1963). The K-factor model provides a way of predicting the rate of spreading of the injected and ambient fluids. To estimate the total rate of spreading involves independently parameterizing the effect of viscous fingering on spreading rate in a homogeneous medium and the effect of the permeability heterogeneities on spreading rate of a passive tracer. The predicted rate of spreading is then simply a product of the two calculated spreading rates. Although this provides a simple way of characterizing both effects, not surprisingly given the highly nonlinear nature of the system, the K-factor model does not accurately predict the evolution of the concentration field in structured porous media (Sajjadi and Azaiez, 2013; Shahnazari et al., 2018).

Sajjadi and Azaiez (2013) used numerical simulations of unstable flows in periodically layered porous media, to identify a series of different flow regimes through which the flow evolves. They demonstrated that adding permeability heterogeneities tended to cause channelling - that is, flow predominantly along permeability layers - rather than chaotic fingering. They also found that the interface could channel and finger across layers. However, while this study highlighted some of the interesting qualitative behaviours that can be observed in miscible displacement flows when heterogeneities and unstable viscosity variations interact, they do not provide quantitative predictions for the evolution of the spreading and mixing, nor a full overview of the different dynamical regimes that occur. In this chapter, our goal is to identify the different flow regimes that arise and the dominant physics at play when a less-viscous fluid is injected into a layered heterogeneous porous medium saturated with a more-viscous fluid, and to develop reduced-order models for the spreading and dispersion of the fluids.

This chapter is laid out as follows. In §4.3, the general patterns and regimes that are seen when the permeability field is composed of a single dominant wavelength are described. In §§4.4-4.6 each of these regimes are discussed in more detail, paying particular attention to the time-evolution of the concentration field, and reduced-order models for its evolution are derived. Finally in §4.7 more realistic permeability fields that have more than one dominant wavelength are briefly considered.

4.2 Problem formulation

We briefly discuss the model setup here as it is identical to that of chapter 3; see §3.2 for the full details. As in chapter 3, the dimensionless governing equations are

$$-(\tilde{u} + 1)\mu = k \frac{\partial p}{\partial \tilde{x}}, \quad -v\mu = k \frac{\partial p}{\partial y}, \quad (4.1)$$

$$\frac{\partial \tilde{u}}{\partial \tilde{x}} + \frac{\partial v}{\partial y} = 0, \quad (4.2)$$

$$\frac{\partial c}{\partial t} + \tilde{u} \frac{\partial c}{\partial \tilde{x}} + v \frac{\partial c}{\partial y} = \frac{1}{\text{Pe}} \left(\frac{\partial^2 c}{\partial \tilde{x}^2} + \frac{\partial^2 c}{\partial y^2} \right), \quad (4.3)$$

$$\mu(c) = e^{-Rc}, \quad (4.4)$$

$$\ln(k) = -\sigma \cos(2\pi n y) - \ln(I_0(\sigma)), \quad (4.5)$$

and the boundary and initial conditions are given by (3.5)-(3.9).

In this chapter we only consider the unstable case where the viscosity variations are larger than the permeability variations $R > \sigma$. Note that the interface can also be unstable if $R < \sigma$ and the Peclet number is sufficiently large. In this chapter we also explicitly consider the effect of the number of layers, n . This is because in contrast to chapter 3 where the transverse length scale of the flow was imposed by the permeability, here there is competition between the evolving wavelength of the viscous fingering and the imposed wavelength of the permeability structure. We find that this competition results in rich intermediate-time dynamics for which the value of n can be important.

4.3 Displacement pattern and regimes

In the absence of any permeability variations, $\sigma = 0$, this configuration is hydrodynamically unstable (provided Pe is sufficiently large). In homogeneous media such unstable miscible displacements evolve through three flow regimes (cf. chapter 2): at

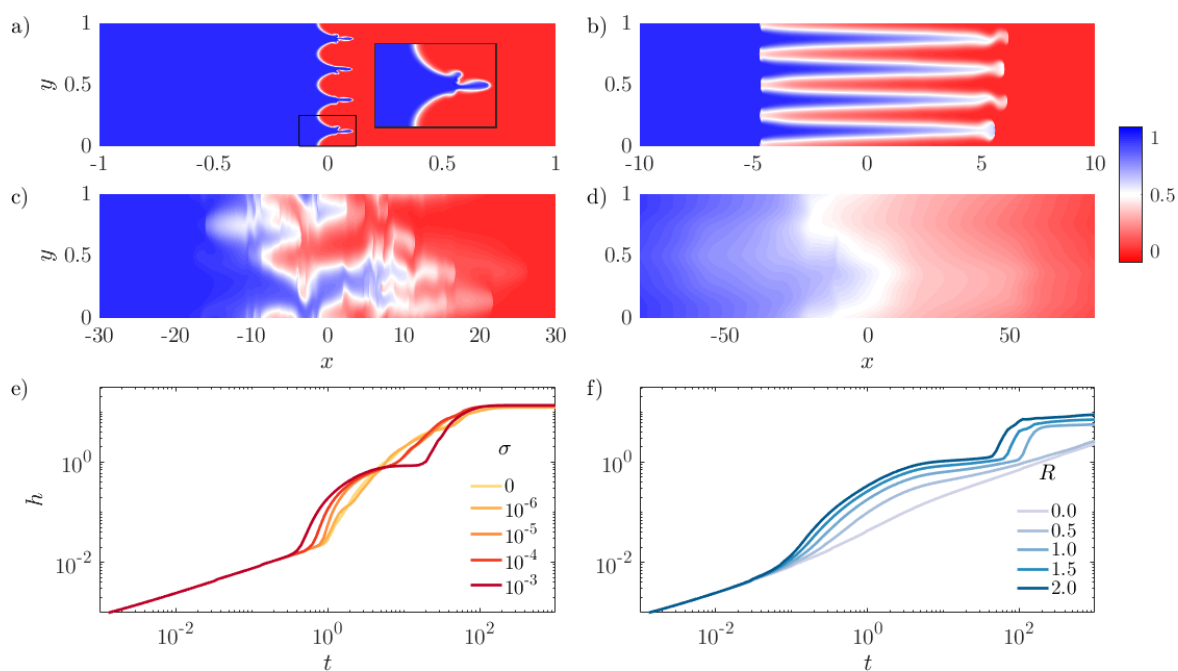


Fig. 4.1 Evolution of the concentration field for $|R| > \sigma$ and $R > 0$. (a-d) Colourmaps of the concentration field for $(R, \sigma, Pe, n) = (2, 0.1, 4000, 4)$ at (a) $t = 0.1$, (b) $t = 8$, (c) $t = 104$ and (d) $t = 1500$. Note that the aspect ratio is increasingly compressed in figures (b-d). (e,f) Evolution of $h(t)$ for $(Pe, n) = (1000, 4)$ and: (e) $R = 2$ with varying σ ; and (f) $\sigma = 0.1$ with varying R .

early times, the flow is linearly unstable, where the interface grows diffusively, and fingers grow exponentially; at intermediate times, the fingers have finite amplitude and propagate and interact with each other nonlinearly leading to coarsening; and at late times, a single pair of counter-propagating fingers remain which propagate and slow, leaving a well-mixed interior.

In the presence of permeability layering, there is a competition between the evolving wavelength of viscous fingering and the imposed wavelength of the permeability structure. The competition between viscous fingering, which acts to coarsen the transverse length-scale, and permeability layering, which acts to impose a fixed length scale, results in rich intermediate-time dynamics. As a result, the number of layers n can no longer be scaled out of the problem. Nonetheless, as before, the early-time dynamics are still dominated by longitudinal diffusion across the sharp interface (cf. §3.3.1), and the late-time dynamics are dominated by shear-enhanced dispersion which becomes independent of the viscosity ratio at long times (cf. §3.4.3).

In general, there are four possible intermediate-time regimes through which the flow can evolve, representative snapshots of which are given in figure 4.1. In the first regime (I), fingering occurs within the permeability layers and these fingers coarsen until they coincide with the imposed permeability layering (figure 4.1(a)). In the second regime (II), the flow follows the imposed layered structure while diffusing across the layers, which causes the flow to slow down (figure 4.1(b)). In some cases, this flow can then be unstable, leading to a third regime (III) which corresponds to fingering over a transverse length-scale that is larger than that imposed by the permeability (figure 4.1(c)). These fingers then also coarsen, leading to a fourth regime (IV) where a single pair of counter-propagating fingers remain (figure 4.1(d)). This pair of fingers slows, leaving a well-mixed region that eventually evolves through shear-enhanced dispersion. Note that regimes III and IV can only occur if $n > 1$.

The growth of the mixing length can be drastically different depending on which regime the flow is in (figure 4.1(e,f)). When the flow fingers (regimes I and III), as with a homogeneous porous medium, the mixing length grows linearly in time. When the flow is channelling or in the single-finger exchange flow regime (regimes II and IV) the mixing length tends to a constant value. As σ is increased from 0 (uniform permeability case), we see a transition from pure viscous fingering to channelling and fingering behaviour (figure 4.1(e)). As R is increased from 0 (uniform viscosity case), we see a transition from pure channelling behaviour to both channelling and fingering (figure 4.1(f)). Exactly which regimes occur depend on all four of the variables (R, σ, Pe, n) in this problem. In general we find fingering behaviour (regimes I and III) is more

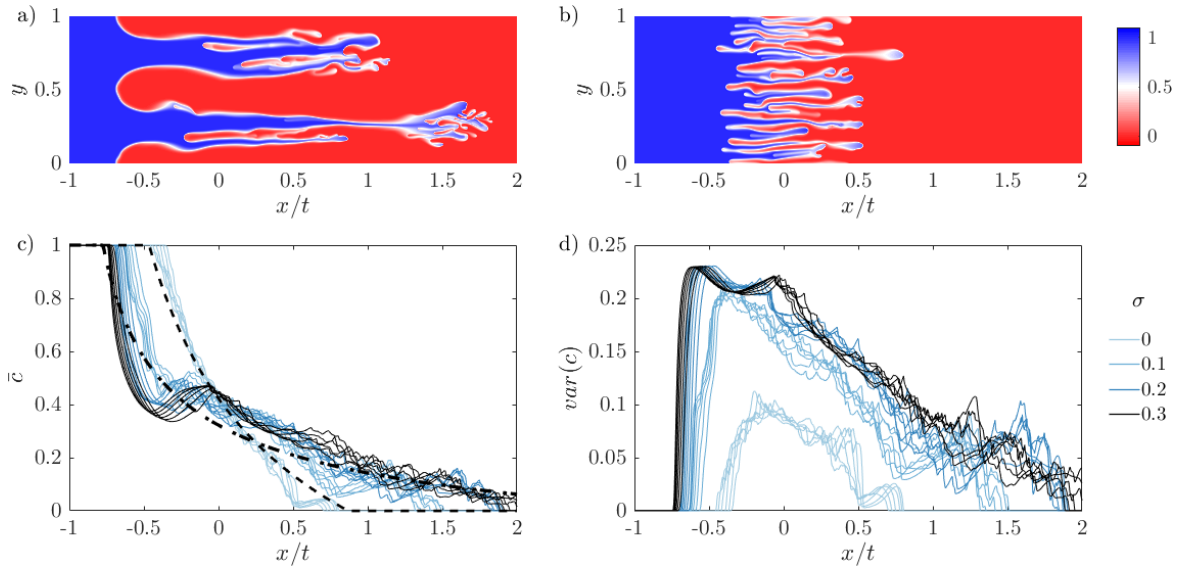


Fig. 4.2 Evolution of the concentration field for $R > \sigma$ in regime I with $(R, Pe, n) = (2, 8000, 2)$. (a,b) Colourmaps of the concentration field for (a) $\sigma = 0.1$ and (b) $\sigma = 0$ at $t = 1$. (c) Plot of the transversely averaged concentration $\bar{c}(x, t)$ and (d) transverse variance in concentration $var(c) = \int_0^1 c'^2 dy$ against the similarity variable x/t for σ ranging from 0 to 0.3. In (c), the theoretical prediction (4.9) with effective viscosities (2.40) and (4.10) are given by dashed and dot-dashed lines respectively.

significant for larger values of R and Pe , while channelling is more significant for larger values of σ . Fingering across layers (regimes III and IV) is only relevant when $n > 1$, and is most notable when the length scale of the permeability variations is small, $n \gg 1$.

In the following sections we review the different regimes and discuss some simple models for the evolution of the transversely averaged concentration.

4.4 Regime I: fingering within layers

The flow is able to finger within the permeability layers when the length-scale of the most unstable mode, $y \sim 1/RPe$ (Tan and Homsy, 1986), is small compared to the length-scale imposed by the permeability $y \sim 1/n$. Hence the flow always fingers for sufficiently large Pe and is also observed to be enhanced when σ is small (De Wit and Homsy, 1997b; Shahnazari et al., 2018). Note that fingering within layers is also possible when permeability effects dominate over viscous effects, $R < \sigma$, so long as Pe is sufficiently large.

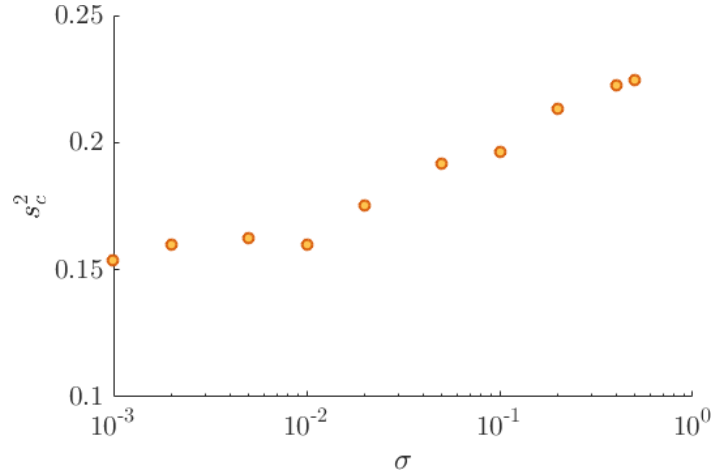


Fig. 4.3 Measure of the mixing zone variance, s_c^2 , as a function of the log-permeability variations for $(R, Pe, n) = (3, 8000, 2)$. The variance is defined as: $s_c^2 = 1/h \int_{x|_{\bar{c}=0.99}}^{x|_{\bar{c}=0.01}} \int_0^1 (c - 1/2)^2 dy dx$

Figures 4.2(a,b) show snapshots of the concentration field for $\sigma = 0.1$ and $\sigma = 0$ respectively. The fingers evolve in a similar manner in both cases, leading to an asymmetric transversely averaged concentration that evolves self-similarly with similarity variable x/t (figure 4.2(c)). The main difference between the two simulations is that the fingers move significantly faster when permeability heterogeneities are present. For example, the mixing length grows at more than double the rate in the simulation in figure 4.2(a) compared to the homogeneous case, which is far larger than one would predict simply by considering the difference in permeability.

This difference is due to the structure of the flow being fundamentally different in the two simulations. Whereas, in the homogeneous medium, the forward and backward propagating fingers are, on average, about the same size, in the heterogeneous medium, the backward propagating fingers are broad and aligned with the low permeability layers. This means the two fluids tend to be much more segregated (figure 4.2(d)), and so the effective viscosity difference between the forward- and backward-propagating fingers is much larger in the heterogeneous medium, which leads to much faster spreading. This fact can be seen in figure 4.3, which shows the variance of the concentration field inside the mixing zone. For $R = 3$, we find that the variance is nearly constant until $\sigma \approx 0.02$ after which there is an increase in the variance, corresponding to more segregated fluid. We find this transition depends weakly on R , and modelling this transition remains the subject of future work. We also observe from the simulations that the transversely averaged concentration is broadly insensitive to σ for $\sigma \gtrsim 0.1$ (for $R = 2$, figure 4.2(c,d)), which supports the idea that the presence of layered heterogeneity changes

the spreading rate through the structure of the flow. In the following subsection we extend the model presented in §2.4.2 for the homogeneous case by accounting for this change in finger structure.

4.4.1 Concentration model

To model the nonlinear evolution of the fingered region, we again assume the flow is in vertical flow equilibrium and that the streamwise velocity is given by (3.26). However, unlike in §3.3.2 and §3.4.2 where the velocity depends on the permeability, here we assume the velocity depends only on the viscosity,

$$u = \frac{e^{Rc(x,y,t)}}{\int_0^1 e^{Rc(x,s,t)} ds} - 1, \quad (4.6)$$

since $\sigma < R$. Substituting the streamwise velocity into (2.18) and neglecting longitudinal diffusion gives

$$\frac{\partial \bar{c}}{\partial t} + \frac{\partial}{\partial x} \left[\frac{\int_0^1 c\mu(c)dy}{\int_0^1 \mu(c)dy} - \bar{c} \right] = 0. \quad (4.7)$$

Next we suppose that the flow is composed of $\eta_f(x)$ forward-propagating fingers of width $w_f(x)$ and $\eta_b(x)$ backward-propagating fingers of width $w_b(x)$. We make the simplifying assumption that the forward- and backward-propagating fingers have uniform concentration $c = 1$ and $c = 0$ respectively, but allow the viscosity to vary inside the finger. We have the additional constraints that the transversely averaged concentration is equal to the proportion of forward-propagating fingers $\eta_f w_f = \bar{c}$ and the total area of the fingers adds up to one, $\eta_f w_f + \eta_b w_b = 1$.

When modelling fingering in a homogeneous medium ($\sigma = 0$), we assumed that the forward- and backward-propagating fingers had viscosities $\mu(y) \approx e^{R(1-y^2/w_f^2)}$ and $\mu(y) \approx e^{R(y^2/w_f^2)}$ across the fingers respectively (cf. §2.4.2). When σ is small but finite (for $R = 3$, this corresponds to $\sigma \gtrsim 0.02$), the backward-propagating fingers are broad and coincide with the low permeability layers. In this case, the viscosity in the fingers is nearly uniform, $\mu(y) \approx 1$.

Substituting our assumptions for the concentration and viscosity into (4.7) gives,

$$\frac{\partial \bar{c}}{\partial t} + \frac{\partial}{\partial x} \left(\frac{\eta_f \int_{-w_f}^{w_f} e^{R(1-y^2/w_f^2)} dy}{\eta_f \int_{-w_f}^{w_f} e^{R(1-y^2/w_f^2)} dy + \eta_b \int_{-w_b}^{w_b} 1 dy} - \bar{c} \right) = 0. \quad (4.8)$$

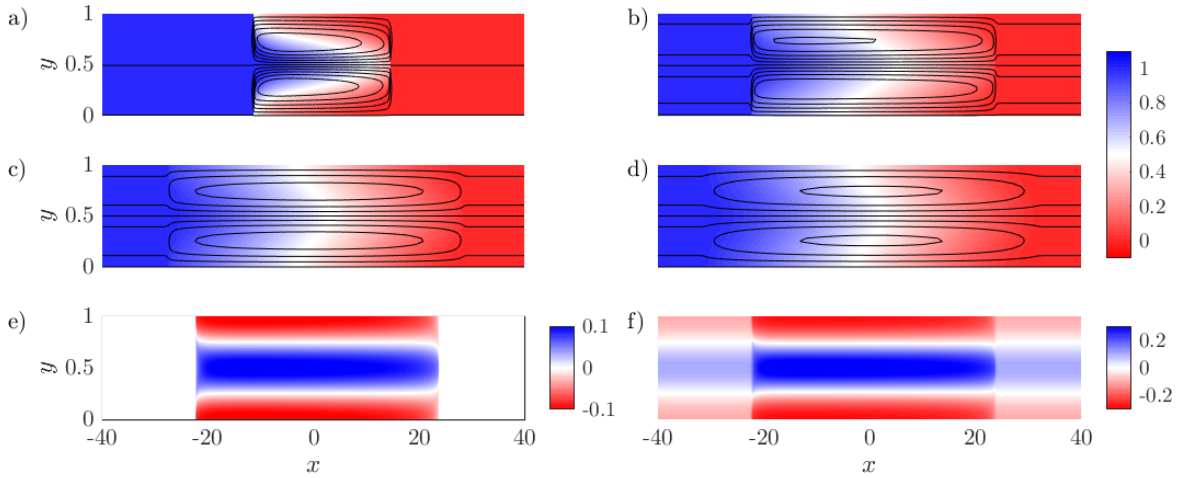


Fig. 4.4 Evolution of the concentration field for $|R| > \sigma$ and $R > 0$ in the channelling regime; $(R, \sigma, Pe, n) = (2, 0.1, 500, 1)$. (a-d) Colourmaps of the concentration field with overlain streamlines at (a) $t = 20$, (b) $t = 60$, (c) $t = 100$ and (d) $t = 140$. (e) Colourmap of the concentration deviations $c' = c - \bar{c}$ at $t = 20$. (f) Colourmap of the streamwise velocity u at $t = 20$. Note that the aspect ratio of the figures is compressed by a factor of 30, so variations in the x -direction seem more pronounced than they actually are.

This has the solution

$$\bar{c}(x, t) = \begin{cases} 1 & x/t < \frac{1}{M_e} - 1 \\ \frac{1}{M_e - 1} \left(\sqrt{\frac{M_e}{x/t + 1}} - 1 \right) & \frac{1}{M_e} - 1 \leq x/t \leq M_e - 1 \\ 0 & x/t > M_e - 1, \end{cases} \quad (4.9)$$

where

$$M_e = \frac{\sqrt{\pi} e^R \operatorname{erf}(\sqrt{R})}{2\sqrt{R}}. \quad (4.10)$$

The transversely averaged concentration evolves in exactly the same manner as in the homogeneous case but with a larger effective viscosity. The model prediction, given by the dot-dashed line in figure 4.2(c), gives good quantitative agreement with the numerical simulations when $\sigma \neq 0$. Thus we find that, although small amounts of permeability heterogeneity would be expected to have a small effect on the spreading rate, they can in fact result in a qualitative change in the structure of the flow and lead to significantly faster spreading and mixing.

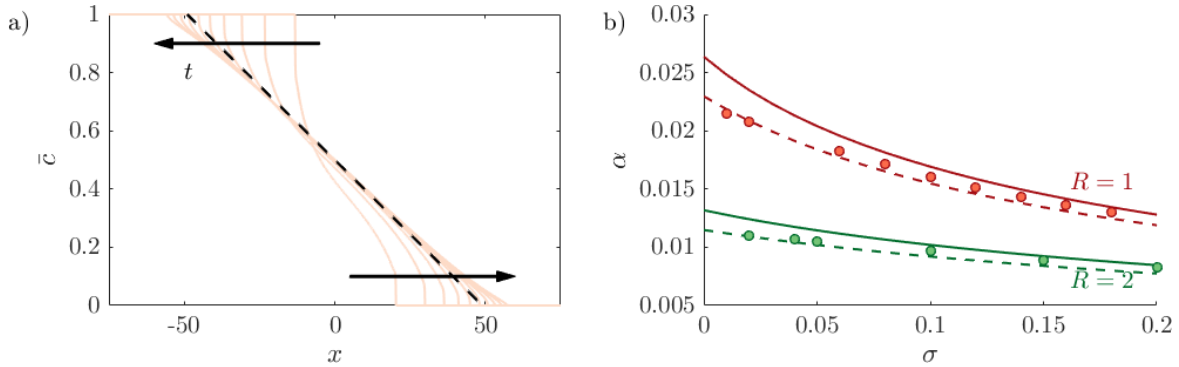


Fig. 4.5 (a) Plot of $\bar{c}(x, t)$ from the numerical simulations (solid lines) and the theoretical prediction overlain (dashed line) for $(R, \sigma, Pe, n) = (2, 0.1, 1000, 1)$. (b) Plot of the linear slope α of \bar{c} , as a function of σ , showing a least-squares fit to the data from numerical simulations (dots) and the theoretical solution (4.16) for $K = 0.5$ (solid line) and $K = 0.6$ (dashed line).

4.5 Regime II: stable channelling

After the fluid fingers inside the high-permeability layers, it coarsens until a single broad finger remains in each layer (figure 4.1(b)). Figures 4.4(a-d) show a sequence of snapshots of the concentration field with overlain streamlines for $(R, \sigma, Pe, n) = (2, 0.1, 1000, 1)$ for which at intermediate times the flow is always in this channelling regime. In this example, $n = 1$ and so the channelling consists of a single pair of counter-propagating fingers. The flow is predominantly longitudinal except in regions localized near large concentration gradients. Initially the streamwise velocity is large and localized in the finger. Upstream and downstream, where the viscosity is uniform, the velocity is imposed by the permeability, but is small relative to the contributions due to viscosity variations (figure 4.4(f)). As time progresses, and the fluids become more mixed, the effect of the viscosity reduces and the streamwise velocity in the fingered region approaches the upstream and downstream velocity (figures 4.4(b,c,d)). The concentration deviations, figure 4.4(e), are uniform in the x -direction, vary sinusoidally in the y direction and are in phase with the velocity.

This behaviour resembles the late-time regime in the miscible viscous fingering instability (i.e. when $\sigma = 0$, cf. §2.5). More specifically, the dynamics consist of an interior region where the background gradient is linear and steady and the ends of which are filled in by the propagating fingers (figure 4.5(a)). Superimposed on the steady background gradient are sinusoidal concentration deviations which decay in time.

4.5.1 Concentration model

Here we generalize the analysis of §3.4.3 by allowing the concentration deviations to evolve in time, and so derive a simplified model for the evolution of the mean concentration field in this regime.

The stable exchange flow regime is characterized by a linear background gradient with superimposed deviations that decay. In §3.5 we found that in the limit of large aspect ratio and small, quasi-statically evolving deviations, (2.19) reduced to (3.29). Here, in the channelling regime, the deviations decay exponentially, independently of the transversely averaged concentration. We therefore generalize the analysis of §3.4.3 by allowing the deviations to evolve in time. Equation (2.18) remains the same, but (2.19) becomes

$$\frac{\partial c'}{\partial t} + u \frac{\partial \bar{c}}{\partial x} = \frac{1}{\text{Pe}} \frac{\partial^2 c'}{\partial y^2}. \quad (4.11)$$

Again, the fluid flow is assumed to be in vertical flow equilibrium and so the velocity is given by (3.27). For simplicity, we also assume $\sigma \ll 1$, although the method below can be generalized to $\sigma = O(1)$. Since $c' \ll \bar{c} = O(1)$, (3.27) can be written, to leading order, as

$$u = Rc' - \sigma \cos(2n\pi y), \quad (4.12)$$

and (4.11) becomes

$$\frac{\partial c'}{\partial t} + Rc' \frac{\partial \bar{c}}{\partial x} - \frac{1}{\text{Pe}} \frac{\partial^2 c'}{\partial y^2} = \sigma \cos(2n\pi y) \frac{\partial \bar{c}}{\partial x}. \quad (4.13)$$

When $\sigma = 0$ this exactly recovers the late-time, single-finger exchange-flow behaviour of the miscible viscous fingering instability (cf. §2.5). Solving (4.13) using separation of variables yields

$$c' = \left(\frac{-\sigma \partial \bar{c} / \partial x}{\gamma} + K e^{-\gamma t} \right) \cos(2n\pi y), \quad (4.14)$$

where $\gamma = R \partial \bar{c} / \partial x + 4n^2 \pi^2 / \text{Pe}$. The constant of integration K corresponds to the initial conditions at the onset of this regime and incorporates the nonlinear early-time spreading. A simple approximation would be that $K \approx 1/2$ corresponding to the maximum amplitude of sinusoidally varying c' .

Depending on which term is dominant in (4.14), one gets one of two limiting solutions to (2.18). When t is small, the second term in (4.14) dominates over the first. The deviations are longitudinally uniform and decay exponentially, and the solution of

(2.18) for \bar{c} is

$$\bar{c} = \frac{1}{2} - \alpha x. \quad (4.15)$$

This tendency to a steady linear profile can be seen in figure 4.5(a). When t is large, the first term dominates over the second. In this case the deviations decay quasi-steadily with the transversely averaged concentration. This case is exactly the small- β limit discussed in §3.4.3 in the limit of small σ , and is dominated by shear-enhanced dispersion. In this case \bar{c} tends to the self-similar error-function solution (3.15) with effective diffusivity (3.22). In addition, if $\sigma > R$, the first term, which scales like $O(\sigma/R)$ (given $\partial\bar{c}/\partial x \sim 1/RPe$), is always larger than $Ke^{-\gamma t}$, consistent with the fact that this channelling behaviour is only present when viscosity variations are more important than permeability variations, $R > \sigma$.

Thus far the model is unable to predict the slope of the well-mixed interior region, α . To close the model, we relate the convective flux to the mixing that occurs. We consider a control volume containing everything to the right of the midplane. Neglecting longitudinal diffusion, the total convective flux into this control volume must balance the net change in concentration

$$\int_0^T \int_0^1 uc' dy dt = \int_0^\infty \bar{c} dx \approx \frac{1}{8\alpha}, \quad (4.16)$$

where T is a timescale marking the end of this regime. Assuming the flow is always in this channelling regime, we can substitute (4.12) and (4.13) into (4.16) to attain an implicit equation for α . This control volume approach inherently depends on the choice of T ; as $T \rightarrow \infty$, the transversely averaged concentration evolves via shear-enhanced dispersion and the estimate for $\alpha \rightarrow 0$. We therefore select T at the boundary between the exchange-flow and shear-enhanced dispersion regimes such that the concentration profile is linearly well-mixed in the interior and has not transitioned to the late-time diffusive solution. For the simulations in figure 4.5, we find the choice $T = 200 \approx 3/\gamma$ appropriate, although we note that predictions are broadly insensitive to the choice of T as long as $T \sim O(1/\gamma)$.

To test the validity of this model, we compare the predicted steady interior slope, α , to the results of the 2D numerical simulations (figure 4.5(b)). As the viscosity ratio and permeability variance are increased, α decreases due to the increased fluid velocity. The model shows reasonable agreement for $K = 1/2$. If we instead fit for a single value of K across all of the simulations, we find excellent agreement with $K \approx 0.6$. This slightly larger value of K seems reasonable as the model likely underestimates the total amount of mixing since it only considered mixing due to a single Fourier mode.

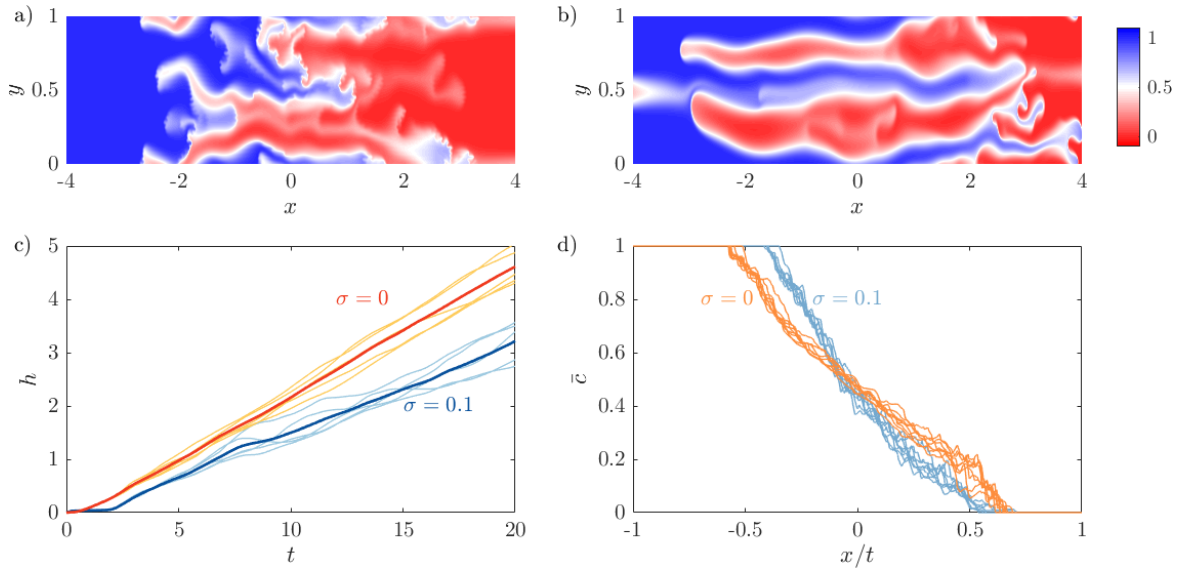


Fig. 4.6 Evolution of the concentration field for $|R| > \sigma$ and $R > 0$ in the viscous fingering across layers regime; $(R, Pe, n) = (2, 2000, 32)$. (a,b) Colourmaps of the concentration field for (a) $\sigma = 0.1$ and (b) $\sigma = 0$ at $t = 8$. (c) Plot of $h(t)$ for five different simulations each (light, thin lines) and their average (dark, thick line). (d) Plot of $\bar{c}(x, t)$ vs. the similarity variable x/t and t ranging from 6 – 20. Each curve corresponds to the average across five different simulations.

4.6 Regimes III and IV: viscous fingering across layers

As noted earlier, if $n > 1$, the channelling regime can become unstable to a viscous fingering instability which has fingers that are wider than the imposed permeability structure. The viscous fingers that develop in the heterogeneous medium are qualitatively similar to the fingers that develop in a homogeneous medium (figure 4.6(a,b)) and go through the same large-scale coarsening until a single finger remains. This single finger then evolves in similar manner to the single-finger state in a homogeneous medium ($\sigma = 0$).

One key difference between fingering in the homogeneous and the heterogeneous media is that in the heterogeneous medium there tends to be more tip-splitting, aligned with the permeability field, due to velocity heterogeneities at the finger tips as well as fading and coalescence of fingers. The fact that the fingers are more unstable leads to more variability from simulation to simulation, more intermittent flow and nonuniform growth of the mixing length (figure 4.6(c)). The concentration field evolves in qualitatively the same manner in both cases, the profile is asymmetric and again

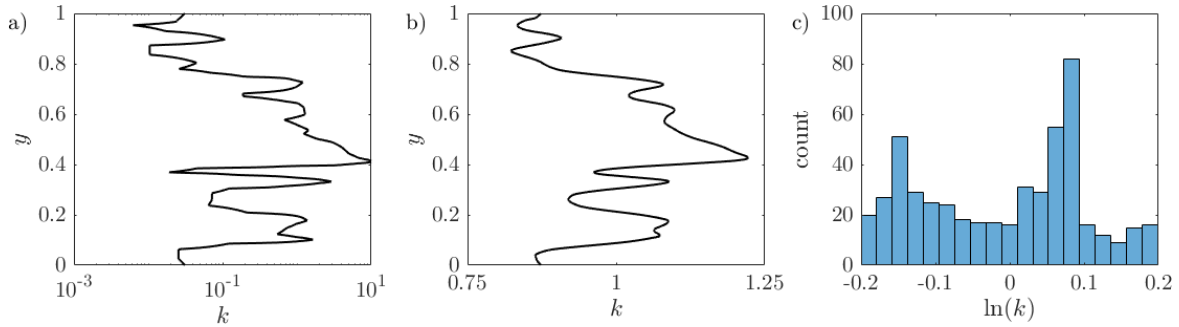


Fig. 4.7 (a) Permeability as a function of depth y at Salt Creek (Bickle et al., 2017). (b) Low-pass filtered and attenuated permeability data used in the numerical simulations. (c) Log-permeability distribution of the simulated data

has the similarity variable x/t (figure 4.6(d)). However the spreading rate is slower in the case when heterogeneities are present. Modelling the difference in spreading rate is the subject of future work.

Note that viscous fingering across layers is also possible when permeability effects dominate over viscous effects, $\sigma > R > 0$. This can occur when the system reaches the late-time regime and the interface is still hydrodynamically unstable. For the interface to be stable, the width of the mixing zone must be $h \sim RPe$ (chapter 2). When $\sigma > R > 0$, the mixing zone at the start of the late-time regime in the permeability dominated scenario is $h \sim Pe\Delta u/n^2 \sim Pe\sigma/n^2$ and so the late-time state may be unstable to further coarsening via a viscous instability if $R > \sigma^2/n^2$.

4.7 Non-sinusoidally varying permeability

Thus far, in this chapter, we have only considered the ideal scenario where the permeability variations have a single dominant wavelength. In this section we briefly consider more complex permeability fields which consist of more than one dominant wavelength. We consider two examples: a permeability field formed by superimposing two different wavelength modes, and an analogue reservoir permeability field.

For the two-mode permeability, we take k to be

$$k = Ae^{\sigma_1 \sin(2n_1\pi y) + \sigma_2 \sin(2n_2\pi y)}, \quad (4.17)$$

where A is chosen to ensure $\int_0^1 k dy = 1$. In this section we will look at one specific two-mode example namely an equal superposition of a two-layer ($n_1 = 2$) and five-layer ($n_2 = 5$) permeability field ($\sigma_1 = \sigma_2 = 0.2$). For our ‘analogue’ reservoir, we use the

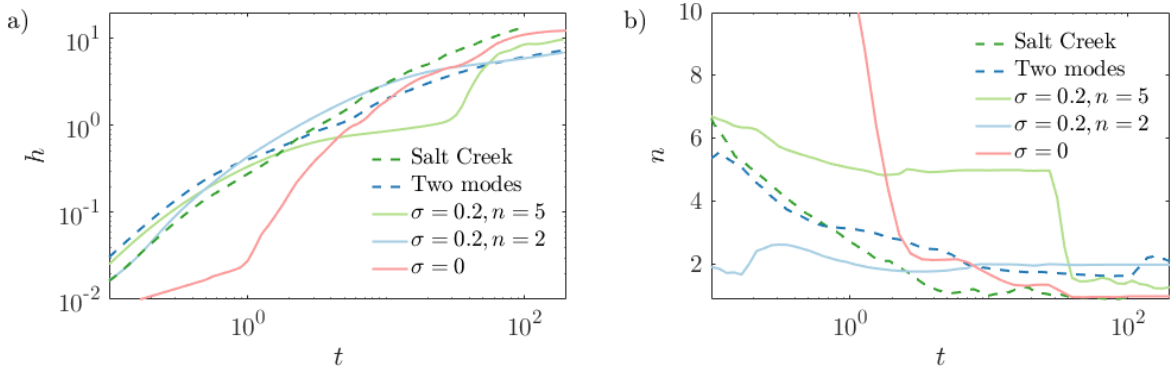


Fig. 4.8 Evolution of the (a) mixing length and (b) number of fingers, n , defined in (2.21) for $(R, Pe) = (2, 1000)$ and different permeability fields including the ‘analogue’, two-mode, single-mode and homogeneous fields.

permeability field data from a recent CO_2 sequestration experiment at Salt Creek (Bickle et al., 2017). The permeability at the injection well is given in figure 4.7(a). The permeability varies in magnitude by a factor of 100, and given we would like to consider the case where the viscosity variations are larger than the permeability variations, numerical simulations with the raw permeability data would be too difficult to perform. Instead, we derive a permeability field that contains all of the same characteristics as the Salt Creek data but with much smaller variations. To do so, we take the Fourier decomposition of the log-permeability field, remove high-frequency modes and attenuate the magnitude of all of the remaining modes. This derived data is given in figure 4.7(b). It has the same characteristic shape as the original data, but with much smaller variations. The derived log-permeability distribution is bimodally distributed, being composed of regions that have relatively large and small permeabilities. Note that our goal here is not to simulate a real reservoir but rather to consider the effect of more realistic structure variations and patterns on viscosity dominated flows.

Figure 4.8(a) shows the evolution of the mixing length for the two example permeabilities as well as the reference cases of uniform permeability and single mode variations. We find that the two-mode case initially follows an evolution comparable to the five-layer medium, but over time tends to evolve like the two-layer medium. This transition suggests that the early-time dynamics are dominated by short-wavelength variations in the permeability and the late-time dynamics are dominated by long-wavelength variations. This corresponds to resonance between the permeability field and the evolving wavelength of the viscous fingering instability. However, we note a continuous decrease in the number of fingers (figure 4.8(b)) as compared to the five-layer case, and find that superimposing two modes mostly suppresses channelling

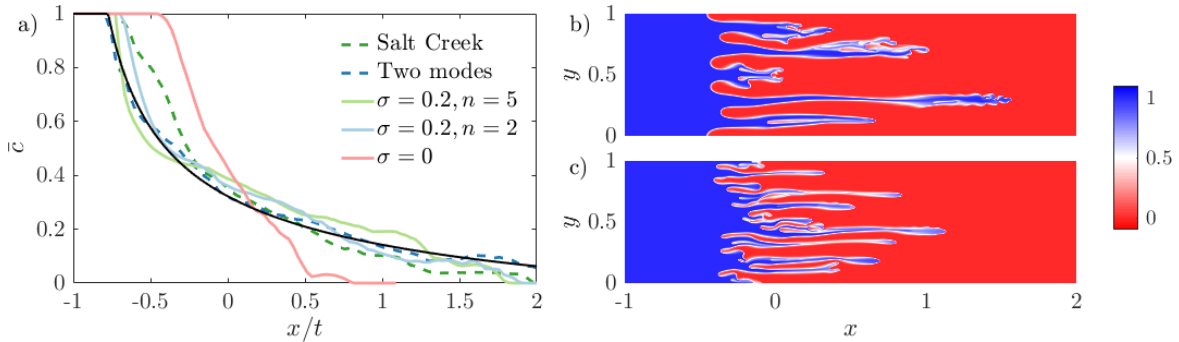


Fig. 4.9 Evolution of the concentration field for $(R, Pe) = (2, 8000)$ for different permeability fields including the derived ‘realistic’, two mode, single mode and homogeneous fields. (a) Plot of the transversely averaged concentration time-averaged from $t = 0.5$ to $t = 1$. The theoretical solution (4.9) with (4.10) is given by the black line. (b,c) Snapshots of the concentration field for the (b) two mode permeability field and (c) derived ‘realistic’ permeability field both taken at $t = 0.6$.

at the smaller wavelengths. This decrease in fingers continues until there are two dominant fingers left and the flow evolves like the two-layer case and eventually shuts down. Flows in the Salt-Creek derived permeability field show no channelling; n tends to 1 and the mixing length grows linearly in time. The growth rate of the mixing zone is much larger than viscous fingering alone in a homogeneous medium, and is larger than one would predict simply by considering the difference in permeability.

Figure 4.9(a) shows the transversely averaged concentration in the fingering regime. All four of the heterogeneous cases have much larger mixing zones compared to the homogeneous case, and similar profiles. These profiles agree with the prediction (4.9) with (4.10) derived in §4.4. This is because the permeability heterogeneities tend to change the structure of the flow. This can be seen in figure 4.9(b,c), where the backward-propagating fingers are broader and have a more uniform concentration than the forward-propagating fingers.

4.8 Discussion and Conclusions

In this chapter, the dynamics of unstable miscible displacements in layered heterogeneous porous media were examined. A series of different regimes were identified that arise due to the interplay between viscous fingering, which tends to cascade through a range of length-scales, and the permeability structure, which has a fixed length scale. Overall, depending on which regime the flow is in, the permeability heterogeneity can either enhance or temper spreading relative to the uniform permeability case.

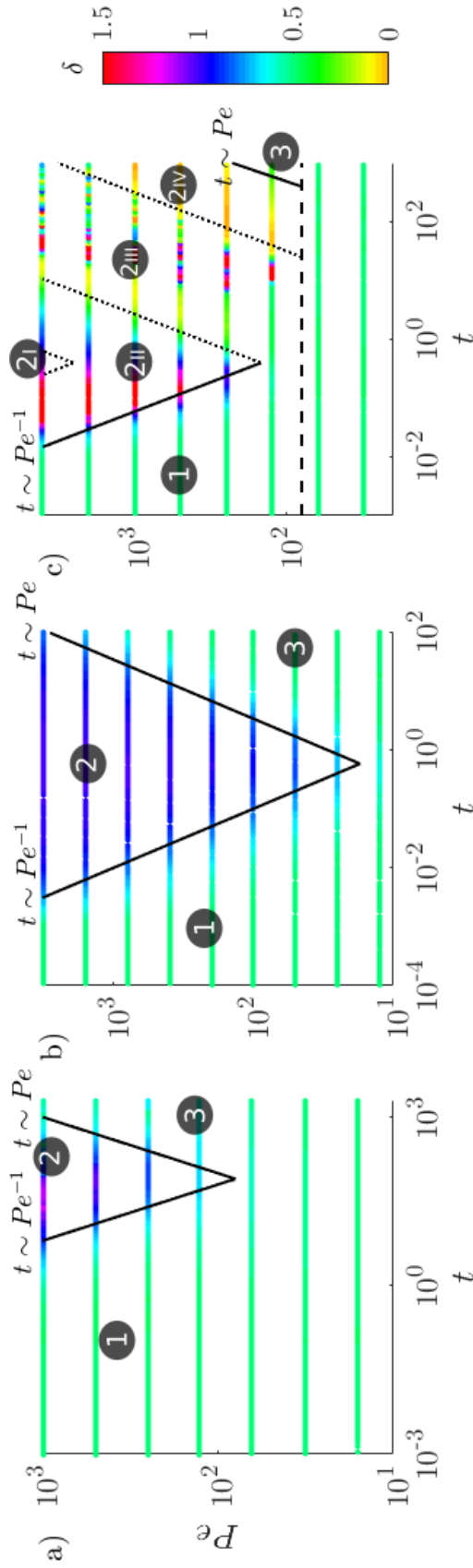


Fig. 4.10 Representative plots of the scaling exponent of the mixing length, δ , found by locally fitting a power-law of the form $h = At^\delta$, for three different parameter sets: (a) $(R, \sigma, n) = (0.1, 1, 1)$, demonstrating a viscously-dominated stable displacement, as in §3.5, (b) $(R, \sigma, n) = (-2, 0.1, 1)$, demonstrating a permeability-dominated displacement, as in §3.4 and (c) $(R, \sigma, n) = (2, 0.1, 6)$, demonstrating a viscously-dominated unstable displacement, as in §4.3. The regime boundaries (black lines) divide the early-time (1), intermediate-time (2) and late-time (3) regimes. The dotted lines in (c) delineate the various intermediate time regimes (§4.4-§4.6) and the dashed line delineates the hydrodynamically stable and unstable regions (Nijjer et al., 2018).

Figure 4.10 summarizes the different possible regimes for viscously-dominated unstable displacements (figure 4.10(c)) as well as viscously-dominated stable displacements (figure 4.10(a); §3.5) and permeability dominated displacements (figure 4.10(b); §3.3). In each case the figure shows the instantaneous scaling exponent of the mixing length, δ , where $h = At^\delta$, for different Pe. At early times (regime 1 in figure 4.10), the concentration field evolves through diffusion across an initially sharp interface ($\delta = 1/2$). Once advection begins to outpace diffusion ($t \sim O(1/Pe)$) the flow transitions to the intermediate-time regime. At intermediate times (regime 2 in figure 4.10), depending on the relative size of the viscosity and permeability variations, a range of possible dynamics ($\delta \neq 1/2$) are possible. At late times (regime 3 in figure 4.10), once the concentration field has become transversely homogenized, transport becomes dominated by shear-enhanced dispersion ($\delta = 1/2$).

For unstable displacements considered in this chapter, a number of different intermediate-time regimes were identified (regimes 2I, 2II, 2III and 2IV in figure 4.10 (c)), which arise due to the interplay between the viscous fingering length scale and the permeability length scale. First, fingering occurs within the permeability layers (regime 2I; §4.4) and the fingers coarsen until they coincide with the imposed permeability structure. Then the fingers stop coarsening and instead channel along the imposed permeability while diffusing causing the fingers to slow down (regime 2II; §4.5). If the permeability field consists of more than one dominant wavelength, this channeling regime can be suppressed (§4.7). The interface then becomes unstable to fingering across layers before tending to a single finger, which ultimately slows leaving a well-mixed interior (regimes 2III, 2IV; §4.6). Overall, depending on which regime the flow is in, the permeability heterogeneity can either enhance or temper spreading relative to the uniform permeability case.

Together with chapter 3, the effect of viscosity and permeability variations on the structure and evolution of miscible displacements in porous media was examined. At early times, transport is diffusively dominated and independent of both the viscosity and permeability, at intermediate times, transport is sensitive to both the viscosity and permeability, and depends on the relative size of their variations and whether the injected fluid is more or less viscous than the ambient fluid, and at late times transport is dominated by shear-enhanced dispersion which only depends on the permeability variations. In each case, by identifying the dominant physics in each of the regimes, simple models that capture the average behaviour of these systems were developed.

Chapter 5

Miscible displacements with gravity override

In the previous chapters, the two fluids only differed in viscosity, while all other physical properties were assumed equal. However, in many geological settings, such as carbon capture and storage, the density difference between the two fluids can be important to understanding their mixing and spreading (Huppert, 2006). Thus, in this chapter, the role of density as well as viscosity differences on the evolution of the displacement front is examined.

Gravity currents in porous media have been studied in a wide array of contexts including geological storage of carbon dioxide (Bickle et al., 2007; Boait et al., 2012), geothermal power generation (Woods, 1999), contaminant migration (Simmons et al., 2001) and coastal aquifer dynamics (Fleury et al., 2007). When a denser (lighter) fluid displaces another in a porous medium, the density difference causes the injected fluid to preferentially tilt and flow along the bottom (top) boundary. Huppert and Woods (1995) studied this problem assuming the fluids had constant viscosity, the flow was purely horizontal (vertical-flow equilibrium) and there was no mixing between the fluids (sharp-interface limit). They found that the interface between the two fluids tilted, leading to self-similar spreading of the fluids. More recently, the effects of diffusion and vertical flow were considered by Szulczewski and Juanes (2013). When the two fluids were fully miscible, and vertical flow was accounted for, it was found that a series of different regimes arose depending on the dominant physical balances. At intermediate times they found that diffusion and vertical flow could be neglected and reproduced the dynamics outlined by Huppert and Woods (1995); however, at early and late times, diffusion played a dominant role in mixing and spreading.

In addition to having different densities, the two fluids can also have different viscosities, a fact neglected by Huppert and Woods (1995) and Szulczewski and Juanes (2013). Hesse et al. (2007), Pegler et al. (2014), and Zheng et al. (2015a) extended the work of (Huppert and Woods, 1995) to study the effect of differing viscosities and densities on the evolution of the displacement front in the limit of sharp interfaces and vertical-flow equilibrium. They found that when the height of the current was comparable to the height of the medium, viscosity played a dominant role in setting the spreading rate of the gravity current, leading to significantly enhanced spreading if the injected fluid was less viscous than the ambient fluid, or reduced spreading if the injected fluid was more viscous than the ambient fluid. However, similar to Huppert and Woods (1995), these works also omit the effects of diffusion and vertical flow. Furthermore, these studies also assumed that the interface between the two fluids is hydrodynamically stable; however, as demonstrated in the previous chapters, when a less-viscous fluid is injected into a more-viscous one, viscous fingering can develop and lead to the interpenetration of the two fluids and a highly non-trivial interface. Thus far, the effect of viscous fingering on mixing and spreading in depth-integrated gravity current models is not well understood.

In a similar vein, a number of authors have looked at the effect of gravity on the viscous fingering instability. Rogerson and Meiburg (1993b) studied the onset of the viscous fingering instability with a gravitationally-driven shear parallel to the interface using linear stability analysis; Rogerson and Meiburg (1993a), Tchelepi et al. (2004), Tchelepi and Orr Jr. (1994), Ruith and Meiburg (2000), Camhi et al. (2000), and Riaz and Meiburg (2003) investigated the nonlinear evolution of the fingering instability using numerical simulations; and Tchelepi and Orr Jr. (1994), and Berg et al. (2010) examined the nonlinear evolution of the fingering instability using laboratory experiments. While these studies highlight some of the interesting qualitative behaviour that can be observed, they do not provide a full overview of the different dynamical regimes, nor do they provide quantitative predictions for the evolution of the spreading and mixing. Furthermore, in all of the work discussed above, the long-time asymptotic behaviour, where mixing is important, is neglected.

The overarching aim of this chapter is to bridge the gap between these two different bodies of work, namely reduced-order modelling and high-resolution numerical modelling to develop a quantitative understanding of the full life cycle of miscible displacements with gravity override.

This chapter is laid out as follows. In §5.1, the problem is briefly outlined as it is similar to the problems discussed in the previous chapters. In §5.2 two limiting

are given in dimensionless form as

$$-(u+1)\mu = \frac{\partial p}{\partial x}, \quad -v\mu = \left(\frac{\partial p}{\partial y} + G\rho \right), \quad (5.2)$$

$$\frac{\partial u}{\partial x} + \frac{\partial v}{\partial y} = 0, \quad (5.3)$$

$$\frac{\partial c}{\partial t} + u \frac{\partial c}{\partial x} + v \frac{\partial c}{\partial y} = \frac{1}{\text{Pe}} \left(\frac{\partial^2 c}{\partial x^2} + \frac{\partial^2 c}{\partial y^2} \right), \quad (5.4)$$

$$\mu(c) = e^{-Rc}, \quad (5.5)$$

$$\rho = \frac{\rho_2}{\rho_1 - \rho_2} + c, \quad (5.6)$$

where we have non-dimensionalized the density by $\rho_1 - \rho_2$. Note that as before the velocity is given relative to a moving frame which travels with the average speed of the injected fluid. We rescale the pressure, p to be the pressure in excess of the hydrostatic pressure of the ambient fluid, $\tilde{p} = p - G\rho_2 y / (\rho_1 - \rho_2)$, in which case (5.2) becomes

$$-(u+1)\mu = \frac{\partial \tilde{p}}{\partial x}, \quad -v\mu = \left(\frac{\partial \tilde{p}}{\partial y} + Gc \right). \quad (5.7)$$

For notational convenience we drop the tildes in all subsequent expressions.

There are three important non-dimensional parameters in this problem:

$$G = \frac{g(\rho_1 - \rho_2)ka}{Q\mu_2}, \quad R = \log(\mu_2/\mu_1), \quad \text{Pe} = \frac{Q}{D}. \quad (5.8)$$

The gravity number, G , measures the ratio of pressures due to density differences and those due to injection. Alternatively, it can be interpreted as a ratio of the rise/fall velocity due to gravity, to the injection velocity. We only consider $G > 0$ since $G < 0$ is equivalent to $G > 0$ with a vertical reflection of the coordinate system $y \rightarrow -y$. Note that in related convection problems the strength of the gravitational force is often defined in terms of a Rayleigh number, $Ra = g(\rho_2 - \rho_1)ka/D\mu_2$ (Hewitt et al., 2012), which is equal to $G\text{Pe}$. In this chapter, we will only consider the case $R > 0$, that is, when the injected fluid is less-viscous than the ambient fluid, and we will focus predominantly on the geologically relevant limit, $\text{Pe} \gg 1$.

Similar to the work in the previous chapters, we consider flows where the upstream and downstream flux (in the moving frame) as well as the transverse velocity are zero:

$$\frac{\partial c}{\partial x} \rightarrow 0 \quad \text{as} \quad x \rightarrow \pm\infty, \quad (5.9)$$

$$\int_0^1 u \, dy \rightarrow 0 \quad \text{as} \quad x \rightarrow \pm\infty, \quad (5.10)$$

$$v \rightarrow 0 \quad \text{as} \quad x \rightarrow \pm\infty. \quad (5.11)$$

The latter constraint is equivalent to a hydrostatic farfield pressure. In contrast to the work in the previous chapters, we consider flows with no-flux boundary conditions along the top and bottom boundaries instead of periodic boundary conditions,

$$\frac{\partial c}{\partial y} = 0 \quad \text{for} \quad y = 0, 1, \quad (5.12)$$

$$v(x, 0, t) = v(x, 1, t) = 0. \quad (5.13)$$

We impose no-flux rather than periodic boundary conditions as there is no longer a natural vertical symmetry in this problem (Rogerson and Meiburg, 1993a; Ruith and Meiburg, 2000). We initialize the concentration field to have a step jump,

$$c(x, t = 0) = c_0(x) = H(-x), \quad (5.14)$$

where $H(x)$ is the Heaviside function. We solve (5.3)-(5.7) numerically along with boundary conditions (5.12)-(5.13) and initial condition (5.14) (for more details see appendix A).

Again, in analyzing the large-scale behaviour of the flow, we focus on the evolution of the transversely averaged concentration $\bar{c}(x, t) = \int_0^1 c \, dy$ and the mixing length $h(t)$ (3.11). In addition we also define the Nusselt number as the convective transport through the midplane (travelling with the mean injection velocity),

$$\text{Nu} = \int_0^1 u c \, dy = \int_0^1 u c' \, dy, \quad (5.15)$$

which we use to quantify the rate of mixing. Note that this is equivalent to the flux, F , defined in chapter 2 by (2.47).

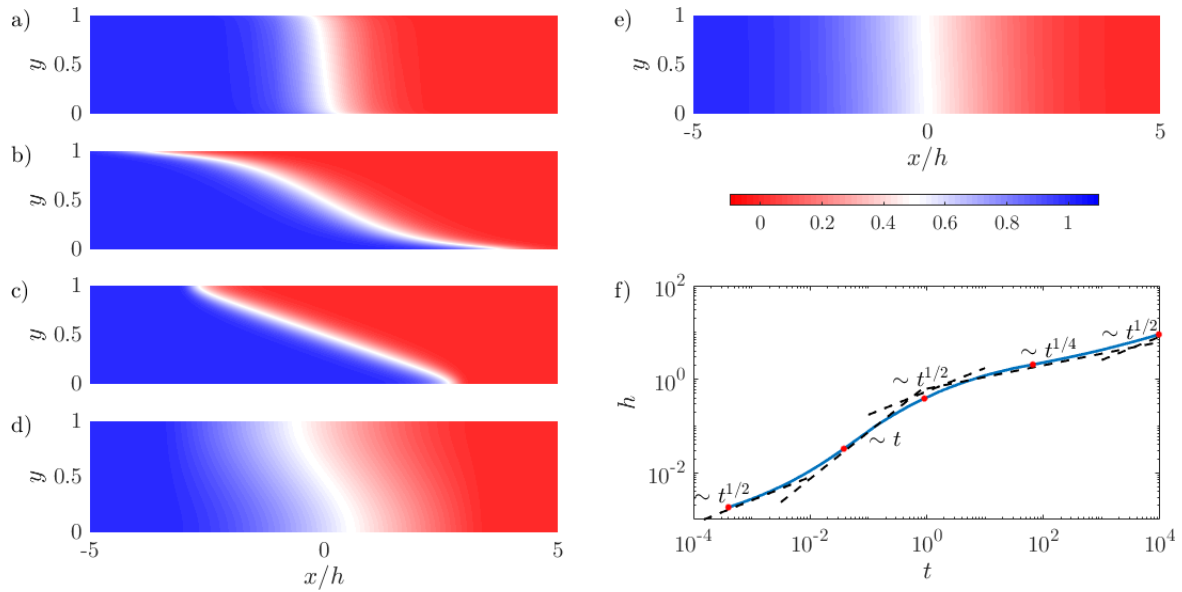


Fig. 5.2 Evolution of the concentration field for $R = 0$ and $(G, \text{Pe}) = (3, 100)$. (a-e) Plots of the concentration field vs. x/h and y at (a) $t = 1 \times 10^{-4}$, (b) $t = 0.036$, (c) $t = 0.83$, (d) $t = 57$ (e) $t = 8000$. (f) Evolution of the mixing length, h , as a function of time, t . The dots correspond to the snapshots (a-e) and the dashed lines correspond to the theoretical predictions from Szulczewski and Juanes (2013).

5.2 Limiting cases

In this section, we consider two limiting cases: the uniform viscosity case (log-viscosity ratio $R = 0$) where the fluids differ only in density, and the uniform density case (gravity number $G = 0$) where the fluids differ only in viscosity.

5.2.1 Uniform viscosity, $R = 0$

When $R = 0$ the problem reduces to the uniform viscosity gravity current problem studied by Szulczewski and Juanes (2013). Snapshots of the concentration field from a representative simulation are given in figure 5.2(a-e). In general, the density difference between the two fluids causes the interface to tilt, with the denser injected fluid travelling along the bottom boundary, which aids the spreading and mixing of the two fluids. To quantify this spreading, we plot the evolution of the mixing length h in figure 5.2(f) along with the corresponding theoretical predictions. In general we find that the mixing length grows in time through five different regimes, each with different power-law growth rates.

First, as was the case in chapters 2-4, the concentration field is vertically homogeneous, and longitudinal diffusion dominates, leading to $h \sim t^{1/2}$ (figures 5.2(a,f)). Second, once diffusion becomes unimportant, occurring at a time $t \sim O(1/G^2\text{Pe})$, the interface slumps due to gravity. Vertical flow in this regime is important because initially the vertical length scale of the mixing zone is larger than the horizontal scale. This leads to so-called S-shaped slumping and linear growth of the mixing zone, $h \sim t$ (figures 5.2(b,f)). Third, once the interface has become long and thin, occurring at a time $t \sim O(1/G)$ vertical flow becomes unimportant and the flow is predominantly horizontal. The interface continues to slump due to gravity and takes on a characteristic straight-line profile (figure 5.2(c)). The mixing length grows sublinearly, $h \sim t^{1/2}$, since the hydrostatic pressure gradient, which drives the flow, diminishes as the interface slumps (figure 5.2(f)). Fourth, once the interface has become even longer and thinner, occurring at a time $O(\text{Pe})$, transverse diffusion becomes important. A balance between horizontal advection and transverse diffusion results in net horizontal transport analogous to the shear-enhanced dispersion discussed in chapter 3. However, because the horizontal velocity is proportional to the horizontal gradient in concentration, the transport is subdiffusive, $h \sim t^{1/4}$ (figures 5.2(d,f)). Fifth, once the shear-enhanced dispersivity becomes small compared to molecular diffusion, occurring at a time $t \sim O(G^2\text{Pe}^3)$, the interface grows diffusively again, $h \sim t^{1/2}$ (figures 5.2(e,f)).

5.2.2 Uniform density, $G = 0$

When $G = 0$, the problem reduces to the miscible viscous fingering problem described in chapter 2. The only difference here is that no-penetration conditions are imposed along the top and bottom boundaries instead of periodic boundary conditions. We find that up until the late-time regime, this difference in boundary conditions has little effect on the dynamics. To recap, at early times the interface grows diffusively, $h \sim t^{1/2}$, while the instability grows exponentially (figures 5.3(a,f)). At intermediate times, the instability saturates, fingers elongate and interact nonlinearly leading to coarsening and advective growth of the mixing zone, $h \sim t$ (figures 5.3(b,f)). At late times, a single dominant finger is left in the centre of the domain with counter-propagating fingers along the top and bottom boundaries (figure 5.3(c)). The fingers eventually slow leaving a well-mixed interior, $h \rightarrow \text{const.}$ (figures 5.3(d,f)).

With the addition of no-penetration top and bottom boundaries, as the single-finger exchange-flow decays, a pair of wider counter-propagating fingers manifest themselves along the boundaries (figures 5.3(e,f)). This is because, in contrast to the case with periodic boundaries, a half wavelength mode is now permissible. Since this mode is

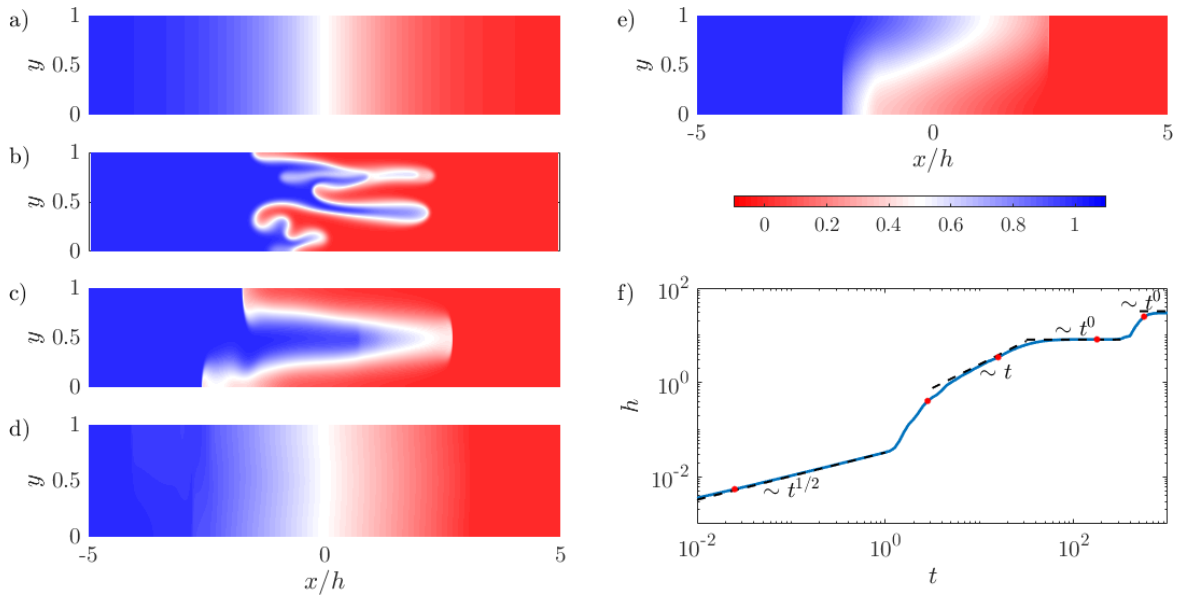


Fig. 5.3 Evolution of the concentration field for $G = 0$ and $(R, Pe) = (2.5, 500)$. (a-e) Plots of the concentration field vs. x/h and y at (a) $t = 2 \times 10^{-2}$, (b) $t = 2.6$, (c) $t = 15$, (d) $t = 170$ (e) $t = 525$. (f) Evolution of the mixing length, h , as a function of time, t . The dots correspond to the snapshots (a-e) and the dashed lines correspond to the theoretical predictions from Nijjer et al. (2018).

wider, it decays more slowly and is still unstable once the central propagating finger decays away. This mode decays four times more slowly and spreads four times further but also eventually decays away. We find that in the absence of any density differences, the fingers cannot nonlinearly coarsen directly to the half wavelength state, and instead the fingers always coalesce in the middle of the domain and decay before the secondary instability is triggered. This is due to the merging mechanism which symmetrically forces forward-moving fingers towards one another, thereby ‘pulling’ the fingers that may be initially propagating along the boundaries away from them. As we will see later, this is not the case when gravity is present as the gravitational forces introduce preferential merging of fingers along the boundaries.

The temporal scalings for the early- to intermediate-time transition and intermediate- to late-time transitions are as before, occurring at times $t \sim O(1/R^2 Pe)$ and $t \sim O(Pe)$ respectively. However, there is an additional time-transition to the half-wavelength mode which occurs at a time $t \sim O(Pe)$ as well, but with a larger pre-factor.

5.2.3 Comparison of the two limiting cases

There are a number of similarities between the two limiting cases discussed. In both cases, the early-time dynamics are dominated by longitudinal diffusion. At intermediate times diffusion becomes unimportant and spreading and mixing is dominated by advection. Initially vertical flow is important but, as the interface is stretched longitudinally, the flow becomes predominantly horizontal. At late times, there is a balance between horizontal advection and transverse diffusion leading to a slow down in the flow.

Despite these similarities, the manner in which the systems evolve are very different. In the uniform viscosity case, there are no hydrodynamic instabilities and the dynamics are insensitive to small changes in the initial conditions, while in the uniform density case, the interface fingers chaotically which is highly sensitive to the initial conditions. At intermediate times, in the uniform viscosity case, the mixing length first grows like $h \sim t$ then like $h \sim t^{1/2}$ while in the uniform density case the mixing length grows like $h \sim t$. At late times, the mixing length grows like $h \sim t^{1/4}$ in the uniform viscosity case but tends to a constant in uniform density case. In the uniform viscosity case, the dynamics are decoupled and independent of the injection flux, whereas in the uniform density case, injection is critical to the formation of fingers. The aim of the remainder of this chapter is to outline how the aforementioned similarities and differences evolve as both the viscosity and density are varied away from the limiting cases.

5.3 Overall dynamics

Consider the case where both the density and viscosity vary ($G \neq 0, R \neq 0$). Depending on the choice of parameters, a range of different behaviours are possible. In figure 5.4, we show a series of snapshots in time of the concentration field for a large and a small value of G , each showing a range of different dynamics. In both cases the interface is stretched longitudinally and eventually becomes well-mixed; however, the manner in which the flow reaches this state depends on G .

At early times, in both cases, molecular diffusion dominates the dynamics. The interface then slumps due to gravity, forming a pair of tongues along the top and bottom boundaries, with the effect being more pronounced for larger G (figure 5.4(a,b)). The slumping is asymmetric, due to the viscosity difference, as the forward propagating tongue propagates much faster than the backward propagating tongue (figure 5.4(b)). At intermediate times, depending on the relative magnitudes of G , and R (and Pe), the interface can finger (figure 5.4(c)) or not finger (figure 5.4(d)). When the interface

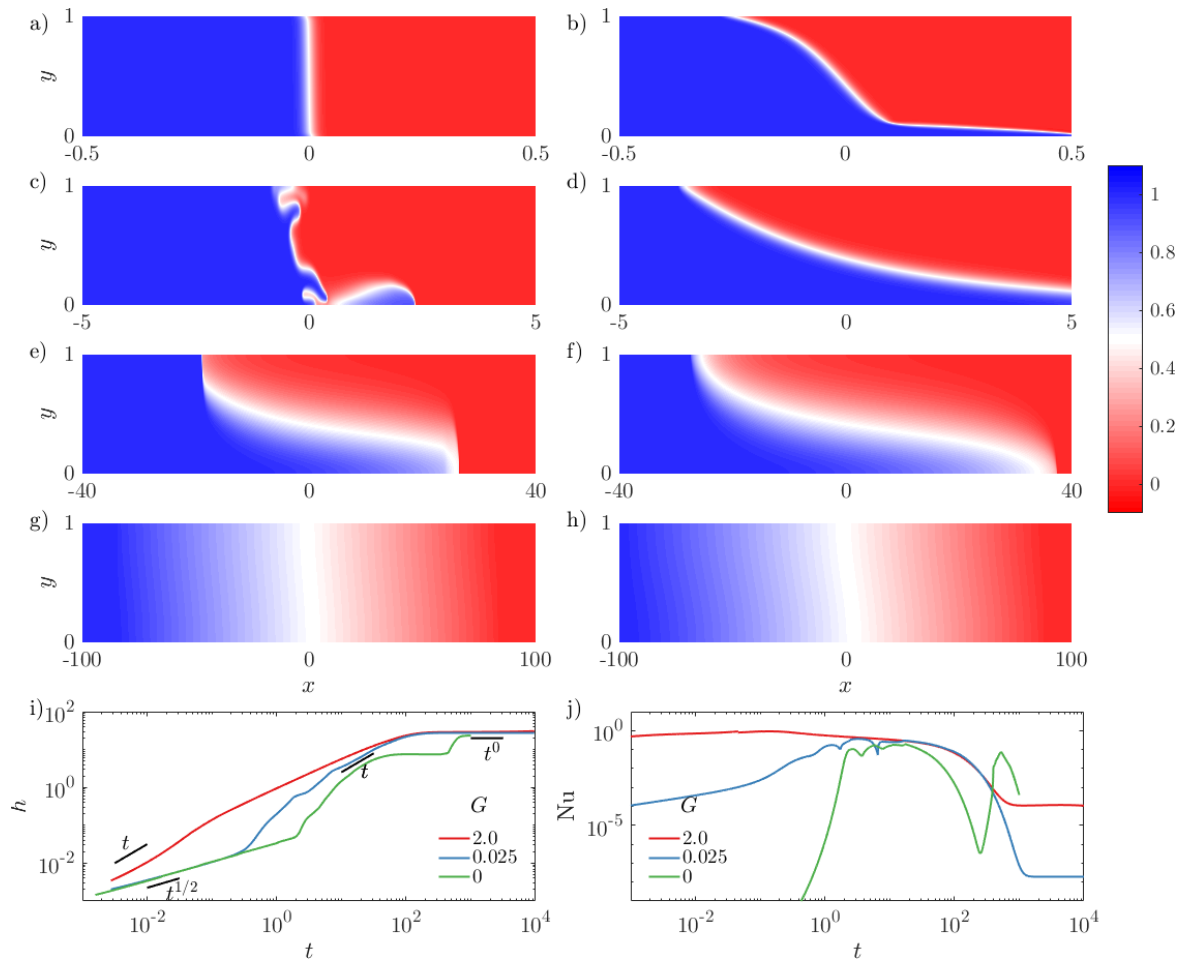


Fig. 5.4 Colourmaps of the concentration field for $(R, Pe) = (2, 500)$ and (a,c,e,g) $G = 0.025$, (b,d,f,h) $G = 2$. The snapshots are taken at times (a,b) $t = 0.05$, (c,d) $t = 2$, (e,f) $t = 30$, and (g,h) $t = 500$. Evolution of (i) the mixing length, h and (j) the Nusselt number, Nu , for the same parameters as (a-h).

fingers, the fluid spreads more slowly as compared to the non-fingered case (figure 5.4(i,j)). Eventually, the fingered interface coarsens until a pair of counter-propagating currents remain which resemble the non-fingered case (figure 5.4(e,f)). At late times, in both cases, the interface becomes vertically homogenized and the growth of the mixing zone slows and tends to the same value (figure 5.4(g,h)). This is analagous to the shutdown of the viscous fingering instability in the $G = 0$ limit. Eventually, horizontal advective transport becomes dominated by Taylor-dispersion, analagous to the $R = 0$ limit, driven by horizontal gradients in c . This too also becomes negligible over very long times and molecular diffusion dominates again.

Figure 5.4(i) shows the evolution of mixing length for large G , small G , and zero G . When G is large, the mixing length initially grows like t , in a manner analogous to the slumping regime in the uniform viscosity case. The mixing length then grows with a scaling exponent less than 1 before tending to a constant mixing length. When G is small, the dynamics are similar to the uniform density case $G = 0$: the mixing length initially grows diffusively, then advectively, before tending to a constant. However, the nonlinear regime is reached earlier, the pre-factor in the fingering regime is larger, and the fingers coarsen directly to the half wavelength mode. In general, increasing G leads to initially faster growth, but all three examples tend to nearly the same constant mixing length. Over longer times the mixing length grows due to shear-enhanced dispersion and $h \sim t^{1/4}$ (not shown), which increases with G and over even longer times the mixing length grows due to longitudinal diffusion and $h \sim t^{1/2}$, independent of G .

Figure 5.4(j) shows the evolution of the convective flux through the midplane, Nu . When G is large, the convective flux starts at a maximum and initially decays slowly. After about $t = 30$, the decay rate increases, characteristic of exponential decay of the flux, before tending to a constant. When G is small, the convective flux initially exhibits power-law growth, then exponential growth, before saturating and fluctuating about constant value. Eventually the flux coincides with the large G case and decays in the same way, before tending to a smaller constant. The constant flux corresponds to the shear-enhanced dispersive flux driven by density differences between the two fluids. Over very long times (not shown), the convective flux decays to zero as the fluids become more mixed. For comparison we show the uniform density case $G = 0$, which grows exponentially, fluctuates about a constant and exponentially decays, before growing again as the single finger state becomes unstable as discussed in §5.2.2.

In the following sections we discuss the different regimes that are possible in more detail. We neglect a discussion of the early-time diffusive regime as the evolution is the same as that described in §3.3.1.

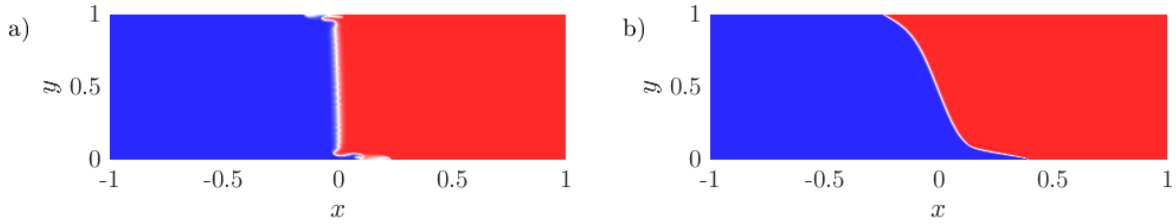


Fig. 5.5 Colourmaps of the concentration field in the slumping regime for $(R, Pe) = (1, 4000)$ and $(G, t) =$ (a) $(0.02, 0.6)$ and (b) $(2, 0.07)$.

5.4 Slumping regime

Once advection begins to outpace diffusion, the interface slumps along the boundaries. This leads to localized regions of fast flow but little motion away from the boundaries. When G is small, small fingers, comparable to the fingering instability, grow along the top and bottom boundaries while fingers along the rest of the interface grow more slowly (figure 5.5(a)). This preference for fingering along the boundaries occurs because the difference in density leads to slumping which preferentially perturbs the instability along the boundaries. In this case the density difference perturbs the interface but the growth of the fingers is still dominated by viscous effects. We therefore expect that the mixing zone grows like $h \sim Rt$ (cf. §2.3.1). This rescaling does a reasonable job of collapsing the data for $G \ll 1$ (figure 5.6(b)) and the transition time only weakly depends on G . Note that even when G is small, the initial growth of the mixing zone is significantly enhanced when compared to the uniform density case (figure 5.6(b)).

When G is large, the interface slumps on a larger scale which is much faster than the growth of the instability. This form of slumping is analogous to the equal viscosity case (§5.2.1); however, because the injected fluid is less-viscous, the forward propagating tongue travels faster than the backward propagating tongue, leading to asymmetric slumping (figure 5.5(b)). We expect that in this regime the mixing zone grows like $h \sim Gt$. This rescaling does a reasonable job of collapsing the data for $G > O(1)$ (figure 5.6(b)) and the transition time depends only weakly on R .

5.5 Intermediate-time fingering and gravity current regime

As was seen in figure 5.4(c,d), two different interface morphologies are possible at intermediate times. The interface can either finger chaotically or be stabilized depending on the size of G . Either way, at intermediate times this leads to asymmetric spreading,

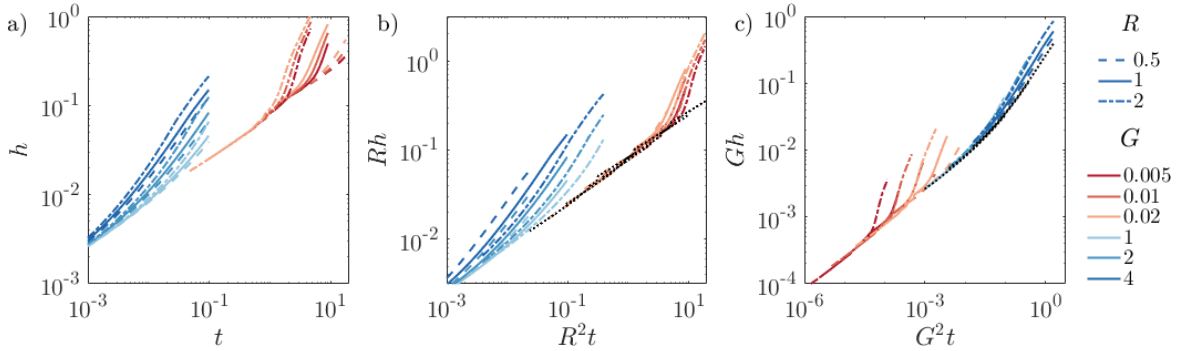


Fig. 5.6 Plots of $h(t)$ for $Pe = 100$, $G = \{0.005, 0.01, 0.02, 1, 2, 4\}$ and $R = \{0.5, 1, 2\}$. The raw data is plotted in (a). (b) The mixing length rescaled by the predicted scalings for the small- G slumping limit. The dotted lines denote simulations with $G = 0$, $Pe = 100$ and $R = \{0.5, 1, 2\}$. (c) The mixing length rescaled by the predicted scalings for the large- G slumping limit. The dotted lines denote simulations with $R = 0$, $Pe = 100$ and $G = \{1, 2, 4\}$.

with the forward-propagating region travelling faster than the backward-propagating region. However, the fingered interface tends to mix the fluids more rapidly and leads to slower spreading. In both cases, the Nusselt number is nearly constant (figure 5.4(j)), and the mixing zone grows nearly linearly in time (figure 5.4(i)).

5.5.1 Gravity stabilization of viscous fingering

Figure 5.7 compares the morphology of the interface for simulations with $(R, Pe) = (1, 4000)$ and different G . As G is increased, the interface goes from fingering chaotically to propagating as a smooth current. This is in qualitative agreement with Rogerson and Meiburg (1993b), who found that tangential shearing can stabilize the interface.

The interface morphology has a pronounced effect on the spreading and mixing of the fluids. When G is small ($G < 0.1$ for the parameters in figure 5.7), the interface fingers and the mixing zone grows linearly in time, with a rate that is insensitive to G . This is analogous to the uniform density limit $G = 0$. As G is increased, there is an abrupt change in the morphology. The mixing zone still grows linearly in time but with a larger growth rate that is also insensitive to G (figure 5.7(g)). The change in morphology is also reflected in the evolution of the Nusselt number which tends to converge to one of two limits (figure 5.7(h)). This qualitatively agrees with the findings of Berg et al. (2010), who found an abrupt change in breakthrough times (the time it takes for the injected fluid to transit a fixed length) as G was varied. For much larger values of G (not shown), the mixing zone grows like $t^{1/2}$ in a manner analogous to the uniform viscosity limit $R = 0$.

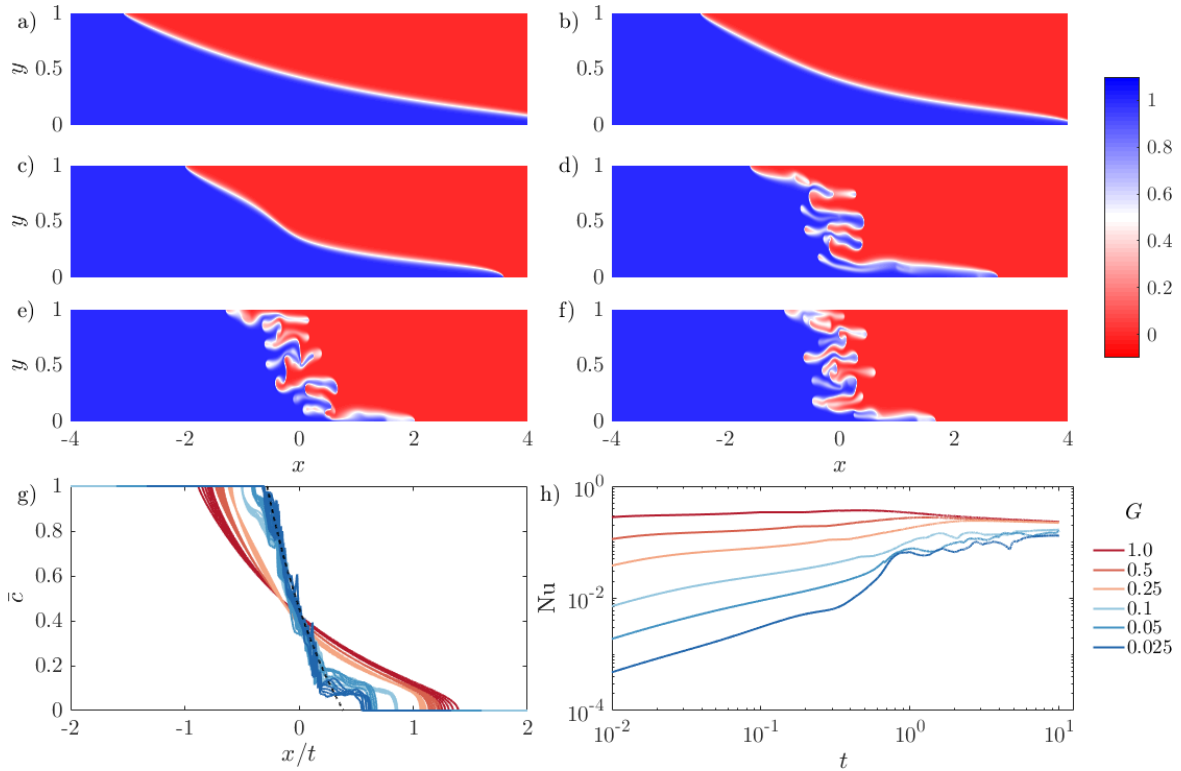


Fig. 5.7 Colourmaps of the concentration field for $(R, Pe) = (1, 4000)$ at $t = 1$ and $G =$ (a) 1, (b) 0.5, (c) 0.25, (d) 0.1, (e) 0.05, and (f) 0.025. (g) The transversely averaged concentration, \bar{c} against the similarity variable x/t along with the $G = 0$ theoretical solution (2.37) with (2.40) (dashed line). (h) $Nu(t)$ for different values of G .

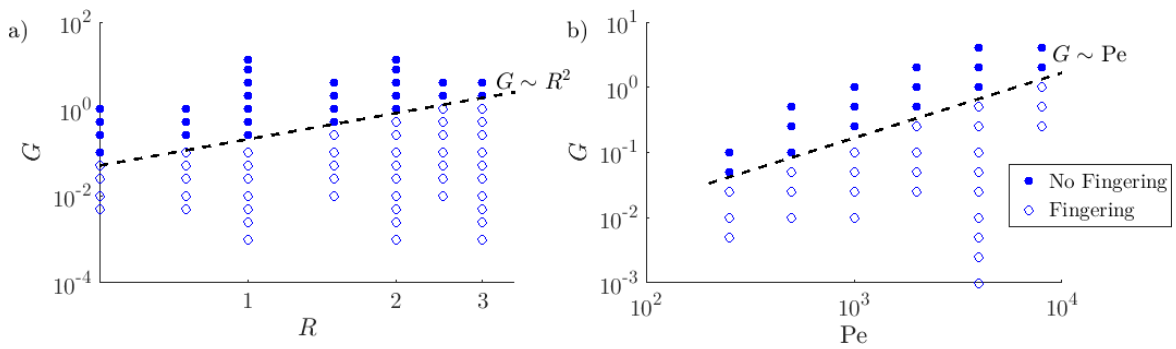


Fig. 5.8 Stable vs. unstable displacements for (a) $Pe = 4000$ and (b) $R = 2$. Filled circles denote simulations where no fingers were observed during the entire length of the simulations, while unfilled circles denote simulations where fingers were observed for at least some portion of the simulation. Dashed lines show predicting stability boundaries $G \sim R^2Pe$.

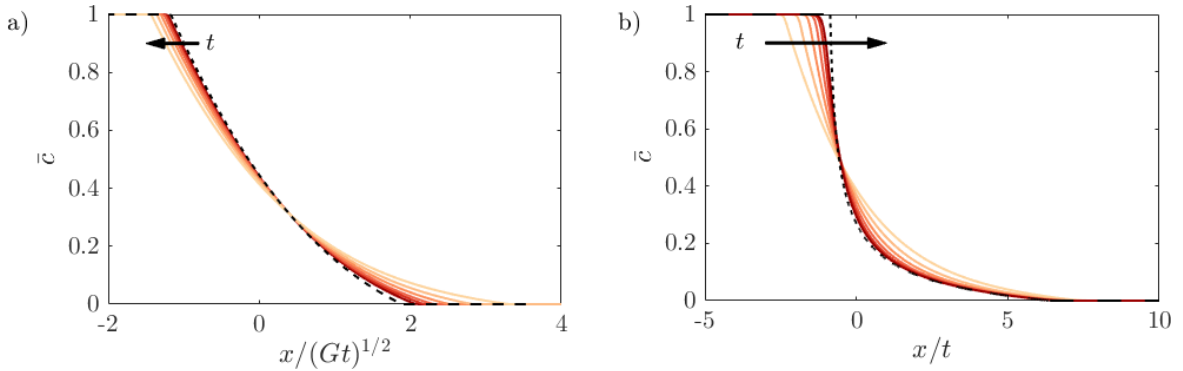


Fig. 5.9 Evolution of the transversely averaged concentration (or equivalently the height of the current above the base) found by solving (5.20) for (a) small-times, $(R, G) = (2, 8)$ and t ranging logarithmically from 0.03 to 1 and (b) large-times, $(R, G) = (2, 2)$ and t ranging logarithmically from 1 to 32. The small-time asymptotic limit found by solving (5.21) and large-time asymptotic limit (5.22) are given by dashed black lines.

To understand the transition from the fingered interface to the smooth current requires comparing the time-scale of the growth of the instability ($O(1/R^2\text{Pe})$) with the rise/fall time of the fluid ($O(1/G)$). If the fluid falls/rises to the boundary faster than the instability can grow, the instability will be suppressed. This suggests that when $G > O(R^2\text{Pe})$, the interface will always spread as a gravity current and will not finger. Figure 5.8 maps the stability boundary in $G - R$ and $G - \text{Pe}$ phases spaces. We find the transition occurs when $G \approx 5 \times 10^{-5} R^2\text{Pe}$ in agreement with the simple scaling argument, where the pre-factor is determined by fitting the numerical results.

5.5.2 Concentration model

At intermediate times, the interface is long and thin and the flow is predominantly horizontal. For small G , the interface fingers, and the transversely averaged concentration evolves similar to the uniform density limit (figure 5.7(g)), for moderate G , the interface is stable, the transversely averaged concentration has the same shape but much larger horizontal extent (figure 5.7(g)), and for large G , the interface is also stable but the transversely averaged concentration is nearly linear (figure 5.10(a)) and the horizontal extent evolves diffusively rather than advectively. In all cases, the horizontal scale is larger than the vertical scale and longitudinal diffusion is negligible.

Combining (5.7), (5.3) and (5.5), assuming the flow is in ‘vertical flow equilibrium,’ that is the flow is long and thin and that vertical gradients in the pressure are small,

gives

$$\frac{du}{dy} - R \frac{\partial c}{\partial y} u = R \frac{\partial c}{\partial y} + G e^{Rc} \frac{\partial c}{\partial x}. \quad (5.16)$$

Integrating with respect to y and imposing no net horizontal flow ($\int_0^1 u dy = 0$),

$$u = \frac{e^{Rc} - \int_0^1 e^{Rc} dy}{\int_0^1 e^{Rc} dy} + G \frac{e^{Rc} \left(\int_0^1 e^{Rc} dy \right) \left(\int_0^y \frac{\partial c}{\partial x} d\eta \right) - e^{Rc} \int_0^1 e^{Rc} \int_0^y \frac{\partial c}{\partial x} d\eta dy}{\int_0^1 e^{Rc} dy}. \quad (5.17)$$

There are two main contributions to the horizontal velocity: the first term corresponds to the background pressure gradient and is driven by the viscosity difference between the two fluids and the second term corresponds to the gradient in buoyancy.

When G is small, the dynamics resemble the uniform density limit discussed in §2.4.2. For stable displacements, i.e. for moderate and large G , we make the simplifying assumption that the two fluids remain completely segregated, that is the concentration field is

$$c = \begin{cases} 1, & 0 \leq y \leq \bar{c}(x, t), \\ 0, & \bar{c}(x, t) < y \leq 1, \end{cases} \quad (5.18)$$

where \bar{c} is the transversely averaged concentration, or equivalently the height of the current above the base. Substituting into (5.17), we find that

$$u = \begin{cases} \frac{(M-1)(1-\bar{c})}{M\bar{c}+(1-\bar{c})} - \frac{GM(1-\bar{c})}{M\bar{c}+(1-\bar{c})} \frac{\partial \bar{c}}{\partial x}, & 0 \leq y \leq \bar{c}(x, t) \\ \frac{\bar{c}(1-M)}{M\bar{c}+(1-\bar{c})} + \frac{GM\bar{c}}{M\bar{c}+(1-\bar{c})} \frac{\partial \bar{c}}{\partial x}, & \bar{c}(x, t) < y \leq 1. \end{cases} \quad (5.19)$$

where $M = e^R$ is the ratio of the ambient to injected viscosity (cf. Pegler et al., 2014). This leads to the prediction of plug-like flow in each of the two fluids. Substituting this form for the velocity into (2.18) yields a nonlinear advection-diffusion equation for the evolution of the transversely averaged concentration,

$$\frac{\partial \bar{c}}{\partial t} + \frac{\partial}{\partial x} \left[\frac{(M-1)\bar{c}(1-\bar{c})}{M\bar{c}+(1-\bar{c})} - \frac{MG\bar{c}(1-\bar{c})}{M\bar{c}+(1-\bar{c})} \frac{\partial \bar{c}}{\partial x} \right] = 0. \quad (5.20)$$

The transport of concentration (in the moving frame) is driven by advection (term two) and gravitational slumping (term three). We solve (5.20) numerically, assuming an initial concentration as in (5.14) and with no-flux boundary conditions in the far-field, using a Crank-Nicolson predictor-corrector method. Representative solutions of (5.20)

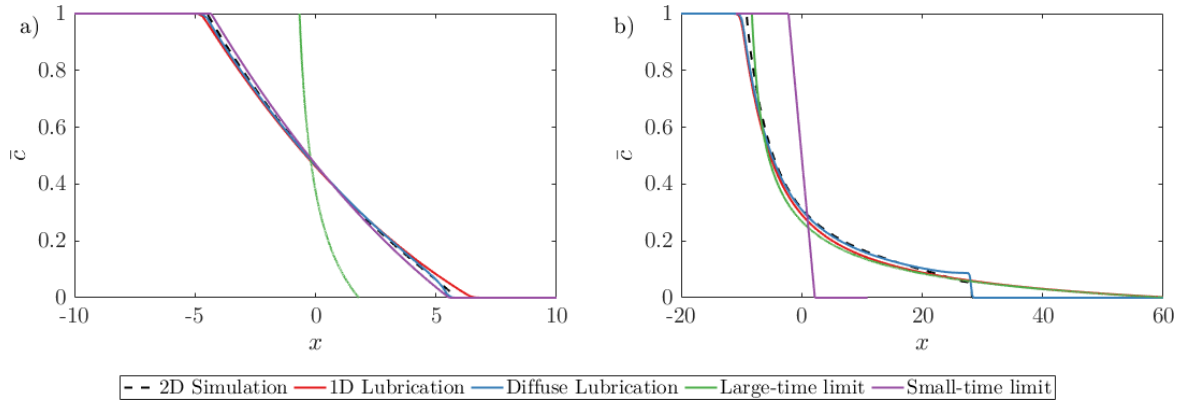


Fig. 5.10 Plot of the transversely averaged concentration for (a) small times, $(R, Pe, G, t) = (1, 4000, 14, 1)$ and (b) large-times $(R, Pe, G, t) = (2, 4000, 0.5, 10)$ from the two dimensional numerical simulations (black lines). The coloured lines represent the four different model solutions: the full sharp-interface model (5.20), the small-time limit of the sharp-interface model (5.21), the large-time limit of the sharp-interface model (5.22) and the diffuse-interface model (5.24) with (5.23)). The size of the diffuse region $l = 0.03$ is chosen to fit the full 2D numerical simulations.

for small and large times are given in figure 5.9(a) and 5.9(b) respectively. In both cases the interface spreads asymmetrically and tends to a self-similar profile in time. For small times the flow may be described by the similarity variable $x/(Gt)^{1/2}$ and for large times the flow may instead be described by the similarity variable x/t . To understand this transition we note that the gravitational slumping term, proportional to $\partial\bar{c}/\partial x$, is initially very large but decreases over time. This leads to two limiting cases of equation (5.20). In the small-time limit, the advective term may be neglected whereas in the large-time limit the gravitational slumping term may be neglected.

By taking the ratio of the gravitational slumping term to the advective term in (5.20), that is the ratio of the buoyancy contribution to the flux to the viscous contribution, we find that the latter can be neglected when $-GM\partial\bar{c}/\partial x/(M-1) \gg 1$, that is for $M \gg 1$, $h \ll G$. If $h \sim (Gt)^{1/2}$, this suggests a transition time of $t \sim O(G)$. If $t \ll O(G)$, the equations admit a similarity solution of the form $\bar{c}(\eta)$ with similarity variable $\eta = x/(Gt)^{1/2}$ where \bar{c} satisfies

$$\eta \frac{d\bar{c}}{d\eta} = \frac{d}{d\eta} \left[\frac{M\bar{c}(1-\bar{c})}{M\bar{c} + (1-\bar{c})} \frac{d\bar{c}}{d\eta} \right]. \quad (5.21)$$

The solution of (5.21) with fixed \bar{c} in the far-field is given in figure 5.10(a). The solution has the same similarity variable as Huppert and Woods (1995) but a different shape. It is asymmetric and depends on the viscosity ratio of the fluids owing to the fact that

the injected less-viscous fluid travels faster than the more-viscous ambient fluid. Note that Pegler et al. (2014) and Zheng et al. (2015a) solve the same equation, (5.21), but in the unconfined limit and find that the mixing zone grows like $h \sim t^{2/3}$.

In the large-time limit, the buoyancy contribution to the flux can be neglected. In this case the concentration evolves self-similarly as

$$\bar{c}(x, t) = \begin{cases} 1 & x/t < \frac{1}{M} - 1, \\ \frac{1}{M-1} \left(\sqrt{\frac{M}{x/t+1}} - 1 \right) & \frac{1}{M} - 1 \leq x/t \leq M - 1, \\ 0 & x/t > M - 1. \end{cases} \quad (5.22)$$

This is exactly the ‘Naive Koval’ model predicted for viscous fingering with a binary concentration distribution (cf. §2.4.2), and is given by the dashed black line in figure 5.9(b).

In figure 5.10(a,b) we compare the full 2D numerical simulations to the full solutions of (5.20) as well as the small- and large-time limits of (5.20) for two different values of G . When $G = 0.5$, that is G is small but the interface does not finger (figure 5.10(b)), the 1D model shows good agreement with the 2D simulations, as does the large-time limit. Gravity acts to force the flow into a single current rather than a set of fine fingers, but does not impact the growth rate of the mixing zone. When $G = 14$, that is when G is large (figure 5.10(a)), the 1D model again shows good agreement with the 2D simulations, as does the small-time limit of (5.20). In both cases, although there is good agreement in the body of the current, the tips tend to propagate slower than predicted. This was also observed in experiments by Pegler et al. (2014), who suggested that diffusion was the cause of the slow spreading. In the next subsection we improve on (5.20) by considering two fluids separated by a diffuse region.

In this section we have considered stable displacements where the two fluids are separated by a nearly sharp interface. However, when the interface does finger, transverse mixing across the fingers leads to a breakdown of this approximation and results in slower spreading. Assuming that the concentration varies smoothly across the fingers, the transversely averaged concentration has the same similarity solution as the ‘Naive Koval’ model but with an effective viscosity ratio $M_e = e^R \operatorname{erf} \sqrt{R} / \operatorname{erfi} \sqrt{R}$ (cf. §2.4.2).

Figure 5.11(a) shows the evolution of the mixing length from simulations with small to moderate G along with the theoretical solution (5.22) with both the actual viscosity ratio (sharp-interface limit) and the effective viscosity ratio (viscous fingering limit). For $(R, \operatorname{Pe}, t_{\text{end}}) = (1, 4000, 10)$, we find that for $G < 0.05$, the mixing length

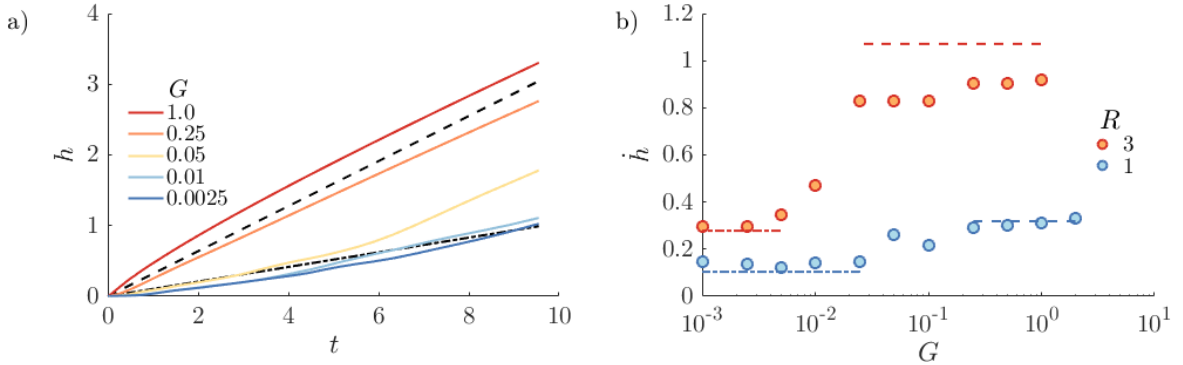


Fig. 5.11 Plot of $h(t)$ for $(R, Pe) = (1, 4000)$ and different values of G in the intermediate-time regime. (b) Plot of the spreading rate \dot{h} calculated by least-squares fitting a function of the form $h = h_0 + \dot{h}t$ to the numerical results for t in the range $5 \leq t \leq 10$, for $Pe = 4000$ and different G and R . The theoretical predictions for h in (a) and \dot{h} in (b) are found from the solution (5.22) with $M = e^R$ and $M = e^R \text{erf}(\sqrt{R})/\text{erfi}(\sqrt{R})$ and are given by dashed and dot-dashed lines respectively.

grows like the viscous fingering limit and when $G > 0.05$, the mixing length grows like the large-time gravity current limit. When $G = 0.05$, the interface first fingers but the fingers coarsen over time due to gravitational coarsening leading to a change in morphology from viscous fingering to gravity current like spreading. This transition occurs at a time $t \sim O(1/G)$, that is when the fingers have had enough time to fall. This transition occurs so long as $1/G < O(Pe)$, that is this change in morphology occurs before the flow transitions to the late-time regime.

Figure 5.11 (b) shows the spreading rate, defined as the rate of change of the mixing length, \dot{h} , as a function of R and G . For both values of R , we find a distinct shift in \dot{h} from the viscous fingering limit to the gravity current limit. The ‘Parabolic Koval’ model shows excellent agreement for both values of R and the ‘Naive Koval’ model shows excellent agreement for $R = 1$, but overestimates the spreading rate for $R = 3$. This discrepancy is likely a result of mixing at the tip of the current, which we address in the next subsection.

5.5.3 The effect of mixing on current propagation

In §5.5.2 we assumed a sharp-interface separated the two fluids. Here we consider the effect of a diffuse interface on the evolution of the interface. In a given vertical slice, for a given transversely averaged concentration \bar{c} , the relative flow of the two fluids is maximized when there is a binary distribution of concentration, and therefore mixing in general tends to slow their relative velocities.

First, combining the general form for the horizontal velocity (5.17) with the evolution equation for the transversely averaged concentration (2.18), yields

$$\frac{\partial \bar{c}}{\partial t} + \frac{\partial}{\partial x} \left[\frac{\int_0^1 c e^{Rc} dy}{\int_0^1 e^{Rc} dy} - \bar{c} + G \frac{\left(\int_0^1 c e^{Rc} dy \right) \left(\int_0^1 e^{Rc} dy \right) \left(\int_0^y \frac{\partial c}{\partial x} d\eta \right)}{\int_0^1 e^{Rc} dy} - G \frac{\left(\int_0^1 c e^{Rc} dy \right) \left(\int_0^1 e^{Rc} \int_0^y \frac{\partial c}{\partial x} d\eta dy \right)}{\int_0^1 e^{Rc} dy} \right] = 0. \quad (5.23)$$

To identify the effect of diffusion and mixing on the shape and evolution of the transversely averaged concentration field, we make the ansatz that

$$c = \frac{1}{2} + \frac{1}{2} \operatorname{erf} \left(\frac{\bar{c}(x, t) - y}{l} \right), \quad (5.24)$$

instead of (5.18), where l is the width of the diffuse region, which we expect depends on the parameters in the problem. Substituting (5.24) into (5.23), results in a nonlinear advection-diffusion equation with one additional parameter l . With this model we now include the effects of a diffuse boundary layer on the propagation of the gravity current; however, we ignore any spatial variations in the thickness of the boundary layer and any time dependence. We make this simplification assuming that the steepening of the concentration gradient due to stretching at the interface balances diffusion leading to a slowly varying boundary layer thickness (see, for example, de Anna et al., 2014).

We plot the solution to (5.23) with (5.24) in figure 5.10(b,c) (dashed dark-blue line). We find that in both the large-time and small-time limits, the diffusive model predicts a much slower tip and gives much better agreement with the 2D simulations than any of the other models.

5.6 Late-time shutdown and viscously-enhanced Taylor slumping regime

Over long times, diffusion in the transverse direction tends to homogenize the concentration field vertically. The concentration gradient in this case is predominantly in the streamwise direction, as is the fluid flow. In this late-time regime, the interface evolves in one of two ways. First, in the same manner as the shutdown of the viscous

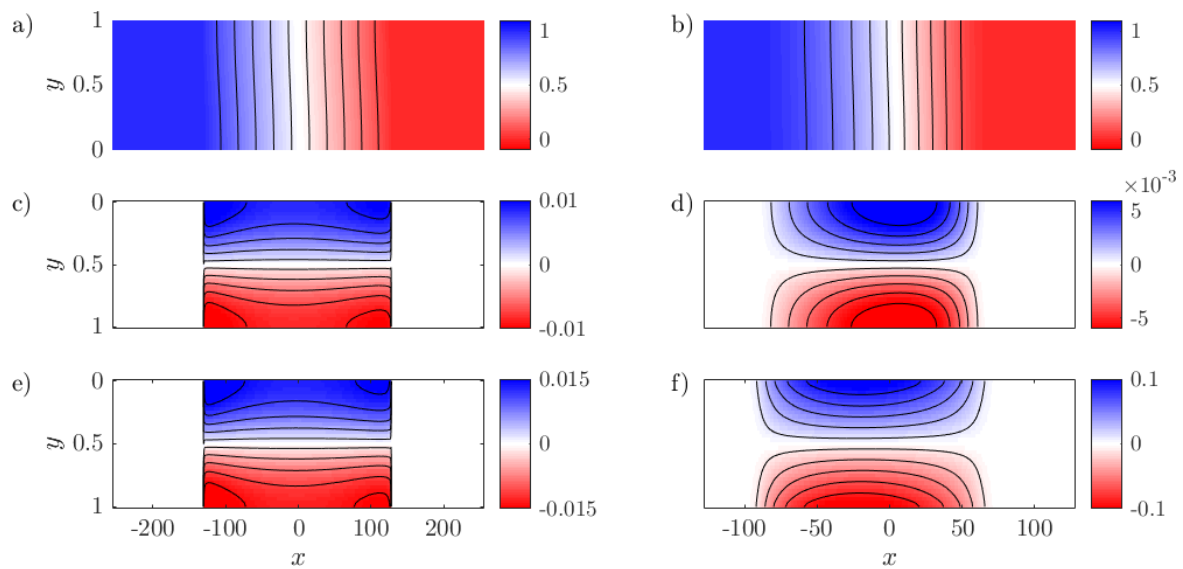


Fig. 5.12 Colourmaps of the (a,b) concentration field, (c,d) concentration deviations c' (with overlain contours), and (e,f) streamwise velocity, u (with overlain contours) for (a,c,e) $(R, Pe, G, t) = (1.5, 1000, 0.1, 1000)$ (small G) and (b,d,f) $(R, Pe, G, t) = (1.5, 100, 10, 1000)$ (large G). The left panels correspond to flow in the shutdown regime and the right panels correspond to flow in the viscously-enhanced Taylor slumping regime. Note that the aspect ratio of the figures is compressed by a factor of 30, so variations in the x -direction seem more pronounced than they actually are.

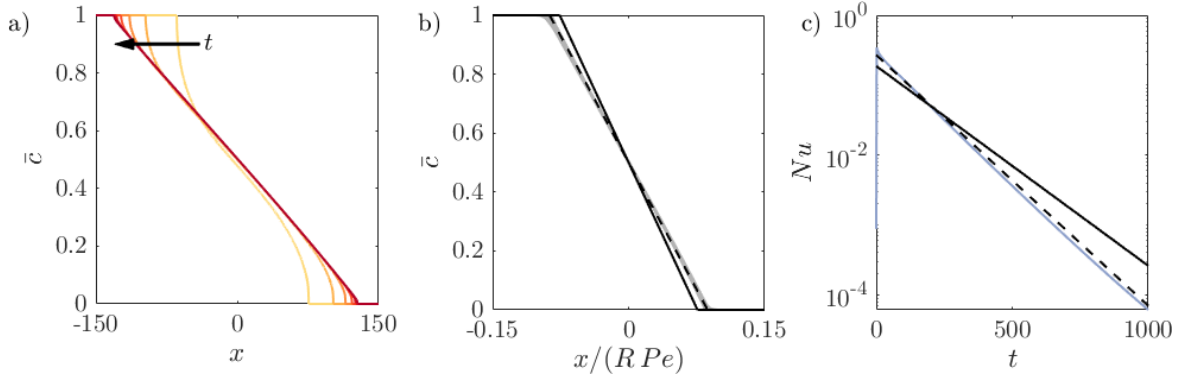


Fig. 5.13 (a) Evolution of \bar{c} for $(R, Pe, G) = (1.5, 1000, 0.3)$ and t spaced evenly from 150 to 900. (b) Plot of $\bar{c}(x)$ at $t = 1000$ for R ranging from 0.5 to 2.5, G ranging from 0.01 to 0.8 and Pe ranging from 300 to 1000. (c) Plot of $Nu(t)$ for $(R, Pe, G) = (1.5, 1000, 0.3)$. The solid and dashed black lines denote theoretical predictions with $K = 0.5$ and $K = 0.6$ respectively.

fingering instability, the concentration field is composed of a steady linear background gradient with decaying deviations superimposed. The streamwise velocity closely tracks the deviations and both are horizontally uniform (figure 5.12(a,c,e)). Second, the background concentration evolves asymmetrically, with the slope being shallower upstream. The velocity no longer tracks the deviations and neither the velocity nor the concentration is horizontally uniform (figure 5.12(b,d,f)).

5.6.1 Concentration model

The late-time regime is characterized by a weak background concentration gradient with small deviations superimposed. Assuming the flow is long and thin, the horizontal velocity is given by (5.17). By making the additional approximation that $\partial\bar{c}/\partial x \gg \partial c'/\partial x$ (5.17) becomes

$$u = \frac{e^{Rc'} - \int_0^1 e^{Rc'} dy}{\int_0^1 e^{Rc'} dy} + Ge^{R\bar{c}} \frac{\partial\bar{c}}{\partial x} \left(\frac{e^{Rc'} \left(\int_0^1 e^{Rc'} dy \right) y - e^{Rc'} \int_0^1 e^{Rc'} y dy}{\int_0^1 e^{Rc'} dy} \right). \quad (5.25)$$

Next, assuming $c' \ll 1$ and $\partial\bar{c}/\partial x \ll 1$, Taylor-expanding and neglecting terms $O(c'^2)$ and $O(c'\partial\bar{c}/\partial x)$ yields

$$u = Rc' + Ge^{R\bar{c}} \frac{\partial\bar{c}}{\partial x} \left(y - \frac{1}{2} \right) + O \left(c' \frac{\partial\bar{c}}{\partial x} \right) + O(c'^2). \quad (5.26)$$

As before, there are two main contributions to the horizontal velocity. The first term, driven by the viscosity difference between the two fluids, is, to leading order, proportional to the vertical deviations in the concentration. The second term, driven by the density difference between the two fluids, is only dependent on the transversely averaged concentration.

By substituting (5.26) into (2.19), and neglecting terms $O(c'^2)$, we find that the evolution equation for the deviations is given by

$$\frac{\partial c'}{\partial t} + Rc' \frac{\partial \bar{c}}{\partial x} + Ge^{R\bar{c}} \left(\frac{\partial \bar{c}}{\partial x} \right)^2 \left(y - \frac{1}{2} \right) = \frac{1}{Pe} \frac{\partial^2 c'}{\partial y^2}. \quad (5.27)$$

Solving (5.27) with no flux boundary conditions in the vertical,

$$c' = \sum_{n \geq 1} \left[K_n e^{-\gamma t} + \frac{2 - 2 \cos(\pi n)}{\pi^2 n^2} \frac{Ge^{R\bar{c}}}{\gamma} \left(\frac{\partial \bar{c}}{\partial x} \right)^2 \right] \cos(\pi n y), \quad (5.28)$$

where $\gamma = R\partial\bar{c}/\partial x + n^2\pi^2/Pe$ and $K_n = 2 \int_0^1 c'(x, y, 0) \cos(\pi n y) dy$ corresponds to the initial conditions at the onset of the regime. When $G = 0$ this reduces to the late-time, shutdown regime of the miscible viscous fingering instability (cf. §2.5.2). When $R = 0$, this reduces to the Taylor-slumping regime described by Szulczewski and Juanes (2013). In general, when both $R \neq 0$ and $G \neq 0$, the flow transitions from the shutdown regime to a viscously-enhanced Taylor-slumping regime. This is analogous to the dynamics in §4.4.1 where the dynamics transition from the shutdown regime to the shear-enhanced dispersion regime. The shutdown regimes in both cases are similar. However, the viscously-enhanced Taylor-slumping regime differs from the shear-enhanced dispersion regime.

In the shutdown regime, i.e. for small t , the exponentially decaying term, which is $O(1)$, dominates. The flow is dominated by the slowest decaying mode and c' and u can be approximated as

$$u \approx Rc' \approx RK_1 e^{-\gamma t} \cos(\pi y). \quad (5.29)$$

As in §2.5.2 and §4.4.1, the concentration deviations and streamwise velocity are horizontally uniform and decay exponentially. Substituting (5.28) into (2.18), we find that the transversely averaged concentration has the steady linear solution

$$\bar{c} = \frac{1}{2} - \alpha x, \quad (5.30)$$

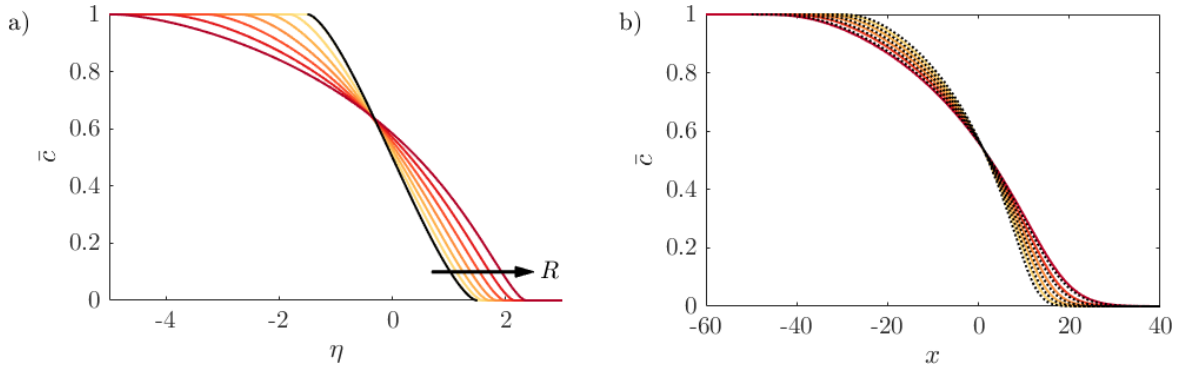


Fig. 5.14 (a) The similarity solution of (5.37) for $R = 0, 0.5, 1, 1.5, 2, 2.5, 3$. The analytical solution for $R = 0$ is given by the black line (Szulcowski and Juanes, 2013). (b) The evolution of \bar{c} for $(R, Pe, G) = (3, 10, 10)$ at $t = \{100, 140, 200, 280, 400\}$. The theoretical predictions, found by solving (5.36), are denoted by dotted lines.

with the fluid flow filling in the linear profile (figure 5.13(a)).

To determine α and γ uniquely, we follow the same approach as §4.5.1. We neglect longitudinal diffusion and relate the time-integrated convective flux through the midplane with the net change in concentration of the right half of the domain, namely,

$$\int_0^{\infty} \int_0^1 u c' dy dt \approx \int_0^{\infty} \bar{c}(x) dx = \frac{1}{8\alpha}. \quad (5.31)$$

Substituting (5.29) into (5.31), and assuming that most of the mixing occurs in the shutdown regime, $\gamma = 2K^2\alpha R$ and so

$$\alpha R = \frac{\pi^2}{(2K^2 + 1)Pe}, \quad \gamma = \frac{2K^2\pi^2}{(2K^2 + 1)Pe}. \quad (5.32)$$

As in chapter 4, we might expect that $K = 0.5$ corresponding to the deviations being at most 1 or 0 at $t = 0$ but we find that this underestimates the mixing. By instead fitting K to the numerical simulations, we find $K \simeq 0.6$. This slightly larger value of K accounts for the fact that the deviations are not sinusoidal from $t = 0$ in addition to nonlinear effects. With this value for K we find much better agreement with the numerical simulations for a wide range of simulations (figure 5.13(b,c)). Note that this value of K matches what was found in chapter 3 and is slightly larger than $K = 0.55$ which was found in chapter 2.

In the viscously-enhanced Taylor-slumping regime, i.e. for large t , the exponentially decaying terms in (5.28) and (5.26) become negligible and the gravitational terms

dominate. Expanding c' and u in powers of $\partial\bar{c}/\partial x$ we find,

$$c' = Ge^{R\bar{c}}\text{Pe} \left(\frac{\partial\bar{c}}{\partial x} \right)^2 \left(\frac{-1}{24} + \frac{y^2}{4} - \frac{y^3}{6} \right) + O \left(\left(\frac{\partial\bar{c}}{\partial x} \right)^3 \right), \quad (5.33)$$

$$u = Ge^{R\bar{c}} \left(\frac{\partial\bar{c}}{\partial x} \right) \left(y - \frac{1}{2} \right) + O \left(\left(\frac{\partial\bar{c}}{\partial x} \right)^2 \right). \quad (5.34)$$

Combining, the convective flux $\overline{uc'}$ is

$$\int_0^1 uc' dy = \frac{\text{Pe}G^2e^{2R\bar{c}}}{120} \left(\frac{\partial\bar{c}}{\partial x} \right)^3 + O \left(\left(\frac{\partial\bar{c}}{\partial x} \right)^5 \right). \quad (5.35)$$

Substituting this flux into (2.18) yields a nonlinear diffusion equation for the evolution of \bar{c} ,

$$\frac{\partial\bar{c}}{\partial t} = \frac{\partial}{\partial x} \left[\left(\frac{1}{\text{Pe}} + \frac{\text{Pe}}{120} \left(Ge^{R\bar{c}} \frac{\partial\bar{c}}{\partial x} \right)^2 \right) \frac{\partial\bar{c}}{\partial x} \right]. \quad (5.36)$$

This is analogous to the shear-enhanced dispersion regime discussed in chapter 3, but with a dispersion coefficient that depends on the local concentration gradient.

By neglecting the effects of molecular diffusion, (5.36) admits a similarity solution of the form $\bar{c}(\eta)$ with similarity variable $\eta = x/(G^2\text{Pe}t/120)^{1/4}$ where \bar{c} satisfies the nonlinear differential equation

$$\frac{d}{d\eta} \left(e^{2R\bar{c}} \left(\frac{d\bar{c}}{d\eta} \right)^3 \right) = -\frac{\eta}{4} \frac{d\bar{c}}{d\eta}. \quad (5.37)$$

The solution of (5.37) for different values of R is given in figure 5.14(a). When $R = 0$, the interface spreads symmetrically, whereas when $R > 0$, the interface slumps preferentially upstream.

The solution to the full diffusion equation (5.36) along with the full numerical simulations are plotted in figure 5.14(b). We find very good agreement between the numerical simulations and the reduced model.

The transition between the shutdown regime and the viscously-enhanced Taylor-slumping regime occurs when the two limiting solutions for \bar{c} , (5.30) and the solution of (5.37), overlap, that is at $t \sim R^4\text{Pe}^3/G^2$. In fact, if G is sufficiently large such that the gravitational term in (5.28) is $O(1)$, the shutdown regime can be skipped entirely, that is, when $G \sim O(R^2\text{Pe})$. Note that this is the same scaling as the transition from stable to unstable displacements described in §5.5.1, but with a larger pre-factor.

Over very long times, the viscously-enhanced Taylor-slumping term in (5.36) becomes negligible compared to the molecular diffusion term, occurring at a time $t \sim O(G^2 Pe^3)$, and the interface evolves through longitudinal dispersion again.

5.7 Discussion and conclusions

5.7.1 Summary

In this chapter, the range of dynamics that are possible during miscible displacements of a more-viscous fluid, by a less-viscous fluid of a different density were examined. Figure 5.15 delineates the different possible regimes in $G - t$ phase space for three different values of Pe . In each case the instantaneous scaling exponent of the mixing length, δ , where $h = At^\delta$, is plotted for representative simulations. In general, nine different regimes are possible.

At very early times (regime I), the interface is very sharp and diffusion across it dominates, leading to $t^{1/2}$ growth of the interface. Once advection outpaces diffusion the interface begins to slump (regimes II,III; §5.4). The dynamics are either dominated by density differences, leading to a transition at $t \sim O(1/G^2 Pe)$ or by viscosity differences, leading to a transition at $t \sim O(1/R^2 Pe)$. In this regime, the interface is sharp and vertical flow is important. Eventually, the interface becomes long and thin and vertical flow becomes unimportant. If $G > O(R^2 Pe)$ the interface is stabilized and does not finger. In this case, spreading is initially dominated by gravity (regime IV; §5.5.2) leading to $t^{1/2}$ spreading, then after $t \sim O(G)$ the dynamics become dominated by the background pressure gradient (regime V; §5.5.2) and the mixing zone grows linearly in time. If, however, $G < O(R^2 Pe)$, the interface can finger, which on average leads to linear growth of the mixing zone in time (regime III; §5.5.2). Note that, because the dynamics are chaotic, the scaling exponent varies over time (note the speckle in figure 5.15), but, on average, the interface spreads linearly. If $G < O(Pe)$, the fingers coalesce until a single dominant finger is left propagating in the centre of the domain with counter-propagating fingers along the top and bottom boundaries. As the single-finger exchange-flow decays, a pair of wider counter-propagating fingers propagating along the boundaries manifest themselves (figures 5.3(e,f)), which also propagate and slow leaving a well-mixed interior (regime VII; §5.2.2). If $G > O(Pe)$, either the interface is stable or it fingers and the fingers coarsen along the boundaries. Eventually, after $t \sim O(Pe)$, diffusion homogenizes the concentration field transversely, and the shutdown regime is reached (regime VI; §5.6). In this regime, the fluid flow

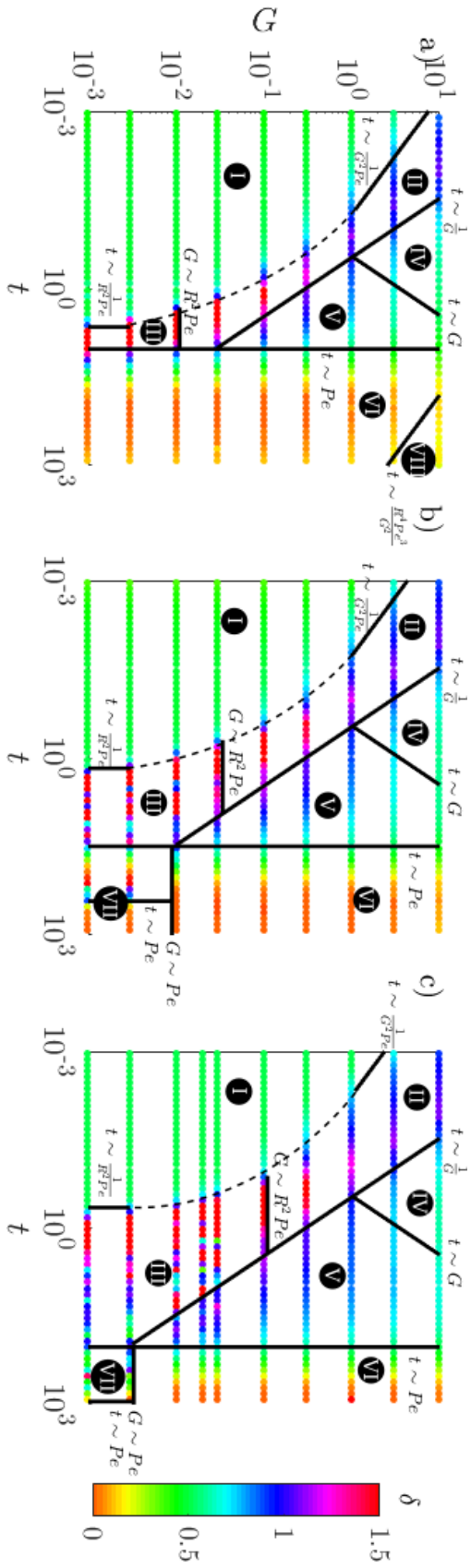


Fig. 5.15 Representative plots of the scaling exponent of the mixing length, δ , found by locally fitting a power-law of the form $h = At^\delta$, for $R = 1.5$ and (a) $Pe = 100$, (b) $Pe = 300$, and (c) $Pe = 1000$. The regime boundaries (black lines) divide the (I) early-time diffusive, (II) large- G slumping, (III) small- G slumping and viscous fingering, (IV) small-time gravity current, (V) large-time gravity current, (VI) shutdown, (VII) central-finger and boundary-finger, and (VIII) viscously-enhanced Taylor-slumping regimes. Over long times, the interface evolves through longitudinal diffusion (regime IX not shown).

	Sleipner	In Salah	Salt Creek
$t_{\text{dim}} = \frac{a^2 \phi}{Q}$	$3.5 \times 10^6 \text{s}$	$6 \times 10^6 \text{s}$	$7 \times 10^3 \text{s}$
$G = \frac{\Delta \rho g k a}{Q \mu_2}$	5	0.08	0.02
$\text{Pe} = \frac{Q}{D}$	2×10^4	5×10^3	1.5×10^4
$R = \log \left(\frac{\mu_2}{\mu_1} \right)$	2.5		

Table 5.1 Characteristic advective time-scale t_{dim} and dimensionless variables G , R , Pe for the three carbon dioxide sequestration case studies.

slows and the concentration field consists of a linear background gradient which is filled in exponentially (i.e. $\delta \rightarrow 0$). After $t \sim O(R^4 \text{Pe}^3 / G^2)$, the density difference between the two fluids becomes important again and the interface evolves through viscously-enhanced Taylor-slumping (regime VIII; §5.6). Over very long times, as the interface becomes more diffuse, Taylor-slumping becomes negligible and the interface evolves through longitudinal diffusion again with the same solution as regime I (regime IX; not shown).

5.7.2 Implications for carbon sequestration

We consider three case studies of carbon dioxide sequestration to demonstrate the physical timescales over which the identified regimes are applicable. We consider the sequestration of CO_2 at Sleipner (Bickle et al., 2007; Boait et al., 2012), In Salah (Vasco et al., 2010), and Salt Creek (Bickle et al., 2017). As was the case in chapter 2, for illustrative purposes, we assume the two fluids are fully miscible, even though the injected and ambient fluids are only partially miscible and the miscibility varies across the three different scenarios. We take the properties of the fluids to be: viscosity of the injected CO_2 , $\mu_1 = 6 \times 10^{-5} \text{Pa s}$, viscosity of the ambient fluid, $\mu_2 = 7 \times 10^{-4} \text{Pa s}$, density of the injected CO_2 , $\rho_1 = 7 \times 10^2 \text{kg/m}^3$, density of the ambient fluid (brine), $\rho_2 = 1 \times 10^3 \text{kg/m}^3$ (Huppert and Neufeld, 2014), and diffusion coefficient $D = 2 \times 10^{-9} \text{m}^2/\text{s}$ (Cadogan et al., 2014). Note that the diffusivity is taken to be constant and equal to the molecular diffusivity of carbon dioxide and brine as we find the pore-scale Peclet number in the three different case studies is less than one. Furthermore, although these properties will vary significantly between these three case studies given the different depths, temperatures, and ambient fluid

compositions (at Salt Creek and In Salah CO₂ is injected into depleted oil fields, whereas at Sleipner CO₂ is injected into a saline aquifer), for simplicity we will assume they are the same in all three cases. The main differences between the three injection scenarios are the injection rates, permeabilities and thicknesses of the formations. The Utsira formation at Sleipner is 200m thick and formed of nine distinct layers and so we take our representative length scale to be thickness of one layer or $a = 20\text{m}$. The formation is relatively homogeneous and has a permeability of $k = 2.5 \times 10^{-12}\text{m}^2$ and porosity $\phi = 0.35$. CO₂ is injected at a rate of about $Q = 4 \times 10^{-5}\text{m}^2/\text{s}$. The Krechba formation at In Salah has a similar characteristic length scale $a = 20\text{m}$, however it is less porous, $\phi = 0.15$, less permeable, $k = 1 \times 10^{-14}\text{m}^2$, and injection is slower, $Q = 1 \times 10^{-5}\text{m}^2/\text{s}$. The Frontier formation at Salt Creek is 20m thick and highly heterogeneous, and fluid flow is believed to be dominated by a few layers that are 1m thick with $\phi = 0.2$ and $k = 1.5 \times 10^{-13}\text{m}^2$. We estimate the injection velocity by dividing the distance between the injection and production wells by the breakthrough time of the bulk of the CO₂, $Q = 3 \times 10^{-5}\text{m}^2/\text{s}$.

The relevant non-dimensional parameters for these three case studies are summarized in table 5.1. Comparing the three scenarios, we find gravity to be relatively important at Sleipner but unimportant at In Salah or Salt Creek. Comparing G to the critical G_{crit} for fingering, we expect that Sleipner is mostly stable to fingering ($G_{\text{crit}} \approx 6$) whereas at In Salah ($G_{\text{crit}} \approx 1$) and Salt Creek ($G_{\text{crit}} \approx 5$) we expect that the interface is initially dominated by fingering. We summarize the dimensional time-scales for the different regimes in each of the three cases in figure 5.16. We find that Sleipner is currently in the large-time gravity current limit, In Salah, by the end of injections would have just transitioned from the viscous fingering limit to the large-time gravity current limit, while at Salt Creek, at the time of breakthrough, we expect that the interface would have reached the shutdown regime. By identifying the important parameters and the appropriate dimensional timescales, we are able to identify the dominant physical balances in the flow and make predictions for how the interface evolves.

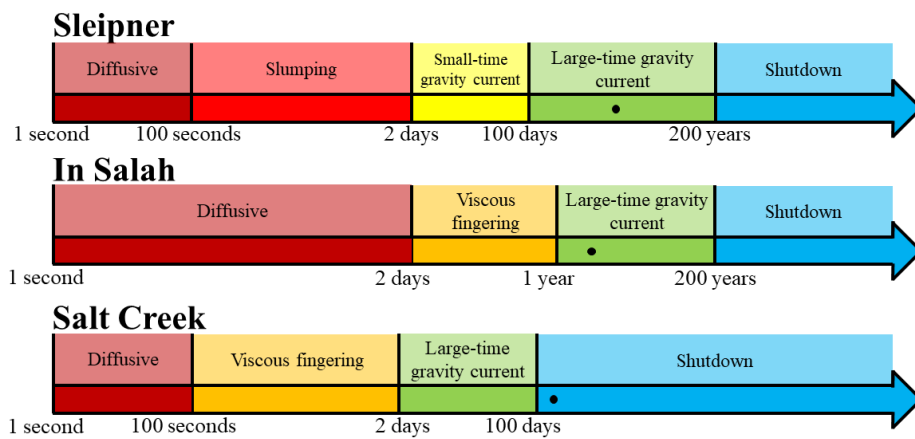


Fig. 5.16 Evolution of the displacement front in the three case studies. The black dots denote the time since injection at Sleipner, the total injection time at In Salah, and time until breakthrough at Salt Creek.

Chapter 6

Flow and deformation in a confined poroelastic medium

6.1 Introduction

In chapters 2-5 injection driven flow and mixing in porous media where the solid phase was rigid were considered. However, fluid flowing through a soft porous medium can significantly deform it and change its flow properties. This coupling of fluid flow and deformation can be seen in a wide array of contexts from the regulation of mucus in the gut (Datta et al., 2016) to the flow of partially molten rock through the Earth's mantle (McKenzie, 1984). In this chapter this coupling is explored using high precision laboratory experiments.

The theory of poroelasticity, the coupling of Darcy flow to elastic deformation in the solid matrix, dates back to the seminal works of Terzaghi and Biot (see for example Biot, 1941; Terzaghi, 1943). This theory for linear poroelasticity is only valid in the limit of small deformations and, since then, efforts have been made to generalize this theoretical frame work for large deformations (see for example MacMinn et al., 2016). In this chapter, the specific case of radial flow in a highly deformable medium is considered. Although there have been a number of related theoretical works in this geometry, including Kenyon (1979) and Barry and Aldis (1993) who considered fluid-driven deformation in linearly elastic porous shells, and Auton and MacMinn (2017, 2018) who considered the fully coupled nonlinear problem in the limit of large deformations, there has been relatively little experimental work to date.

Experimentally, fluid injection in deformable granular packings acts as a prototypical example of fluid-solid coupling in porous media and has been studied in a variety of contexts and can result in a wide range of morphologies of flow. These include

multiphase displacements, where the ambient and injected fluids are different phases (Dalbe and Juanes, 2018; Eriksen et al., 2015; Sandnes et al., 2011, 2007), and single-phase displacements, where the ambient and injected fluids are the same (Berhanu et al., 2012; Kudrolli and Clotet, 2016; Mahadevan et al., 2012). Although these systems can exhibit large deformations, the deformation tends to be plastic.

More recent experiments have examined flow through deformable granular packings where the individual grains are elastic. In this case the matrix is able to go through substantial elastic deformation in addition to plastic deformation. These packings have been used to study gravity-driven flow (Hewitt et al., 2015), centrifugal compaction, (Nordstrom et al., 2010), and fluid-driven compaction in uniaxial (Hewitt et al., 2016) and cylindrical geometries (MacMinn et al., 2015). However, all of these experiments have considered packings that are initially at or near the ‘jammed state’ and have not considered the systematic variation of the initial packing fraction. In experiments with rigid granular media, it was found that the choice of initial packing fraction could lead to very different dynamics from pore invasion to a fluidised solid-phase (Sandnes et al., 2011). The use of elastic particles here allows interrogation of a wide range of initial porosities from weakly confined cases where the solid has porosity much larger than the jamming transition to strongly confined cases where the porosity is much smaller than the jamming transition.

In this chapter the fluid-driven deformation of a packing of soft elastic spheres in a cylindrical geometry is studied. In doing so, the effect of changing the initial confinement of the solid on the dynamic and steady-state behaviour of the porosity field is examined. This chapter is laid out as follows. In §6.2 the experimental setup is discussed as well as the techniques used to measure the porosity field. In §6.3 an axisymmetric model for the evolution of the porosity field is derived and both the transient and steady-state behaviour of the system are considered. In §6.4 and §6.5 the model predictions are compared to the experimental results.

6.2 Experiments on flow through a deformable matrix

We consider a deformable porous cylinder of radius b surrounded by a rigid permeable barrier. The medium has some unstrained thickness d_0 corresponding to an unstrained porosity ϕ_0 and is fully saturated with a fluid with viscosity μ . The medium is then strained to some new thickness d corresponding to some initial porosity Φ . Fluid is then injected from a point source at the center of the medium. The fluid flow deforms

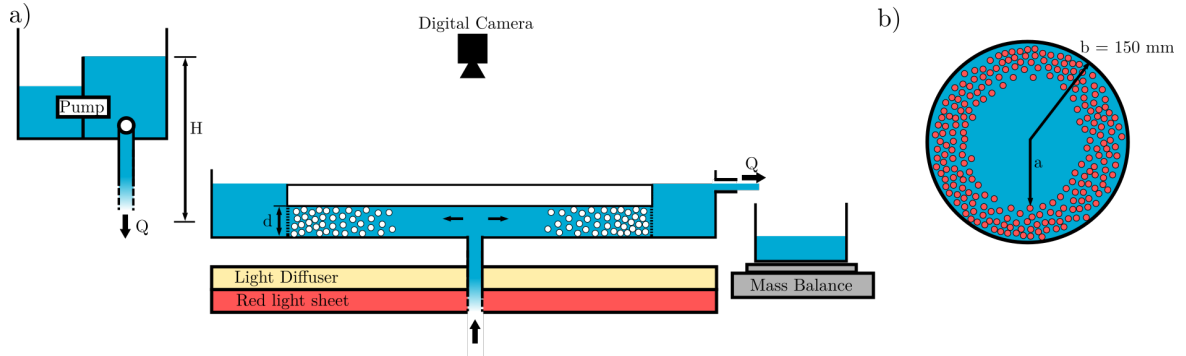


Fig. 6.1 (a) A schematic showing the experimental setup. The apparatus consisted of a circular cell with impermeable top and bottom boundaries and a rigid permeable circumference. The top boundary was adjustable to impose a fixed initial confinement, d . The cell was filled with a packing of transparent soft hydrogel spheres, which formed an idealized poroelastic medium. The medium was saturated with blue-dyed water and the same fluid was injected through an inlet in the centre of the cell with a flux Q set by a constant head H . Time-lapse images are taken at a regular interval and dye-attenuation was used to measure the depth integrated porosity field. (b) Top view of the confined porous region showing the imaging section. Since the particles are undyed, regions of high porosity appeared dark. When fluid is injected into the cell, a cavity of radius $a(t)$ opened.

the medium resulting in a cavity of size $a(t)$ and porosity field, $\phi(r, \theta, t)$. In this section, we describe a suite of experiments used to study this coupling of fluid flow and deformation in a variably confined deformable porous medium.

6.2.1 Experimental setup

The experimental setup, shown schematically in figure 6.1, consisted of $\sim 750,000$ polydisperse soft hydrogel spheres packed in a cylindrical cell of diameter $2b = 300\text{mm}$. The cell had a metal circumference with a lattice of holes with mean diameter $0.8 \pm 0.1\text{mm}$ and mean spacing $0.8 \pm 0.1\text{mm}$ which acted as a porous barrier that allowed fluid to flow but prevented the beads from passing. The size and spacing of the holes was smaller than the beads and ensured that the beads did not align to block all of the holes. The cell had an impermeable top boundary that was adjustable so that the depth of the cell, d , could be varied as well as an impermeable bottom boundary. The cell was contained within a larger tank and the packing was always saturated with water. An outlet in the larger tank ensured the fluid height outside the cell was maintained at a fixed height larger than d . The inlet to the cell, located in the middle of the bottom boundary, was connected to a header tank at a height H above the base

of the cell and the height of the header tank was varied from 5 – 80cm. The header tank consisted of two reservoirs. Fluid was pumped from one reservoir to the other and allowed to overflow back into the source reservoir. This ensured that the height of the fluid was fixed, thereby maintaining a constant head. The header tank was connected to the inlet of the cell with two tubes joined by a valve. It was found that the hydraulic resistance of this tubing was typically much larger than the packing of spheres and so the constant header tank acted as a source of constant volumetric flux $Q \sim H$ into the cell.

The soft spheres used in the experiments were sodium poly-acrylamide hydrogel spheres (JRM Chemical). The hydrogel spheres, which started as dry grains with radius ~ 0.15 mm, were swollen in a bath of deionized water. The resulting swollen spheres were nearly index-matched and density-matched with the deionized water and had mean radius 0.64 ± 0.17 mm (figure 6.2(c)). The experiments were initialized by first filling the cell and larger containing tank with blue-dyed deionized water (0.08%; Ingram Brothers blue food colouring). The spheres were then poured into the cell and were spread to a roughly uniform height. Since the beads were not dyed, they could be visualized in the dyed water. This fact is used to measure the solid fraction using dye attenuation techniques (cf. §6.2.2). Deionized water was used throughout the experiments as it was found that it produced the largest (most swollen) beads and prevented dye leaching into the spheres.

6.2.2 Calibration

In addition to measuring the cavity size a , dye attenuation techniques were used to measure the depth averaged porosity, ϕ of the analogue porous medium. To do so, a panel of red LEDs was used to produce a nearly uniform light sheet, which illuminated the cell from below and a Nikon D7000 camera imaged the packing from above. The blue-dyed interstitial water absorbed and attenuated the light whereas the un-dyed spheres allowed the light to pass through unperturbed. The total amount of attenuation imaged from above could therefore be related to the depth-integrated quantity of dye. From this the spatial distribution of the depth-integrated volume of dyed fluid and hence the depth-averaged porosity field can be inferred. To calibrate the light intensity against the depth-integrated fluid volume, the cell was incrementally filled with varying depths of dyed fluid, h , and the mean light intensity in the cell was measured (figure

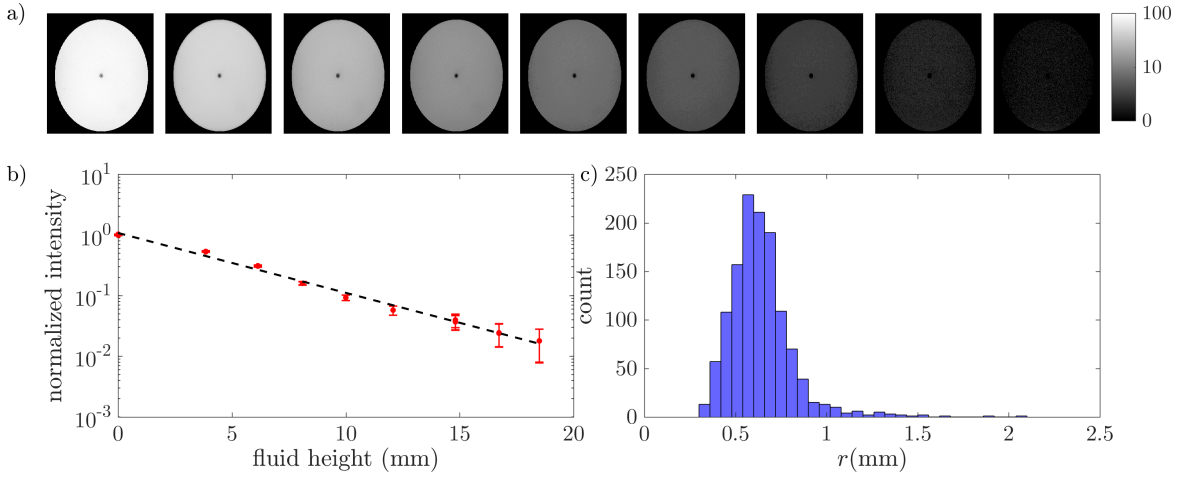


Fig. 6.2 (a) A series of images showing the light intensity (a.u.) after passing through varying depths of dyed fluid. From left to right, $h = \{0, 3.86, 6.14, 8.1, 10, 12.07, 14.81, 16.72, 18.49\}$ mm. The black dot in the centre of the images is the inlet into the cell. (b) Calibration data from the different images in (a). The equation for the dashed best fit line is $I(h)/I(0) = e^{-0.23h}$. (c) Histogram of the radii of the swollen hydrogel spheres from a sample of 1249 spheres. The mean radius is $r_{\text{sphere}} = 0.64 \pm 0.17$ mm.

6.2(a,b)). It was found that the intensity obeyed a classical Lambert-Beer law,

$$\frac{I(h)}{I(0)} = e^{-Ah}, \quad (6.1)$$

where $I(h)/I(0)$ is the normalized light intensity and A is the absorbency of the dye. Fitting to the calibration data, it is found that for the specific choice of dye concentration, $A = 0.23 \pm 0.01\text{mm}^{-1}$.

6.2.3 Validation

First the calibration data is independently validated to ensure that the addition of the hydrogel spheres did not interfere with the dye attenuation measurements, that is, they did not absorb or scatter any light. To do so, the experimental set up described above was used to uniaxially compress a known volume of spheres (without any externally imposed flow). With the addition of the spheres, there are now two phases, one of which is colourless, and so the effective depth-averaged fluid height h is now $h = \phi d$. To compress the medium, the cell depth d was reduced, which reduced ϕ and h but the difference $d - h$ remained unchanged, since the fluid but not the solid could escape. Figure 6.3(a) shows the azimuthally-averaged depth-integrated fluid height for different

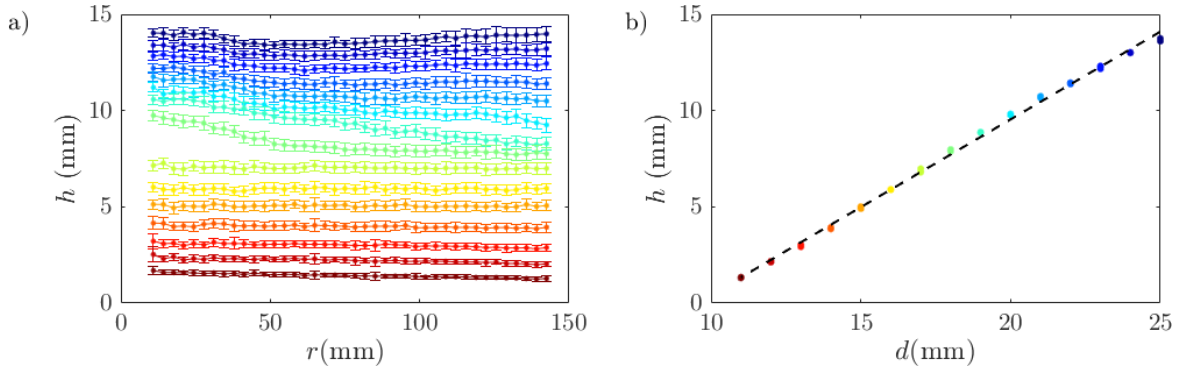


Fig. 6.3 Validation of the dye attenuation technique through uniaxial compression of the packing of spheres without any externally imposed flow. (a) Plot of the azimuthally averaged depth integrated fluid volume. Here the colours correspond to different confinements, d , which can be seen in (b). (b) Plot of the mean depth integrated fluid volume for varying d . The x-intercept of the dashed line of best fit, 9.5mm, corresponds to the mean depth integrated solid quantity in the cell.

confinements. As expected, decreasing d reduces the fluid height h . Interestingly, above $d > 21$ mm, a reduction in d resulted in a uniform reduction in h suggesting little movement in the solid. However, for $17 < d < 21$ mm ($0.44 < \Phi < 0.55$, which corresponds to packings near jamming), h is smallest near the boundary suggesting build-up of the solid phase near the boundary. This occurs because as the confinement is changed, outward flow is induced, resulting in compression of the solid towards the outer boundary. For $d < 17$ mm, the fluid and therefore the solid evens out and h decreases uniformly again. A plot of the mean depth integrated fluid volume versus the confinement is given in figure 6.3(b). As expected, h decreases linearly with d and the x-intercept of 9.5mm corresponds to the mean depth integrated solid quantity in the cell. This measurement of the solid volume agrees with the measurement of the solid volume outside of the cell, thereby providing an independent validation of the calibration methods.

6.2.4 Experimental results

A total of 30 different experiments were conducted with different injection rates, Q , and different initial confinement d . Since the amount of solid remained constant across experiments, changing d amounted to changing the initial porosity of the packing Φ . The areal flux (the total volumetric flux divided by the depth of the medium) was varied from $Q/d = 1 \times 10^{-4} \text{m}^2/\text{s}$ to $Q/d = 1 \times 10^{-3} \text{m}^2/\text{s}$ and the initial porosity was varied from strongly confined media, $\Phi = 0.37$ (smaller than the critical porosity for jamming)

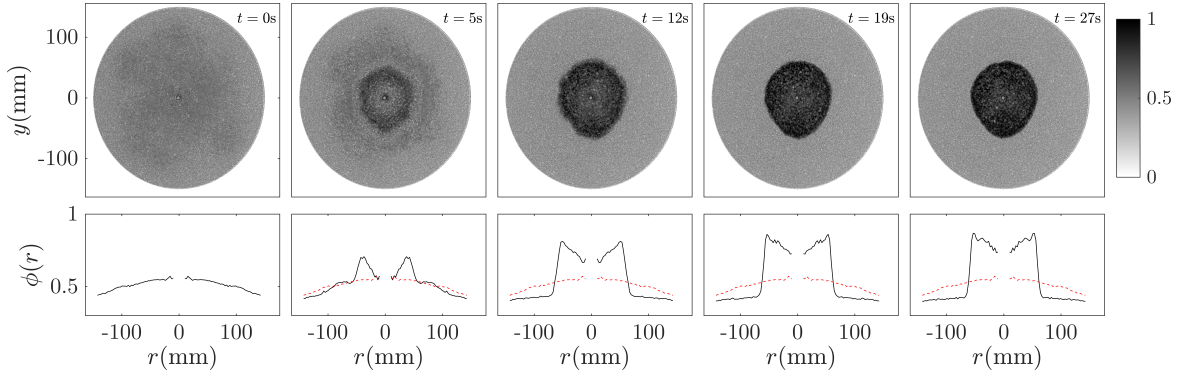


Fig. 6.4 Porosity field measurements for an experiment with $\Phi = 0.49$ and $Q/d = 6 \times 10^{-4} \text{m}^2/\text{s}$. (top) Greyscale images showing the depth-averaged porosity field. (bottom) The azimuthally-averaged depth-averaged porosity field. The porosity at $t = 0$ is given by the dashed red lines. Note that for clarity we show the azimuthally averaged data reflected about the origin as well. Also note that the experimental data starts at $r = 10\text{mm}$ corresponding to the edge of the inlet. The porosity field is nearly, but not quite, uniform to start. This is because as the confinement d is set, fluid is driven outward driving compaction along the boundary (cf. §6.2.3).

to weakly confined media, $\Phi = 0.62$ (above the jamming transition) summarized in appendix 6.A. In each case, the spatial distribution of the depth-integrated porosity field $\phi(r, \theta, t)$ as well as the cavity size, $a(t)$ were measured.

Between experiments the spheres were spread to a roughly uniform height before fixing the lid. At $t = 0$, the inlet to the cell was opened and fluid flowed radially outwards and compacted the analogue porous medium. The fluid exited the cell and filled the larger containing tank which overflowed into a reservoir on a mass-balance. Time-lapse images of the bead pack were taken at a rate of 1 picture per 1-4 seconds and dye attenuation techniques were used to infer the spatial distribution of the porosity field.

A representative series of snapshots from an experiment with $\Phi = 0.49$ and $Q/d = 6 \times 10^{-4} \text{m}^2/\text{s}$ are given in figure 6.4. The porosity field starts as nearly uniform. As fluid is injected, the medium compacts and a cavity opens. In the second panel, although not immediately obvious, there are two bright compacted regions: one near the outer boundary, which travels inwards, and one at the edge of the cavity region, which travels outwards. Eventually these compacting fronts converge and a steady-state is reached. The steady-state porosity field consists of a ‘cavity region’ of relatively high porosity surrounded by a ‘compacted region’ of relatively low porosity. Note that within the dark cavity region some bright particles can be seen, which suggests that the the cavity region is not pure fluid but rather a dilute suspension of spheres.

However, the number of particles in this region is small and so when modelling the cavity region we will assume it is pure fluid. Across the suite of experiments we find that the transient evolution of the deformable medium depends on the experimental parameters; compaction can be driven inward from the outer boundary or outward from the inner boundary. However, the steady-state behaviour remains qualitatively the same across the experiments.

For the experiments discussed in this chapter, the porosity remains relatively axisymmetric and we can therefore azimuthally average it without any loss of information. All of the results presented in this chapter will involve the azimuthally averaged porosity field or quantities derived from it. In §6.3 we derive an axisymmetric mathematical model for the evolution of the porosity field and the cavity size. In §6.4 and §6.5 we compare the model with the steady-state and transient experimental results, respectively.

6.3 Mathematical modelling

To describe this system we consider a simple axisymmetric model for the coupling of flow and deformation in an idealized poroelastic medium. We start by describing the general model before considering the results for specific choices of constitutive equations. For a detailed discussion on the effect of the choice of boundary conditions and choice of constitutive equations see Auton and MacMinn (2017, 2018) and MacMinn et al. (2016).

6.3.1 Governing equations

Consider an axisymmetric deformable porous medium centered around an injection point. The medium is constrained by a rigid but porous barrier at a distance b from the injection point. The local fluid and solid fractions are $\phi(r, t)$ and $1 - \phi(r, t)$ respectively. We assume that both the fluid and solid are incompressible and so continuity of the fluid and solid phases require,

$$\frac{\partial \phi}{\partial t} + \frac{1}{r} \frac{\partial}{\partial r} (r \phi v_f) = 0, \quad (6.2)$$

$$\frac{\partial (1 - \phi)}{\partial t} + \frac{1}{r} \frac{\partial}{\partial r} (r (1 - \phi) v_s) = 0, \quad (6.3)$$

where v_f and v_s are the interstitial fluid velocity and solid velocity respectively. We further assume that the flow of the fluid relative to the solid obeys Darcy's law,

$$\phi(v_f - v_s) = -\frac{k}{\mu} \frac{\partial p}{\partial r}, \quad (6.4)$$

where μ is the viscosity of the fluid phase, p is the fluid pressure, and k , is the permeability.

A total stress balance in the medium gives

$$\nabla \cdot \boldsymbol{\Sigma} = 0, \quad (6.5)$$

where $\boldsymbol{\Sigma}$ is the total stress which is equal to the phase-averaged stress in the fluid and solid phases, $\boldsymbol{\Sigma} = \phi p \mathbf{I} + (1 - \phi) \boldsymbol{\Sigma}_s$, where, in common with Darcy's law we have assumed that the stress in the fluid phase is isotropic and given by the pressure p , and $\boldsymbol{\Sigma}_s$ is the stress in the solid phase. Note that we take compression in the solid as positive. Defining the effective solid stress $\boldsymbol{\sigma} = (1 - \phi)(\boldsymbol{\Sigma}_s - p \mathbf{I})$ and substituting into (6.5) yields,

$$\nabla \cdot \boldsymbol{\sigma} = -\nabla p. \quad (6.6)$$

For axisymmetric fluid flow and solid displacement, (6.6) reduces to

$$\frac{\partial \sigma_{rr}}{\partial r} - \frac{\sigma_{\theta\theta} - \sigma_{rr}}{r} = -\frac{\partial p}{\partial r}, \quad (6.7)$$

where σ_{rr} is the radial stress and $\sigma_{\theta\theta}$ is the hoop stress. Following Terzaghi's principle, we assume that the effective stress is related to the Eulerian strain, ζ in the solid phase, $\boldsymbol{\sigma} = \boldsymbol{\sigma}(\zeta)$.

6.3.2 Initial and boundary conditions

At time $t = 0$, prior to injection, we assume that the medium has uniform porosity Φ and initial cavity size $a(0) \ll b$. In general, we find that the model results are insensitive to the choice of $a(0)$ and take it to be $0.01b$ in all of the results presented.

At $t = 0$, fluid is injected at a constant volumetric flux Q . Combining (6.2) and (6.3) and integrating, we relate the interstitial fluid and solid velocities to the flux Q ;

$$\phi(v_f - v_s) + v_s = \frac{Q}{2\pi r d}. \quad (6.8)$$

The relative fluid velocity, $\phi(v_f - v_s)$ can then be related to the solid stress using (6.4), (6.6) and (6.7), yielding

$$\frac{k}{\mu} \left(\frac{\partial \sigma_{rr}}{\partial r} - \frac{\sigma_{\theta\theta} - \sigma_{rr}}{r} \right) + v_s = \frac{Q}{2\pi r d}. \quad (6.9)$$

Along the outer boundary, the solid is constrained by the porous barrier and so $v_s(b) = 0$ such that

$$\frac{k}{\mu} \left(\frac{\partial \sigma_{rr}}{\partial r} \Big|_{r=b} - \frac{\sigma_{\theta\theta}(b) - \sigma_{rr}(b)}{b} \right) = \frac{Q}{2\pi b d}. \quad (6.10)$$

At the inner boundary, we assume that the solid is mechanically free, so the stress normal to the boundary goes to zero, that is

$$\sigma_{rr}(a) = 0. \quad (6.11)$$

Note that, in the experiments we will find that this is not necessarily the case - see §6.4.

Finally, the inner boundary evolves with the solid velocity there,

$$\frac{da}{dt} = v_s(a). \quad (6.12)$$

Another choice of boundary conditions is to impose a pressure drop across the packing. Imposing a constant pressure drop is equivalent to setting the solid stress and therefore porosity at the outer boundary (see Hewitt et al., 2016). This is because the total stress is conserved and taken up by both the fluid and the solid phases. Since the fluid (gauge) pressure is zero at the outer boundary, the pressure drop in the fluid phase must be compensated by an equal stress increase in the solid phase.

6.3.3 Constitutive equations

To close the model, one requires constitutive laws for the permeability and solid stress. The permeability for a packing of spheres of radius r_{sphere} is often given by the simplified Carman-Kozeny relation (Bear, 1988),

$$k(\phi) = \frac{r_{\text{sphere}}^2}{45} \frac{\phi^3}{(1 - \phi^2)}. \quad (6.13)$$

In general, the permeability also depends on the sphericity of the particles and the tortuosity of the flow paths (Bear, 1988), both of which can vary substantially as the packing is deformed. For simplicity we ignore these geometrical effects.

A number of different constitutive laws have been proposed for the solid stress in a poroelastic medium; for a discussion of different constitutive laws see Auton and MacMinn (2017, 2018); MacMinn et al. (2016). Here we assume that the solid only resists changes in volume and that the stress is isotropic, $\boldsymbol{\sigma}(\boldsymbol{\zeta}) = \sigma(e)\mathbf{I}$, where e is the volumetric strain in the solid measured in an Eulerian reference frame. This is motivated by previous work with packings of soft, frictionless spheres that found that the medium had negligible shear strength and that the solid stress could be taken to isotropic and only dependent on the bulk strain (Hewitt et al., 2016; MacMinn et al., 2015; Nordstrom et al., 2010).

The volumetric strain is related to the porosity through

$$e = \frac{\phi - \phi_0}{1 - \phi_0}, \quad (6.14)$$

where ϕ_0 is a reference porosity corresponding to zero stress in the solid. In the case of a granular packing of frictionless particles, this corresponds to a randomly closed packing of spheres ($\phi_0 \approx 0.41$). Note that given the solid is deformable but incompressible, the maximum volumetric strain is $e_{max} = -\phi_0/(1 - \phi_0)$. MacMinn et al. (2015) proposed the solid stress be Hertzian elastic, Nordstrom et al. (2010) proposed a variety of constitutive laws before settling on one that was Hertzian elastic for small strain and diverged at some maximum strain and Hewitt et al. (2016) proposed a constitutive law that was linearly elastic for small strain and diverged at some maximum strain. Here we use the same constitutive law as Hewitt et al. (2016),

$$\sigma = -\frac{\sigma_0 e}{1 - e/e_{max}} = \sigma_0 \left(\frac{\phi_0}{1 - \phi_0} \right) \left(\frac{\phi_0 - \phi}{\phi} \right). \quad (6.15)$$

6.3.4 Nondimensionalization

We nondimensionalize the model equations by defining

$$\tilde{r} = \frac{r}{b}, \quad \tilde{a} = \frac{a}{b}, \quad \tilde{\sigma} = \frac{\sigma}{\sigma_0}, \quad \tilde{k} = \frac{k}{k_0}, \quad \tilde{t} = \frac{t}{t_0}, \quad \tilde{Q} = \frac{Q}{Q_0}, \quad (6.16)$$

where we have defined the characteristic permeability, $k_0 = r_{\text{sphere}}^2/45$, time, $t_0 = b^2\mu/k_0\sigma_0$ and flux, $Q_0 = 2\pi dk_0\sigma_0/\mu$.

Combining (6.3) and (6.9) yields a nonlinear advection-diffusion equation for the evolution of the porosity field

$$\frac{\partial \phi}{\partial \tilde{t}} + \frac{\mathcal{Q}}{\tilde{r}} \frac{\partial \phi}{\partial \tilde{r}} = \frac{\phi_0^2}{1 - \phi_0^2} \frac{1}{\tilde{r}} \frac{\partial}{\partial \tilde{r}} \left[\tilde{r} (1 - \phi) \tilde{k} \frac{d\tilde{\sigma}}{d\phi} \frac{\partial \phi}{\partial \tilde{r}} \right]. \quad (6.17)$$

The constitutive equations (6.13) and (6.15) become

$$\tilde{k} = \frac{(1 - \phi^2)}{\phi^3} \quad \text{and} \quad \tilde{\sigma} = \left(\frac{\phi_0}{1 - \phi_0} \right) \left(\frac{\phi_0 - \phi}{\phi} \right) \quad (6.18)$$

respectively. Furthermore, the boundary conditions (6.10) and (6.11) become

$$\tilde{k} \frac{d\tilde{\sigma}}{d\phi} \frac{\partial \phi}{\partial \tilde{r}} \Big|_{\tilde{r}=1} = \mathcal{Q} \quad \text{and} \quad \phi(\tilde{a}) = \phi_0, \quad (6.19)$$

and the kinematic condition (6.12) becomes

$$\frac{d\tilde{a}}{d\tilde{t}} = \frac{\mathcal{Q}}{\tilde{a}} - \tilde{k} \frac{d\tilde{\sigma}}{d\phi} \frac{\partial \phi}{\partial \tilde{r}} \Big|_{\tilde{r}=\tilde{a}}. \quad (6.20)$$

There are three dimensionless parameters in the problem: the dimensionless injection flux, \mathcal{Q} , the stress-free porosity ϕ_0 , and the initial porosity Φ . In the experiments and in the model results presented in §6.3.5, the injection flux \mathcal{Q} and initial porosity Φ are varied and the cavity size $\tilde{a}(\tilde{t})$ and porosity $\phi(\tilde{r}, \tilde{t})$ are measured.

6.3.5 Model results

Equation (6.17) is solved numerically using a semi-implicit Crank-Nicolson time-stepping scheme that is second-order accurate in space. For all of the results presented in this section the stress-free porosity is set to $\phi_0 = 0.4$. Figure 6.5 shows the evolution of the porosity field, $\phi(\tilde{r}, \tilde{t})$ and the cavity size $\tilde{a}(\tilde{t})$ for different \mathcal{Q} and Φ . We consider three different cases: a medium that is initially strongly confined, $\Phi < \phi_0$ (figure 6.5(a,d)), a medium that is moderately confined, $\Phi = \phi_0$ (figure 6.5(b,e)), and a medium that is weakly confined, $\Phi > \phi_0$ (figure 6.5(c,f)). When the medium is strongly confined, the porosity is initially less than the stress-free porosity. The medium therefore compacts at the outer boundary while decompacting at the inner boundary. In the weakly confined case on the other hand, the porosity is initially above the stress-free porosity everywhere and compacts at both the inner and outer boundary. In both cases, a boundary layer structure grows inward from the two boundaries. When

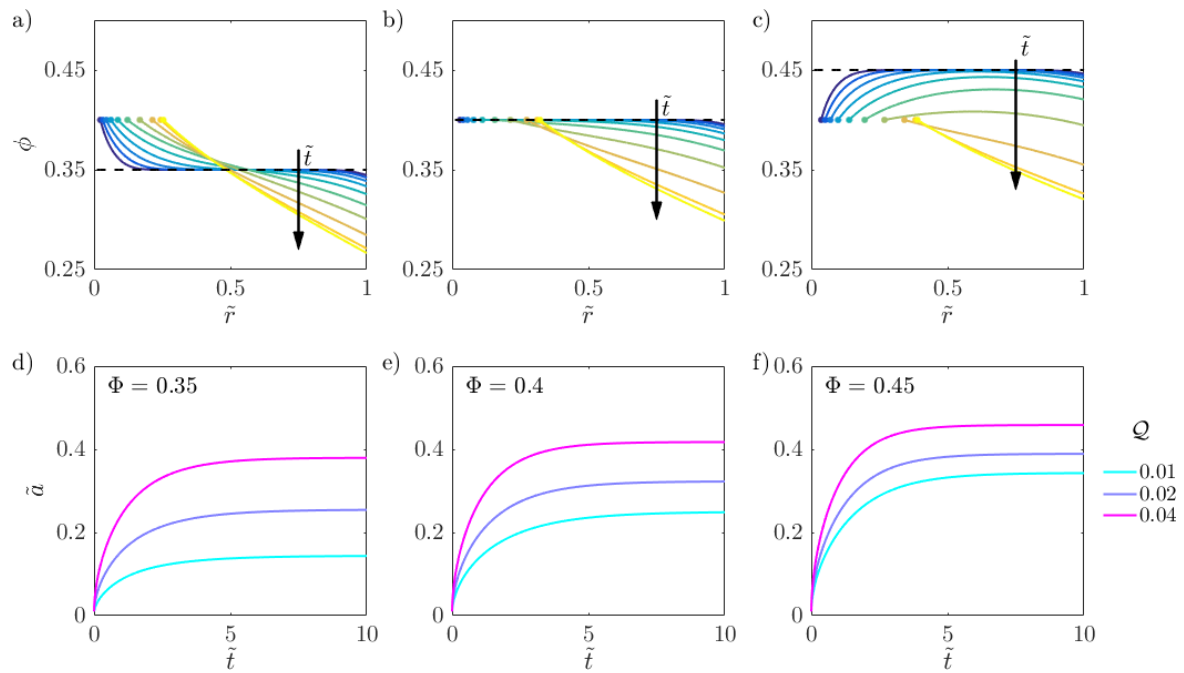


Fig. 6.5 Transient results of the theoretical model. The medium is initially (a,d) strongly confined ($\Phi = 0.35$) (b,e) moderately confined ($\Phi = 0.4$) or (c,f) weakly confined ($\Phi = 0.45$) relative to the zero stress porosity $\phi_0 = 0.4$. (a-c) The evolution of the porosity field, $\phi(\tilde{r}, \tilde{t})$ for flux $\mathcal{Q} = 0.04$. The lines correspond to time \tilde{t} between $\tilde{t} = 0.02$ and $\tilde{t} = 5.1$ separated by a factor of 2. (d-f) The evolution of the cavity size $\tilde{a}(\tilde{t})$.

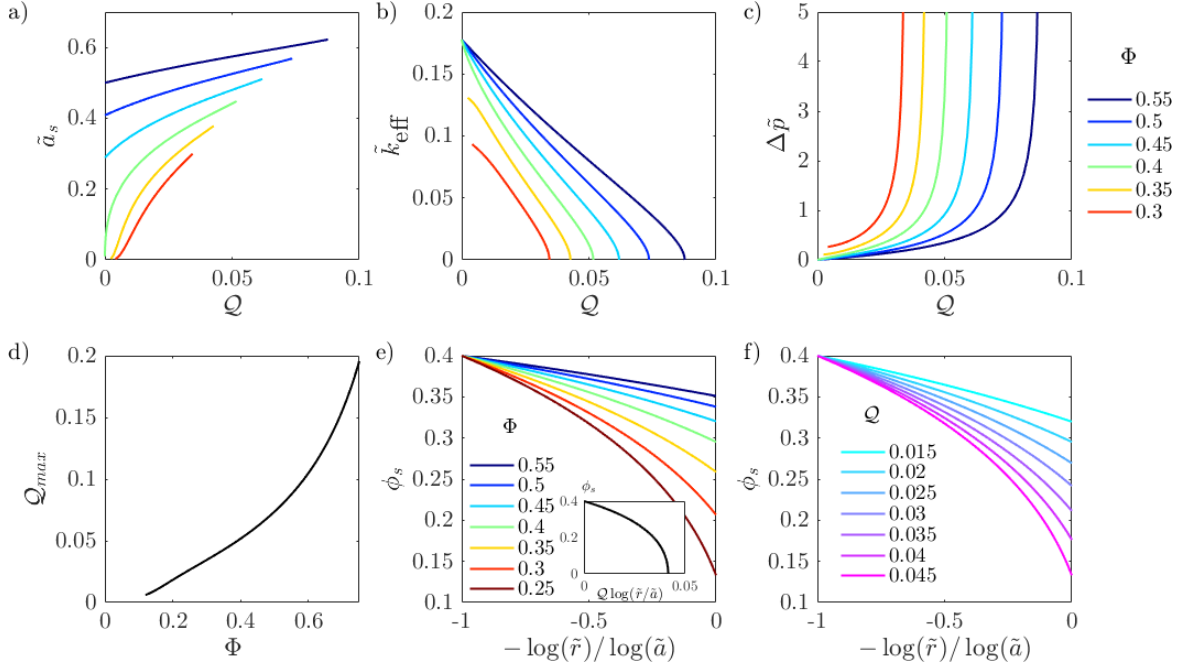


Fig. 6.6 Steady-state results of the theoretical model. (a) Plot of the cavity size, \tilde{a} , (b) effective permeability, \tilde{k}_{eff} , and (c) pressure drop $\Delta\tilde{p}$ as a function of \mathcal{Q} for different initial porosities, Φ . (d) Plot of the maximum flux, that is the point where $\tilde{k}_{\text{eff}} \rightarrow 0$ and $\Delta\tilde{p} \rightarrow \infty$. (e,f) Plots of $\phi_s(\tilde{r})$ for (e) different initial porosities and $\mathcal{Q} = 0.02$ and (f) different injection fluxes and $\Phi = 0.4$.

the medium is moderately confined, the inner boundary is already at the stress-free porosity and so the medium compacts from the outer boundary inwards. In all three cases, we find that the system, after an initial transient period, tends to evolve to a steady-state and we find that this time scale varies only slightly with \mathcal{Q} and Φ . We look for these steady-state solutions in the following section.

Steady-state results

At steady-state the solid is stationary and the fluid flows through the pore space. The viscous flow through the pore space tends to compress the solid and is balanced by elasticity which tends to decompress it. Setting the time-derivative in (6.17) to zero and integrating twice with boundary conditions (6.19) gives the steady-state porosity, ϕ_s , implicitly as

$$\frac{-\phi_0^2}{1-\phi_0} \left[\frac{1}{1-\phi_s} - \frac{1}{1-\phi_0} + \log \left(\frac{1-\phi_s}{1-\phi_0} \right) \right] = \mathcal{Q} \log \left(\frac{\tilde{r}}{\tilde{a}_s} \right). \quad (6.21)$$

We also have the additional constraint that the solid mass must be conserved,

$$\int_{\tilde{a}_s}^1 (1 - \phi) \tilde{r} d\tilde{r} = \pi(1 - \Phi) [1 - \tilde{a}(0)^2]. \quad (6.22)$$

The steady-state cavity size can then be found using standard root-finding techniques. The shape of the porosity field can be collapsed onto a single master curve, and the two parameters set the porosity at the right boundary $\phi_s(1)$ and the cavity size, \tilde{a}_s .

In addition to the cavity size and porosity field, we also define two physically useful quantities: the pressure drop across the packing

$$\Delta p = \mathcal{Q} \int_{\tilde{a}_s}^1 \frac{d\tilde{r}}{\tilde{r} \tilde{k}}, \quad (6.23)$$

and the effective permeability

$$\tilde{k}_{\text{eff}} = -\log(\tilde{a}_s) \left[\int_{\tilde{a}}^1 \frac{d\tilde{r}}{\tilde{r} \tilde{k}} \right]^{-1}, \quad (6.24)$$

which measures the effective resistance of the medium. Figures 6.6(a-c) show the above defined quantities for different initial porosities Φ and injection fluxes \mathcal{Q} . If $\Phi > \phi_0$, for arbitrarily small flow rates, the medium compacts until it is uniformly at the zero stress-state, that is $\phi_s = \phi_0$. By mass conservation, this means a cavity of size $\tilde{a}_s = [(\Phi - \phi_0)/(1 - \phi_0)]^{1/2}$ will open, and the effective permeability is $\tilde{k}_{\text{eff}} = \phi_0^3/(1 - \phi_0)^2$, independent of the initial porosity. If $\Phi < \phi_0$, a minimum injection flux is required to open a finite cavity. This is because the fluid flow needs to sufficiently compact the medium downstream for the medium to decompact at the inner boundary. In general, increasing Φ increases the cavity size as the medium becomes weakly confined and easy to deform and as \mathcal{Q} is increased, the cavity size also increases. However, for all Φ , there is a maximum flux \mathcal{Q} beyond which the permeability asymptotes to zero and the pressure diverges, as no more flow can be forced through the medium. Equivalently, if a pressure drop is imposed across the packing, the flux tends to a constant for large pressure drops (see appendix 6.B). Figure 6.6(d) shows this maximum flux \mathcal{Q}_{max} as a function of the initial porosity, which we find increases monotonically with the porosity. One interesting application of this is for the passive flow control of viscous flows (Gomez et al., 2017), as a way of limiting the maximum flux through a system, regardless of the input pressure. The monotonic increase of the maximum flux with the porosity suggests a simple way of tuning the passive flow control properties in this model system.

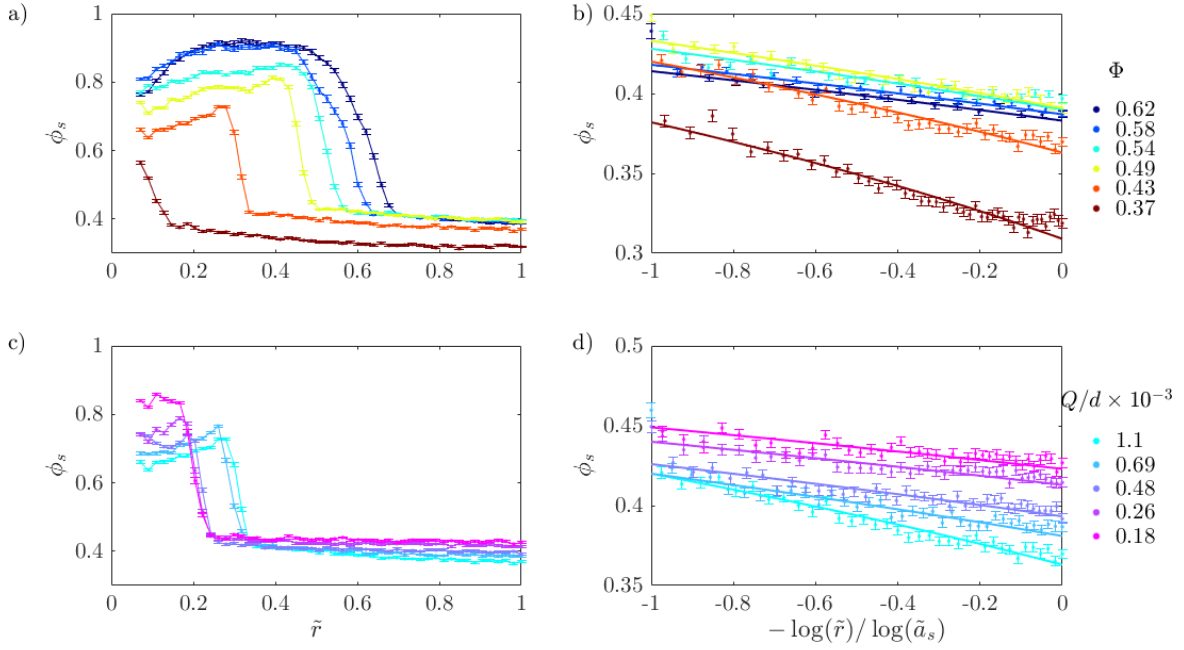


Fig. 6.7 Steady-state experimental measurements of the azimuthally averaged porosity $\phi_s(\tilde{r})$ for (a,b) different Φ and $Q/d \approx 1 \times 10^{-3} \text{m}^2/\text{s}$ and (c,d) different Q/d and $\Phi = 0.43$. To minimize noise, five consecutive measurements of the porosity are averaged. (a,c) Un-scaled data showing both the cavity and compacted regions. (b,d) Scaled-data showing only the compacted region. The theoretical model, (6.21), with unknown parameters ϕ_0 and \mathcal{Q} is fit to the experimental data. To do so, we first extract the cavity size from the experimental results by fitting a linear profile near the edge of the cavity and picking the point \tilde{a}_s that deviates from the linear profile by more than 1%. Note that for $\Phi \geq 0.58$, the porosity in the cavity region is likely under-estimated as the measurements are near the threshold of the dye-attenuation technique.

The steady-state porosity field is given in figures 6.6(e,f) for different Φ and different \mathcal{Q} . The porosity field takes on the same stress-free porosity at the inner boundary but the porosity on the outer boundary is smaller for small Φ and large \mathcal{Q} . Rescaling the horizontal axis (figure 6.6(e) inset), we find the porosity collapses to a single master curve; \mathcal{Q} and Φ set the portion of the curve that is sampled as well as setting the size of the cavity \tilde{a}_s .

In the following sections we present the steady-state and transient experimental results and make quantitative comparisons with the model solutions.

6.4 Steady-state experimental results

Each experiment was run for between 2 and 4 minutes and in that time 20 of the 30 experiments had reached a steady-state. As discussed before, the steady-state is nearly axisymmetric and consists of a ‘cavity region’ of size a_s , which is mostly devoid of particles, and a ‘compacted region’ where most of the particles accumulate. Figure 6.7 shows the steady-state azimuthally-averaged porosity field for different initial porosities Φ (figures 6.7(a,b)) and different areal fluxes Q/d (figures 6.7(c,d)). In general we find that the size of the cavity region increases with both Φ and Q/d .

The flow inside the cavity region consists of a large-scale circulation that is radially outwards along the top boundary and radially inwards along the bottom boundary. The Reynolds number inside the cavity region, defined using the characteristic depth of the medium, is $Re_{cav} \equiv Q/2\pi r\nu$. The Reynolds number ranges from $0.8m/r$ to $4m/r$, decays away from the inlet and ranges from a maximum of 400 at the edge of the inlet at the highest flow rates to a minimum of 20 at a_s at the lowest flow rates. This relatively high Reynolds number flow results in a small number of particles that remain in suspension as particles are continuously eroded and deposited at the inner boundary. This occurs because the particles are nearly frictionless and density matched with the fluid, and are therefore easy to mobilize. We expect that the rate at which particles are eroded is proportional to the Shields parameter $\Theta \equiv \rho Q^2/a_s d \Delta \rho g r_{sphere}^3$, which measures the momentum of the fluid to the relative weight of the solid (Hogg et al., 1996). We therefore expect to see more suspended particles for larger Q and smaller a_s (smaller Φ), in qualitative agreement with the experiments.

Inside the compacted region, the porosity decreases with \tilde{r} as the medium is more compacted near the outer boundary. The porosity at the outer boundary is lowest for initially strongly confined media and large flow-rates. The characteristic (pore-scale) Reynolds number in this region is $Re_{com} \equiv Q r_{sphere}/2\pi a_s d \nu$ and ranges from a minimum of 0.2 at the outer boundary at the lowest flow rates to a maximum of 8 at the inner boundary at the highest flow rates. Given the pore-scale Reynolds number is less than 10, we expect Darcy’s law to apply in the compacted region (Bear, 1988). We fit the theoretical model (6.17) to the experimental measurements in the compacted region. In §6.3 we assumed ϕ_0 was a material parameter corresponding to zero stress at the inner boundary. Experimentally, we find that $\phi_s(\tilde{a}_s) = \phi_0$ is not uniform across experiments. To account for this fact, we fit ϕ_0 in each of the experiments. We also fit the dimensionless injection flux, \mathcal{Q} , in order to determine the characteristic dimensional flux $Q_0 = 2\pi k_0 \sigma_0/\mu$. For $\Phi \geq 0.43$, the porosity on the inner boundary ranges from 0.41 to 0.44, in agreement with previous experiments (Hewitt et al., 2016), and is

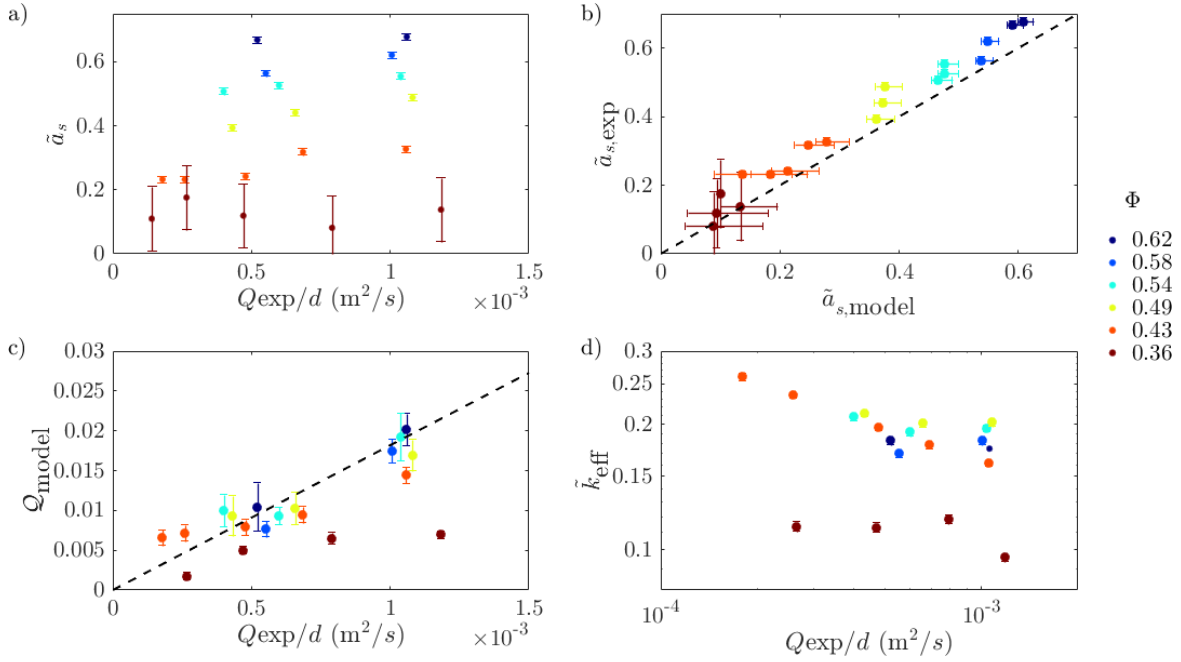


Fig. 6.8 Steady-state comparison of experimental and model results for different initial confinement Φ and injection fluxes Q/d . (a) Plot of the cavity size, \tilde{a} . The cavity size is found by fitting a linear profile near \tilde{a} and picking the point which deviates from the linear profile by more than 1%. (b) Comparison of the experimentally measured cavity size and the inferred cavity size from the model using fits for ϕ_0 and Q . (c) Comparison of the model fit Q and the experimentally imposed flux Q/d . The slope of the line of best fit is 17 ± 2 and its inverse is the dimensional flux $2\pi k_0 \sigma_0 / \mu$. (d) The inferred effective permeability from the model using fits for ϕ_0 and Q .

higher for slower injections. The systematically larger ϕ_0 for slower injections could be due to the boundary between the compacted and cavity regions being sloped leading to seemingly larger porosities for more sloped interfaces. Note that there is a significant amount of uncertainty in the measurement of the inner boundary porosity as the boundary between the compacted and cavity regions is not precise. This is in part due to the near, but not exactly, axisymmetric structure of the porosity field. For $\Phi = 0.36$, that is for a packing that is initially confined past the jamming criterion, ϕ_0 ranges from 0.36 to 0.39. These values of ϕ_0 are larger than Φ but smaller than the values found in experiments that were not initially jammed ($\Phi \geq 0.43$). Also, unlike the other experiments the transition from the cavity region to the compacted region is not as sharp, which leads to large amounts of uncertainty in \tilde{a}_s and a potential breakdown of the modelling assumptions.

Figure 6.8 shows steady-state global quantities \tilde{a}_s , Q and \tilde{k}_{eff} . The steady-state cavity size is an increasing function of Q and Φ . In figure 6.8(b) we compare the

measured cavity size (measured directly from the images) and the inferred cavity size (calculated based on the model fit to the porosity data *in the compacted region*). We find good agreement between the two, although the model systematically underestimates \tilde{a}_s . This is because, in writing (6.22) all of the particles are assumed to lie within the compacted region. One could account for this discrepancy by modifying (6.22) to account for a finite number of suspended particles which depend on Θ . We also use the fitted porosity profiles to infer the effective permeability of the media (figure 6.8(d)). The effective permeability is relatively similar in the weakly to moderately confined cases, in qualitative agreement with the model for small fluxes. Nonetheless, even in this small flux limit, we see a nearly 50% reduction in the permeability between the smallest and largest flow rates for $\Phi = 0.43$. The permeability in the strongly-confined limit is much smaller and varies much less, suggesting the fluid flow does not significantly deform the solid.

In figure 6.8(c) we compare the inferred flux (found from fitting the model to the porosity data in the compacted region) to the actual flux imposed. For the experiments with initial porosity larger than or equal to 0.43, the inferred flux scales linearly with the imposed flux and the inverse of the slope of the line of best fit corresponds to the dimensional flux $2\pi k_0 \sigma_0 / \mu = 0.059 \pm 0.007 \text{m}^2/\text{s}$. Given the viscosity of water is $\mu = 0.95 \pm 0.02 \times 10^{-3} \text{Pa}\cdot\text{s}$ and the characteristic permeability scale is $k_0 = r_{\text{sphere}}^2 / 45 = 9 \pm 5 \times 10^{-5} \text{m}^2/\text{s}$ we find that the elastic modulus of the packing of spheres is $\sigma_0 = 1000 \pm 700 \text{Pa}$. This is quite close to the measured elastic modulus in Hewitt et al. (2016) who found that a similar packing of spheres had an elastic modulus of about 1900Pa. The main difference between the two experiments is that here de-ionized water was used as the working fluid, which led to more swollen and hence more elastic particles (Hoshino et al., 2018).

The pre-jammed case, $\Phi = 0.36$, deviates from the rest of the experiments. This discrepancy is likely because it is much more difficult to rearrange particles that are pre-jammed into a particular configuration. This implies that our assumption that the pressure is an isotropic function of ϕ may not be valid for initially compacted media and that a more complicated constitutive law is required. One potentially simple way of modelling the solid rheology in this limit would be to take $\sigma_0(\Phi)$, an initial porosity-dependent bulk elasticity that takes on the value $1000 \pm 700 \text{Pa}$ for $\Phi \geq 0.42$ and is larger otherwise. For the experiments with $\Phi = 0.37$, we find the effective elastic modulus is about 2000Pa. Determining whether this is a reasonable assumption, and determining how the isotropy of the solid stress changes as it is compacted, is the subject of future work.

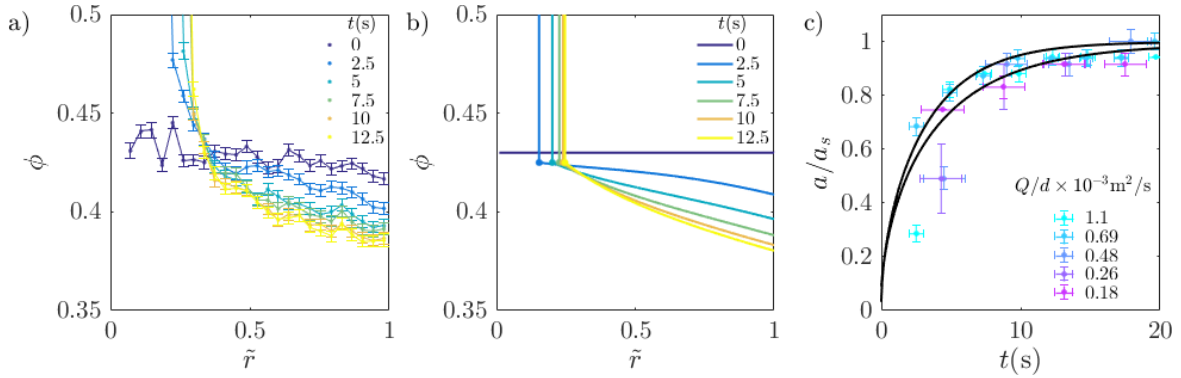


Fig. 6.9 Transient behaviour of the porosity field and cavity size for moderately confined media ($\Phi = 0.43$). (a) Experimental measurements of the transient evolution of the porosity field for $Q/d = 0.69 \times 10^{-3} \text{ m}^2/\text{s}$. (b) Time-evolution of the model for $\phi_0 = 0.425$ and $Q = 0.0125$. (c) Evolution of the normalized cavity size for different injection rates and $\Phi = 0.43$. The solid lines denote the model solution for the largest and smallest fluxes.

6.5 Transient experimental results

In this section, we discuss the transient evolution of the porosity field in the moderately confined and weakly confined limits. Note that, the experiments in strongly confined media were not temporally resolved enough to make comparisons with the model results.

6.5.1 Transient behaviour for $\Phi \approx \phi_0$

In addition to steady-state measurements, we also examine the transient evolution of the porosity field. The experimental results are given in figure 6.9(a) for a moderately confined packing ($\Phi = 0.43$). A cavity opens quickly and the medium compacts primarily at the outer boundary. The slope of the porosity remains relatively constant on the boundary and the medium continues to compact until it reaches a steady state (in about 10 – 15s). Using the steady-state fit for parameters Q and ϕ_0 from §6.4, we solve (6.17) for the transient evolution of the porosity field. Contrary to previous experiments (Hewitt et al., 2016), which found that the dynamics evolved on a much longer time scale than predicted, here we find that the model quantitatively agrees with the experiments. Although our steady-state porosity measurements do not evolve (within the errors of the experiments), it is possible that there is a secondary time-scale over which the solid matrix continues to deform slowly, for instance through creep (Allen and Kudrolli, 2018) or de-swelling of the individual spheres (Hewitt et al., 2016).

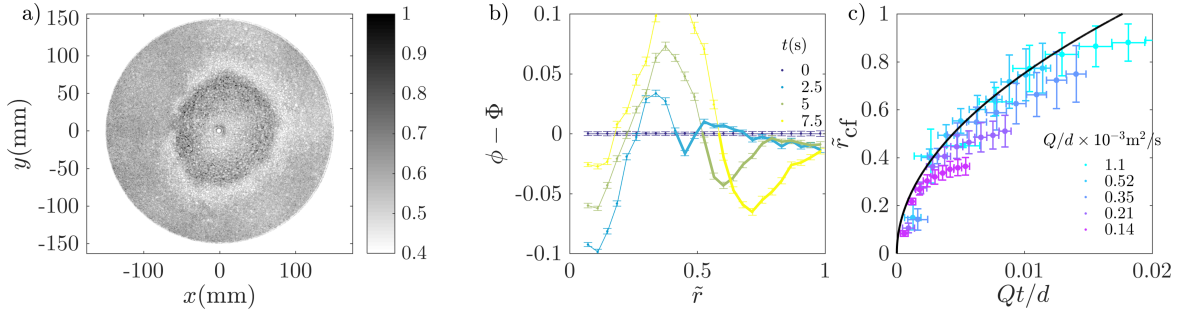


Fig. 6.10 Transient behaviour of the porosity field and cavity size for weakly confined media, $\Phi = 0.62$. (a) A snapshot of the porosity field for $Q/d = 1 \times 10^{-3} \text{m}^2/\text{s}$ and $t = 5\text{s}$. (b) Experimental measurements of the deviations of the porosity field from the initial porosity for $Q/d = 1 \times 10^{-3} \text{m}^2/\text{s}$. Solid rich regions are denoted by thick lines. (c) Plot of the location of the compaction front, \tilde{r}_{cf} . \tilde{r}_{cf} is defined as the $(\phi - \Phi)$ weighted) centre of mass of the solid rich region. The solid line denotes a point simply advected with the injected fluid.

This could result in small, experimentally unnoticeable, changes in ϕ but drastically different upscaled quantities \tilde{k}_{eff} and $\Delta\tilde{p}$.

In figure 6.9(c) we show the evolution of the normalized cavity size for different injection fluxes. Across the five experiments, we see very little variation in the characteristic time scale with the flux. This finding agrees with the theoretical model (§6.3.5), where the time scale only weakly depended on the injection rate \mathcal{Q} . In fact, the model does a reasonable job of capturing the transient evolution of the cavity size across all of the experiments.

6.5.2 Transient dynamics for $\Phi > \phi_0$

Whereas for $\Phi \approx \phi_0$ the model and the experiments show that the medium compacts inwards from the outer boundary, when $\Phi > \phi_0$, a compaction front, which propagates outward from the inner boundary, forms. Figure 6.10(a) shows a snapshot of one such compaction front from an experiment with $\Phi = 0.62$. When injection begins, the particles near the inlet are fluidized forming a particle rich front. These fluidized particles are then advected downstream by the background fluid flow. As they are advected, the front accumulates particles downstream leading to a growing front (figure 6.10(b)). Downstream of the compaction front some compaction also occurs at the outer boundary but it is small compared to the compacting front. The compacted region eventually hits the outer boundary before tending to a steady-state profile. Note that although the transient behaviour does not match the theoretical model (figure

6.5(c,f)), the steady-state behaviour does, as the dominant balance at steady-state is still a balance between the background fluid pressure and elastic deformation.

The reason the packing behaves differently from the previous section is because the porosity is much larger than the jamming threshold, and therefore the particles cannot communicate stresses elastically. Instead the packing deforms viscously through microstructural rearrangement of the particles. The rheology of the packing in this case is more analogous to a compacting viscous fluid seen in magma dynamics (Spiegelman, 1993a,b). Because the particles are nearly frictionless and density matched with the injected fluid, we find that the cavity boundary is simply advected by the fluid flow and travels with the background fluid speed $\tilde{r}_{cf} \sim (Qt)^{1/2}$ (figure 6.10(c)). This is in stark contrast to the transient behaviour observed in §6.5.2 where the cavity growth was only weakly dependent on the injection rate.

Similar compacting behaviour has been also been seen in air injections in weakly confined fluid-saturated granular packings (Sandnes et al., 2011, 2007) and suspension flow in Hele-Shaw cells (Kim et al., 2017). One key difference however is that in those experiments, surface tension was important; either to push grains ahead or act as an impermeable boundary for particles to accumulate. In the experiments presented here, there is no surface tension and the fluid is free to seep through the medium. The compaction front here instead grows because particles near the inlet are easily fluidized and compact the particles downstream through inter-particle interactions.

6.6 Conclusions

In this chapter experiments of fluid-driven compaction in a deformable porous medium were presented. The experimental setup consisted of deformable hydrogel beads packed to varying degrees in a cylindrical cell. The initial packing was varied from strongly confined (the initial porosity was below the jamming threshold) to weakly confined (the initial porosity was above the jamming threshold). Fluid was then injected into the cell at a constant volumetric flux and the deformation of the medium was tracked using time-lapse imaging.

It was found that as fluid was injected, the medium compacts and a cavity opens. The compaction front tended to either propagate inwards from the outer boundary for initial porosities near the stress-free porosity, $\Phi \approx \phi_0$, or outward from the inner boundary when the initial porosity is larger than the stress-free porosity $\Phi > \phi_0$. In either case the porosity field consisted of two regions: a ‘cavity region’ mostly devoid of particles and a ‘compacted region’ where particles accumulate. Eventually the

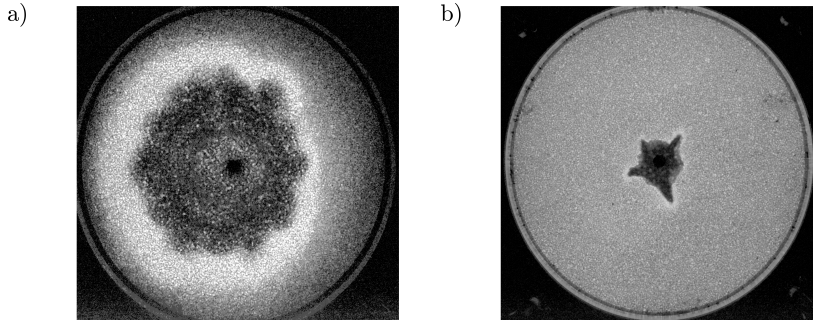


Fig. 6.11 Two experiments showing asymmetric porosity fields. (a) Finger-like protrusions due to the de-stabilization of an outwardly propagating compaction front. (b) Fingering behaviour due to flow in a cohesive porous medium. The greyscale denotes the measured light intensity (a.u.).

system reached a steady-state where viscous stresses imparted by the fluid on the solid balanced the compaction of the solid.

Correspondingly, an axisymmetric poroelastic continuum model was derived, assuming a pair of nonlinear isotropic constitutive laws for the permeability and solid stress. When fit, the model gave good agreement with the steady-state experimental results and gave a fitted bulk modulus in line with previous measurements. Furthermore, the transient evolution of the model was also in agreement with the experimental results when $\Phi \approx \phi_0$. When $\Phi > \phi_0$, the solid phase was easily fluidized and behaved as a suspension, which was simply advected by the injected fluid, rather than as an elastic solid.

In addition to altering the flow properties, deformation of the solid phase can play a critical role in transport and mixing of passive scalars. This can be important in CCS technologies where pore-scale dilation or contraction could lead to enhanced or reduced residual trapping or dissolution. Another example is in the understanding of temperature and composition transport in the mantle (Rees-Jones and Katz, 2018). More generally, the topics discussed in chapters 2-5 could now also be modified to consider transport in deformable media as well.

6.6.1 Asymmetric flows

To conclude, we briefly discuss experiments where the deformation was not axisymmetric, two examples of which are given in figure 6.11. Figure 6.11(a) shows a snapshot of the porosity field from an experiment with $\Phi = 0.62$ and a large injection flux. We find that the compaction band that propagates outwards becomes unstable to finger-like structures. We suspect that the instability in this case is driven by a mechanism

analogous to viscous fingering. Specifically, compacting the solid leads to locally higher effective viscosity, which is invaded by the less viscous displacing fluid. Such a configuration can be unstable to viscous fingering, resulting in unstable finger growth (note that an analogous instability was seen in suspension flows in a Hele-Shaw cell, Kim et al., 2017). In a different set of experiments of injection into a deformable porous medium with cohesive particles, we also find asymmetric deformation. Figure 6.11(b) shows a snapshot of the porosity field that is near jamming but where the particles are cohesive. In the experiment, we chemically treated the hydrogel beads to promote adhesion and find that when fluid is injected, finger-like structures grow on a much larger scale than the grain size. Understanding these two phenomena is the subject of future work.

Appendix 6.A List of experiments

Appendix 6.B Large pressure drop limit of the model

In this appendix we briefly consider the large pressure drop limit of the model where Δp across the packing is imposed instead of \mathcal{Q} . As noted in §6.3.2, imposing a pressure drop across the packing is equivalent to imposing the porosity at the outer boundary and therefore the limit $\Delta p \rightarrow \infty$ is equivalent to $\phi(1) = \phi_b \rightarrow 0$. The general steady-state flux for arbitrary constitutive laws for the permeability and solid stress is given by:

$$\mathcal{Q} \log \left(\frac{1}{\tilde{a}_s} \right) = \int_{\phi_0}^{\phi_b} k \sigma' d\phi. \quad (6.25)$$

After differentiation we find

$$\frac{\partial \mathcal{Q}}{\partial \phi_b} \log \tilde{a}_s = -k(\phi_b) \sigma'(\phi_b) - \frac{\mathcal{Q}}{\tilde{a}_s} \frac{\partial \tilde{a}_s}{\partial \phi_b}. \quad (6.26)$$

Assuming the constitutive laws are monotonic functions of ϕ and assuming $\partial \tilde{a}_s / \partial \phi_b < 0$, that is the cavity size grows as the outer porosity decays, then $\partial \mathcal{Q} / \partial \phi_b$ is always negative, and never takes on a maximum or minimum.

In the limit of vanishing ϕ_b , if we suppose the stress diverges like $\sigma \sim \phi_b^{-\beta}$, the permeability decays like $k \sim \phi_b^\alpha$, \tilde{a}_s is finite, and $\partial \tilde{a}_s / \partial \phi_b \rightarrow 0$, then

$$\frac{\partial \mathcal{Q}}{\partial \phi_b} \sim -\phi_b^{\alpha-\beta-1}. \quad (6.27)$$

$H(\pm 1\text{cm})$	$d(\pm 0.5\text{mm})$	$Q/d(\times 10^{-3}\text{m}^2/\text{s})$	Reached steady state?
80	25	1.1	yes
80	23	1.0	yes
80	21	1	yes
80	19	1.1	yes
80	17	1.1	yes
80	15	1.2	yes
40	25	0.52	yes
40	23	0.55	yes
40	21	0.6	yes
40	19	0.66	yes
40	17	0.69	yes
40	15	0.79	yes
20	25	0.35	no
20	23	0.37	no
20	21	0.34	yes
20	19	0.43	yes
20	17	0.48	yes
20	15	0.47	yes
10	25	0.21	no
10	23	0.22	no
10	21	0.24	no
10	19	0.26	no
10	17	0.26	yes
10	15	0.27	yes
5	25	0.14	no
5	23	0.15	no
5	21	0.16	no
5	19	0.17	no
5	17	0.18	yes
5	15	0.14	yes

Table 6.1 List of experiments.

This means that for $\alpha > \beta + 1$, the flux tends to a finite value for vanishing ϕ_b , while for $\alpha < \beta + 1$, the flux diverges. For the constitutive laws described in §6.3, $\alpha = 3$ and $\beta = 1$, which means the flux tends to a finite value for vanishing ϕ_b or large Δp .

Chapter 7

Conclusions and Future Work

7.1 Conclusions

In this thesis two distinct and fundamental features of flow through porous media were examined; the mixing of two fully miscible fluids of differing viscosity and density in homogeneous and heterogeneous porous media, and the flow-induced compaction of deformable porous media. In each case, the work was motivated by constraints related to the geological storage of carbon dioxide (CO₂).

In chapters 2-5, the displacement of one fluid by another fully miscible fluid in a semi-infinite porous medium was considered using high-resolution numerical simulations. In doing so, the aim was to identify the main flow regimes and the dominant physical balances in each of those regimes in order to develop simple models for the evolution of the concentration field.

In chapter 2, the displacement of a more-viscous fluid by a less-viscous fluid in a homogeneous porous medium was considered. Three distinct flow regimes were identified: an early-time linearly unstable regime, an intermediate-time nonlinear regime, and a late-time single-finger exchange-flow regime. The early-time growth of the interface was found to be dominated by longitudinal diffusion and the early-time fingering dynamics were set by a local balance between advection and diffusion at the finger scale. It was also showed that for a given log-viscosity ratio, R , there is a critical Peclet number, Pe_c , such that the instability is always suppressed. For the range of R considered, this stability boundary could be estimated by $Pe_c \approx 55/R$. At intermediate times the fingers spread longitudinally while coarsening and a model for the transversely averaged concentration was derived, which agreed with previous empirical models as well as the numerical simulations. At late times a new shutdown regime was found, which consisted of a single pair of counter-propagating fingers

that exponentially slowed leaving a linearly well-mixed interior. We also derived a model for this asymptotic behaviour, which showed good agreement with the numerical simulations and the total amount of convective mixing, F , was found to be well described by $F \approx 5.3 \times 10^{-3} R(\text{Pe} - 45/R)$. The implications for a specific CO₂ sequestration case study were also considered.

Next, stable and unstable displacements in layered heterogeneous porous media were examined in chapters 3 and 4, respectively. Specifically, the idealized case where the log-permeability varied sinusoidally with magnitude σ and frequency n was considered. In chapter 3 displacements where the injected and ambient fluids had the same viscosity were first considered. As in chapter 2, it was found that the early-time growth of the interface was dominated by longitudinal diffusion. At intermediate times the fluids spread advectively while at late times the interface between the fluids evolved through shear-enhanced dispersion. Next, the case where the injected and ambient fluids had different viscosities was considered, but when the viscosity difference was small compared to the permeability variations. In this limit the intermediate-time dynamics evolved as if the medium had effective permeability variations $\sigma_{\text{eff}} = \sigma + R/2$, and the late-time behaviour asymptotically approached the uniform viscosity case. The case where the injected fluid was more viscous than the ambient fluid and the viscosity variations were larger than the permeability variations was also considered. In this limit, the viscosity variations tended to prevent channelling and reduced spreading and mixing (as compared to the uniform viscosity case). Finally, a non-idealized permeability field derived from a real reservoir was considered and comparisons between the reduced-order models and the direct numerical simulations were made.

In chapter 4, injections of a less-viscous fluid into a layered heterogeneous porous medium saturated with a more-viscous fluid where the viscosity variations were larger than the permeability variations, were examined. As in chapter 2, it was found that this configuration could be hydrodynamically unstable, and that there was a competition between the evolving wavelength of the instability and the wavelength imposed by the permeability. At intermediate times this competition lead to four different possible regimes. First, the flow could finger within layers, resulting in nonlinear fingers that elongated and coarsened, leading to, on aggregate, advective growth of the mixing region. In this regime, small amounts of permeability heterogeneity qualitatively changed the structure of the flow and resulted in significantly enhanced spreading (as compared to a homogeneous medium). Second, the flow could channel along the layers, with no finger-finger interactions or large-scale coarsening, which resulted in exponentially slowing and diffusing fingers. Third, the interface fingered on a scale

much wider than the imposed permeability, and resulted in advective growth of the mixing region, which was slower than spreading in a homogeneous medium. Finally, these fingers coarsened until a single pair of fingers were left, which evolved in a manner similar to the shutdown regime in chapter 2. Finally, two non-idealized permeability fields were considered, one that was the superposition of two different wavelength modes, and one derived from a real reservoir.

In chapter 5, unstable displacements in homogeneous porous media were again considered (as in chapter 2), but now the density of the two fluids was assumed to be different, parameterized by G . Displacements where $G \neq 0$ but the injected and ambient fluids had the same viscosity were first considered before examining the overall dynamics when both the density and viscosity varied. In general, at early times, vertical flow was important and lead to either small-scale fingers along the boundary, in the viscosity dominated limit, or large-scale slumping, in the density dominated limit. At intermediate times, vertical flow could be neglected and the interface evolved through either fingering, in the small G limit, a single pressure-driven gravity current, in the moderate G limit, or a single density-driven gravity current, in the large G limit. Over time the fingering and density-driven gravity current limits both tended to the pressure-driven gravity current limit. Finally at late times, transverse diffusion was important and a transition in the dynamics from a shutdown regime (analogous to the shutdown regime in chapter 2) to a viscously-enhanced Taylor slumping regime was found. Finally, the dominant physical balances in three different CO₂ sequestration case studies were considered, and it was found that viscous fingering was important at In Salah and Salt Creek but unimportant at Sleipner.

In the final portion of this thesis (chapter 6) the fluid-driven compaction of a deformable porous medium was examined. The experimental setup involved the injection of water into a variably confined, water-saturated packing of soft hydrogel spheres, and dye-attenuation techniques were used to measure the depth-averaged porosity field. An axisymmetric, large-deformation, poroelastic model was derived for the fluid flow and deformation of the porous medium. The steady-state results of the model were then compared to the experiments, which showed good agreement for packings with initial porosities above jamming, but there were discrepancies for initially strongly confined porous media. The transient results of the poroelastic model also showed good agreement with the experiments for initial porosities near jamming, but for initially high porosities, the solid deformed viscously rather than elastically.

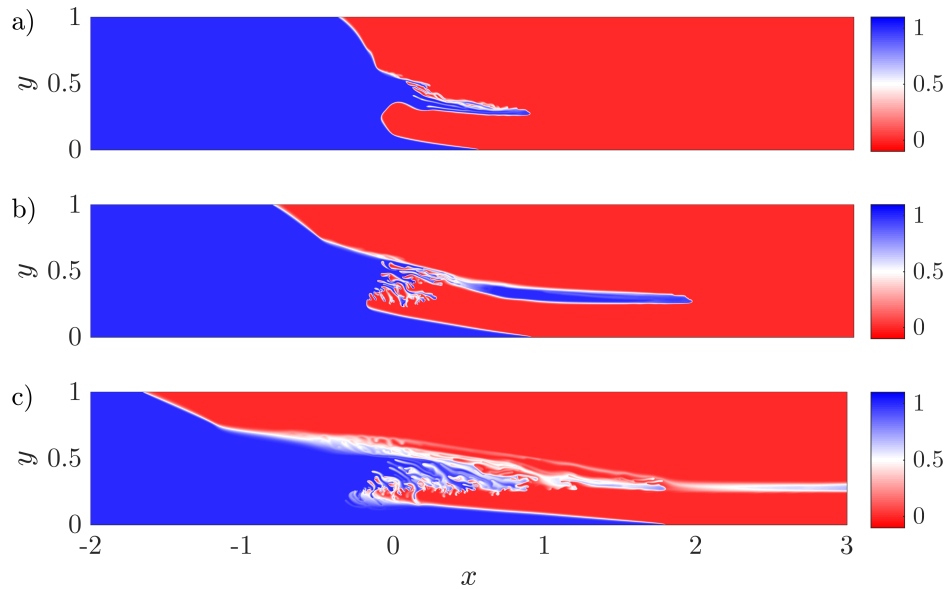


Fig. 7.1 Preliminary numerical simulations of a less-viscous, more-dense fluid injected into a layered porous medium saturated with a more-viscous, less-dense fluid. The permeability field consists of four alternating layers of high and low permeability. (a) $t = 0.15$, (b) $t = 0.4$, and (c) $t = 1$.

7.2 Future work

This thesis lays the ground work for a number of directions of further study. A natural extension of the analyses in chapters 2-5 would be to consider the combined effects of viscous fingering, layered permeability heterogeneities and buoyancy gradients. First, this requires understanding the uniform viscosity case, where the permeability varies and the injected and ambient fluids have different densities. Hinton and Woods (2018) studied gravity currents in layered porous media in the limit of sharp-interfaces and vertical-flow-equilibrium, which ignores any small scale fingering or mixing. Huppert et al. (2013) studied, using experiments, the transition from convectively stable configurations to convectively unstable ones. This transition resulted in small-scale fingering, but the rate of mixing in the unstable configurations remain unknown. In addition, by introducing different viscosity fluids, the interface can also be unstable to viscous fingering, which can greatly enhance mixing and spreading. Some preliminary numerical simulations are given in figure 7.1, which show a range of different small-scale behaviour including viscous fingering, and Rayleigh-Taylor fingering, in addition to stable regions that are channelized by the permeability field. The goal would be to model the amount of mixing as a function of the different parameters.

Another natural extension of the work in this thesis would be to consider the effect of changing the geometry. Throughout this thesis only a two-dimensional planar geometry was considered, and it is unknown as to how much the quantitative analyses in chapters 2-5 change with different geometries. In two-dimensions, miscible flows in cylindrical porous geometries have received relatively little attention. Although there is a significant body of work that has examined miscible instabilities in Hele-Shaw cells (see for example, Bischofberger et al., 2014; Lajeunesse et al., 1999), they have, for the most part, been limited to fast, non-Darcian, flows. Two notable exceptions are the works of Chui et al. (2015) and Videbaek and Nagel (2019) who considered slow flows in Hele-Shaw cells; however, a quantitative description of the viscous fingering instability, and the effects of permeability heterogeneities and buoyancy gradients is yet to be explored. Similarly, investigations of miscible displacements in three-dimensional geometries are relatively scarce. Although in three-dimensions, the flow evolves in qualitatively the same way as the two-dimensional case (Zimmerman and Homsy, 1992a), there are quantitative differences (Riaz and Meiburg, 2003). Elucidating these differences, and determining the long-time asymptotic behaviour is one potential avenue for further work.

In chapters 2-5, it was assumed that the two fluids were fully miscible. However, as alluded to in chapter 1, in many geological settings, including in the subsurface storage of CO₂, the fluids are only partially miscible. One way to extend the results in this thesis would be to consider fully immiscible displacements using a Buckley-Leverett-type formulation for the evolution of the saturation. This has been used to study the onset of viscous fingering and qualitatively describe its nonlinear evolution (Riaz et al., 2007; Riaz and Tchelepi, 2004, 2006), but a quantitative description of the overall life-cycle of evolution remains to be understood. There are qualitative similarities between miscible and immiscible displacements in porous media, but these similarities and differences have not been systematically described.

To validate the modelling assumptions, and for a more complete understanding of mixing due to miscible displacement processes, comparisons need to be made to simple laboratory experiments, to check that the correct physics has been incorporated into the models. Furthermore, direct comparisons need to be made to field-scale experiments to quantify the effects of geological inhomogeneities.

In chapter 6, the model and the experimental results were, for the most part, axisymmetric. However, in the conclusions of that chapter it was noted that finger-like structures in weakly-confined and cohesive media also formed. One potential avenue for future work would be to better understand, both using laboratory experiments and

theoretical-modelling, the formation of the finger-like structures and their implications to flow and transport.

More generally, outstanding questions remain at the intersection of these two topics. Specifically, during the geological storage of carbon dioxide, the coupling of mixing and deformation can influence the long-term storage capacity of a reservoir. For example, mixing can impact deformation through the dissolution of the solid phase, while flow-induced deformation can affect the transport properties through the narrowing or dilation of pores. Therefore, further understanding the dynamics of mixing in deformable porous media is critical to better inform the constraints on the safe storage of CO₂, in order to move this technology forward.

References

- Abriola, L. (1987). Modeling contaminant transport in the subsurface: an interdisciplinary challenge. *Rev. Geophys.*, 25(2):125–134.
- Adams, J. (1999). Computational information systems laboratory. mudpack: Multigrid software for elliptic partial differential equations.
- Afshari, S., Hejazi, S., and Kantzas, A. (2018). Role of medium heterogeneity and viscosity contrast in miscible flow regimes and mixing zone growth: A computational pore-scale approach. *Phys. Rev. Fluids*, 3:054501.
- Afshari, S., Hejazi, S., and Kantzas, A. (2019). Pore-level modeling of effective longitudinal thermal dispersion in non-isothermal flows through granular porous media. *Chem. Eng. Sci.*, 199:451–462.
- Al-Housseiny, T., Tsai, P., and Stone, H. (2012). Control of interfacial instabilities using flow geometry. *Nat. Phys.*, 8:747–750.
- Allen, B. and Kudrolli, A. (2018). Granular bed consolidation, creep, and armoring under subcritical fluid flow. *Phys. Rev. Fluids*, 3:074305.
- Almarcha, C., Trevelyan, P., Grosfils, P., and De Wit, A. (2010). Chemically driven hydrodynamic instabilities. *Phys. Rev. Lett.*, 104:144501.
- Araktingi, U. and Orr Jr., F. (1993). Viscous fingering in heterogeneous porous media. *SPE Adv. Tech. Ser.*, 1:71–80.
- Aris, R. (1956). On the dispersion of a solute in a fluid flowing through a tube. *Proc. R. Soc. Lond. A*, 235:67–77.
- Auton, L. and MacMinn, C. (2017). From arteries to boreholes: steady-state response of a poroelastic cylinder to fluid injection. *Proc. Roy. Soc. A*, 473:20160753.
- Auton, L. and MacMinn, C. (2018). From arteries to boreholes: transient response of a poroelastic cylinder to fluid injection. *Proc. Roy. Soc. A*, 474:20180284.
- Barry, S. I. and Aldis, G. K. (1993). Radial flow through deformable porous shells. *J. Austral. Math. Soc. B. Appl. Math.*, 34:333.
- Bear, J. (1988). *Dynamics of fluids in porous media*. American Elsevier Publishing Company.

- Berentsen, C., Verlaan, M., and van Kruijsdijk C.P.J.W. (2005). Upscaling and reversibility of Taylor dispersion in heterogeneous porous media. *Phys. Rev. E*, 71:046308.
- Berg, S., Oedai, S., Landman, A., Brussee, N., Boele, M., Valdez, R., and van Gelder, K. (2010). Miscible displacement of oils by carbon disulfide in porous media: Experiments and analysis. *Phys. Fluids*, 22(113102).
- Berhanu, M., Petroff, A., Devauchelle, O., Kudrolli, A., and Rothman, D. (2012). Shape and dynamics of seepage erosion in a horizontal granular bed. *Phys. Rev. E*, 86:041304.
- Bickle, M., Chadwick, R., Huppert, H., Hallworth, M., and Lyle, S. (2007). Modelling carbon dioxide accumulation at sleipner: implications for underground carbon storage. *Earth Planet. Sci. Lett.*, 255:164–176.
- Bickle, M., Kampman, N., Chapman, H., Ballentine, C., Dubacq, B., Galy, A., Sirikitputtisak, T., Warr, O., Wigley, M., and Zhou, Z. (2017). Rapid reactions between co₂, brine and silicate minerals during geological carbon storage: Modelling based on a field co₂ injection experiment. *Chem. Geo.*, 468:17–31.
- Biot, M. (1941). General theory of three-dimensional consolidation. *J. App. Phys.*, 12:155–164.
- Bischofberger, I., Ramachandran, R., and Nagel, S. (2014). Fingering versus stability in the limit of zero interfacial tension. *Nat. Comm.*, 5265(5).
- Blackwell, R., Rayne, J., and Terry, W. (1959). Factors influencing the efficiency of miscible displacements. *Petr. Trans. AIME*, 216:1–8.
- Boait, F., White, N., Bickle, M., Chadwick, R., Neufeld, J., and Huppert, H. (2012). Spatial and temporal evolution of injected co₂ at the sleipner field, north sea. *J. Geophys. Res.*, 117.
- Booth, R. (2010). On the growth of the mixing zone in miscible viscous fingering. *J. Fluid Mech.*, 655:527–539.
- Boulogne, F., Kong, Y. L., Nunes, J. K., and Stone, H. A. (2016). Effect of the polydispersity of a colloidal drop on the drying induced stress as measured by the buckling of a floating sheet. *Phys. Rev. Lett.*, 116:238001.
- Cadogan, S., Maitland, G., and Trusler, J. (2014). Diffusion coefficients of co₂ and n₂ in water at temperatures between 298.15 k and 423.15 k at pressures up to 45 mpa. *J. Chem. Eng. Data*, 59:519–525.
- Camacho, J. (1993). Purely global model for Taylor dispersion. *Phys. Rev. E*, 48:310–321.
- Camhi, E., Meiburg, E., and Ruith, M. (2000). Miscible rectilinear displacements with gravity override. Part 2. Heterogeneous porous media. *J. Fluid Mech.*, 420:259–276.

- Catchpoole, H., Shalliker, R., Dennis, G., and Guiochon, G. (2006). Visualising the onset of viscous fingering in chromatography columns. *J. Chromatography A*, 1117:137–145.
- Celia, M., Bachu, S., Nordbotten, J., and Bandilla, K. (2015). Status of co2 storage in deep saline aquifers with emphasis on modeling approaches and practical simulations. *Water Resour. Res.*, 51:6846–6892.
- Chen, C.-Y. and Meiburg, E. (1998a). Miscible porous media displacements in the quarter five-spot configuration. part 1. the homogeneous case. *J. Fluid Mech.*, 371:233–268.
- Chen, C.-Y. and Meiburg, E. (1998b). Miscible porous media displacements in the quarter five-spot configuration. part 2. effect of heterogeneities. *J. Fluid Mech.*, 371:269–299.
- Chen, C.-Y. and Meiburg, E. (1998c). Miscible porous media displacements in the quarter five-spot configuration. part 2. effect of heterogeneities. *J. Fluid Mech.*, 371:269–299.
- Chen, J.-D. (1987). Radial viscous fingering patterns in hele-shaw cells. *Exp. Fluids*, 5:363–371.
- Chen, J.-D. and Wilkinson, D. (1985). Pore-scale viscous fingering in porous media. *Phys. Rev. Lett.*, 55:1892–1895.
- Chui, J., De Anna, P., and Juanes, R. (2015). Interface evolution during radial miscible viscous fingering. *Phys. Rev. E*, 92:041003(R).
- Cowin, S. (1999). Bone poroelasticity. *J. Biomech.*, 32:217–238.
- Dalbe, M. and Juanes, R. (2018). Morphodynamics of fluid-fluid displacement in three-dimensional deformable granular media. *Phys. Rev. App.*, 9:024028.
- Datta, S., Preska Steinberg, A., and Ismagilov, R. (2016). Polymers in the gut compress the colonic mucus hydrogel. *Proc. Nat. Acad. Sci.*, 113:7041–7046.
- de Anna, P., Dentz, M., Tartakovsky, A., and Le Borgne, T. (2014). The filamentary structure of mixing fronts and its control on reaction kinetics in porous media flows. *Geophys. Res. Lett.*, 41:4586–4593.
- De Wit, A. and Homsy, G. (1999). Viscous fingering in reaction-diffusion systems. *J. Chem. Phys.*, 110:8663–8675.
- De Wit, A. and Homsy, G. M. (1997a). Viscous fingering in periodically heterogeneous porous media. I. Formulation and linear instability. *J. Chem. Phys.*, 107:9609.
- De Wit, A. and Homsy, G. M. (1997b). Viscous fingering in periodically heterogeneous porous media. II. Numerical simulations. *J. Chem. Phys.*, 107:9619.
- Dentz, M. and Carrera, J. (2007). Mixing and spreading in stratified flow. *Phys. Fluids*, 19:017107.

- Dentz, M., Le Borgne, T., Englert, A., and Bijeljic, B. (2011). Mixing, spreading and reaction in heterogeneous media: A brief review. *J. Contam. Hydrol.*, 120:1–17.
- Detournay, E. (2016). Mechanics of hydraulic fractures. *Ann. Rev. Fluid Mech.*, 48:311–339.
- Ennis-King, J. and Paterson, L. (2005). Role of convective mixing in the long-term storage of carbon dioxide in deep saline formations. *Soc. Petr. Eng. J.*, 10:349–356.
- Eriksen, F., Toussaint, R., Maloy, K., and Flekkoy, E. (2015). Invasion patterns during two-phase flow in deformable media. *Front. Phys.*, 3:00081.
- European Academies Science Advisory Council (2018). Negative emission technologies: What role in meeting paris agreement targets? Technical report.
- Fayers, F. J., Blunt, M. J., and Christie, M. A. (1992). Comparisons of empirical viscous-fingering models and their calibration for heterogeneous problems. *SPE Reservoir Eng.*, 7:195–203.
- Fleury, P., Bakalowicz, M., and de Marsily, G. (2007). Submarine springs and coastal karst aquifers: a review. *J. Hydrol.*, 339:79–92.
- Fritton, S. and Weinbaum, S. (2009). Fluid and solute transport in bone: Flow-induced mechanotransduction. *Ann. Rev. Fluid Mech.*, 41:347–374.
- Gomez, M., Moulton, D., and Vella, D. (2017). Passive control of viscous flow via elastic snap-through. *Phys. Rev. Lett.*, 119:144502.
- Gummer, J., Brown, B., Chater, N., Heaton, R., Hoskins, B., Johnson, P., Le Quere, C., and Skea, J. (2018). Reducing uk emissions: 2018 progress report to parliament. Technical report.
- Hesse, M., Orr Jr., F., and Tchelepi, H. (2008). Gravity currents with residual trapping. *J. Fluid Mech.*, 611:35–60.
- Hesse, M., Tchelepi, H., Cantwell, B., and Orr Jr., F. (2007). Gravity currents in horizontal porous layers: transition from early to late self-similarity. *J. Fluid Mech.*, 577:363–383.
- Hewitt, D., Neufeld, J., and Balmforth, N. (2015). Shallow, gravity-driven flow in a poro-elastic layer. *J. Fluid Mech.*, 778:335–360.
- Hewitt, D., Neufeld, J., and Lister, J. R. (2012). Ultimate regime of high rayleigh number convection in a porous medium. *Phys. Rev. Lett.*, 108:224503.
- Hewitt, D., Neufeld, J., and Lister, J. R. (2013). Convective shutdown in a porous medium at high Rayleigh number. *J. Fluid Mech.*, 719:551–586.
- Hewitt, D., Nijjer, J., Worster, M., and Neufeld, J. (2016). Flow-induced compaction of a deformable porous medium. *Phys. Rev. E*, 93(2-1):023116.
- Hill, S. (1952). Channelling in packed columns. *Chem. Eng. Sci.*, 1:247–253.

- Hinton, E. and Woods, A. (2018). Buoyancy-driven flow in a confined aquifer with a vertical gradient of permeability. *J. Fluid Mech.*, 848:411–429.
- Hogg, A., Huppert, H., and Dade, W. (1996). Erosion by planar turbulent wall jets. *J. Fluid Mech.*, 338:317–340.
- Homsy, G. (1987). Viscous fingering in porous media. *Ann. Rev. Fluid Mech.*, 19:271–311.
- Hoshino, K., Nakajima, T., Matsuda, T., Sakai, T., and Gong, J. (2018). Network elasticity of a model hydrogel as a function of swelling ratio: from shrinking to extreme swelling states. *Soft Matter*, 14:9693–9701.
- Huppert, H. (2006). Gravity currents: a personal perspective. *J. Fluid Mech.*, 554:299–322.
- Huppert, H. and Neufeld, J. (2014). The fluid mechanics of carbon dioxide sequestration. *Ann. Rev. Fluid Mech.*, 46:255–272.
- Huppert, H., Neufeld, J., and Strandkvist, C. (2013). The competition between gravity and flow focusing in two-layered porous media. *J. Fluid Mech.*, 720:5–14.
- Huppert, H. and Woods, A. (1995). Gravity-driven flows in porous layers. *J. Fluid Mech.*, 292:55–69.
- Islam, M. and Azaiez, J. (2005). Fully implicit finite difference pseudo-spectral method for simulating high mobility-ratio miscible displacements. *Int. J. Num. Meth. Fluids*, 1:161–183.
- Jha, B., Cueto-Felgueroso, L., and Juanes, R. (2011a). Fluid mixing from viscous fingering. *Phys. Rev. Lett.*, 106:194502.
- Jha, B., Cueto-Felgueroso, L., and Juanes, R. (2011b). Quantifying mixing in viscously unstable porous media flows. *Phys. Rev. E*, 84:066312.
- Jha, B., Cueto-Felgueroso, L., and Juanes, R. (2013). Synergetic fluid mixing from viscous fingering and alternating injection. *Phys. Rev. Lett.*, 111:144501.
- Jiao, C.-Y. and Hotzl, H. (2004). An experimental study of miscible displacements in porous media with variation of fluid density and viscosity. *Trans. Por. Med.*, 54:125–144.
- Katz, R., Spiegelman, M., and Holtzman, B. (2006). The dynamics of melt and shear localization in partially molten aggregates. *Nature*, 442:676.
- Kenyon, D. (1979). A mathematical model of water flux through aortic tissue. *Bull. Math. Biol.*, 41:79–90.
- Khataniar, K. and Peters, E. (1992). The effect of reservoir heterogeneity on the performance of unstable displacements. *J. Pet. Sci. Eng.*, 7:263 – 281.
- Kim, J., Xu, F., and Lee, S. (2017). Formation and destabilization of the particle band on the fluid-fluid interface. *Phys. Rev. Lett.*, 118:074501.

- Koval, E. (1963). A Method for Predicting the Performance of Unstable Miscible Displacement in Heterogeneous Media. *Soc. Petr. Eng. J.*, 3(02):145–154.
- Krupp, A. (2017). *Mathematical modelling of membrane filtration*. PhD thesis, Oxford University.
- Kudrolli, A. and Clotet, X. (2016). Evolution of porosity and channelization of an erosive medium driven by fluid flow. *Phys. Rev. Lett.*, 117:028001.
- Lajeunesse, E., Martin, J., Rakotomalala, N., Salin, D., and Yortsos, Y. (1999). Miscible displacement in a Hele-Shaw cell at high rates. *J. Fluid Mech.*, pages 299–319.
- Lake, L. (1989). *Enhanced oil recovery*. Prentice Hall.
- Lanir, Y., Sauob, S., and Maretsky, P. (1990). Nonlinear finite deformation response of open cell polyurethane sponge to fluid filtration. *J. Applied Mech.*, 57:449–454.
- Le Borgne, T., Dentz, M., and Villermaux, E. (2013). Stretching, coalescence, and mixing in porous media. *Phys. Rev. Lett.*, 110:204501.
- Lee, S., Lee, J., Le Mestre, R., F., X., and C.W., M. (2018). Capturing gas in a soft granular material. available at <https://arxiv.org/abs/1808.02921>.
- Lele, S. (1992). Compact finite difference schemes with spectral-like resolution. *J. Comp. Phys.*, 103:16–42.
- Litster, S. and McLean, G. (2004). Pem fuel cell electrodes. *J. Power Sources*, 130:61–76.
- Loggia, D., Rakotomalala, N., Salin, D., and Yortsos, Y. (1996). Phase diagram of stable miscible displacements in layered porous media. *Europhys. Lett.*, 36(2):105–110.
- Loggia, D., Rakotomalala, N., Salin, D., and Yortsos, Y. (1999). The effect of mobility gradients on viscous instabilities in miscible flows in porous media. *Phys. Fluids*, 11:740–742.
- Lyu, X. and Woods, A. (2016). Experimental insights on the development of buoyant plumes injected into a porous media. *Geophys. Res. Lett.*, 43:709–718.
- MacMinn, C., Dufresne, E., and Wettlaufer, J. (2015). Fluid-Driven Deformation of a Soft Granular Material. *Phys. Rev. X*, 5(1):011020.
- MacMinn, C., Dufresne, E., and Wettlaufer, J. (2016). Large Deformations of a Soft Porous Material. *Phys. Rev. Appl.*, 5(4):044020.
- MacMinn, C. and Juanes, R. (2013). Buoyant currents arrested by convective dissolution. *Geophys. Res. Lett.*, 40:2017–2022.
- Mahadevan, A., Orpe, A., Kudrolli, A., and Mahadevan, L. (2012). Flow-induced channelization in a porous medium. *Europhys. Lett.*, 98:58003.
- Malhotra, S., Sharma, M. M., and Lehman, E. (2015). Experimental study of the growth of mixing zone in miscible viscous fingering. *Phys. Fluids*, 27:014105.

- Matter, J., Stute, M., Snaebjornsdottir, S., Oelkers, E., Gislason, S., Aradottir, E., Sigfusson, B., Gunnarsson, I., Sigurdardottir, H., Gunnlaugsson, E., Axelsson, G., Alfredsson, H., Wolff-Boenisch, D., Mesfin, K., Fernandez de la Reguera Taya, D., Hall, J., Dideriksen, K., and Broecker, W. (2016). Rapid carbon mineralization for permanent disposal of anthropogenic carbon dioxide emissions. *Science*, 352:1312–1314.
- Mayfield, K., Shalliker, R., Catchpoole, H., Sweeney, A., Wong, V., and Guiochon, G. (2005). Viscous fingering induced flow instability in multidimensional liquid chromatography. *J. Chromatography A*, 1080:124–131.
- McCloud, K. and Maher, J. (1995). Experimental perturbations to Saffman-Taylor flow. *Phys. Rep.*, 260:139–185.
- McKenzie, D. (1984). The Generation and Compaction of Partially Molten Rock. *J. Petro.*, 25:713–765.
- Miller, W., Alexander, R., Chapman, N., McKinley, I., and Smellie, J. (2000). *Geological disposal of radioactive wastes and natural analogues*. Elsevier Science.
- Mishra, M., Martin, M., and De Wit, A. (2008). Differences in miscible viscous fingering of finite width slices with positive or negative log-mobility ratio. *Phys. Rev. E*, 78:066306.
- Mishra, M., Trevelyan, P., Almarcha, C., and De Wit, A. (2010). Influence of double diffusive effects on miscible viscous fingering. *Phys. Rev. Lett.*, 105:204501.
- Mogilner, A. and Manhart, A. (2017). Intracellular fluid mechanics: Coupling cytoplasmic flow with active cytoskeletal gel. *Ann. Rev. Fluid Mech.*, 50:347–370.
- Mukherjee, P., Kang, Q., and Wang, C.-Y. (2011). Pore-scale modeling of two-phase transport in polymer electrolyte fuel cells—progress and perspective. *Energy Environ. Sci.*, 4:346–369.
- Murphy, H., Tester, J., Grigsby, C., and Potterm, R. (1981). Energy extraction from fractured geothermal reservoirs in low-permeability crystalline rock. *J. Geophys. Res.*, 86:7145–7158.
- Neufeld, J. A., Hesse, M. A., Riaz, A., Hallworth, M. A., Tchelepi, H. A., and Huppert, H. E. (2010). Convective dissolution of carbon dioxide in saline aquifers. *Geophys. Res. Lett.*, 37(22):L22404.
- Nicolaides, C., Jha, B., Cueto-Felgueroso, L., and Juanes, R. (2015). Impact of viscous fingering and permeability heterogeneity on fluid mixing in porous media. *Water Resour. Res.*, 51:2634–2647.
- Nijjer, J., Hewitt, D., and Neufeld, J. (2018). The dynamics of miscible viscous fingering from onset to shutdown. *J. Fluid Mech.*, 837:520–545.
- Nijjer, J., Hewitt, D., and Neufeld, J. (2019). Stable and unstable miscible displacements in layered porous media. *J. Fluid Mech.*, 869:468–499.

- Nordstrom, K. N., Verneuil, E., Ellenbroek, W. G., Lubensky, T. C., Gollub, J. P., and Durian, D. J. (2010). Centrifugal compression of soft particle packings: theory and experiment. *Phys. Rev. E*, 82(4 Pt 1):041403.
- Norouzi, M. and Shoghi, M. (2014). A numerical study on miscible viscous fingering instability in anisotropic porous media. *Phys. Fluids*, 26:084102.
- Parker, K., Mehta, R., and Caro, C. (1987). Steady flow in porous, elastically deformable materials. *J. Applied Mech.*, 54:794–799.
- Paterson, L. (1985). Fingering with miscible fluids in a Hele Shaw cell. *Phys. Fluids*, 28:26–30.
- Pegler, S., Huppert, H., and Neufeld, J. (2014). Fluid injection into a confined porous layer. *J. Fluid Mech.*, 745:592–620.
- Pihler-Puzovic, D., Illien, P., Heil, M., and Juel, A. (2012). Suppression of complex fingerlike patterns at the interface between air and a viscous fluid by elastic membranes. *Phys. Rev. Lett.*, 108:074502.
- Pramanik, S., De Wit, A., and Mishra, M. (2015). Viscous fingering and deformation of a miscible circular blob in a rectilinear displacement in porous media. *J. Fluid Mech.*, 782:R2.
- Pramanik, S. and Mishra, M. (2015). Effect of Peclet number on miscible rectilinear displacement in a Hele-Shaw cell. *Phys. Rev. E*, 033006.
- Rabbani, H., Or, D., Liu, Y., Lai, C.-Y., Lu, N., Datta, S., Stone, H., and Shokri, N. (2018). Suppressing viscous fingering in structured porous media. *Proc. Natl. Acad. Sci.*, 115(19):4833–4838.
- Rees-Jones, D. and Katz, R. (2018). Reaction-infiltration instability in a compacting porous medium. *J. Fluid Mech.*, 852:5–36.
- Riaz, A. and Meiburg, E. (2003). Three-dimensional miscible displacement simulations in homogeneous porous media with gravity override. *J. Fluid Mech.*, 494:95–117.
- Riaz, A., Tang, G.-Q., Tchelepi, H., and Kovscek, A. (2007). Forced imbibition in natural porous media: comparison between experiments and continuum models. *Phys. Rev. E*, 75:0363305.
- Riaz, A. and Tchelepi, H. (2004). Linear stability analysis of immiscible two-phase flow in porous media with capillary dispersion and density variation. *Phys. Fluids*, 16:4727.
- Riaz, A. and Tchelepi, H. (2006). Numerical simulation of immiscible two-phase flow in porous media. *Phys. Fluids*, 18:014104.
- Rogerson, A. and Meiburg, E. (1993a). Numerical simulation of miscible displacement processes in porous media flows under gravity. *Phys. Fluids*, 5:2644–2660.
- Rogerson, A. and Meiburg, E. (1993b). Shear stabilization of miscible displacement processes in porous media. *Phys. Fluids*, 5:1344–1355.

- Ruith, M. and Meiburg, E. (2000). Miscible rectilinear displacements with gravity override. Part 1. Homogeneous porous medium. *J. Fluid Mech.*, 420:225–257.
- Saffman, P. G. and Taylor, G. (1958). The Penetration of a Fluid into a Porous Medium or Hele-Shaw Cell Containing a More Viscous Liquid. *Proc. Roy. Soc. A*, 245(1242):312–329.
- Sajjadi, M. and Azaiez, J. (2013). Scaling and unified characterization of flow instabilities in layered heterogeneous porous media. *Phys. Rev. E*, 88:033017.
- Sandnes, B., Flekkoy, E., Maloy, K., and See, H. (2011). Patterns and flow in frictional fluid dynamics. *Nat. Comm.*, 2:288.
- Sandnes, B., Knudsen, H., Maloy, K., and Flekkoy, E. (2007). Labyrinth patterns in confined granular-fluid systems. *Phys. Rev. Lett.*, 99:038001.
- Schoonman, C., White, N., and Pritchard, D. (2017). Radial viscous fingering of hot asthenosphere within the icelandic plume beneath the north atlantic ocean. *Earth Planet. Sci. Lett.*, 468:51–61.
- Shahnazari, M., Maleka Ashtiani, I., and Saberi, A. (2018). Linear stability analysis and nonlinear simulation of the channeling effect on viscous fingering instability in miscible displacement. *Phys. Fluids*, 30(034106).
- Sharma, V., Pramanik, S., Chen, C.-Y., and Mishra, M. (2019). A numerical study on reaction-induced radial fingering instability. *J. Fluid Mech.*, 862:624–638.
- Simmons, C., Fenstermaker, T., and Sharp Jr, J. (2001). Variable-density groundwater flow and solute transport in heterogeneous porous media: approaches, resolutions and future challenges. *J. Contam. Hydrol.*, 52:245–275.
- Spiegelman, M. (1993a). Flow in deformable porous media. part 1 simple analysis. *J. Fluid Mech.*, 247:17–38.
- Spiegelman, M. (1993b). Flow in deformable porous media. part 2 numerical analysis—the relationship between shock waves and solitary waves. *J. Fluid Mech.*, 247:39–63.
- Stone, H., Stroock, A., and Ajdari, A. (2004). Engineering flows in small devices: microfluidics toward a lab-on-a-chip. *Ann. Rev. Fluid Mech.*, 36:381–411.
- Szulczewski, M. and Juanes, R. (2013). The evolution of miscible gravity currents in horizontal porous layers. *J. Fluid Mech.*, 719:82–96.
- Szulczewski, M., MacMinn, C., Herzog, H., and Juanes, R. (2012). Lifetime of carbon capture and storage as a climate-change mitigation technology. *Proc. Nat. Acad. Sci.*, 109:5185–5189.
- Talon, L., Martin, J., Rakotomalala, N., and Salin, D. (2004). Stabilizing viscosity contrast effect on miscible displacement in heterogeneous porous media, using lattice bhatnagar-gross-krook simulations. *Phys. Fluids*, 16(12):4408–4411.
- Tan, C. and Homsy, G. (1986). Stability of miscible displacements in porous media: Rectilinear flow. *Phys. Fluids*, 29:3549.

- Tan, C. and Homsy, G. (1987). Stability of miscible displacements in porous media: Radial source flow. *Phy. Fluids*, 30(5):1239–1245.
- Tan, C. and Homsy, G. (1988). Simulation of nonlinear viscous fingering in miscible displacement. *Phys. Fluids*, 31:1330.
- Tan, C. and Homsy, G. (1992). Viscous fingering with permeability heterogeneity. *Phys. Fluids*, 4(6):1099–1101.
- Taylor, G. I. (1953). Dispersion of Soluble Matter in Solvent Flowing Slowly through a Tube. *Proc. Roy. Soc. A*, 219(1137):186–203.
- Tchelepi, H., Orr, F., Rakotomalala, N., Salin, D., and Woumeni, R. (2004). Stabilizing viscosity contrast effect on miscible displacement in heterogeneous porous media, using lattice bhatnagar-gross-krook simulations. *Phy. Fluids*, 16(12):4408–4411.
- Tchelepi, H. and Orr Jr., F. (1994). Interaction of viscous fingering, permeability heterogeneity, and gravity segregation in three dimensions. *SPE Reservoir Eng.*, pages 266–271.
- Terzaghi, K. (1943). *Theoretical soil mechanics*. John Wiley and Sons.
- Van den Broeck, C. and Mazo, R. (1983). Exact results for the asymptotic dispersion of particles in n-layer systems. *Phys. Rev. Lett.*, 51(15):1309–1312.
- Vasco, D. W., Rucci, A., Ferretti, A., Novali, F., Bissell, R. C., Ringrose, P. S., Mathieson, A. S., and Wright, I. W. (2010). Satellite-based measurements of surface deformation reveal fluid flow associated with the geological storage of carbon dioxide. *Geophys. Res. Lett.*, 37.
- Videbaek, T. and Nagel, S. (2019). Diffusion-driven transition between two regimes of viscous fingering. *Phys. Rev. Fluids*, 4:033902.
- Villiermaux, E. (2012). Mixing by porous media. *Comptes Rendus Mécanique*, 340:933–943.
- Waggoner, J., Castillo, J., and Lake, L. (1992). Simulation of eor processes in stochastically generated permeable media. *SPE Formation Evaluation*, 7:173–180.
- Weber, K. (1986). How heterogeneity affects oil recovery. *Proceedings of the reservoir characterization technical conference*, pages 487–544.
- Welty, C. and Gelhar, L. (1991). Stochastic analysis of the effects of fluid density and viscosity variability on macrodispersion in heterogeneous porous media. *Water Resour. Res.*, 27(8):2061–2075.
- Woods, A. (1999). Liquid and vapor flow in superheated rock. *Ann. Rev. Fluid Mech.*, 31:171–199.
- Woods, A. (2015). *Flow in porous rocks: Energy and environmental applications*. Cambridge University Press.

- Woods, A. and Mingotti, N. (2016). Topographic viscous fingering: fluid-fluid displacement in a channel of non-uniform gap width. *Phil. Trans. Royal Soc. A*, 374:20150427.
- Yang, Z. and Yortsos, Y. C. (1997). Asymptotic solutions of miscible displacements in geometries of large aspect ratio. *Phys. Fluids*, 9:286–298.
- Yortsos, Y. (1995). A theoretical analysis of vertical flow equilibrium. *Trans. Por. Med.*, 18:107–129.
- Yortsos, Y. C. and Salin, D. (2006). On the selection principle for viscous fingering in porous media. *J. of Fluid Mech.*, 557:225.
- Zheng, Z., Guo, B., Christov, I., Celia, M., and Stone, H. (2015a). Flow regimes for fluid injection into a confined porous medium. *J. Fluid Mech.*, 767:881–909.
- Zheng, Z., Kim, H., and Stone, H. (2015b). Controlling viscous fingering using time-dependent strategies. *Phys. Rev. Lett.*, 115:174501.
- Zhou, Q. (2013). Temporal evolution and scaling of mixing in two-dimensional Rayleigh-Taylor turbulence. *Phys. Fluids*, 25.
- Zimmerman, W. and Homsy, G. (1992a). Three dimensional viscous fingering: A numerical study. *Phys. Fluids*, 4:1901–1914.
- Zimmerman, W. B. and Homsy, G. M. (1991). Nonlinear viscous fingering in miscible displacement with anisotropic dispersion. *Phys. Fluids*, 3:1859.
- Zimmerman, W. B. and Homsy, G. M. (1992b). Viscous fingering in miscible displacements: Unification of effects of viscosity contrast, anisotropic dispersion, and velocity dependence of dispersion on nonlinear finger propagation. *Phys. Fluids*, 4:2348.

Appendix A

Numerical method

In chapters 2 to 5, Darcy's law, incompressibility and an advection-diffusion equation along with the form for the permeability and equations of state for the viscosity and density are solved numerically. The method in which these coupled equations are numerically solved is outlined in this appendix.

A.1 Introduction

The non-dimensional equations in the moving frame that are solved in chapters 2 to 5 are

$$-(\tilde{u} + 1) = \frac{k(y)}{\mu(c)} \frac{\partial \tilde{p}}{\partial \tilde{x}}, \quad -v\mu = \frac{k(y)}{\mu(c)} \left(\frac{\partial \tilde{p}}{\partial y} + Gc \right), \quad (\text{A.1})$$

$$\frac{\partial \tilde{u}}{\partial \tilde{x}} + \frac{\partial v}{\partial y} = 0, \quad (\text{A.2})$$

$$\frac{\partial c}{\partial t} + \tilde{u} \frac{\partial c}{\partial \tilde{x}} + v \frac{\partial c}{\partial y} = \frac{1}{\text{Pe}} \left(\frac{\partial^2 c}{\partial \tilde{x}^2} + \frac{\partial^2 c}{\partial y^2} \right), \quad (\text{A.3})$$

where c is the local concentration of the injected fluid, $\mathbf{u} = (u, v)$ is the Darcy velocity through the medium, p the pressure. For more details about the problem formulation see §2.2. We assume the non-dimensional viscosity μ depends on the concentration

$$\mu(c) = e^{-Rc}, \quad (\text{A.4})$$

the permeability varies transversely

$$\ln(k) = -\sigma \cos(2\pi ny) - \ln(I_0(\sigma)), \quad (\text{A.5})$$

and the density varies linearly with the concentration

$$\rho = \frac{\rho_2}{\rho_1 - \rho_2} + c. \quad (\text{A.6})$$

In total there are five important non-dimensional parameters: the log-viscosity ratio R , the Peclet number Pe , the log-permeability variance σ , permeability wavenumber n , and the gravity number G . In chapter 2 we consider flows where $\sigma = G = 0$, in chapters 3 and 4 we consider flows where $G = 0$ and in chapter 5 we consider flows where $\sigma = 0$.

Along the top and bottom boundaries we either impose periodic boundary conditions

$$c(x, 0, t) = c(x, 1, t), \quad u(x, 0, t) = u(x, 1, t), \quad v(x, 0, t) = v(x, 1, t) \quad (\text{A.7})$$

(chapters 2, 3 and 4) or no-flux boundary conditions

$$\frac{\partial c}{\partial y}(x, 0, t) = \frac{\partial c}{\partial y}(x, 1, t) = v(x, 0, t) = v(x, 1, t) = 0 \quad (\text{A.8})$$

(chapter 5). Along the horizontal boundaries we either impose

$$u(-\infty, y, t) = u(\infty, y, t) = 0, \quad (\text{A.9})$$

$$c(-\infty, y, t) = 1, \quad c(\infty, y, t) = 0, \quad (\text{A.10})$$

(chapter 2) or

$$v(-\infty, y, t) = v(\infty, y, t) = 0, \quad (\text{A.11})$$

$$\frac{\partial c}{\partial x}(-\infty, y, t) = 1, \quad \frac{\partial c}{\partial x}(\infty, y, t) = 0 \quad (\text{A.12})$$

(chapters 3, 4, and 5), although the precise choice of boundary conditions in the horizontal direction do not effect the dynamics.

A variety of techniques have been used to solve the system of equations (A.1) to (A.6). These include spectral methods (De Wit and Homsy, 1997b; Tan and Homsy, 1988; Zimmerman and Homsy, 1991, 1992b, etc.), pseudo-spectral methods (Islam and Azaiez, 2005) and finite-difference methods (Jha et al., 2011a,b, 2013). Here we use a modified finite-difference method, which is numerically stable for all R .

First, given that the flow is incompressible, we write the velocity in terms of a streamfunction $\Psi(x, y, t)$:

$$u = \partial\Psi/\partial y, \quad v = -\partial\Psi/\partial x. \quad (\text{A.13})$$

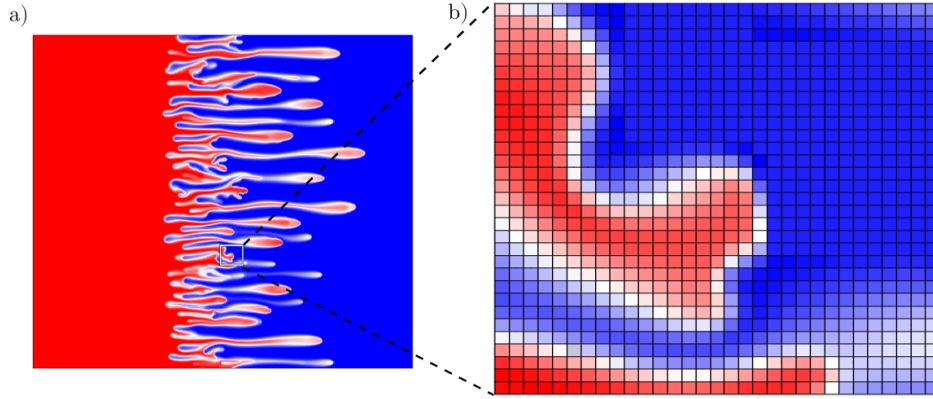


Fig. A.1 (a) Sample snapshot of the concentration field (b) magnified region showing the corresponding gridding. Note that the streamfunction is also solved on the same grid.

Combining equations (A.1) and (A.2) yields an elliptic equation for the streamfunction

$$\frac{\partial^2 \Psi}{\partial x^2} + \frac{\partial^2 \Psi}{\partial y^2} - \frac{\partial \Psi}{\partial x} \left(R \frac{\partial c}{\partial x} \right) - \frac{\partial \Psi}{\partial y} \left(R \frac{\partial c}{\partial y} + 2n\pi\sigma \sin(2n\pi y) \right) = R \frac{\partial c}{\partial y} + Ge^{Re} \frac{\partial c}{\partial x} + 2n\pi\sigma \sin(2n\pi y). \quad (\text{A.14})$$

The boundary conditions on the velocity (A.7), (A.8), (A.9), and (A.11) become

$$\begin{aligned} \Psi(x, 0, t) &= \Psi(x, 1, t), & \Psi(x, 0, t) &= \Psi(x, 1, t) = 0, \\ \Psi(-\infty, y, t) &= \Psi(\infty, y, t) = 0, & \frac{\partial \Psi}{\partial x}(-\infty, y, t) &= \frac{\partial \Psi}{\partial x}(\infty, y, t) = 0 \end{aligned} \quad (\text{A.15})$$

respectively

A.2 Gridding

In order to simulate an infinite strip, we impose the horizontal boundary conditions at $x = \pm\Gamma/2$, where Γ is chosen to be sufficiently large such that these boundaries are far from the interface. We discretize the domain on a rectangular grid with $(n_x(t), n_y(t))$ grid points in the (x, y) direction (figure A.1).

To minimize computational time we use an adaptive grid. Firstly, since previous work has shown that solutions are independent of the aspect ratio as long as the fingered region is sufficiently far from the boundaries (Ruith and Meiburg, 2000; Tan and Homsy, 1988), we use a growing computational domain. Each simulation is initialized with a

domain length $\Gamma = 1$ and whenever the fingered region approaches the boundary Γ and n_x are doubled. Specifically, the domain is doubled whenever $\bar{c}(x = -0.3\Gamma) < 0.999$ or $\bar{c}(x = 0.3\Gamma) > 0.001$. We also allow the number of gridpoints to decrease in time as the concentration gradients weaken. n_x and n_y are initially chosen such that fingers are well resolved (see figure A.1(b)) and decrease in time as the concentration gradients weaken. Specifically, the number of gridpoints in either the x or the y direction are halved every time the maximum concentration gradient in that direction quarters. This process only starts once the maximum concentration gradient has fallen below 10 and $t > 100$. These values were chosen empirically to ensure numerical accuracy and stability while also minimizing computation time. We compared simulations with the adaptive gridding scheme and simulations with fixed domain sizes to confirm that this had no measurable effect on the dynamics.

A.3 Streamfunction equation

At each time step, we solve (A.3) using a second-order accurate iterative multi-grid solver (Adams, 1999) with the solution at the previous time step used as an initial guess. In doing so, the spatial derivatives of the concentration are discretized using compact finite differences (see next section).

A.4 Advection-diffusion equation

At a given time step s , the diffusive terms $D_{xx} := \frac{\partial^2 c}{\partial x^2}/\text{Pe}$ and $D_{yy} := \frac{\partial^2 c}{\partial y^2}/\text{Pe}$ in (A.3) are discretized using sixth order compact finite differences (Lele, 1992). These spatial derivatives are found by solving the system of equations

$$\mathbf{M}D_i(\mathbf{c}^s) = \mathbf{N}\mathbf{c}^s. \quad (\text{A.16})$$

For a given row or column of \mathbf{c} , the matrices \mathbf{M} and \mathbf{N} in the case of periodic boundary conditions are band diagonal cyclic matrices with $(M_{k-1,k}, M_{k,k}, M_{k+1,k}) = (2/11, 1, 2/11)$ and $(N_{k-2,k}, N_{k-1,k}, N_{k,k}, N_{k+1,k}, N_{k+2,k}) = (3, 48, -102, 48, 3)/44(\delta i)^2$. In the case of non-periodic boundary conditions, lower-order accurate discretizations are used on the boundaries.

The advective terms $U_x := u_x \partial c / \partial x$ and $U_y := u_y \partial c / \partial y$ in (A.3) are discretized using a third-order upwinding scheme. For a given grid point l, k , the advective

component in the x -direction is

$$U_{x,l,k} = \frac{\mathbf{u}_{x,l,k}}{12\delta x} \left[\begin{aligned} &(\text{sgn}(\mathbf{u}_{x,l,k}) - 1) \mathbf{c}_{l-2,k} + (4\text{sgn}(\mathbf{u}_{x,l,k}) - 8) \mathbf{c}_{l-1,k} + \\ &(-6\text{sgn}(\mathbf{u}_{x,l,k})) \mathbf{c}_{l,k} + (8\text{sgn}(\mathbf{u}_{x,l,k}) + 4) \mathbf{c}_{l+1,k} + (-\text{sgn}(\mathbf{u}_{x,l,k}) - 1) \mathbf{c}_{l+2,k} \end{aligned} \right], \quad (\text{A.17})$$

and y -component can be similarly discretized. For non-periodic boundary conditions, lower-order accurate discretizations are used on the boundaries.

Equation (A.3) is then advanced explicitly in time using a third-order Runge-Kutta scheme:

$$\begin{aligned} \frac{\mathbf{c}^{s+1/2} - \mathbf{c}^s}{\Delta t/2} &= \mathcal{L}\mathbf{c}^s, \\ \frac{\mathbf{c}^{s+1} - \mathbf{c}^s}{\Delta t} &= 2\mathcal{L}\mathbf{c}^{s+1/2} - \mathcal{L}\mathbf{c}^s, \\ \frac{\mathbf{c}^{s+1} - \mathbf{c}^s}{\Delta t} &= \frac{1}{6}\mathcal{L}\mathbf{c}^s + \frac{2}{3}\mathcal{L}\mathbf{c}^{s+1/2} + \frac{1}{6}\mathcal{L}\mathbf{c}^{s+1}, \end{aligned} \quad (\text{A.18})$$

where

$$\mathcal{L}\mathbf{c} := \mathbf{U}_x(\mathbf{u}_x, \mathbf{c}) + \mathbf{U}_y(\mathbf{u}_y, \mathbf{c}) + \mathbf{D}_{xx}(\mathbf{c}) + \mathbf{D}_{yy}(\mathbf{c}). \quad (\text{A.19})$$

The time step, $\delta t = \min(10^{-6}\text{Pe}, \min(\delta x/u_{\max}, \delta y/v_{\max}))$ is chosen to be sufficiently small to ensure stability of both the advective and diffusive parts.

A.5 Validation

We first validated the solver for the streamfunction by comparing to known analytical solutions and found that errors decayed with the square of the grid resolution. We similarly found that errors of the combined code decayed with both the grid resolution and time-step. To validate the numerical scheme we first compare the numerical results to the linear stability analysis of Pramanik and Mishra (2015) (figure A.2(a)) and find very good agreement. We also find that the results are grid-independent; doubling of the number of grid points has no qualitative or quantitative effect on the dynamics in the nonlinear regime (figure A.2(b)). Note that in figure A.2(b), there are initially discrepancies due to discretization error, but these errors become insignificant over time.

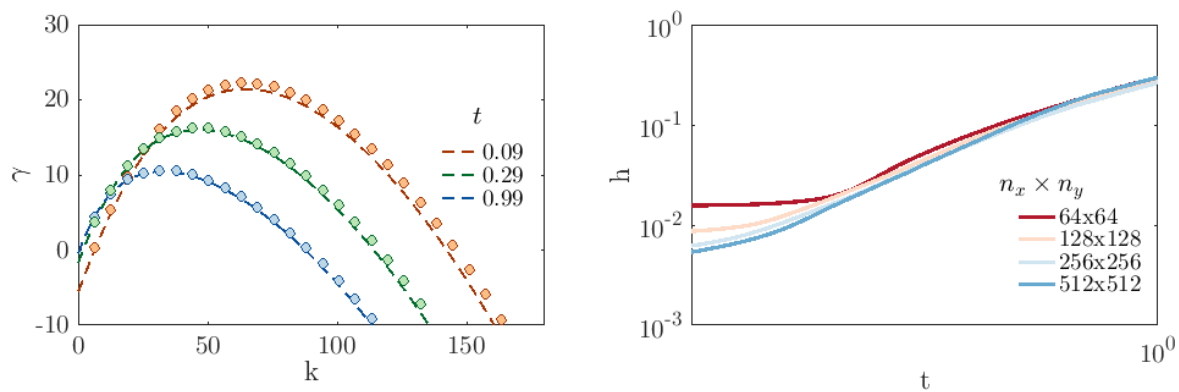


Fig. A.2 (a) Growth rate, γ , vs. wavenumber, k for $(R, Pe, \sigma, n, G) = (3, 500, 0, 0, 0)$ from the full 2D numerical simulations (dots) and linear stability analysis (dashed lines). (b) Evolution of the mixing length, h , as a function of time t for $(R, \sigma, Pe, n, G) = (2, 0.01, 4000, 2, 0)$ and different grid-resolutions, $n_x \times n_y$.